The effect of process parameter variation on the emissivity and resistivity of 316L stainless steel manufactured by Selective Laser Melting

Christopher Oladipo Ogunlesi

ORCID: 0000-0001-9078-1901

Aeronautical and Astronautical Engineering Department

Engineering and Physical Sciences

University of Southampton

This dissertation is submitted for the degree of Doctor of Philosophy

July 2022

University of Southampton Research Repository

Abstract

The Super High Temperature Additively manufactured Resistojet (STAR) is an ongoing project to develop a novel resistojet thruster which will act as the primary propulsion device on small satellites. To enable the complicated geometry of the resistojet, Selective Laser Melting (SLM) was chosen as the production method. Post processing on internal features was limited for this same reason. Multiphysics modelling was used to predict the temperatures reached in the hottest parts of the thruster. However initial simulations revealed large discrepancies between the actual and predicted temperatures. These differences were attributed to the materials properties used for emissivity and resistivity. Emissivity is largely dependent on surface texture while resistivity can be influenced by the density and microstructure. Both properties are also highly dependent on temperature. SLM as-built parts can have vastly different surface textures and microstructure compared to cast or machined parts, but there is little data on resistivity and emissivity available. Furthermore, material structure and properties from SLM can vary significantly depending on process parameters. This motivated the project aim to obtain accurate emissivity and resistivity data of SLM metals and to study the relationship between SLM process parameters and the total hemispherical emissivity and resistivity of representative test coupons for as built 316L stainless steel. This was achieved by varying process parameters and measuring how these affected the output factors (responses) of surface texture, microstructure and part density which were then related to emissivity and resistivity. The relationship between the inputs and surface texture parameters (Sa, Sq, Ssk, Sku and Sdq) was a particular focus as there are currently no standards on how to measure or quantify surface roughness of SLM parts, leading to a lack of consistency in the literature. The input parameters chosen were those that make up the volumetric energy density (laser power, scanning speed, hatch spacing and layer thickness) and build orientation. A definitive screening Design of Experiments method was used to gain as much understanding of the influence of these input parameters on responses with as few experimental runs as possible. Seventeen experimental runs were completed, each varying the input parameters over one of three levels (low, mid, and high). Emissivity and resistivity were measured over a range of elevated temperatures using the calorimetric and four probe methods respectively. Finally, multiple linear regression models were created to identify which factors more strongly affected the responses. Results showed that emissivity ranges of most of the as-built SLM

parts were similar to cast parts, but the 0° samples were consistently higher. SLM resistivity was also consistently higher than cast parts over the entire measured temperature range. When emissivity was determined using surface area from nominal sample dimensions measured using callipers, some of the values obtained were higher than the maximum emissivity of a black body. Using X-ray microcomputed tomography (microCT) imaging to determine sample dimensions gave higher surface areas and yielded lower emissivity values that were within physically admissible limits. Emissivity was found to correlate strongly to surface area regardless of temperature or emissive power, decreasing as surface area increased. When considering roughness on the size scale similar to the wavelength of the radiation, emissivity is governed by internal reflections within surface features. The SLM surfaces produced may not have had the types of features that led to more internal reflections but only increased the overall surface area. Thus the emissive power per unit area decreased, as did the emissivity. No trend was found between emissivity and any of the surface texture parameters. Resistivity was found to strongly correlate with the density of the samples, increasing as the density decreased, likely due to the interruption of conductive pathways. Multiple linear regression models found that build angle and layer thickness were the most significant factors that affected surface area and emissivity. More accurate temperature predictions were successfully obtained with multiphysics simulations using the newly measured values for emissivity and resistivity, particularly at higher temperatures. Emissivity values based on nominal sample dimensions, despite being impossibly high, were found to produce accurate simulation results by incorporating the effect of the higher surface area revealed by microCT but not directly included in the simulated geometry. The emissivity and resistivity measurements done using the techniques described in this thesis enabled accurate temperature simulations of the resistojet thruster which allowed for better estimation of the performance of the thruster. Whilst only 316L stainless steel is described in this thesis, the same setup and techniques were used to also measure the emissivity and resistivity of other, higher temperature materials used to build the resistojet. These measurements and the better understanding of emissivity and resistivity of SLM materials are also useful in wider application areas, such as predicting temperatures in nuclear reactors or making in-situ temperature measurements during the SLM process.

Acknowledgements

First, a massive thank you goes to my two supervisors I've had over the last four years, Prof Andrew Hamilton, and Dr. Angelo Grubišić for supporting me throughout the PhD programme. Andrew, your expertise, advice, and helpful discussion over countless meetings (both in-person and online!) helped me to see think things through and tackle the challenges from different angles. Thank you also for the thankless task of proofreading this thesis which wouldn't be complete without your help. Angelo, thank you for giving me the opportunity to do this research in the first place. You left this world far too soon and I hope this work makes you proud. Special thanks also to Federico who helped focus my research efforts and to Phillipa Reed for introducing me to the engineering materials group.

Thank you to the staff at Southampton that helped me make this work possible. To Richard Dooler and the rest of the EDMC team for building my samples, and to Katy, Richard, Sebastian, Mark, and the rest of the μ-vis team for the hours spent scanning and analysing my samples (and sorry for all the times you had to un-archive my data)

Huge amounts of love and gratitude goes to my friends and family that both kept me sane and suffered with me through this. To my parents whose love and support have made me everything I am and given me everything I am. Hopefully you won't mind another doctor in the family. To my brother Daps and Sophie, thanks for all the meals and for not complaining about all the times I vented at you. To all my friends, especially Matt and Rike. We've all laughed and suffered together over the last few years, and I can't wait for all of us to be doctors together.

And absolutely the biggest thanks go to Silvia, the love of my life. You have put up with my lowest lows that I've endured because of this thesis and your infinite patience, kindness and JMP expertise have made these last few years not only bearable, but wonderful. In your thesis a few years ago, you wrote that there's no one you'd rather co-doctor with. That wouldn't be possible without your help, and there's no one I'd rather share a life with.

And finally. To pizza. For all the yums.

Table of Contents

List of Figures

List of Tables

1. Introduction & Objectives

Background and motivation

Resistojets are electrothermal thrusters that have a long history of being used in numerous different roles for spacecraft propulsion including station-keeping, orbit adjustment and de-orbiting manoeuvres [1]. They operate by passing a propellant gas over a resistive heating element at high pressure before expanding and accelerating the gas through a nozzle to produce thrust. For a given nozzle shape and propellant the efficiency of a resistojet, described as the specific impulse (I_{sp}) and measured in seconds, is directly tied to the maximum temperature to which it can heat the gas propellant: the hotter the gas the higher the efficiency. This is described through equation [1], where u_e is the exhaust velocity g_0 is acceleration due to gravity (9.08 m/s^2), η_n is the nozzle efficiency, c_p is the constant pressure specific heat of the propellant gas and T_c is the chamber temperature.

$$I_{sp} = \frac{u_e}{g_0} \approx \eta_n \sqrt{\frac{2c_p T_c}{g_0}} \qquad [1]$$

Thus, the efficiency is directly linked to the material and design of the resistojet, which has been limited in the past due to the melting temperature of materials and costly or laborious manufacturing methods [2]. A benchmark for current resistojets is the T-50 thruster produced by Surrey Satellite Technology Ltd. (SSTL) which, when using xenon propellant, can achieve a specific impulse of up to 57 s at a temperature of 923 K [2].

Due to their potential high efficiency, low complexity compared to other electric propulsion systems and ability to work with non-toxic propellants, resistojets have been identified as potential candidates to be used as a secondary propulsion system for attitude control on fully all-electric propulsion spacecraft. Creating an improved resistojet design to meet these needs by reaching a temperature of 1200 K and an I_{sp} of at least 80 s with xenon was the focus of the work of F. Romei *et al.* [3].

They used additive manufacturing, specifically Selective Laser Melting (SLM), to develop a novel thin-walled concentric tubular heat exchanger in 316L stainless steel. This resistojet was referred to as the Super-high Temperature Additive-manufactured Resistojet (STAR), a rendering of which is shown in Figure 1. F. Romei *et al.* used multiphysics modelling to evaluate the electrothermal characteristic of the thruster and found that there was a notable difference in temperature between the experimental results and the model results. This difference was attributed to the material properties assumed for emissivity and resistivity, which were taken from literature for cast metals and so may not accurately reflect the properties of additively manufactured metals.

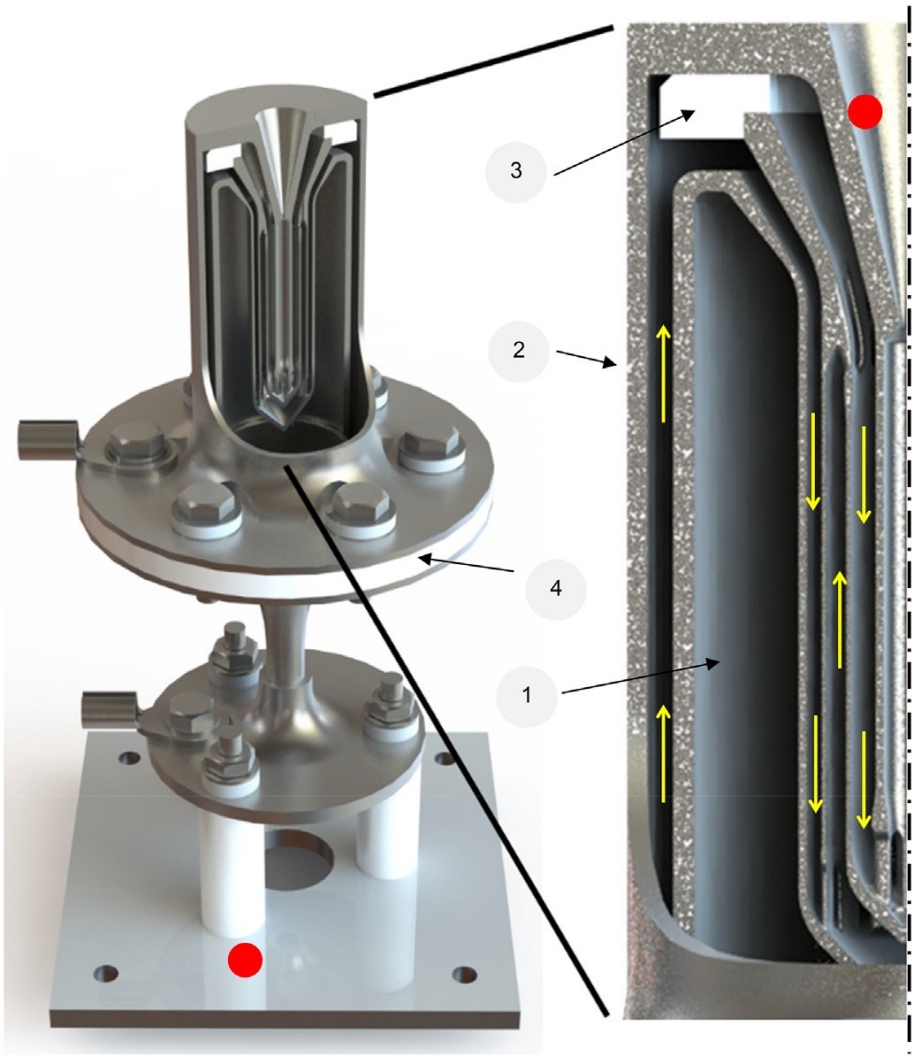

Figure 1: Rendered CAD cutaway of STAR thruster prototype. Labelled features: 1- AM heat exchanger/nozzle, 2- pressure case, 3-ceramic nozzle spacer, 4-ceramic collar. Yellow arrows indicate propellant gas flow. This image was originally by M. Robinson *et al.* [1]. Reproduced with permission Creative Commons CC-BY

Emissivity, a measure of the thermal energy radiated from a surface, is highly dependent on several variables including surface temperature, roughness, and composition. Resistivity, a measure of a material's inherent resistance to electrical current, is a bulk phenomenon and can be affected by microstructural features such as grain boundaries and porosity. The high cooling rates and layer-by-layer build process of SLM can result in vastly different microstructures and surface topographies for as-built parts compared to cast or wrought metals, which can in turn affect materials properties such as emissivity and resistivity. From reviewing the literature, there was little data on the emissivity and resistivity of SLM metals, and no relevant data for SLM 316L over the desired operating temperature range of the STAR, representing a notable gap in knowledge.

The work in this thesis was a continuation of the work of F. Romei *et al.* and aimed to investigate how the SLM process and the input parameters affected the emissivity and resistivity of 316L stainless steel, and to measure the relevant data to improve the multiphysics model of the resistojet. Although originally inspired by the needs of the STAR, given the recent increase in use of additive manufacturing in numerous industries [4], this work has further application in areas where high temperature materials properties are needed, such as in-situ process monitoring and nuclear applications.

1.1. Aims and objectives

The primary aims of this work is to investigate the cause behind the temperature difference between the simulation and experiments and to investigate the relationship between SLM process parameters and their effects on the emissivity and resistivity of 316L stainless steel. These aims will be divided into specific objectives including:

- Selection of an experimental window of process parameters to create samples representative of the resistojet and to cover as wide a design space as possible.
- Measuring the emissivity and resistivity of representative test coupons over the operational temperature range of the thruster.

- Performing an in-depth study of how altering the SLM process parameters affects the microstructure and surface topography of test samples and how these in turn affect the emissivity and resistivity.
- Creating a multiphysics model of the experimental setup using measured values of emissivity and resistivity and comparing the results against simulations using literature values for cast 316L stainless steel.

1.2. Outline of thesis

To address the aims and objectives identified here in the first chapter, the following outline was adopted for the remainder of this thesis .

The second chapter provides the fundamental theory and knowledge behind the SLM process including the different process parameters and the effects they can have on the parts produced, surface roughness and how it is defined, electrical resistivity and emissivity.

The third chapter is a literature review covering the state of the art on methods for measuring surface roughness, electrical resistivity, and emissivity. It also reviews the process parameters used to produce thin-walled and high-density parts in 316L stainless steel, which informed the process parameters used in this work.

The fourth chapter details the methodologies adopted to measure surface topography, microstructure, emissivity, and resistivity. This includes a detailed overview of the Design of Experiments method and the process parameter ranges chosen.

The fifth chapter presents and discusses surface roughness results. First an overview of the data collected is given, discussing trends in the results that may have occurred due to variables not considered when designing the experiment. This is followed by an in-depth look at how the results vary with the changing process parameters before using a multiple linear regression model to investigate what the most significant input factors are and why.

Following the roughness results, the sixth chapter presents the emissivity results. First an overview of the data is presented before determining if and how these results correlate with the different surface texture parameters, surface area,

and volumetric energy density. Finally, a regression model is used to determine the most significant input factors before discussing the reason for observed effects and comparing with the roughness model.

The seventh chapter presents the electrical resistivity results, beginning with an overview of the data before discussing how the relative density and microstructural features of the parts are impacted by changing process parameters and how these in turn affect the resistivity. Throughout the chapter, models are presented linking the process parameters to the outputs in terms of significance. Comparisons are also made between the different methods used to measure the microstructural features and how these might have affected the results.

The eighth chapter is a summary of the different multiphysics models that were created to simulate the experimental setup. A brief overview of the software COMSOL Multiphysics is presented before detailing the different models that were created. The resulting temperature predictions are presented and compared with experimental results.

Lastly the ninth chapter provides a summary of the main conclusions and recommendations for future work on this topic.

2. Background & Theory

Before describing the experiments carried out to tackle the objectives listed in the previous chapter, it is first necessary to understand the key fundamental concepts that make up the bedrock of this thesis. This chapter will go over these concepts which include selective laser melting, surface roughness, thermal radiation heat transfer and electrical resistivity.

2.1. Theory of Selective Laser Melting

2.1.1. Overview and principles

The American Society for Testing and Materials (ASTM) international committee F42 on Additive Manufacturing (AM) technologies defines AM as [4]

"The process of joining materials to make objects from 3D model data, usually layer upon layer, as opposed to subtractive manufacturing technologies."

Additive manufacturing allows for the direct deposition of material where it is required, allowing for increased complexity of design compared to traditional subtractive manufacturing. AM can also reduce cost, as less material is required to build components. In recent years there has been a reduction in barriers for industrial adoption of AM and a boom in research interest in AM [5][6] due to its ability to manufacture replacements or components with unique or complex geometries [7].

Powder Bed Fusion (PBF) is a blanket term used to refer to all additive manufacturing processes that use a high-power density energy source to melt and fuse together thin layers of powder [8]. There are numerous different types of PBF processes with slight variations, such as whether the energy source is a laser or electron beam. The focus of this thesis was Selective Laser Melting (SLM). This technique can produce near net-shape parts with up to 99.9% relative density from various metals and metal alloys including aluminium, iron, titanium and nickel [9].

SLM creates components based on Computer Aided Design (CAD) data files. These files are first converted into Stereolithography (STL) files using specialised software and "sliced" into numerous layers to later be sequentially laser scanned and combined to produce the shape. At this stage support structures may also be added for overhanging features of the CAD design. The SLM process begins with a thin layer of metal powder spread evenly on a substrate plate using a roller mechanism in a building chamber. A high energy density laser then melts selected areas of the metal powder according to the sliced layer data of the STL file. Once the laser has finished scanning, the substrate plate is lowered, a new layer of powder spread, and scanned by the laser. This process is repeated until the complete component has been built. Loose powder is then removed from the build chamber, and the part removed from the substrate build plate [9]. To prevent oxidation of the metal parts during the build process, the chamber is filled with an inert gas such as nitrogen or argon.

The SLM process has numerous process parameters as well as physical phenomena that control the quality of the resultant components [7]. Numerous sources have found that the thermal history experienced by the components during the build process influenced the resultant surface quality and microstructure which in turn affected mechanical properties [10]–[12]. The next section discusses in more detail the physical processes that occur during the build process and how these influence the parts produced.

2.1.2. Physical processes

During the SLM build process, a pool of molten metal known as the melt pool (or melted zone) is formed as the laser melts the powder particles. The size of this melt pool grows into an amalgamated area as the laser moves forward to melt the next area of powder. According to Pal *et al.* [13], and as shown in Figure 2, during the melting process there are 8 action zones:

- Inert gaseous zone
- Powdered zone
- Melted zone
- Re-melted zone
- Mushy zone
- Solidified zone
- Heat affected zone
- Vapor zone

Other than the vapor zone, defects occur when there are instabilities in these zones, causing improper transitions between them.

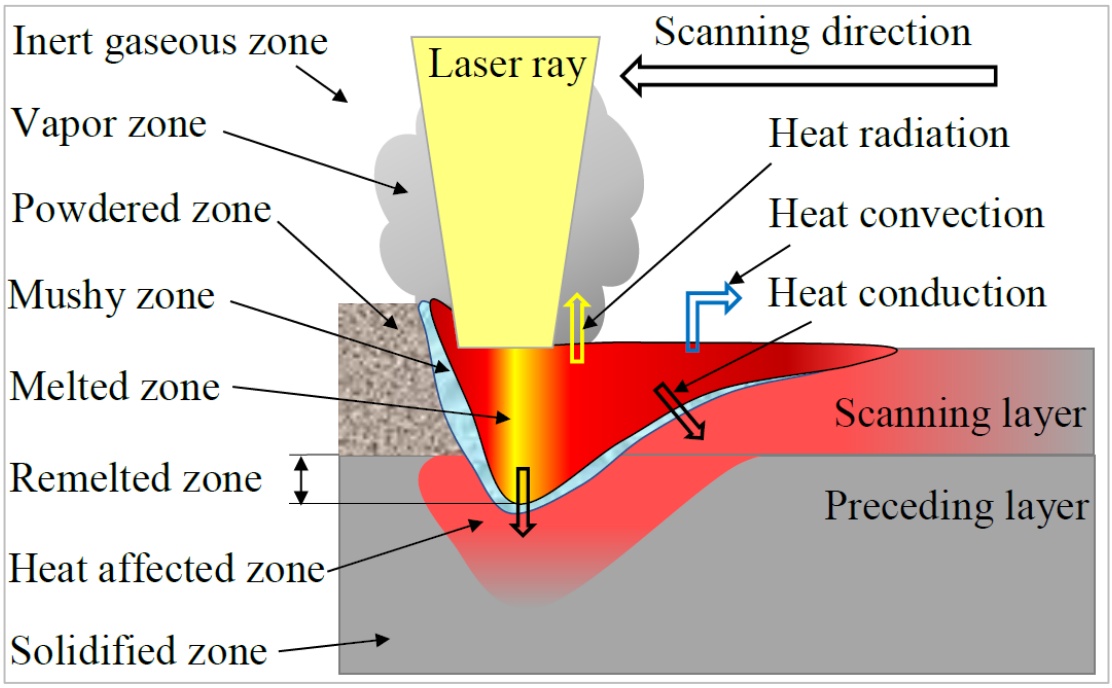

Figure 2: Diagram showing the 8 different actions zones that occur during the SLM build process. This image is originally by Pal *et al.* [13]

Melt pool dynamics

The melt pool is made up of loose powder particles melted by the laser and partial melting of the previous layer and track dubbed the "re-melted zone". The depth of the melt pool and thus the amount of re-melting of the previous layer is partially determined by the amount of energy applied per volume of material (known as the energy density and explained further in the next section). The spacing between each of the scan tracks determines the amount of overlapping and thus re-melting. Re-melting of previous layers and tracks is key to building up an overall solid structure by connecting previous layers to the melt pool. The shape of the melt pool is influenced by a mass transfer phenomenon known as the Marangoni effect in which low surface tension fluid is moved to areas with higher surface tension [14]. Surface tension, caused by cohesive forces between molecules within a liquid at its surface, causes a liquid surface to shrink by reducing its surface area [15]. The difference in surface tension seen in melt pools is known as a surface tension gradient and is affected by both temperature and composition. Generally, areas with a higher temperature have a lower surface tension [16]. The direction of fluid flow is

determined by the sign of the gradient. A negative gradient indicates that surface tension reduces with an increasing temperature and prompts a radial outward flow of the molten metal and produces a wider and shallower melt pool. A positive gradient causes radial inward flow and produces a deeper and narrower melt pool.

The "mushy zone" shown in Figure 2 is comprised of a mixture of partially melted powder next to the surface of the melt pool. This material absorbs heat from the melt pool, becoming soft and pulpy [13] [17]. As this mushy zone is surrounded by colder material on the outside surface, it solidifies quickly. Due to its rapid cooling rate and high viscosity, particles adhere to the mushy zone with ease.

After the laser has moved on, the melt pool cools into the solidified zone. Cooling and solidification rates determine the microstructure and other features of this zone, such as distortion and pore formation. These in turn can be controlled by variation of the process parameters discussed in the next section.

The heat affected zone is created due to the conduction of heat away from the melt pool by the surrounding particles and can extend up to hundreds of micrometres. On the front side of the melt pool (in the direction the laser is travelling) this heat helps to reduce thermal shock and release inert gas trapped between particles. This thus reduces the chances of material being ejected from the melt pool, known as spattering.

Microstructure

The solidified microstructure is dependent on the thermal history of the part including the local solidification rates within the melt pool, the cooling rate, and the temperature gradient [18]. Differences in thermal history can result in different microstructural morphologies:

- Columnar: Elongated grain morphologies
- Columnar plus equiaxed
- Equiaxed: Isotropic grain morphologies

Higher solidification rates and lower temperature gradients promote the transition from columnar to equiaxed morphologies and increased cooling rates leads to finer microstructures [18]. Such morphologies are also dependent on their location

within the part. At the bottom of a part heat is quickly conducted away by the build plate which acts as a thermal sink. At the top, increased surface area and fewer re-heating cycles result in greater heat loss through convection and radiation. Thus, at both the bottom and top of parts, the microstructure is typically finer due to these increased cooling rates. A coarser microstructure is typically seen in the middle region of parts due to lower cooling rates and more cyclic reheating [12] [19].

2.1.3. Process parameters

There are several different SLM process variables that can influence the quality of the output component. Yadroitsev *et al.* [20] separated the input parameters into three categories:

a) Powder: composition, size distribution, shape, optical and heat transfer properties, thickness of deposited layer for each cycle of fabrication
b) Laser: power, spot size, beam spatial distribution, scanning velocity and application of protective gas atmosphere
c) Strategy of manufacturing: decomposition of each plane to be sintered on several elementary elements (vectors), definition of orientation and distance between them, definition of relative positions of elements into consecutive planes

While all of these play a part in determining the overall part quality, from reviewing the literature it was found that for the SLM process there are five process parameters that are commonly varied to influence the quality of the output component. These variables are laser power, scanning speed, hatch spacing, layer thickness and build orientation [9][7][21].

Energy density

There are over 50 process parameters, as well as interactions between them, which can affect the output quality of parts fabricated through SLM [22]. The volumetric energy density combines four key process parameters to provide a single variable that can be used as a simple predictor of overall part quality [7], [22]. The energy density is a measure of the average amount of energy applied per volume of

material during the SLM process [23] and relates to the volume of powder melted and the resulting melt pool size [24]. Volumetric energy density (ω) is defined in equation [2] as:

$$\boldsymbol{\omega = \frac{P}{vsl}} \qquad [2]$$

Where P is the laser power, v is the scanning speed, s is the hatch spacing and l is the powder layer thickness (as shown in Figure 3). The amount of energy input to the powder is dependent on the power of the laser and dwell time of the laser, as determined by the scanning speed. The distance between adjacent melt tracks, as determined by the hatch spacing, and the powder layer thickness both affect the volume of material over which energy input is required in order to form overlapping melt pools [13].

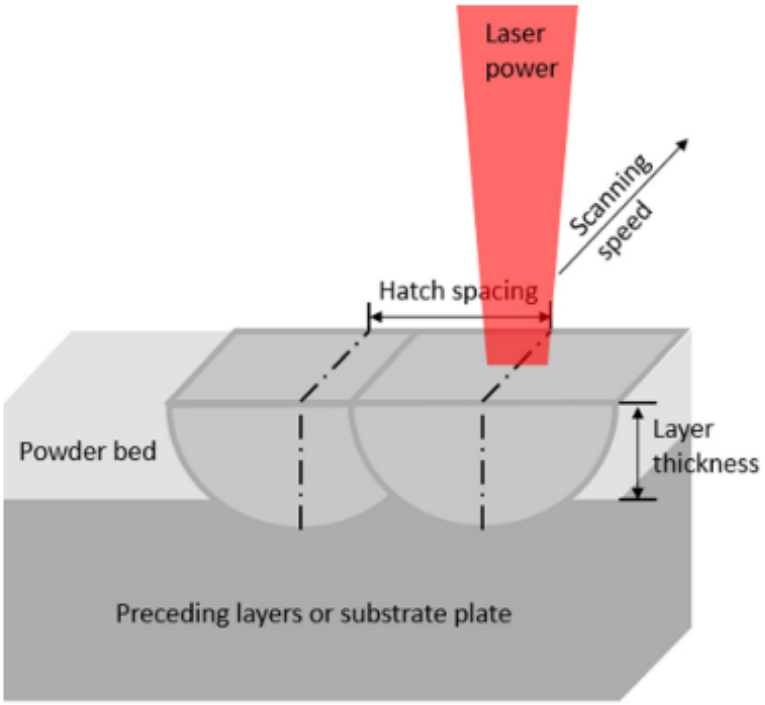

Figure 3: Diagram of the different SLM process parameters that make up energy density – laser power, scanning speed, hatch spacing and layer thickness. This image is originally by C. Yap *et al.* Reproduced with permission. [9]

A lower energy density may result in improper or incomplete melting of the powder particles, whilst a higher energy density may cause turbulence, instability and vaporisation of the melt pool [13]. Fayazfar *et al.* stated [7] that energy density

is commonly seen as a very good predictor for the relative density of parts and numerous sources were found investigating energy density as a critical factor in the fundamental properties of as-built parts such as porosity, microstructure and phase proportion [21][25][23][26].

Build orientation

SLM parts can be built in different directions relative to the build plate. This build orientation will affect the cooling and solidification rates of the parts as it affects how much of the part is connected to the build plate below which acts as a heat sink. This can lead to anisotropic microstructure and properties due to directional and spatially varying thermal conditions [27][25].

Columnar grains tend to orient inclined from the build plate and towards the laser beam or melt pool direction of travel in each layer. Grains develop in parallel with local heat transfer through conduction and solidify perpendicular to isotherms. Thus, these local heat transfer conditions determine features sure as grain orientation and texture. As the build height of parts increase, the bulk temperature of these parts during processing increases and thus heat transfer through the build plate may decrease due to an increase in convection and radiation of the part. This causes more epitaxial growth of grains [12]. These changes in grain orientation led to anisotropic responses in mechanical properties. Generally, the literature reports similar or superior quasi-static mechanical properties, such as fracture toughness and tensile strength, of AM parts compared to their cast or wrought counterparts [28][25][5]. However post processing techniques generally are required to obtain comparable dynamic mechanical properties such as fatigue lifetime [5].

SLM parts are sometimes built with overhanging features that are not supported during building either by solidified material or the substrate build plate. These overhanging features are prone to defect formation that affects the surface quality and microstructure. The uppermost, visible layers of a part are referred to as the upskin while the area of a part that faces down towards the build plate, such as the underside of an overhanging part, is referred to as the downskin. The process of discretising CAD models into discrete layers for AM results in stepwise

approximations of inclined features with surface normals that are not parallel to either the build plate or the build direction. This is known as the staircase or stair-step effect, which increases the roughness of printed part and becomes more pronounced as the inclination angle relative to the build plate increases and as layer thickness increases [29] [30].

Unlike features directly connected to the build plate, overhanging features only have unmelted powder to support them. The heat conduction rate for these overhanging features is much lower compared to solid supported features. Thus, the concentration of energy absorbed by the laser in these regions will be much higher, causing the melt pool to grow large and sink into the powder due to gravity and capillary forces [29], reducing the dimensional accuracy, and increasing the surface roughness of the part. Overhanging features can also become warped due to thermal stresses caused by rapid solidification and a lack of support structures [29].

Scanning strategy

Numerous authors have stated that the scanning strategy, which defines the speed and direction that the laser moves, influences the residual stress, microstructure and texture of the resultant parts [31][32][33] [34]. This is because the path that the laser follows has a large effect on the heat distribution and can directly influence localised temperature peaks [35].

Scanning is separated into two stages: contour and fill modes. In contour mode, the outline of the parts slice section is scanned [35]. This is usually done to improve the quality of the surface finish around the perimeter of the part and can be scanned either before or after the rest of the cross section. Four common strategies for the fill mode are: meander, stripes, island (or chess), and contour as shown below in Figure 4.

The island scan strategy, which was used in this work, involves dividing each slice of the build layer into squares (known as islands) resulting in a checkerboard pattern. Within the squares themselves the laser is scanned in alternating vectors, the spacing of which is defined by the hatch spacing and the speed defined by the scan speed.

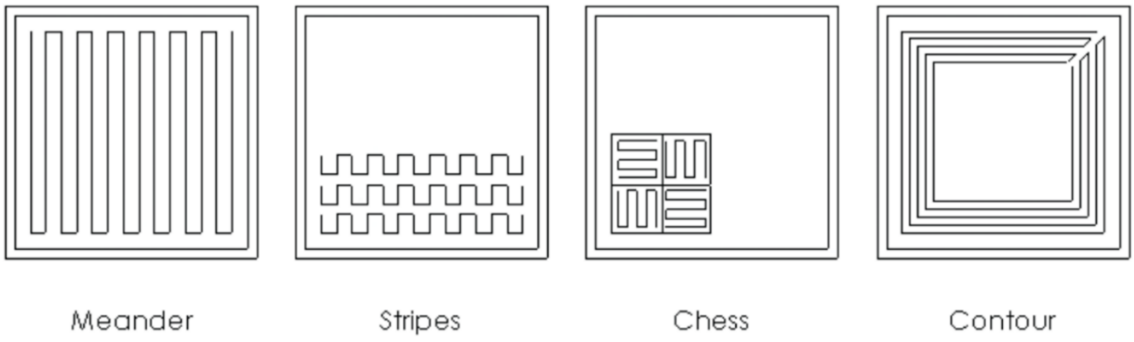

Figure 4: Diagram of four different scanning strategies. This image is originally by D. Pitassi *et al.* Reproduced under Creative Commons Attribution 3.0 License [35]

These squares are melted in a random order in order to reduce residual stresses to avoid cracks and deformation [32]. After each layer is scanned, the scan strategy is rotated to help balance the temperature distribution in the part and reduce the chance of the powder recoater blade becoming caught on straight boundaries.

2.1.4. Unwanted physical phenomena

Energy density and its individual process parameters were previously discussed as being key factors in predicting the overall density of a part produced through SLM. Unsuitable combinations of parameters could otherwise cause unwanted physical phenomena that lower the overall build quality by increasing the roughness or reducing the accuracy of the actual part compared to the nominal CAD geometry.

Balling

Balling is the term given to the formation of spherical or elliptical particles on the surface of a part due to surface tension and the melted powder layer not wetting the substrate layer [9][36]. This is caused by insufficient energy being delivered through a combination of too low laser power, high scanning speed and large layer thicknesses [9]. These beads can obstruct the formation of continuous melt lines and cause increases in surface roughness or in worse cases interrupt the powder coating mechanisms. Li *et al.* reported that balling could be reduced by reducing the oxygen content to 0.1% and by remelting of the SLM surface as this would allow the beads to be melted and wet the surface properly [36]. Further details from the literature will be expanded upon in the roughness literature review section of this thesis.

Porosity

Porosity is a blanket term used to refer to voids within SLM structures that lower the overall density of a part. These pores can be irregular in shape causing corners, trenches, or ripples within the volume. Corner edges can be the initiation site for microcracks, while trenches and ripples can act as stress concentrators [13]. Sizes of these pores can vary from the nanoscale to hundreds of micrometres and may contain unwanted remnants of the build process such as raw or partially melted powder or trapped inert gas. Pores may also occur on the surface of parts, leading to an increase in surface roughness and decrease of surface quality. There are numerous mechanisms that can lead to the formations of pores through different combinations of process parameters such as lack of fusion, sputtering, the keyhole effect, or the entrapment of gaseous bubbles.

Lack of fusion

Insufficient overlap of successive melt pools, caused by low energy densities, can create gaps of partially and unmelted particles between adjacent melt pools [37][13]. As the melt pool solidifies and shrinks, this can create microcracks between the partially melted powder and the melt pool. Increased track overlapping can ensure the complete melting of all particles within the action zone; however, this increase in energy density may result in spattering of material from the melt pool.

Spattering

A high energy density can cause spattering which is the ejection of molten metal particles due to instabilities within the melt pool. The high laser power beam causes vaporisation of the liquid metal and the subsequent gas expansion of the powder creates recoil pressure and causes molten metal ejection from the melt pool. This pressure can also cause ejection of non-melted powder particles and liquid metal which forms droplets that adhere to the surface resulting in increased surface roughness [38].

Keyhole effect

The keyhole effect is caused by too slow a scanning speed and too high a laser power, resulting in excessive materials evaporation [39]. Some of the laser is reflected from the top of the powder, whilst some penetrates deeper into the powder bed where it is scattered. This scattering results in a higher temperature compared to the top powder layer resulting in evaporation and formation of a melt pool under the powder surface [13]. Higher scanning speeds help to reduce keyhole formation as they increase solidification rates and lower local energy densities.

Entrapment of gaseous bubbles

Gaseous bubbles from interparticle gaps can become mixed in with the melt pool, potentially breaking into several smaller bubbles and forming spherical pores within the part that lower the overall density. Increasing the energy density reduces the viscosity of the melt pool, increasing the likelihood of ejection of the gaseous bubbles however this can lead to explosions of the melt pool due to expansion of the gas [13].

Poor surface quality

Energy density and build orientation are the key parameters that influence surface quality. Mumtaz *et al.* found that high laser power can reduce balling formation and increase recoil pressure within the melt pool to flatten it out, reducing top and side part roughness [40]. Increasing the repeat scanning rate whilst reducing scan speed was also found to reduce top side roughness. As previously stated, build orientation has a large effect on surface roughness, with the surface topography of parts manufactured at 0° relative to the build plate mostly determined by the ripple effect [30] [41]. Ripples can be left on the surface due to the quick solidification of the melt pool not giving enough time for ripples caused by temperature gradient induced shear forces to flatten out [30]. As the inclination of the parts increases, roughness is mostly determined by the staircase effect. Strano *et al.* found that partially melted particles tend to stick to these edges due to insufficient heating [30].

This phenomenon increases with the sloping angle and becomes the primary source of roughness for surfaces within inclination angles greater than 45° relative to

the build plate [41]. Downskin surfaces of inclined parts typically have lower surface quality compared to upskin parts as the melt pools sag due to gravity. Balling and porosity can also both affect the overall surface quality of SLM parts, leading to increases in surface roughness and reductions in both density and mechanical behaviour.

Post processing such as machining and etching are usually required to improve surface quality, however these can be costly or laborious and depending on the complexity of the parts geometry cannot always be employed on areas such as on internal surfaces.

Whilst there are many definitions and standards for surface roughness of traditionally made parts, no such standards exist for AM parts. This makes it difficult to define exactly what constitutes as roughness and how to measure it. Numerous different sources in the literature gave different definitions and methods. This will be further expanded upon in the literature review section of this thesis.

2.2. Theory of surface roughness

2.2.1. Overview and principles

R. Leach *et al.* [42] described three methods of defining surface features:

- Surface topography – the overall surface structure of a part, including features over all spatial wavelengths
- Surface form – the underlying shape of a part
- Surface texture – The surface features that remain after the form has been removed, usually of shorter wavelength than the surface form

Surface texture can be further divided into roughness and waviness, as defined by EN ISO 4287:1998 [43]. Both roughness and waviness are derived from the surface by supressing longwave and shortwave components of the surface. However, they differ by the size of the wavelengths filtered. The filter which defines the intersection between the roughness and waviness components of a surface is known as the λc profile filter [43]. Generally, it can be stated that the cut-off wavelengths for

roughness are smaller than those for waviness. This is demonstrated in Figure 5 which shows a generalised difference between length scales for roughness and waviness. The work carried out in this thesis will focus on the roughness rather than waviness as roughness was identified as a key factor influencing emissivity.

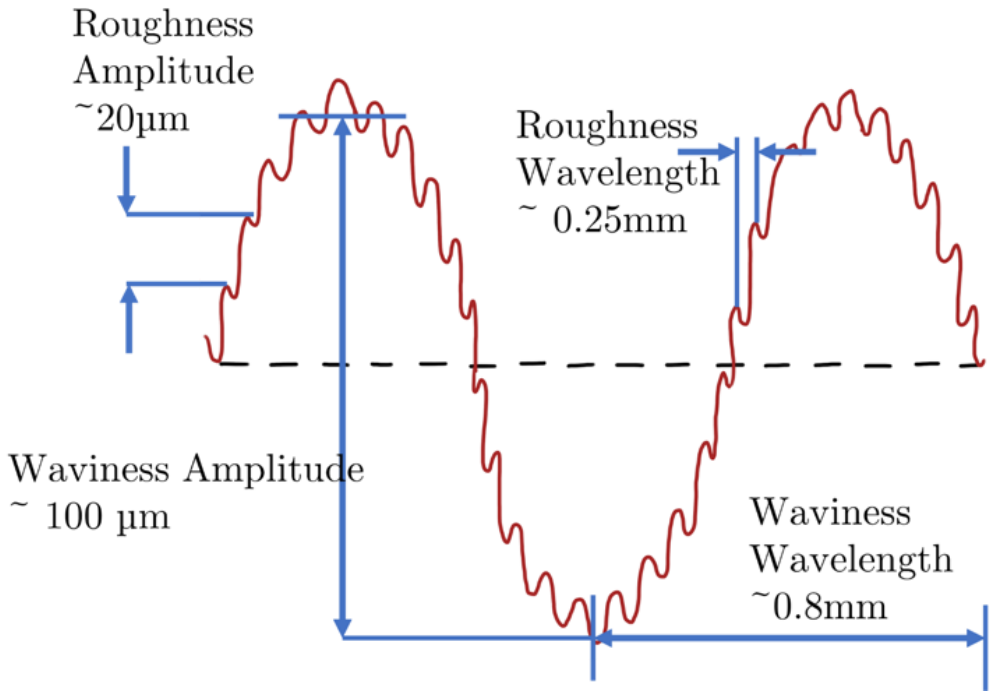

Figure 5: Diagram showing the difference between roughness and waviness with representative values given as examples. This is based on an image from [44]

2.2.2. Parameters and Measurement techniques

Roughness is most commonly measured by surface profile measurement: drawing a line across a surface and translating that measured line into a height function. This uses Cartesian coordinates where the x-axis lies in the direction of the line, the y axis lies normal on the surface and the z axis in the direction of the height displacement [42]. Although there are numerous parameters available to describe surface texture, the most commonly used parameters are the profile parameters Ra, the arithmetic mean deviation of the assessed profile and Rq, the root mean square value of the ordinate values within a sampling length [43]. As defined in ISO 4287:1998, the direction of measurement is perpendicular to the direction of the predominant surface form, known as the lay [42], [43]. Several other important characteristics for roughness measurements such as the length of the evaluation line and size of the cut off filters are also clearly defined in standards.

However, it is worth noting that at the time of writing, the majority of current standards for defining and measuring surface roughness are intended for machined surfaces rather than as-built additively manufactured surfaces, and have historically been used for certifying that surface texture complies with drawing and specification requirements [45] [41]. Roughness of such surfaces are typically periodic in nature, referring to grooves, crack and dilapidations due to process kinematics and the shape of the cutting edges used to machine the surfaces [46]. As previously mentioned, due to the layered nature of the SLM process and heat dissipation during solidification as-built SLM surfaces can contain numerous unique surface features, such as balling, unmelted particles, rippling and the staircase effect. Combinations of these factors can result in aperiodic surfaces and a multi-directional particulate texture with a lay that varies around the component as the slope of the surface and orientation during AM varies locally [47].

Profile measurements and the related parameters are limited in their ability to accurately capture the complex features of SLM surfaces, giving incomplete descriptions, and may be difficult to determine the exact nature of the topographical features that influence these parameters, such as pits or re-entrant features [42]. Figure 6 shows an example of a surface captured using both profile and areal techniques. From the profile technique alone the feature "A" could be misidentified as a pit, while the areal measurement shows that this same feature (labelled as "B") is actually a much larger scratch.

Despite this, profile measurements and the related parameters are commonly used when describing surface texture of additively manufactured surfaces. A. Townsend, *et al.* found that they were used in 40% of the literature they surveyed and A. Triantaphyllou *et al.* found that prominent AM machine manufacturers such as EOS, Renishaw and Concept Laser characterise their AM component surfaces using tactile profile measurements and Ra [47][45].

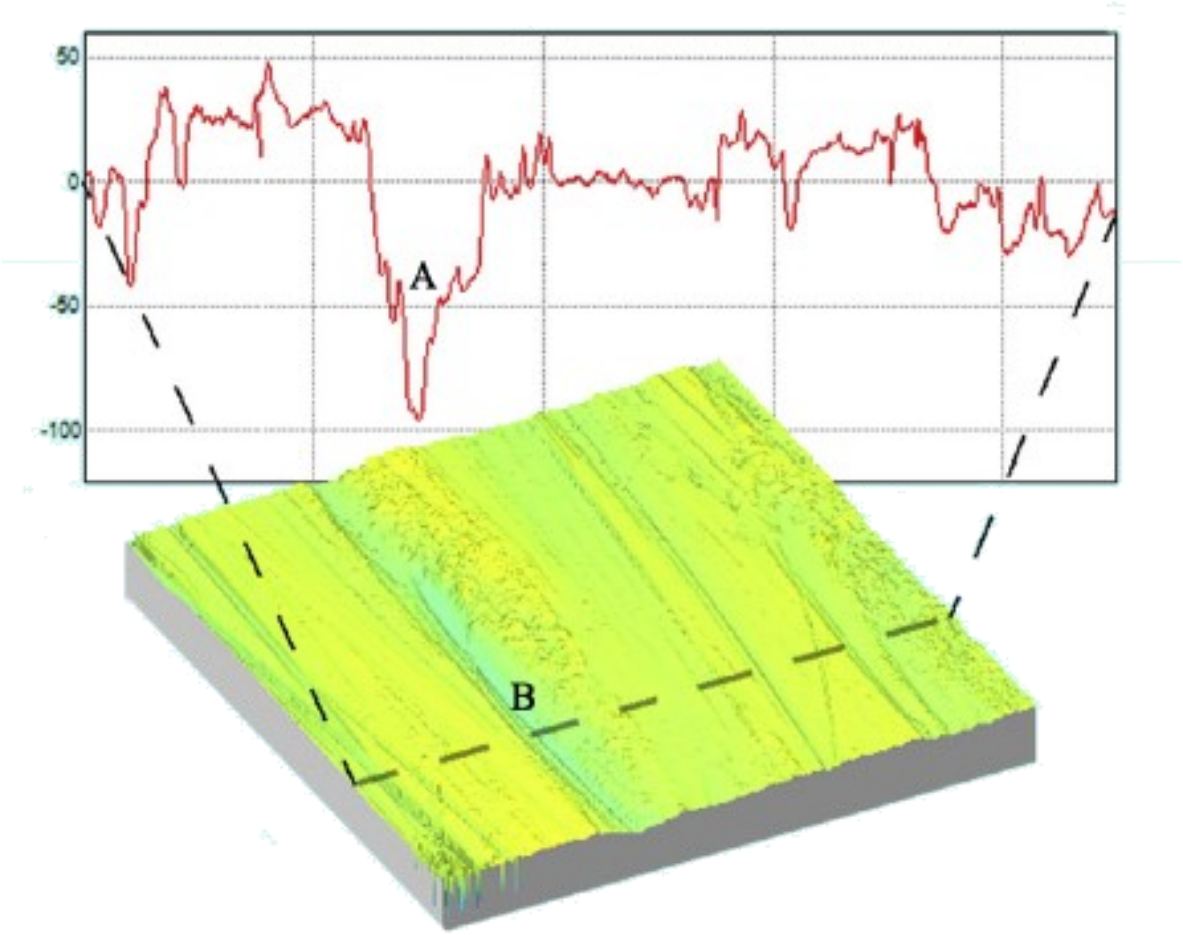

Figure 6: Diagram showing the same surface measured using profile and areal techniques. From the profile "A" could be misidentified as a pit while the areal trace shows that the same feature "B" is clearly a scratch. This image is originally by A. Townsend *et al.* [45], [48] Reproduced under Creative Commons CC-BY

However, in recent literature there has been a trend towards areal topography characterisation techniques for AM surfaces such as focus variation microscopy, confocal microscopy, and X-ray CT scanning. Areal topography has the advantage of producing a 3D image of a surface allowing for more information on the surface to be captured. Despite the existence of standards for areal texture measurement [49][50][51], this shift towards more suitable characterisation techniques for AM surfaces is hindered by the lack of specificity for AM surfaces. This has resulted a lack of consensus and numerous different techniques and parameters being used in the literature. This will be discussed in more detail in the Literature Review section of this thesis.

2.3. Theory of thermal radiation heat transfer

2.3.1. Thermal radiation and emissivity

The three main types of heat transfer are conduction, convection, and radiation. Unlike conduction and convection that transfer energy through a material medium, radiation enables heat to be transferred through a perfect vacuum. When specifically discussing electromagnetic radiation emitted by a body because of a temperature difference between the body and the surrounding medium, this is defined as thermal radiation [52]. Figure 7 shows the spectrum of electromagnetic radiation. Radiation stimulated by temperature encompasses wavelengths between 0.1 µm to 1000 µm and includes the visible, infrared and a small part of the Ultraviolet (UV) regions.

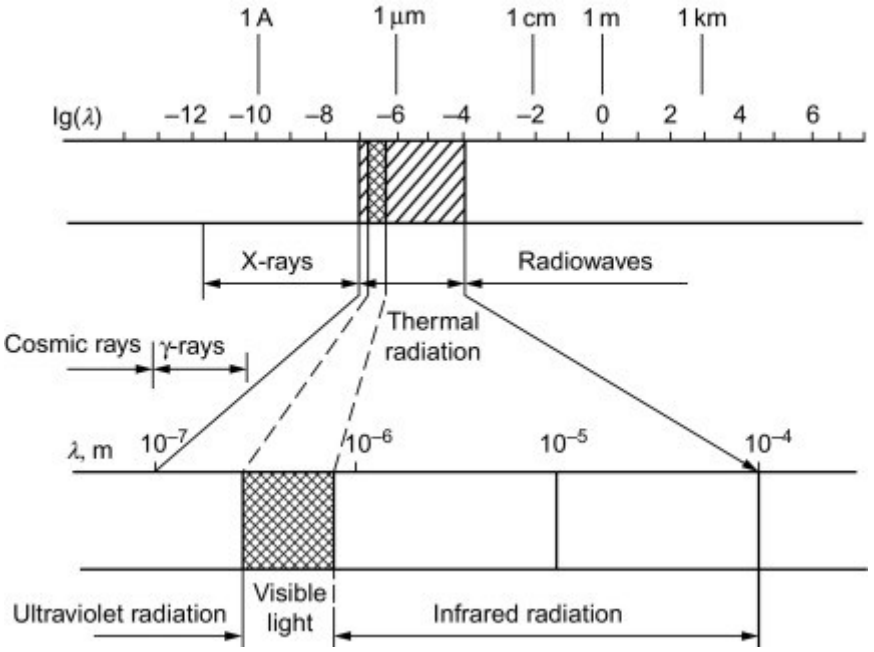

Figure 7: Classification of electromagnetic waves based on production and wavelength range. This image is originally by Kirillov [53]. Reproduced with permission.

Thermal effects are associated with thermal radiation. For radiative heat transfer the effects are greatest for visible and infrared rays although for most engineering applications the heat emitted in the range between 400-1000 µm is very small [54], [55]. Thermal radiation is a phenomenon observed in all solids, liquids and gases and is generated due to agitation of molecules and atoms because of their internal energy which is dictated by their temperature.

The electromagnetic waves emitted from a surface as radiation consist of various wavelengths of varying intensity. This radiation is described in terms of emissive power, which is related to the intensity of the radiation emitted and may be defined as *"... the energy emitted by the body per unit area and per unit time."* [52] [55]. As the temperature of the surface changes, so does the intensity of the wavelengths emitted. The total radiation heat flux vector covers the entire range of wavelengths and all possible angles of emission, which make up a hemisphere covering the surface [55]. Total refers to average values over all wavelengths and hemispherical referring to average values with respect to all directions [56]. When discussing the energy emitted by a surface in all directions but at a specific wavelength, this is known as the spectral or monochromatic emissive power of the body [54]. An ideal emitter, known as a blackbody, is one that emits the maximum possible amount of radiation over all wavelengths and in all direction at any given temperature.

The total hemispherical emissive power of a blackbody can be related to the temperature of the body through the Stefan- Boltzmann law shown in equation [3]:

$$\boldsymbol{E_b = \sigma T_s^4} \qquad [3]$$

Where E_b is the emissive power of a blackbody, T_s is the absolute temperature of the surface in Kelvin and σ is the Stefan-Boltzmann constant, which has the value

$$\boldsymbol{\sigma = 5.699 \times 10^{-8}\, W/m^2\, K^4}$$

For a given temperature and wavelength, no surface can emit more energy than a blackbody. Blackbodies are thus used a reference when describing the emissive power of real surfaces. Emissivity, ε, is defined as the ratio of the radiation emitted by a real surface to the radiation emitted by a blackbody at the same temperature. The spectral, directional emissivity of a surface can be described through equation [4].

$$\boldsymbol{\varepsilon(T, \lambda, \theta, \Phi) = \frac{E(T, \lambda, \theta, \Phi)}{E_b(T, \lambda)}} \qquad [4]$$

Where E is the emissive power of a real surface and Φ and ϑ are angles used to define the direction of the emitted radiation with respect to the surface normal [55]. Emissivity is a dimensionless value that varies between 0 and 1. By combining equations [3] and [4], the spectral, directional emissive power of a real

surface can be expressed in terms of the emissive power of a blackbody shown in equation [5].

$$\boldsymbol{E(T,\lambda,\theta,\Phi) = \varepsilon(T,\lambda,\theta,\Phi)\sigma T_s^4} \qquad [5]$$

However, for most engineering applications including the resistojet thruster that is the subject of this thesis it is more useful to consider the total heat flux, the same as the total emissive power, emitted by a surface over all wavelengths and directions. This is determined by integrating the spectral directional emissivity over all the wavelengths and directions as shown in equation [6].

$$\boldsymbol{\varepsilon = \frac{1}{\sigma T^4}\int_0^\infty E_\lambda d\lambda} \qquad [6]$$

This is also known as the total hemispherical emissivity of a substance and was the emissivity term used in this thesis. Emissivity henceforth shall refer to total hemispherical emissivity unless specified otherwise.

2.3.2. Kirchhoff's law and surface effects

When a surface is irradiated, the energy is partly absorbed, partly reflected, and partly transmitted through the specimen. Each of these fractions of energy are defined by the absorptivity α, reflectivity ρ and transmissivity τ of the material respectively. However most solid bodies are opaque to incident radiation and thus the transmissivity is taken as zero. Absorptivity and reflectivity can be related through equation [7]

$$\boldsymbol{\rho + \alpha = 1} \qquad [7]$$

If the angle of incidence of the radiating beam is equal to the angle of reflection, the reflection is said to be specular. If however the incident beam distributed uniformly in all directions after being reflected, the reflection is defined as being diffuse [52]. Although no real surfaces are perfectly specular or diffuse, generally it can be said that rough surfaces exhibit diffuse behaviour more so than polished surfaces. Similarly, polished surfaces exhibit more specular behaviour than rough surfaces. Absorptivity and reflectivity are surface properties that are highly influenced by the surface quality of the material. The absorptivity and emissivity of a material can be related to each other through Kirchhoff's Law which states that the total hemispherical emissivity for a material is equal to its total hemispherical

absorptivity [52], [57]. Thus, by substituting back into equation [7], emissivity can be related to the reflectivity of a material through equation [8].

$$\boldsymbol{\varepsilon = 1 - \rho} \qquad [8]$$

As reflectivity is highly dependent on the overall surface quality of the material, emissivity can thus also be seen to be highly dependent on overall surface quality determined by factors such as surface roughness [52]. The relationships between emissivity, reflectivity and absorptivity are the basis for several methods of measuring the emissivity which will be discussed in greater detail in the literature review section of this thesis.

Surface effects and Emissivity

When discussing gases and semi-transparent solids such as glass, emission is considered a volumetric phenomenon; the radiation is the integrated effect of emission throughout the entire volume of the body. However, in most solids and liquids, radiation emitted by molecules within the bulk is strongly absorbed by adjoining molecules. Thus, for most solids the radiation emitted originates from roughly 1μm from the exposed surface. Thus for solid bodies, such as the SLM metals in this thesis, emission is viewed as a surface phenomenon and thus surface quality can have a large effect on the emissivity of the body [57], [58].

Numerous surface characteristics including temperature, roughness, physical structure, and chemical composition can affect emissivity. Touloukian *et al.* stated that metallic surfaces could be described by three different characteristics, each of which had an influence on emissivity [58]. These characteristics are shown in Table 1. It is difficult to consider these entirely separately from one another as altering one has an influence on another.

Of these characteristics, the influences on radiative properties from surface roughness (topographical) and films such as oxide growth (chemical) were reported to have the largest effect [58]. This is particularly true when the variation of the surface profile or the thickness of the film is on the same order of magnitude as the wavelength of interest.

Table 1: Table showing the different characteristics of metallic surfaces that influence emissivity[58]

Characteristic	Description [58]
Topographical	Describes the profile/geometry of the surface and is the boundary between the material and the surrounding medium. Surface textures such as roughness are described by this category
Chemical	Describes the composition of the surface layer and includes inhomogeneities and contaminants
Physical	Describes the structure of the surface on the atomic level, such as the crystal lattice or particle size

Surface roughness and Emissivity

Surfaces can be divided into two broad categories depending on their roughness: optically smooth (ideal) or rough (real) [58]–[63]. Rough surfaces can then be further divided into three different regions depending on optical roughness, which is described as the ratio of the root mean square (rms) surface roughness, Rq, to wavelength of the incident radiation, λ. These three regions are:

- The Specular region: $0 < \frac{R_q}{\lambda} < 0.2$
- The Intermediate region: $0.2 < \frac{R_q}{\lambda} < 1$
- The Geometric region: $\frac{R_q}{\lambda} > 1$

In the geometric region, surface roughness is on a comparable length scale to the wavelength of the radiation. In this case, geometric optics which describes radiation in terms of rays of light can be used to describe the interaction between radiation and surfaces. As the roughness increases, so does the contact between incident light and the surface as there are more internal reflections of light. This results in fewer immediate reflections away from the surface and greater absorption which, following Kirchhoff's law leads to greater emissivity [61], [62]. This difference between high and low roughness surfaces is shown in Figure 8. Surface roughness on this geometric length scale is commonly found for as-built SLM surfaces.

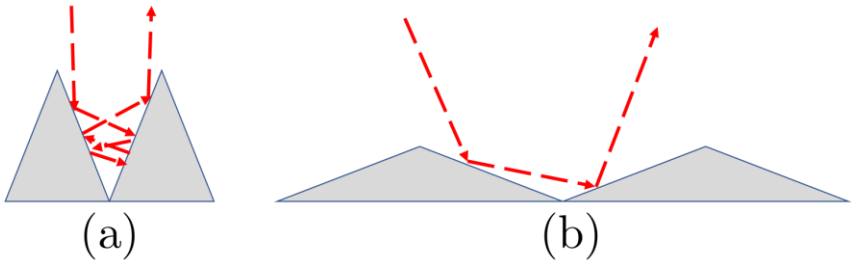

Figure 8: Diagram showing how higher surface roughness can cause more internal reflections of light and thus higher emissivity for (a) high roughness surfaces and (b) low roughness surfaces

Despite this being a common method used to describe the relationship between roughness and emissivity, some studies have questioned its applicability. Recent studies have shown that the relationship between surface roughness and emissivity cannot solely be described by the rms roughness, and that the slope of the peaks that make up the surface and other surface texture parameters may have a larger effect on the emissivity [60], [61]. This was due to the aperiodic nature of real surfaces and thus may be particularly true for SLM surfaces. Other studies have stated that the geometric optics is only applicable for simple, periodic models of surfaces and that it breaks down for more irregular surfaces [61]. Both will be discussed in greater detail in the literature review section of this thesis.

2.4. Theory of Resistivity

2.4.1. Overview and principles

Electronic conduction within a solid describes the motion of electrons under the influence of an externally applied electric field [64]. Electrons must be free to move for this to occur. The energy of the electrons must be above a certain level, known as the Fermi energy, to participate in the conduction process. For metals, relatively little energy is generally required to excite large numbers of electrons into becoming free. Metals are thus regarded as being good conductors of electricity. Free electrons accelerate in the direction opposite to an electric field. As described by the free electron model, there is no interaction between accelerating free electrons and the atoms in a perfect, periodic crystal lattice [64].

Theoretically, under an applied electric field, electrons should be able to continuously accelerate causing the electric current to increase with time. However in reality currents reach constant values due to frictional forces acting against the acceleration of the electrons [65]. These frictional forces scatter the electrons and come from the fact that in practice, no crystal structure is perfectly periodic. Departures from the periodicity can come from numerous different sources. These include thermal vibrations of the atoms, imperfections in the lattice such as dislocations, vacancies or grain boundaries and substituted or interstitial atoms [64], [65]. As described by the Drude model, each scattering event causes an electron to change its direction of motion and lose kinetic energy, transferring it to the solid [64], [65]. However, there is still a net electron motion in the direction opposite the electric field, which is the electric current. Resistivity can be defined as a material's inherent resistance to this flow of electrons, caused by collisions or scattering of the electrons.

2.4.2. Pure metals and alloys

For well annealed pure metals temperature is the dominant contributor to resistivity. As temperature increases so do the amplitude of vibrations of atoms about their mean positions. This thus changes the interatomic spacing and periodicity of the crystal lattice resulting in changes to the electrical resistivity. Dislocations can cause temperature independent resistivity, but the contribution of dislocations to the overall resistivity is negligible at high temperatures and only significant at cryogenic temperatures [64].

However, when considering metallic alloys such as the metal that is the subject of this thesis, the impact of foreign atoms on the resistivity must be considered and can have greater contributions to resistivity than temperature. Alloys can be divided into two different categories depending on the concentration of alloys added to the host crystal lattice.

Dilute alloys are those for which the alloy addition is typically less than 5% [64]. For such alloys, when foreign atoms are randomly substituted for host alloys,

if the foreign atoms do not interact with one another and the host lattice structure is preserved then the resistivity increases proportionally to the number of atoms added. Because these foreign atoms vibrate similarly to the host atoms, their contribution to the overall resistivity is temperature independent [64]. This relationship can be explained through Matthiessen's rule, shown in equation [9].

$$\boldsymbol{\rho_a(T) = \rho_p(T) + \rho(c)} \qquad [9]$$

Where $\rho_a(T)$ is the overall resistivity of the dilute alloy, $\rho_p(T)$ is the resistivity due to temperature variations of the host and $\rho(c)$ is the resistivity contribution due to foreign atoms.

Concentrated alloys, which have alloy additions greater than 5%, are notably more complex. Such alloys include 316L stainless steel, the metal under investigation for this thesis. Concentrated alloys can contain regions where foreign atoms order themselves at distinct lattice points, resulting in a degree of periodicity that may actually have a lower resistivity compared to surrounding random states [64]. Such ordered states generally only occur below certain critical temperatures, however they generally add to the degree of complexity when describing the resistivity of alloy systems.

The term $\rho_p(T)$ in equation [9] becomes less significant as there is less distinction between host and foreign atoms. At the same time that the concentration of foreign atoms increases, their contribution to the resistivity increases and becomes the dominant factor over temperature [64]. Such alloy systems can have multiple phases coexisting at the same temperature, each of which can have their own characteristic resistivity which may vary differently with temperature. As a result of this, it becomes difficult to estimate the resistivity of alloys without empirical data [64].

2.4.3. SLM metal microstructure

As previously described, due to the rapid heating and cooling that occurs during the SLM build process, the microstructure of SLM metals can be notably different compared to their cast counterparts.

For 316L stainless steel, a notable difference is the presence of columnar grains with cellular structures, defined by sub-grain boundaries enriched with heavy elements [66], [67]. The presence of many sub-grain boundaries may result in a larger deviation from periodicity compared with cast 316L, and thus greater resistivity. In addition to this, SLM parts may suffer from defects during the build process such as porosity. Such defects may also reduce the periodicity of the metal, increasing the resistivity. From reviewing the literature, few studies were found that investigated how the microstructure of SLM metals affected the resistivity, presenting a notable gap in the knowledge that this work intend to fill. The work that was found is presented in the literature review section of this thesis.

3. Literature review and state-of-the-art

This chapter is an overview of the current state of the art of several key concepts that helped to define the methods and experimental windows used in this thesis. The concepts explored in this chapter include 316L stainless steel, surface roughness, total hemispherical emissivity, and electrical resistivity.

3.1. 316L Stainless steel

3.1.1. Introduction

As previously stated, this work was a continuation of the work by F. Romei *et al.* Due to low cost and ease of availability, the prototype resistojet was built using 316L stainless steel. Although at the time of writing M. Robinson *et al.* are continuing the development of the resistojet with new materials capable of reaching higher temperatures [1], 316L was also chosen as the material to be investigated in this work. This was not only also due to the low cost and ease of availability but because characterisation of the resistojet had already been carried out in 316L meaning there was data to compare the results of this work against.

This section aims to provide an overview of the state of the art of SLM of 316L stainless steel. An emphasis is placed on the microstructure and crystal growth mechanisms as they influence the resistivity, and on values of process parameters as they informed the ranges of values used in this thesis.

3.1.2. Cast 316L stainless steel

Stainless steels (SS) are alloys of iron that contain a minimum of 10.5% chromium and varying amounts of carbon, silicon, and manganese. The addition of chromium helps to form a 'passive layer' on the surface, preventing the further corrosion of the surface. Other elements may be added to stainless steel to improve properties such as formability and corrosion resistance such as nickel and molybdenum [68].

Stainless steel is commonly divided into five different types depending on the microstructure and alloying elements: ferritic, austenitic, martensitic, duplex and precipitation hardening [69]. Type 316 steel is an austenitic chromium-nickel stainless steel containing between 2-3% molybdenum. The addition of a minimum of 8% nickel results in the austenitic grain structure defined by the face-centred cubic (FCC) crystal structure whilst the addition of molybdenum improves corrosion resistance and increases strength at high temperatures [70]. There are numerous different types of 316 stainless steel, including the L, F, N and H variants, each letter corresponding to variations in the chemical composition. The L variant refers to the low carbon content (0.03% max) compared to regular 316 stainless steel (0.08% max) [70]. This lower carbon content minimises deleterious carbide precipitation, when carbon is drawn out of the metal and reacts with chromium at elevated temperature, thus lowering corrosion resistance [70]. The suitability at high temperatures and good corrosion resistance are reasons why 316L stainless steel is commonly used for SLM applications. Table 2 shows the composition ranges for 316L stainless steels.

Table 2: Composition ranges for 316L stainless steel

Element	C	Mn	Si	P	S	Cr	Mo	Ni	N
Min (wt. %)	-	-	-	-	-	16.0	2.00	10.0	
Max (wt. %)	0.03	2.00	0.75	0.045	0.03	18.0	3.00	14.0	0.10

The microstructure of 316L stainless steel is typically made up of equiaxed grains with straight boundaries, the size of which highly dependent on the method used to form the results parts. An example of this is shown in Figure 9. Song *et al.* investigated the microstructure and mechanical properties of solution treated and hot rolled specimens of 316L stainless steel. The average grain size of the hot rolled specimen was 21 µm and 33 µm for the solution treated specimens [71] whilst other sources have reported grain sizes for 316L ranging from 10 µm – 40 µm [72]. The solution treated 316L possessed a single-phase austenite microstructure and a decreased ferrite content of 6% compared to the 10% of the hot rolled steel.

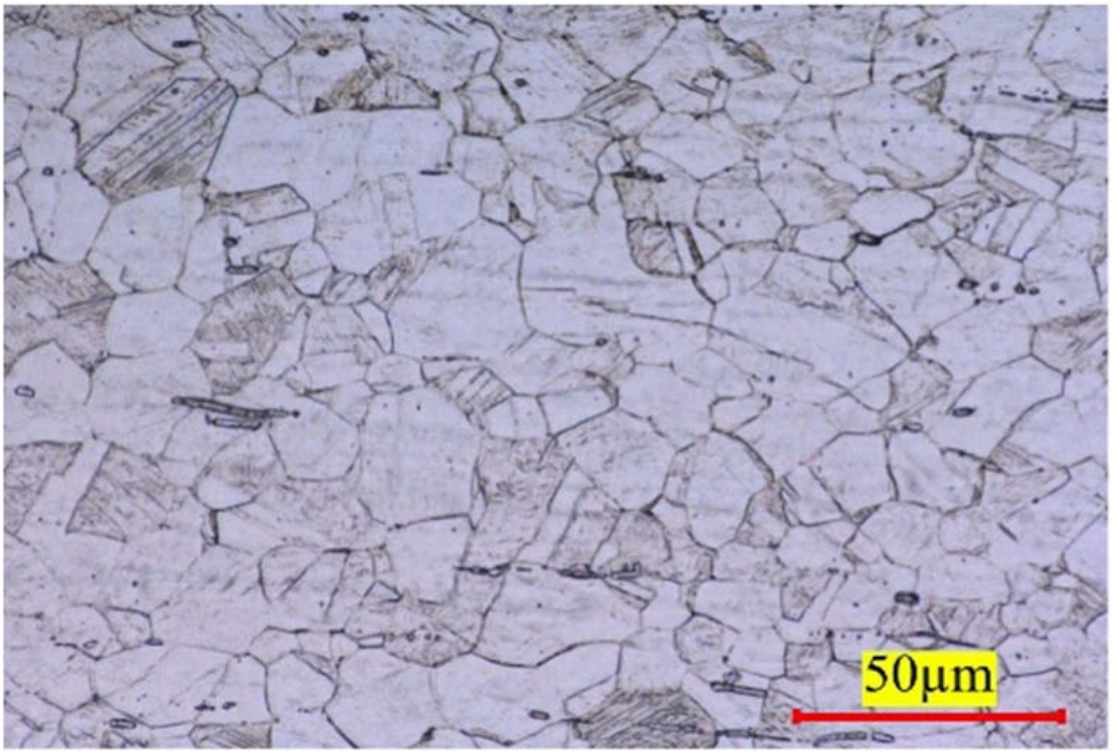

Figure 9: Optical microscope image showing a typical microstructure of cast 316L stainless steel. This image was originally by Tascioglu *et al.* Reproduced with permission [73]

3.1.3. SLM 316L stainless steel

Microstructure overview

From reviewing the literature, the reported morphology of SLM 316L is notably different compared to cast or wrought 316L. Zhong *et al.* [67] discussed the morphology at macro and microstructure scales. Rather than the equiaxed grains seen in Figure 9 for cast 316L, at the macro level SLM samples show a layered structure characterised by melt pools of width 200 µm and height 80 µm, however these dimensions were dependent on the spot size and input energy density. Liverani *et al.* reported that the orientation of the melt pools are dependent on the build angle [25]. Within these melt pools were columnar grains which grew through melt pool boundaries in the direction of the thermal gradient, as seen in Figure 10. The sizes of these columnar grains were generally found to vary between 10 µm - 100 µm [67] [66]. These differences in size and crystal anisotropy found in the grains were reportedly due to the large temperature gradients and different solidification rates in melt pools when forming due to the rapid movement of the laser beam [66].

At the micro level, within these columnar grains a cellular structure was reported with sizes of cells varying from 0.5 µm - 2 µm and defined by sub grain boundaries [66] [25][67]. Saeidi *et al.* reported that these sub grin boundaries were resistant to etching as they were enriched with heavier elements, specifically molybdenum. This was due to the fast cooling rates during the laser melting process and insufficient time for diffusion and alloying of large atoms heavier than molybdenum during the rapid crystal growth [66]. This cellular structure resulted in high concentrations of dislocations and residual stresses at these cellular boundaries. Decreasing the scanning speed however resulted in greater accumulation of thermal energy around the cells, providing more internal energy for their growth and thus larger sizes.

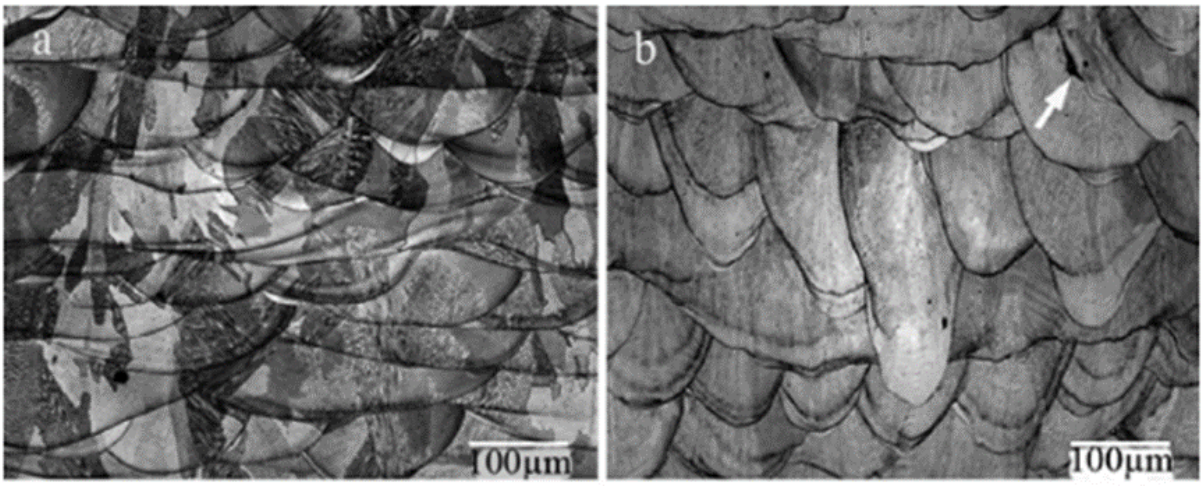

Figure 10: Etched surfaces of SLM 316Lshowing (a) an optical microscope image of the columnar grain structure and (b) an SEM image of elongated melt pools. This image was originally by Zhong *et al.*[67]. Reproduced with permission

The shape of the cells, as shown in Figure 11, was described as equiaxed polygonal or elongated depending on their growth direction which was strongly influenced by the thermal gradient direction [25]. Wang *et al.* found that the size of these cells varied with SLM process parameters. As the energy density was increased, the primary cell spacing also increased resulting in a coarsening of the grains [74]. Similar results were found by Yadroitsev *et al.* as they investigated the effects of energy input on primary dendrite spacing [75]. This was explained in terms of the scanning speed of the laser. Increasing the scanning speed increased the amount of kinetic undercooling in the melt pool which increased the nucleation rate. This thus

refined the microstructure and decreased the primary cell spacing [74]. Decreasing the scanning speed however increased the energy density and heat transfer between the melt pool and heat affected zone, providing internal energy for the growth of larger cellular dendrites [74] [76].

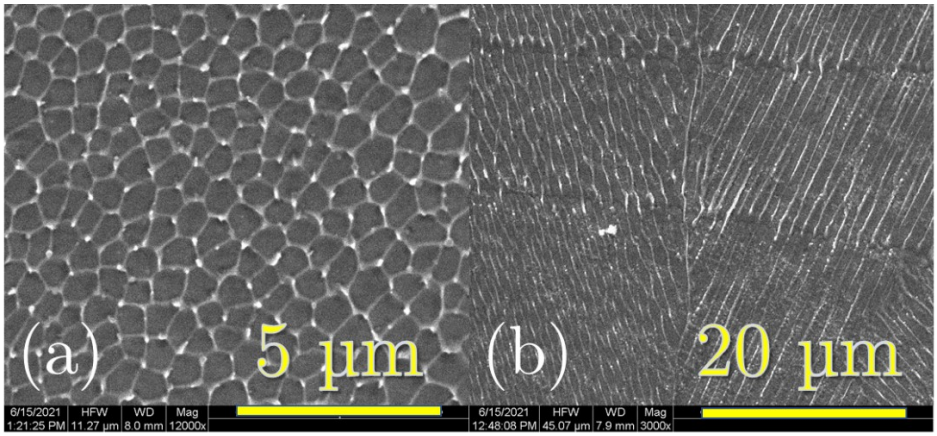

Figure 11: SEM images showing the typical cellular structures seen in SLM 316L. image (a) shows equiaxed polygonal cells while (b) shows elongated cells

Certain sources reported circular nano-inclusions throughout the microstructure which appeared as black circles under SEM imaging, the composition of which was dominated by silicon, chromium and oxygen [66][67]. These inclusions were described as amorphous glass phases of chromium containing silicate nano-inclusions. These formed due to silicon and chromium reacting with the trace amounts of oxygen within the steel powder or laser chamber during the forming process [66].

Kinetics

Whilst a columnar structure is typically seen in conventionally cast steel due to undercooling, it is different from the columnar sub-grain structure seen in laser melted steel. Saeidi *et al.* stated that the columnar sub-grain structure probably formed due to the slow kinetics of homogeneous alloying of large atoms of heavier elements resulting in compositional fluctuations [66]. Zhong *et al.* gave similar reasoning stating that the cellular structure was likely formed due to the high cooling speed and non-equilibrium conditions during the melting process [67]. Both Saeidi *et al.* and Zhong *et al.* described the formation of the cellular structure in terms of the G/R ratio, where G is the temperature gradient in the liquid and R is the

solidification rate. The G/R ratio determines the solidification microstructure while G*R, the cooling rate, determines the fineness of the microstructure. From high to low G/R ratios, planar, cellular, cellular dendritic (columnar) and finally dendritic structures are expected [66][74].

Despite many sources only identifying cellular microstructure within SLM 316L, Wang *et al.* observed planar, cellular, and cellular dendritic regions within SLM 316L and used finite element analysis (FEA) to explain the origin of the different microstructures. They found that the thermal gradient 45° from the melt pool in the build direction was smaller compared to the gradient directly down from the melt pool in the build direction. This smaller gradient resulted in the formation of a constitutional undercooling zone thus inducing dendritic growth. The higher temperature gradient directly beneath the melt pool however had such a high cooling rate that there was insufficient time to form secondary dendrite arms and thus only cellular morphologies were observed.

Generally, it can be said that the SLM process results in a high G/R value and thus cellular dendrite growth is preferred compared to planar front growth resulting in the intragranular cellular structure. The G values reportedly can reach as high as 10^5-10^7K/s resulting in an extremely fine microstructure on the order of 0.5-2 µm as previously described [66][74][67].

Phases/Texture

Several sources were found discussing the phases present in 316L manufactured through SLM. Generally both precursor metal powders and SLM samples showed only the FCC austenite phase [25] [66], corresponding to XRD peaks at (111), (200) and (220) [74]. However, XRD analysis commonly showed that SLM samples had a broadening of peaks due to residual stresses and lattice distortion [25] [67]. E. Liverani *et al.* investigated how build angle affects these phases and found that samples built at 45° showed a preference for (111) planes, whilst samples at 90° showed a preference for (220) planes. This was reportedly due to the presence of preferential crystallite growth orientations induced by the SLM process. Saeidi *et al.* found that SLM samples showed a preference for the (100) plane however it was not

stated at what angle these samples were built [66]. Saeidi *et al.* however stated that due to the resolution of XRD, they could not rule out the formation of other minor phases. They used EBSD to clarify this and determined that there was also a very small fraction of ferrite with BCC structure [66]. However, no other sources were found with similar results.

Process parameters

To reiterate, an overall goal of this thesis was to understand how process parameter variation affected the material properties emissivity and resistivity, and to use this to create an improved thermal model of the resistojet. When building the samples for this thesis, it was important that the process parameters produced fully dense parts to be as representative of the resistojet as possible and that they covered a range of values to better map out the design space and understand how the inputs and their interactions affected the measured outputs. (More information on the experimental design is given in the methodology section of this thesis).

To achieve this, process parameters from literature were reviewed and used as a basis for the parameters chosen in this study. Focus was given to process parameters used to produce high relative density (>99%) thin-walled parts on the order of hundreds of microns as these were similar to the thin walls of the STAR resistojet. A review on how process parameters affected surface roughness is presented in section 3.2.4 of this chapter.

Thin-walled specimens

While little information in the literature was found discussing process parameters specifically focused on thin-walled 316L parts, two reports by Y. Liu *et al.* and X. Su *et al.* investigated similar ranges of values [22], [77]. Y. Liu *et al.* used Design of Experiments (DoE) to investigate how varying the laser power, scanning speed and layer thickness affected the track width, surface roughness (Ra) and hardness of thin-walled parts. The ranges of their process parameters were produced through trial and error and are shown in Table 3. While they did not give the nominal part width, they produced thicknesses varying from 134 µm – 320 µm. They

found that, within their design window, laser power had the most significant effect on track width and the least on roughness. Higher laser powers led to higher energy densities and larger melt pools which resulted in larger track widths. They produced a set of optimised process parameters with the goal of maximising the track width, which are shown in Table 3. X. Su *et al.* fabricated a 3 mm long gridded radiator with thin walls that varied gradually along the length of the part from 80 µm – 120 µm using fixed process parameters chosen from previous experimental work [77]. They reported that the minimal fabricated geometric feature was mostly dependent on the laser spot size, with spot sizes larger than the CAD part geometry resulting in larger than intended parts being produced. They successfully produced parts with absolute errors of around 20 µm, with the largest factor affecting the dimensional precision being half-melted particles stuck to the sample. While neither of these reports gave information on the relative densities of the parts produced, the parameters they reported still give a good baseline to build from for this thesis.

High density specimens

When discussing AM parts, density is commonly described in terms of relative density. This is the percentage density of a part compared against a theoretical completely dense part of the same material. Several reports from the literature were found that gave details on the process parameters used to produce high relative density (<99%) parts. A summary of such values is shown in Table 4.

Fayazfar *et al.* reported that energy density was commonly referred to as one of the best predictors for the relative density of a part produced through PBF techniques [7]. While many sources did relate relative density to energy density, a wide range of energy densities have been reported to produce high density parts. Thus, energy density alone should not be used as a predictor and it is important to understand the influence of the individual process parameters that make up energy density on the densification behaviour of parts.

S. Greco *et al.* considered this by varying the laser power and layer thickness on cubic samples, but holding energy density constant at two different levels by adjusting the scanning speed (33.3 J/mm^3 and 119 J/mm^3) [78]. They reported a

large variation in density varying from 70% - 99%. They found that the relative density generally did increase with energy density and laser power but decreased with increasing layer thickness. Higher laser powers led to higher amounts of thermal energy and thus more of the part being heated above its melting point and increasing the density. Higher layer thicknesses however led to insufficient amounts of energy being delivered to raw or already melted layers, lowering cohesion of new layers with already existing material, and thus reducing the relative density.

Y. Deng *et al.* used DoE to vary the laser power, scanning speed and hatch spacing with the specific goal of producing a set of optimised parameters to maximise relative density and minimise surface roughness [79]. Despite optimisation attempts, their highest density was less than S. Greco *et al.* at 98.72%. Y. Deng *et al.* found that laser power and scanning speed were significant to the density and both had produced curved responses. They explained the relationship of density and laser power similarly to S. Greco *et al.,* that higher laser powers increased the amount of melted material and thus density. However, they also stated that too low laser powers did not melt the powder completely resulting in balling and too high laser powers caused melt pool instabilities and keyhole effects, both reducing the density. They related scanning speed to the solidification rate of the melt pool. Higher scanning speeds caused the melt pool to solidify before the powder was completely melted, decreasing the density.

D. Wang *et al.* also investigated how process parameter variation affected densification behaviour for tensile specimens [74]. They varied the scanning speed while keeping the laser power, layer thickness and hatch spacing constant and produced parts varying from 94% - 98% density. Like S. Greco *et al.* they found that generally as the volumetric energy density increased so did the relative density of the part, though they described the rational slightly differently. They claimed low energy densities led to low temperatures within the melt pool and insufficient liquid formation. This decreased the viscosity of the melt pool and limited the densification behaviour. Viscosity of the melt pool reportedly increased enough to improve the densification at energy densities greater than 125 J/mm^3.

Table 3: Table showing process parameters for thin-walled 316L structures from literature. *These values are optimised to maximise track width

Paper	Average particle size (µm)	Machine	Laser spot size (µm)	Hatch pattern	Laser Power (W)	Scanning speed (mm/s)	Hatch spacing (mm)	Layer thickness (mm)	Build direction (°)	Fluence (J/mm3)	Sample shape
Y. Liu *et al* [22]	17.11	DiMetal-100	70	single track	70-170	65-235	N/A	0.0215-0.0385	90	-	grid structure radiator
Y. Liu *et al* * [22]	17.11	DiMetal-100	70	single track	150	105	N/A	0.0344	90	-	grid structure radiator
X. Su *et al.* [77]	17	Dimetal280	70	inter-layer stagger	150	600	0.12	0.035	90	59.52	grid structure radiator

Table 4: Table showing process parameters for 316L structures from literature that investigated relative density. *These values are optimised to maximise relative density and minimise surface roughness

Paper	Powder size (µm)	Machine	Hatch pattern	Laser power (W)	Scan speed (mm/s)	Layer thickness (mm)	Hatch spacing (mm)	Build direction (°)	Fluence (J/mm3)	Relative density (%)
E. Liverani *et al.* [25]	15 - 45	SISMA MYSINT100	Island	100, 150	700	-	0.05-0.07	45-90	102 - 214.3	98 - 99.9
Saeidi *et al.* [66]	22 - 53	EOSINT M 270	bi-directional	195	800	0.02	0.1	-	-	98.6
Zhong *et al.* [67]	10-45	AM250 Renishaw	Stripe	-	1000	0.05	0.1	-	-	99.8
D. Wang *et al.* [74]	21.6	Dimetal-100	Inter-layer stagger	300	700 - 1200	0.03	0.08	-	125 – 178.57	94-98
S. Greco *et al.* [78]	-	Mlab Cusing	Island	30 - 90	-	0.025 - 0.045	0.056	-	33.3, 119	70 - 99
Y. Deng *et al.* [79]	-	FS271M	-	150 - 300	700 - 1300	-	0.06 - 0.12	-		98.25 - 98.71
Y. Deng *et al.* [79]*	-	FS271M	-	259.1	900	-	0.0867	-		98.72

Reports of note were by E. Liverani *et al.* who produced tensile specimens and Zhong *et al.* who produced rectangular and cylindrical specimens [25], [67]. They reported the highest densities at 99.9% and 99.8% respectively. However, neither report detailed the physical reasons why their chosen parameters resulted in such high-density parts. E. Liverani *et al.* did find that, contrary to S. Greco *et al.,* parts with relative densities greater than 98% were only produced with energy densities of 100 J/mm^3 or higher and that build orientation had no effect on the relative density. Zhong *et al.* stated that because their parameters were adjusted for the bulk specifically that border and overhanging regions would experience different thermal histories and had different microstructures compared to the bulk.

3.1.1. Summary

The microstructure of SLM 316L is notably different compared to cast 316L due to the rapid cooling and high thermal gradients that occur during the SLM build process. Cast 316L consists of equiaxed grains with straight boundaries on the order of 10 µm – 40 µm, while SLM 316L microstructure is characterised by layered melt pools through which grow columnar grains between 10 µm – 100 µm. Within these grains is a cellular structure formed due to compositional changes that occur during the rapid solidification. The cells vary between 0.5 µm – 2 µm and the boundaries of these cells are rich in heavy elements like molybdenum and can have high concentrations of dislocation and residual stresses.

Process parameters play a large role in determining the overall quality of parts produced through SLM. For thin-walled specimens, different factors were given as being the most critical to determine the accuracy of the parts compared to the nominal CAD geometry. Y. Liu *et al.* were able to successfully produce thin-walled parts varying between 134 µm – 320 µm, with laser power having the largest effect on track width as it resulted in higher energy densities and melt pools. X. Su *et al.* also produced thin-walled parts, from 80 µm – 120 µm, with the biggest factor that affected the dimensional precision being half melted particles adhered to the sides and part width mostly affected by the diameter of the laser spot size.

For high density (>99%) parts, although generally energy density was commonly described as being key for determining the relative density, S. Greco *et al.* found the same energy densities (33.3 J/mm^3 and 119 J/mm^3) could give different results and that it was important to understand how the individual parameters that make up energy density interact with the parts. Both S. Greco *et al.* and Y. Deng *et al.* were able to produce high density (>98%) parts, both claiming that higher laser powers led to increased melting and thus higher density.

3.2. Surface Roughness

At the time of writing there are several ISO/ASTM standards from the ASTM committee F42 on additive manufacturing. However, these standards focus on materials, test methods and design of AM parts [80]. There are currently no standards on how to define and measure roughness on additively manufactured surfaces. This has resulted in a lack of consensus in the literature as to the best methods to quantify and qualify roughness on AM surfaces. Although common techniques were found between different sources in the literature, the specific applications of these techniques and the parameters used to qualify roughness were found to vary significantly. Presented here is a summary of the different techniques and parameters found for qualifying AM surfaces. Finally, a short summary on the effects of SLM parameter variation on roughness is presented.

3.2.1. Review papers and state of the art

Both A. Townsend *et al.* and R.K. Leach *et al.* reviewed the current state of the art of surface texture measurements for AM surfaces [45], [81]. In general it was found that, with few exceptions, AM surface texture research is still at an early stage with few real industrial applications or specific requirements [45]. Most of the research was focused on metal PBF, and specifically challenges around SLM and Electron Beam Melting (EBM) parts. Within that, stainless steel comprised 39% of the examined literature, with 70% of that focused on 316L stainless steel making stainless steel the most investigated metal. The research included in this thesis will focus on PBF techniques that used materials relevant to high temperature resistojet applications, including 316L stainless steel.

3.2.2. Measurement techniques

Generally, surface texture metrology can be performed by either profile or areal measurement techniques. Profile measurements involve drawing a line across a surface and generating a two-dimensional height profile of the surface from that data, whilst areal measurements create three-dimensional height maps of surfaces. As reported by A. Townsend *et al.*, there are a variety of different methods through which these techniques can be applied including contact, optical, non-contact/non-optical and pseudo-contact [45]. The choice of which technique is most appropriate to the surface is dependent on several factors including the complexity of the information trying to be acquired, the nature of the material and the length scale of the features of interest. Each of these methods possess strengths and weaknesses depending on the type of surface and information they are trying to capture. Different techniques are critically reviewed here before deciding which is most appropriate to use in this thesis.

Profile measurements

To reiterate, although profile measurements are more commonly used, they are limited in their ability to fully describe surfaces and may give incorrect information. Despite this, numerous papers were found using profile measurement techniques on AM surfaces, possibly due to the long heritage of profile measurements for surface texture characterisation and perceived easier use of profile techniques. Using profile roughness measurement and the associated parameters would also allow for direct comparison with machined or turned surfaces as well as other AM surfaces in literature.

The basic process of extracting a line profile from a surface involves drawing a line across a surface and translating that measured line into a height function using Cartesian coordinates to describe the direction of the height and measurement. After drawing the line profile, filters are applied to separate the form, roughness, and waviness components and then parameters are measured on the resulting profile. This process is outlined below in Figure 12 and these filters are [43]:

- λ_s profile filter – defines the intersection between the roughness and shorter wave components
- λ_c profile filter – defines the intersection between the roughness and waviness components
- λ_f profile filter – defines the intersection between waviness and longer wave components

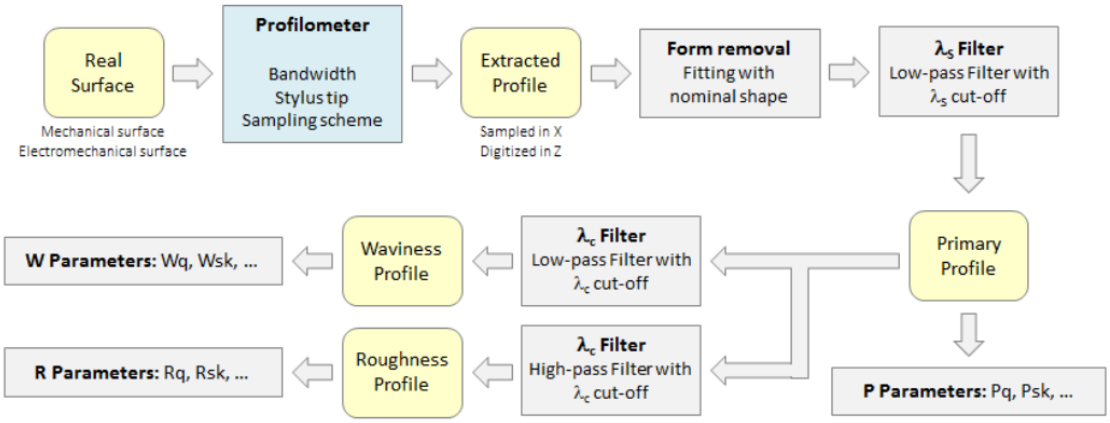

Figure 12: Diagram outlining surface operations for profile measurements. This image is originally by F. Blateyron [82]

Cut-off is the term used to describe the wavelength at which the filter attenuates the amplitude of the surface by 50% to differentiate between the different surface components [82]. The lengths of the cut-off filters for machined and turned surfaces are well defined in standards. ISO 4288 gives several cut-off filter lengths depending on the parameter that is being measured (such as Ra) and the range of the parameter value that is expected [83]. For example, if the surface is expected to have Ra values between 0.02 µm - 0.1µm, a cut-off wavelength for the λ_c profile filter of 0.25 mm is recommended. It is not stated exactly how these lengths were determined. The average value of the surface measurement over the line profile and below the cut-off filter is taken as the parameter value. The length of this line profile, known as the evaluation line, should be equal to five times the cut-off wavelength. Thus, a cut-off wavelength of 0.25 mm would have an evaluation line of 1.25 mm.

However, the ISO 4288 standard makes several references to drawings and technical specifications and was intended for machined or turned surfaces. Although it does give cut-off wavelengths and evaluation lines for the large roughness values

commonly seen in AM surfaces, as previously stated AM surface features can be very different compared to machined surfaces. The exact boundary between roughness and waviness is more uncertain and it is unclear whether the relevant surface features will still be accurately captured when using the cut-off filters recommended in the standards. F. Cabanettes *et al.* supported this statement by claiming that classical filters and cut-offs are difficult to transpose to AM surfaces [84].

A prevalent profile measurement method found in the literature was contact profilometry in which a stylus is dragged across a surface and the displacements of the stylus correspond to the materials surface profile. Several examples of AM surfaces measured using contact profilometry were found in the literature [22], [40], [47], [84]–[93]. However, because of the uncertainty of how to apply the existing standards to AM surfaces there was little to no consensus on the cut-off filters used to determine the roughness of the surfaces. As a result, it is difficult to compare roughness values between sources as they each define the boundary between roughness and waviness differently. Many of papers that mentioned using contact profilometry did not state the cut-off wavelengths making it difficult to properly evaluate or repeat these measurements [89]–[91]. In several instances it was found that cut-off filters were used that did not correspond to the surfaces recommended by the standard. For example, K. Mumtaz *et al.* and Y. Tian *et al.* both used evaluation lengths of 12.5 mm and cut-off lengths of 2.5 mm. However both of these papers reported Ra values of up to 40 µm which is significantly higher than the 2 µm – 10 µm range recommended in the standard [40][86]. Only one source by A. Triantaphyllou *et al.* was found to apply the standard recommended cut-off wavelength of 8 mm for their reported Ra values between 5 µm – 45 µm [47]. F. Cabanettes *et al.* compared contact profile measurements with optical techniques and found that contact methods did not measure the topography as accurately, not capturing the fact that the surface degraded with increasing build angle relative to the build plate. This may have been due to physical factors affecting the stylus such as deterioration, adhesion of melted particles to the stylus or mechanical filtering [84].

Although less widely used there are also non-contact methods of acquiring surface profile data. Only two instances of applying these to AM surfaces were found in the literature, both using digital optical microscopes [94], [95]. Neither of these sources however gave information on the cut-off wavelengths applied. Rather than using a stylus, non-contact measurement techniques typically use light to scan a surface although the exact principle behind each technique varies depending on the method used [96]. These methods differ in how they acquire the profile line data, but after the data has been acquired the steps to process the data as outlined in the ISO standards remains the same. These techniques offer certain advantages over contact measurements such as not potentially altering or damaging the measured surface, increased measurement speed and being able to measure smaller asperities [96]. However, these techniques were not commonly used in the literature for AM surfaces. This may suggest these techniques are more difficult to use compared to contact measurements, that a lack of heritage gives less confidence or that AM surfaces may be unsuitable for these techniques. Although the sources found in the literature used these techniques to capture profile roughness data, they can also be used for areal measurements. As such, these instruments often suffer the same limitations as other areal measurement devices and will be expanded upon in the next section.

Areal measurements

From reviewing the literature, areal measurements are slowly becoming more accepted as the norm for AM surface measurements. However, the lack of standards results in a similar problem as seen in with profile measurements: A lack of consistency between different sources on how these measurements should be applied leading to difficulty comparing results. The general principles of areal surface measurements are similar to profile measurements. A three-dimensional map of the surface is extracted and then filtration techniques are applied to this map to separate the form, waviness, and roughness components. The parameters are then measured on the surface that remains after filtration. This process is outlined below in Figure 13 , and these filters are [49]:

- S-filter: surface filter which removes small features below the length scale of interest, the result of which is called the primary surface
- F-operation: operation which removes form from the primary surface, the result of which is the S-F surface
- L-filter: surface filter which removes large feature above the length scale of interest from the primary surface or S-F surface

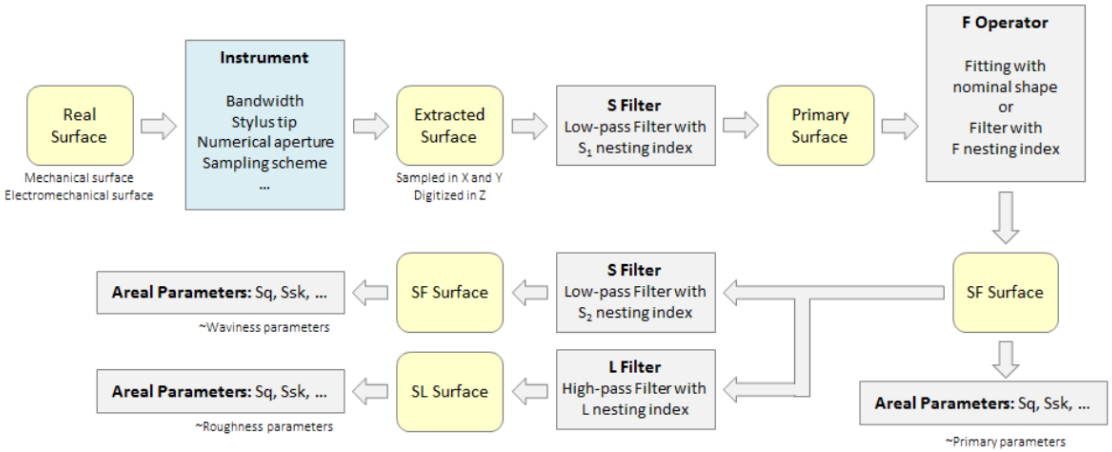

Figure 13: Diagram of surface operations for area measurements. This image is originally by F. Blateyron [82]

As previously stated, there are a variety of different contact and non-contact methods through which areal measurements can be performed. Non-contact methods were found to be the most common for areal measurements, particularly optical techniques including focus variation microscopy (FVM), confocal microscopy (CM) [97] and coherence scanning interferometry (CSI) [98]. [81]. As well as optical methods, the volumetric technique X-ray Computed Tomography (XCT) has occasionally been used to capture topographical or form information at scales similar to those used by optical methods [99] [100]. However, XCT was significantly less common for texture measurements compared with optical techniques.

Although the exact methods of these techniques differ, they suffer from similar limitations when scanning metal PBF surfaces. N. Senin *et al.* conducted a thorough investigation comparing optical and non-optical techniques on PBF surfaces including FVM, CSI, CM and XCT, focusing on the quality of the topographic reconstructions of surface features for each of these techniques [100]. They found that generally the

differences between the techniques were not significant when it came to investigating surface characterisation of large regions of interest through texture parameters on the micron scale. However, when investigating localised, small-scale features on the sub-microns scale the differences then became more significant with some local height differences between the techniques on the same order of magnitude as the features being measured. Interactions between the surface and instruments were the reasons for these differences, particularly due to features unique to PBF surfaces such as attached particles or weld tracks. High local slopes and variations in the amounts of light returned to the detector for the optical techniques were the dominant factors that caused discrepancies. XCT generally suffered from low resolution, although it was the only technique able to resolve some re-entrant features. It was concluded that although generally for large scale topography information all the techniques returned consistent results and that while none of the methods were superior or inferior, none of them should be considered reliable. Understanding how and why each instrument reacts as it does to specific topography formations is critical for proper understanding of texture parameters. It is worth noting that for this investigation, surface features and textures on the micron scale were of most interest and so the discrepancies caused by each of these techniques on the sub-micron scale had a smaller bearing on the choice of measurement technique.

3.2.3. Focus variation microscopy

Ultimately Focus Variation Microscopy (FVM) was chosen to measure the surface roughness of samples for this thesis. Areal techniques could give more information compared to profile techniques and of the optical techniques, given that little difference was reported in performance at the micron scale FVM was chosen because it was the most commonly used method for AM surfaces giving more published results for direct comparison [41], [48], [84]. The common use may have been due to its perceived ease of use, low measurement times and robustness against certain limitations of other optical systems such as being able to capture high slope angles and surfaces with varying levels of light reflectivity [99] [101]. For these reasons as well as ease of access, FVM was chosen as the areal roughness measurement technique for this research and thus will be

explored in greater detail. FVM combines optics with a small depth of focus with vertical scanning [48] [102]. Light from a white light source is inserted into the optical path of the system and focused onto the specimen via the objective lens. Light reflected from the specimen that hits the objective lens is gathered by a sensor. Due to the small depth of field of the optics, only small regions of the object are sharply imaged. To obtain complete detection of the surface with full depth of field, the optics are moved vertically along the optical (z) axis while continuously capturing data. A sequence of images is captured, creating a vertical stack of images. For each pixel within an image, local contrast is acquired by gathering information about surrounding brightness of pixels. This is repeated for the same pixel in every image in the vertical stack, resulting in a series of contrast values (known as a contrast curve) for every x, y location. Algorithms then use this contrast information and corresponding locations along the z axis to create a three-dimensional topographical map. RGB colour information associated with the contrast information is used to generate a colour map of the surface [48], [102]. A schematic diagram detailing the components and basic principles of FVM is presented in Figure 14.

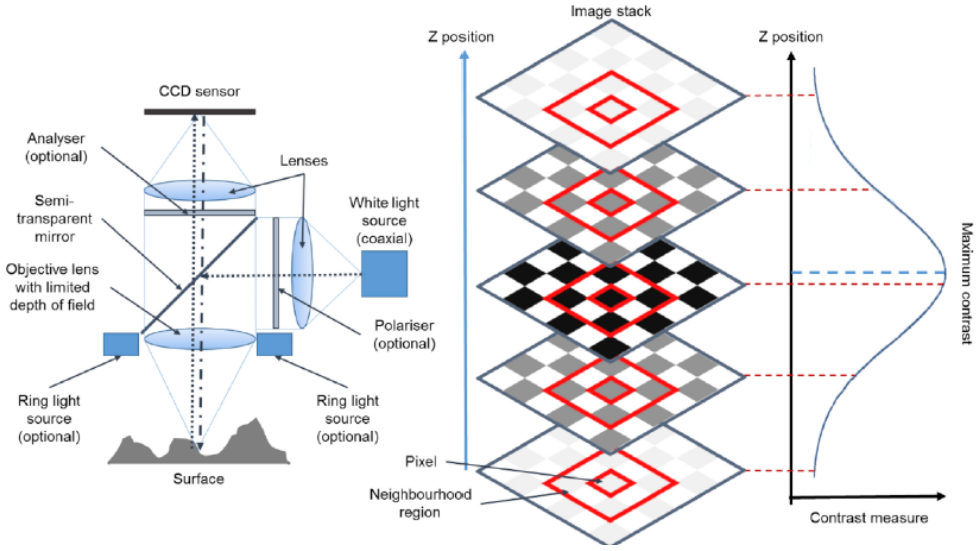

Figure 14: Schematic diagram of FVM technology [48]. Reproduced under Creative Commons CC-BY

However, there are limitations to FVM. Because it relies on analysing variation of focus, it is much less effective on surfaces where the focus does not vary sufficiently during the vertical scanning process. This can include transparent surfaces and surfaces

with only small local roughness [102]. Because these images are taken from directly above the surface, this makes it difficult to capture shadowed or overhanging regions. This may be a particular concern for re-entrant features commonly seen on PBF surfaces.

Measurement Settings

Magnification, Vertical and Lateral Resolutions

Many settings that can affect results on FVM can be changed. Magnification, vertical and lateral resolutions, illumination type, filters and cut-off wavelengths were identified as the key control parameters. Vertical resolution is the distances between images in the Z direction of the focal stack, while lateral resolution is the size of the region within which the contrast for each point is determined within each image of the stack [48]. Numerous papers were found that contained control parameters for FVM of AM surfaces, however few offered reasoning for their selected parameters. Although there is no standard for FVM measurements of AM surfaces, the literature was surveyed to see if there were common or recommended control parameters. A summary of the various control parameters found in literature are presented in

Table 5.

L. Newton *et al.* did a thorough study using Design of Experiments on how changing control parameters affected roughness measurements on metal PBF surfaces of different metals and build orientations [48]. Measurement quality was determined by the local repeatability error and percentage of non-measured points. Although they gave recommendations on how the illumination, lateral and vertical resolutions could be varied to improve the quality, they ultimately found that regardless of changes in the control parameters, variations of the surface texture parameter values were limited only to sub-micron scales and consistently within 5% of the average value for the same surface and objective.

N. Senin *et al.* particularly highlighted the importance of lateral resolution in resolving topographic details at small scale on the surface plane [100]. Both F. Cabanettes *et al.* and A. Triantaphyllou *et al.* described the S-filter, the filter which

removes small scale components from the surface, as being limited by the lateral resolution of the microscope [47], [84]. A. Triantaphyllou *et al.* used the same instrument that would be used in this work: An Alicona InfiniteFocus. They used a lateral resolution of 8 µm and a vertical resolution of 800 nm and reported that they achieved suitable measurements of areal texture parameters (although they did not specify the exact values). Given this reported suitability on the same instrument used in this thesis and the fact that their suggested value for the measurement area was adopted (described in the next section) it was decided to also adopt these values for the lateral and vertical resolutions. It should be noted that, as seen in

Table 5 this value for the lateral resolution was larger than others reported in literature and that L. Newton *et al.* found that larger lateral resolutions caused smoothing effects [48]. However as previously stated they also found that changing the measurement settings had little effect on the surface texture parameter values.

Filtration, Cut – off wavelengths and Sampling Area

As previously stated, filtration is the technique by which the roughness, waviness and form error are extracted from the measured surface for characterisation. According to R. Leach *et al.*, there are two steps necessary to applying a filter operation. The first is to choose a suitable filter method and the second to choose the appropriate filter parameter [42]. Choosing either of these incorrectly could lead to erroneous results. There are various different filtration methods including Gaussian, Spline and morphological filters however Gaussian is the most common and considered the standard for surface texture analysis [41].

S. Lou *et al.* conducted a review of numerous different papers that measured AM surface textures and found that, although they all applied a Gaussian filter the cut-off wavelengths used varied greatly [47], [97], [103], [104]. These differences in the cut-off filter were due to the previously discussed uncertainty between roughness and waviness for AM surfaces and applicability of ISO standards. S. Lou *et al.* proposed a new method of FVM measurements specifically for AM surfaces which separated not only roughness,

waviness and form but also features unique to AM surfaces such as globules and surface pores [41]. This first involved using a robust Gaussian filter rather than the standard Gaussian filter when extracting waviness from the surface, as the standard filter is particularly susceptible to outliers such as sharp peaks or valleys which can be common on AM surfaces resulting in inaccurately filtered surfaces [41], [105]. Robust Gaussian filters are instead insensitive to such outliers making them ideal for AM surfaces and also do not require surface form removal further simplifying the process [42]. The second novel technique was using watershed segmentation techniques to then extract out globules and surface pores, distinguished by their geometry, from the filtered surface. Whilst the idea of using watershed segmentation on surface topography is not novel, this was the first instance of it found specifically in the context of AM surfaces [42]. It was on the surface that then remained that roughness parameters were calculated. The measurement settings used are detailed in Table 5. The cut-off wavelength was estimated using the ball radius technique as described by R. Leach *et al.* [106] which estimates the smallest wavelength of sinusoidal profile that a spherical probe of known radius could faithfully reproduce.

Whilst this method of surface extraction is specifically designed and offers certain advantages for AM surfaces, there are a few issues that must be considered. First, as this is a novel technique at the time of writing no other instances of this method have been seen in the literature. Secondly the watershed segmentation technique used was specifically developed by the authors and not easily reproducible from the information given in the text. Recreating such a technique was outside the scope of this thesis. This watershed technique also relies on arbitrarily defining the boundaries between surface textures and outliers and although the authors gave values, this did not remove all outliers and was mentioned as an issue requiring further investigation. This paper was also the only instance found where features such as surface pores and globules on AM surfaces were explicitly defined as outliers and not part of the surface texture. Whilst such features on machined surfaces are less common and thus easily defined as outliers, they can be common on as built SLM surfaces depending on the process parameters used

to build them. Overall, the key feature taken from this paper was the use of the robust Gaussian filter.

Table 5: Table showing a summary of the different control parameters for focus variation microscopy found in the literature

Author	Magnifi-cation	Illumi-nation	L-filter (mm)	Vertical resolution (nm)	Lateral resolution (µm)	Measurement area (mm)
L. Newton *et al.*[48]	10, 20, 50	coaxial, polarised coaxial, ring light	-	50 - 900	1-4	1.62*1.62, 0.81*0.81, 0.32*0.32
N. Senin *et al.* [100]	20	ring light	-	-	0.44	0.81*0.81
F. Cabanettes *et al.* [84]	5,10,20, 50	-	-	50	2	3.22*1.9
A. Triantaphyllou *et al.* [47]	5	-	2.5	800	8	2.5*2.5
S. Lou *et al.* [41]	20	ring light	1.5	0.67	2.93	1.91*1.95

As seen in Table 5, different values for cut-off filters and evaluation areas were given in the literature. However, few of these provided reasoning behind their choices. A. Triantaphyllou *et al.* performed optical areal measurements on SLM surfaces and, using an area scale analysis method, concluded that a 2.5 mm by 2.5 mm evaluation area was sufficient to capture the significant characteristics of their measured AM surfaces [47]. This method can be used to determine the length scales at which no further topographical information can be determined [42]. Using this area scale analysis method, they were able to determine that this limit corresponded to a spatial wavelength of 2.5 mm and thus that there was no need for an L-filter larger than 2.5 mm. It is worth noting that this was performed on as-built coupons of different materials and not using the exact process parameters that were used in this investigation. However, the range of roughness values seen in this paper was similar to those expected in this investigation. This was the most comprehensive reasoning behind evaluation area size and cut-off

wavelength found in the literature. As a result, these values were adopted in this investigation.

Surface Texture Parameters

There are numerous different parameters that can be used to qualify the texture of a surface. However, it is beyond the scope of this thesis to provide a comprehensive summary on all the different parameters. Instead, a summary will be provided of the different textures parameters that were used in this investigation. The parameters used are summarised below in Table 6.

Table 6: Summary of the different areal surface texture parameters used in this thesis

Texture Parameter (µm)	Definition	Physical meaning	Equation [49]
Sa	Arithmetic mean of the absolute of the ordinate values	Average height deviation from a mean plane	$$Sa = \frac{1}{A}\iint_A \lvert z(x,y)\rvert dxdy$$
Sq	Root mean square value of the ordinate values		$$Sq = \sqrt{\frac{1}{A}\iint_A z^2(x,y)dxdy}$$
Ssk	Quotient of the mean cube value of the ordinate values	Measure of symmetry of roughness profile about mean plane	$$Ssk = \frac{1}{Sq^3}\frac{1}{A}\iint_A z^3(x,y)dxdy$$
Sku	Quotient of the mean quartic value of the ordinate values	How closely roughness profile matches Gaussian distribution	$$Sku = \frac{1}{Sq^4}\frac{1}{A}\iint_A z^4(x,y)dxdy$$
Sdq	Root mean square of the surface gradient	Average slope of the surface	$$Sdq = \sqrt{\frac{1}{A}\iint_A \left(\frac{\partial z^2}{\partial x}+\frac{\partial z^2}{\partial y}\right)dxdy}$$

Both Sa and Sq were used to describe the average height of the surface texture. These were by far the most commonly used parameters to describe areal surface texture. Although Sa is the areal equivalent to the profile texture parameter Ra, it does not allow

for direct comparison. However general trends in Sa values do follow the same general trends as Ra values [48]. As Sq is the root mean square of the ordinate values, it is equivalent to the standard deviation of the surface heights [42]. R. Leach *et al.* described Sq for this reason as having more statistical significance than Sa as well as being directly related to physical qualities such as surface energy and the surface light scattering [42].

Though Sa and Sq were the most commonly used parameters, they alone provide little insight to the complex nature of AM surfaces. Molyan *et al.* recommended other parameters that may help to better explain AM surfaces [45]. The skewness, Ssk, represents the degree of bias of a roughness distribution relative to the mean plane. In general this can be used to distinguish whether the surface is dominated more by peaks, which would show as positive skew, or valleys which would show as negative skew [42]. A. Triantaphyllou *et al.* showed that the Ssk parameter could also be used to differentiate between upskin and downskin surfaces of SLM coupons, with downskin surfaces being negatively skewed and upskin being positively skewed [47], [84]. The kurtosis, Sku, measures the spread of the surface height distribution and gives an indication of how well it matches a Gaussian distribution and the presence of outliers. A perfect Gaussian distribution would give a kurtosis value of three. A surface with inordinately high peaks or deep valleys would have a kurtosis greater than three, whilst gradually varying surfaces free of extremes tend to have kurtosis values less than three. Kurtosis can also give a measure of the spikiness of an area, a spiky area having a high kurtosis value whilst a bumpy area would have a low value [42].

The previous parameters were chosen as they were found to give a good general indication of the quality of an as-built SLM surface. The final parameter, the root mean square gradient (Sdq), was chosen specifically because of its relation to emissivity. S. Taylor *et al.* conducted a study investigating the relationship between surface topography and emissivity of AM parts [60]. They discovered strong correlations between the root mean square gradient and emissivity. However, it is worth noting that they studied profile texture parameters rather than areal texture parameters. This paper by S. Taylor *et al.*, as well as other studies discussing the relationship between roughness

and emissivity, will be discussed in greater detail in the emissivity literature review section 3.3 of this thesis.

3.2.4. Process parameter variation on roughness

Numerous studies have been conducted on how process parameters affect various output factors in the SLM process including surface roughness. This section will focus on how parameter variation influenced the surface roughness of 316L stainless steel in particular. The parameters varied and the ranges of values found in the literature influenced those used in this thesis. A summary of these parameters is presented in Table 7. It should be noted that build angle is described as the angle relative to the build plate. An angle of 0° is equivalent to a sample built parallel to the plate while 90° corresponds to a sample built perpendicular.

Three papers were found that studied the effects of varying energy density on surface roughness of 316L stainless steel [22], [79], [107]. Two of these papers used Design of Experiments (DoE), specifically Central Composite Designs, to establish the influence of each of the process parameters on the surface roughness. Y. Liu *et al.* built single track thin walled parts varying the laser power, scanning speed and layer thickness whilst Y. Deng *et al.* varied laser power, scanning speed and hatch spacing [22], [79]. Possibly because Y. Liu *et al.* was looking at thin-walled parts whilst Y. Deng *et al.* was looking at cubic samples, the ranges of the values for the process parameters varied quite considerably between them. For example, a laser power of 150 W was the second highest value used by Y. Liu *et al.* for thin-walled parts, whilst it was the lowest value used by Y. Deng *et al.* for cubes. It is worth mentioning that this may have been influenced by the maximum laser powers on the different printers. Y. Liu *et al.* had a maximum power of 200 W while Y. Deng *et al.* had a maximum power of 500 W. Y. Liu *et al.* focused on the surface roughness of the side faces of thin-walled parts, built at 90° to the build plate whilst Y. Deng *et al.* focused on the top faces (oriented at 0°) of their cubic samples. Given these differences, it is not surprising that the results of these investigations differed. Y. Liu *et al.* reported that layer thickness and its interactions with laser power and scanning speed had the greatest effect on roughness of the side faces of thin-walled

parts, whilst laser power had the least. Y. Deng *et al.* reported the opposite, claiming that laser power and scanning speed had the greatest influence on roughness of the top faces of cubic samples.

Both investigations showed that laser power and scanning speed had parabolic relationships with surface roughness and recommended optimised settings to produce samples with low surface roughness. Y. Liu *et al.* recommended a laser power of 150W, scanning speed of 105 mm/s, a layer thickness of 34.4 µm and a track width of 0.273 mm for the side surface of thin-walls. Y. Deng *et al.* recommended a laser power of 259.1 W, a scanning speed of 900 mm/s and a hatch spacing of 86.7 µm for the top surface of cubes. That these two investigations show almost contrary results demonstrates the need for a comprehensive study looking at all the factors of energy density.

D. Wang *et al.* also studied how energy density affected surface roughness, varying the laser power, hatch spacing and scanning speed whilst keeping the layer thickness constant [107]. They first studied the characteristics of single tracks and then, based on that analysis, built cubic parts and attempted to create a model to predict the surface roughness of top facing (0°) surfaces. This model estimated the shape of shape of single melt tracks as semi-circles in a 2D coordinate system. The surface profile was then expressed through a periodic equation before the Ra was calculated as the minimum of the least squares mid-line. This model made assumptions that the shape of every melt track was semi-circular and was the same. They found that the predicted roughness values were much lower than the measured values and that multi-layer fabrication was much more complicated than single or multi-track fabrication. Given this result and that starting with single track may eliminate key variables or interactions which affect the process in multi-layer experiments, it was decided not to start the work of this thesis with single track experiments.

Table 7: Table showing summary of process parameters and equivalent roughness values found from the literature.

***This paper reported energy density, but in units of J/cm² and so have been omitted**

Source	Machine	Average Powder size (µm)	Laser Power (W)	Scanning Speed (mm/s)	Layer Thickness (mm)	Hatch Spacing	Build Direction (°)	Energy input (J/mm³)	Ra (µm)
Y. Liu et al [22]	DiMetal-100	17.11	70 - 170	65 - 235	0.0215 - 0.0385	-	90	*	8.6 - 18.2
D. Wang et al[107]	DiMetal-100	17	100 - 150	250 - 1300	30	80 - 100	0 (cubic)	48.08 - 166.67	4.79 - 13.89
			150	350 - 800	30	60 - 100	0 (cubic)	78.13 - 208.33	6.03 - 24.16
G. Strano et al [91]	EOS M270	20	195	900	20	100	0 - 90	108.34	9 - 16
Y. Deng [79]	FS271M	-	150 - 300	700 - 1300	-	60 - 120	0 (cubic)	-	8.04-12.18

Through their investigation, D. Wang *et al.* concluded that energy density could be separated into four distinct categories depending on the level of Ra. These are shown in Figure 15.

Finally, G. Strano *et al.* investigated how surface roughness was affected by build orientation, keeping all other process parameters constant [91]. They found that as the sloping angle increased, so did the density of particles adhered to the step edges. However, this only really affected surface roughness when the layer thickness was comparable to the particle diameter as then particles along the step edges filled the gaps between layers. They found that roughness was lowest at 0° relative to the build plate, constant in the range of 5-45° and slowly decreased in the range of 50-90°.

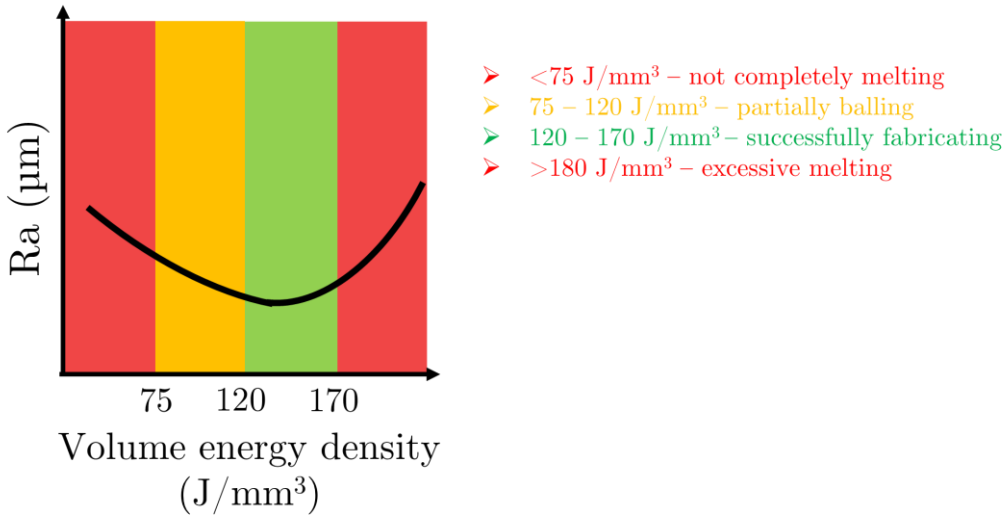

Figure 15: Diagram showing the four different energy density zones as described by D. Wang *et al.* and their effects on Ra measurements

3.2.5. Build plate positional effects on roughness

As mentioned in section 2.1, cooling and solidification rates greatly affect the microstructure and surface quality of AM parts. These rates can be affected by local heat transfer conditions which themselves can vary depending on the position of the part on the build plate. J. Kozhuthala *et al.* studied the effect of gas flow on the dimensional accuracy of SLM cylindrical 316L samples [1]. They built thirty-six identical cylindrical samples on a single build plate using a laser power of 90 W, scanning speed of 1500 mm/s and layer thickness of 30 µm (hatch spacing was not reported). Based on a nominal diameter of 10 mm, they found that the samples closer to the gas nozzle

showed a greater dimension deviation of roughly 0.095 mm on average than samples positioned farther away which averaged roughly 0.09 mm deviation. However they also found that the deviation perpendicular to the gas flow, roughly 0.11 µm on average, was larger than the deviation parallel which was on average 0.08 mm. This was due to the gas differently affecting the cooling rate depending on the position of the samples and the pressure of the gas on the samples affecting the rheology of the melt pool.

S. Kleszczynski *et al.* also investigated how the position of SLM samples on a build plate affected their roughness [2]. Using identical build parameters they built twenty-four funnel shaped samples with overhang angles of 45° and 70° relative to the build plate, as shown in Figure 16. The samples were built in Inconel 718 nickel alloy. It should be noted that they only chose one surface texture parameter Rz, a measure of the maximum profile height, to represent the surface roughness so the results of this study are somewhat limited. Generally they found that roughness did vary with position, with surfaces facing the walls of the build chamber having slightly higher roughness values (from 20 µm – 53 µm for the 45° samples) compared to other orientations. Samples positioned in the middle of the chamber had the lowest surface roughness (13.92 µm for the 45° samples), within the range of standard deviation.

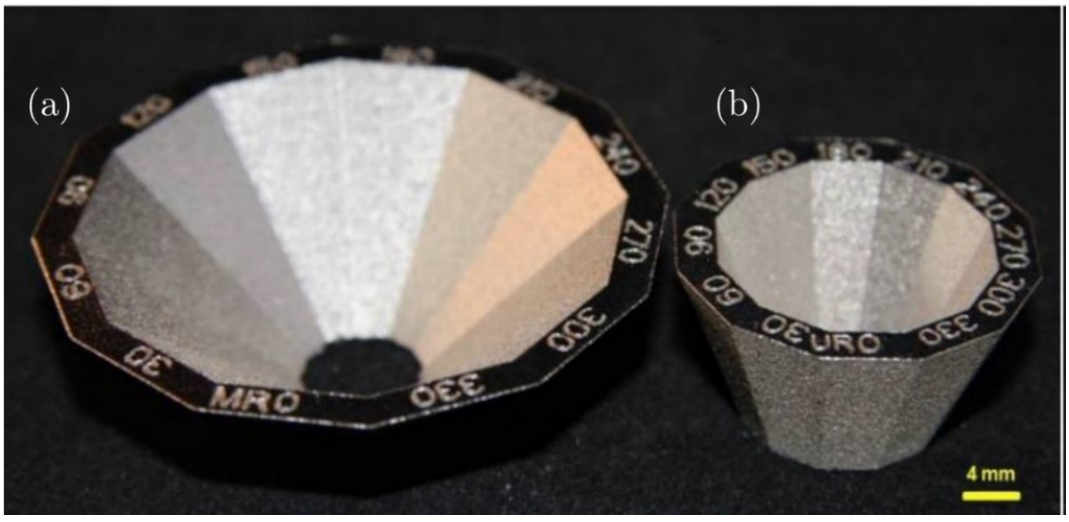

Figure 16: Picture showing the funnel specimen geometry for the (a) 70° and (b) 45° samples manufactured and investigated by S. Kleszczynski *et al.* This image is originally by S. Kleszczynski *et al.*[108]. Reproduced with permission

Additionally they also built specimens with nominal wall thicknesses of 0.5 mm to examine the potential effect of thin-wall features on the surface roughness. However

while they did see differences in the absolute values of surface roughness compared to the thicker samples, the trends due to position on the build plate remained the same. Given the identical build parameters, S. Kleszczynski *et al.* concluded that only the laser incidence angle was varied between samples and thus must have been the cause of the differences in roughness. The laser window was in the middle of the process chamber, so the laser beam was only circular in the middle of the chamber and potentially elliptical elsewhere. Different reflection conditions at different incidence angles were another possible cause, which could have caused differences in energy input and hence differences in surface roughness upon solidification.

3.2.6. Summary

Profile roughness measurement techniques, specifically contact profilometry, have a lot of heritage and numerous uses of it on AM surfaces were found in the literature. However as there are no standards for AM surfaces, little consensus was found on the cut-off filters that should be used to distinguish roughness from waviness. Areal techniques allow more information to be captured than profile measurement techniques which may make them more suitable for AM surfaces. Although they are becoming more commonly used in the literature, they still suffer from similar filtration problems as profile techniques due to a lack of standardisation. Focus Variation Microscopy was chosen as the measurement technique used in this thesis due to ease of access and the relatively larger amount of literature on its use for AM surfaces to compare against.

The measurement settings chosen were: lateral resolution 8µm, vertical resolution 800nm, robust Gaussian filter, evaluation area 2.5 x 2.5 mm, L-filter 2.5 mm. Sa, Sq, Ssk, Sku and Sdq were chosen as the surface texture parameters to be investigated. These were chosen to describe the surface in as much detail as possible while Sdq was chosen specifically for its relation to emissivity. Numerous papers were found that studied the link between process parameters and roughness for 316L stainless steel. None of these however varied all the parameters in energy density representing a notable gap in knowledge that the work in this thesis aims to fill.

3.3. Total hemispherical emissivity

Generally from surveying the literature it was found that, as surface roughness increased so did the emissivity [62], [109]–[113]. Reviewing all the different sources that discuss this is beyond the scope of this thesis, particularly given all the different factors that may influence these trends including material, emissivity and temperature ranges and surface conditions. Instead this section will focus on the summarising the state of the art for the different factors investigated as part of this thesis. These include the effects of surface roughness on emissivity (in the geometric region), emissivity of 316L stainless steel and emissivity of metal AM surfaces. A summary on the different measurement techniques is also presented.

3.3.1. Surface Effects on Emissivity

Geometric region and Modelling

Numerous sources stated that for surfaces with roughness on length scales greater than the wavelengths of thermal radiation, interactions between the surface and radiation can be described in terms of geometric optics. Both Touloukian *et al.* and W. Sabuga *et al.* found that, although there were many studies focused on this geometric region, accurate links between experimental results and theoretical models were limited to cases when the surface contained simple, regular shaped asperities [58], [61]. For more irregular surfaces such as sandblasted surfaces or where the ratio of rms roughness to wavelength was much greater than 1, there was poor agreement between theoretical models and experiments. W. Sabuga *et al.* theorised that this may be because irregular surfaces contained substructures with different roughness scales, and that the structure with the steepest slope would be decisive for the radiative properties of the surface. Experimentally validating models of such surfaces was challenging because of the difficulty of creating surfaces with different roughness parameters but with all other properties remaining the same [61]. Even after reviewing more recent literature, few studies were found that attempted to explain the link between roughness and emissivity beyond simplified models in the Geometric region [110][59]

Such real surfaces may be very comparable to as-built AM surfaces which are often described as irregular or aperiodic due to their numerous unique surface features such as balling and surface pores. As a result few models from studies found in the literature explaining the link between roughness and emissivity may be applicable to as-built AM surfaces. A study worth noting however was by S. Taylor *et al.* which was the only study in the literature that specifically focused on the relationship between surface topography and emissivity of metal AM surfaces [60]. They simulated the surface as periodic isosceles triangles to determine effects of certain geometric characteristics on emissivity rather than establish a concrete relationship between topography and emissivity. Similar to other works [58], [61] they found that slope of the surfaces, particularly the angle of the valleys, had a stronger influence on emissivity that the overall size of the features. This was explained by the "Mendenhall wedge effect". As a valley angle decreases it causes the incident radiation to undergo more reflections [114]. This results in more absorptions and thus a greater emissivity. They used these results to determine what surface texture parameters would be best to relate to emissivity. They chose the root mean square slope (Rdq) because of its relation to slopes and Ra because it was commonly used to describe the roughness of AM surfaces. As previously mentioned in this literature review, choosing which surface texture parameters to describe the surface was very important for this work as each parameter gives different information about the surface. In addition to other parameters, the areal texture parameter Sdq was used in this thesis because of the relationship between slope and emissivity.

Emissivity of metal AM surfaces

Several of the papers that have reported emissivity in relation to laser PBF additive manufacturing were focused on in-situ monitoring during the build process [115]–[118]. Whilst this did give information on potential ranges of emissivity values over wide temperature ranges, the emissive surfaces were the melt pool or powder layers rather than fully formed and solidified parts, and so emissivity might differ considerably. Nevertheless, the emissivity and temperature ranges reported in these papers by C. G. Ren *et al.* [115] and G. Mohr *et al.* [118] are presented in Table 8. Only one paper by

S. Taylor *et al.* was found that investigated the emissivity of solidified SLM metal surfaces, specifically for 316 stainless steel [60]. The results of S. Taylor *et al.* are also presented in Table 8, as are results for traditionally manufactured 316L stainless steel. As previously mentioned, only the paper by S. Taylor *et al.* was found to discuss the relationship between surface topography and emissivity of AM parts. The study focused emissivity from the top surfaces (0°) of cubic samples made from 316 stainless steel using SLM. Parts were manufactured with different processing parameters to produce surfaces with different roughness. These experiments showed, as many other reports had found, the slope of the surface measured by the texture parameter Rdq had a stronger correlation with emissivity than the average height parameter Ra. Different surfaces could have the same Ra but different shapes leading to different amounts of internal reflections and thus emissivity. However, it was the combination of these parameters (Rdq*Ra) that had the strongest reported correlation. Overall these results agreed with simulations that steeper and taller valleys on surfaces provided more opportunities for internal reflections and thus emissivity.

This work by S. Taylor *et al.* represents an excellent foundation for investigating emissivity of AM surfaces, however there were some limitations that this thesis hopes to address. The study only varied two control parameters, the laser power (50 W – 180 W) and scanning speed (600 mm/s – 2000 mm/s), to produce a variety of different surface roughness values (approximately 10 µm – 28 µm Ra). However, there are numerous other parameters which can affect the surface texture of AM parts such as layer thickness and build orientation. By varying only two parameters, S. Taylor *et al.* may have narrowed the types of surfaces capable of being produced by AM and thus limited the results of the study. They also used profile roughness parameters for surface texture which numerous reports have stated is less appropriate for AM parts than areal parameters. Characterisation of the surface was also limited to roughness measurements. Although thorough, these may have provided more information about the surface if provided in context with microscopy images. A more detailed comparison against results of this thesis will be given in the results chapter.

Table 8: Table showing a summary of 316L stainless steel emissivity values and methods found in the literature

Author	Build method	Spectral Range (µm)	Measurement Method	Temperature (K)	Surface(s)	Emissivity (a.u.)
C. G. Ren *et al.* [115]	SLM	1.65 - 1.8.	pyrometer	-	melt pool	0.64
	SLM	1.4 - 1.65	pyrometer	-	melt pool	0.7
G. Mohr *et al.* [118]	SLM	2 - 5.7	infrared thermography	423.15 - 853.15	powder (bulk)	0.2 - 0.25
	SLM	2 - 5.7	infrared thermography	423.15 - 853.15	powder (surface)	0.37 - 0.45
S. Taylor *et al.* [60]	SLM	2.5 - 24	infrared spectrometer	293.15	10 µm Ra - 27 µm Ra	0.15 - 0.25
F. Valiorgue *et al.* [119]	cast	3.4 - 5	infrared thermography	323.15 - 823.15	-	0.4 - 0.9
T. S. Hunnewell *et al.* [120]	cast	total hemispherical	calorimetric	400 - 1100	0.13 µm Ra	0.26 - 0.36
	cast	total hemispherical	calorimetric	400 - 1100	2.36 µm Ra	0.29 - 0.42
	cast	total hemispherical	calorimetric	400 - 1100	1.22 µm Ra	0.32 - 0.44
	cast	total hemispherical	calorimetric	400 - 1100	0.59 µm Ra	0.37 - 0.47
S. Frachet *et al.* [121]	cast	total hemispherical	calorimetric	400 - 900	-	0.39 - 0.45

Oxidation

Parts built using PBF are typically processed under an inert environment to ensure that parts are not oxidised. Nevertheless, parts might be contaminated during handling or testing and so it is important to understand the effects of oxide layers on emissivity to explain any potential trends or errors seen. H. Jo *et al.* investigated the effects of oxide layers on the spectral emissivity of roughened surfaces (0.011 µm – 1.86 µm Ra) [62] of SA508 steel. They found that the effects of oxide layer on emissivity were greater than surface roughness, and that emissivity strongly depended on the thickness of the oxide layer. They attributed these effects to the different optical constants of the oxide layer compared with the base steel.

3.3.2. Emissivity of traditionally manufactured 316L stainless Steel

As the focus of this thesis is 316L stainless steel, presented in this section are emissivity values for 316L stainless steel found in the literature as they vary with roughness and temperature. A summary of these are presented in Table 8.

T. S. Hunnewell *et al.* conducted a thorough experimental campaign on the effects of surface roughness on the total hemispherical emissivity of 316L SS [120]. They investigated as received, sandblasted, oxidised and graphite coated samples using the calorimetric method over a temperature range of roughly 400 K – 1200 K. Generally the results were as expected, with emissivity increasing with temperature for all the samples tested. As the grit size used to roughen the samples increased, so did the emissivity due to the higher grit surfaces causing more internal reflections of radiation, leading to a higher absorptivity and thus higher emissivity. Interestingly T.S. Hunnewell *et al.* also found that as the grit size increased, the surface area and surface texture parameter (Ra) values decreased. Thus the emissivity was inversely proportional to the surface Ra and surface area. This goes against other reports in literature that found emissivity generally increased with increasing Ra [60], [122], though no explanation was given for these trends and no other source was found comparing sure area with emissivity. A more

in-depth discussion of these results and comparison against the results obtained in this thesis will be given in the results chapter.

3.3.3. Measurement Techniques

Emissivity measurement methods can be divided into two different categories: direct and indirect [58], [111], [123], [124]. With direct methods, emissivity is calculated from the ratio of the emissive power of the sample and a blackbody at the same temperature. With indirect methods emissivity is assessed from the spectral reflectance of an opaque material, based on application of Kirchhoff's law. Brief summaries of different techniques to measure emissivity using these methods are presented in Table 9.

Table 9: Table showing the different methods and techniques for measuring emissivity

Method	Technique	Description [125]
Direct	Calorimetric	Directly measure energy necessary to maintain the temperature of a sample surface when there are only radiative exchanges by heating sample and measuring dissipated power
Indirect	Radiometric	Measure the radiation of the heated surface of a sample
	Reflectometric	Measure the total or spectral reflection coefficient and use Kirchhoff's law to calculate emissivity
	Spectral Reflectometric	

After reviewing the literature it was decided that direct measurement techniques, specifically the calorimetric technique, would be best for this thesis. The calorimetric technique was reportedly better for high temperature, high emissivity measurements than the indirect techniques [123], [125]. Generally indirect techniques required additional analysis to transform spectral and directional measurements into total hemispherical measurements. They also require specialised optics that are not suitable for measuring emissivity at elevated temperatures [123]. Much of the equipment needed for calorimetric measurements such as a vacuum chamber, power supply and temperature probes were readily available which greatly simplified the process. This was also a much more commonly found technique to measure total hemispherical emissivity, especially over the desired temperature range [113], [120], [126], [127]. Details of this technique including the exact setup will be given in the Methodology section of this thesis.

3.3.4. Summary

Generally as surface roughness of metals increased so did the emissivity, due to this causing higher amounts of internal reflections of radiation. Correlating theoretical models of irregular surfaces with experimental values was difficult due to complicated surface features at different length scales.

Despite being commonly used to measure surface roughness, S. Taylor *et al.* reported Ra was not a good indicator of emissivity of metal SLM surfaces because similar values could have different shapes and thus different amounts of internal reflections. Instead, they reported surface slope was a much better indicator of emissivity. This is likely because as the slope increases radiation undergoes more reflections. S. Taylor *et al.* found that the surface texture parameter Rdq, the root mean square slope, correlated well with emissivity, though the product of Ra*Rdq had the strongest correlation.

T. S. Hunnewell *et al.* measured the emissivity of cast 316L and found for surfaces of increasing roughness (0.13 µm – 2.36 µm Ra) it varied between 0.26 – 0.47 between 400 K – 1100 K. They also showed that for sandblasted surfaces, as the surface area of cast 316L decreased, the emissivity increased.

The calorimetric technique was chosen to measure the emissivity due to the ease of setup and its suitability for high temperatures and high emissivity values

3.4. Electrical resistivity

Although papers were found that looked at the electrical resistivity of AM metals, not many studies were found that investigated the relationship between electrical resistivity and process parameters for PBF processes. This indicates that this is still a novel field with much to be investigated. It is worth noting that none of the resistivity studies investigated SLM 316L stainless steel, and while many of them did investigate process parameter variation, all the studies found were performed at room temperature. Regardless, the studies that were found provided insight into what was to be trends could be expected for electrical resistivity of AM parts, as well as gaps that could be investigated further. A summary of these studies is presented here.

3.4.1. Resistivity of AM metals

Copper, due to its high electrical conductivity, was common subject of AM electrical property investigations. A particularly thorough study by C. Silbernagel *et al.* looked into the effects of build orientation and heat treatment on pure copper [128]. The authors noted some issues with other reports of electrical properties of AM copper. Some back calculated resistivity from measurements of surface conductivity [129], [130] which C. Silbernagel *et al.* found to be inaccurate for AM parts as it incorrectly assumes isotropic properties [131]. Other reports referred to electrical properties without actually stating the conductivity or resistivity or the AM copper [132], [133]. C. Silbernagel *et al.* used Design of Experiments to obtain process parameters that achieved a maximum relative density of 85.8%, and built samples at 0°, 45° and 90° relative to the build plate. They measured the resistivity using the four-wire Kelvin method. They found a strong correlation between build orientation and resistivity, with 0° horizontal specimens having the lowest resistivity and vertical 90° specimens having the highest. These differences correlated with porosity variations between the samples rather than grain structure, as the horizontal samples had more continuous melt tracks and fewer discontinuities between layers than the vertical samples.

Several papers have investigated the resistivity of AM alloys [131], [134]–[137], the electrical properties of which can be affected by different mechanisms compared to pure metals. C. Silbernagel *et al.* studied AlSi10Mg aluminium alloy and found that, similar to pure copper, build orientation had a large effect on the resistivity [131]. However, the results were opposite, with vertically built samples having the lowest resistivity and the horizontal having the highest. These differences were attributed to variations in the microstructure rather than porosity. Rapid cooling during manufacturing resulted in dendritic structure along the build direction with silicon rich areas segregating the structures. Horizontal orientations produced specimens with conductive pathways that saw more silicon rich regions, and thus electrical resistivity was higher. SLM 316L stainless steel also exhibits cellular structures with sub grain boundaries composed of heavier elements [25], [66], [67], but the potential effect of this on electrical properties are unknown.

Y. Shi *et al.* found that different factors dominated the impact on resistivity depending on the energy density [137] used to process a different Al–Mg–Sc–Zr aluminium alloy. At lower densities (<99.5%) which corresponded to lower volumetric energy densities, porosity was the dominant factor that affected resistivity. However above 99.5% density, the amount of solute in solid solution had the largest effect on resistivity. As the solute became supersaturated the resistivity increased. A study by KA. Ibrahim *et al.* is worth noting, as they studied the effects of process parameter variation on electrical conductivity of 316L stainless steel manufactured by selective laser sintering (SLS) [138]. This sintering, rather than full melting in SLM, resulted in high porosity from 5% to 40% and corresponding increase in resistivity by roughly 86%.

While these studies offer insights into what trends to expect, there remain several gaps in knowledge. Each of the studies only measured resistivity at room temperatures. Temperature is known to greatly affect resistivity and may alter the trends mentioned in these reports. While process parameters were varied, like the reports found on roughness, no study was found that varied all the factors that make up volumetric energy density. As a result, a key interaction between process parameters and its influence on resistivity may have been missed. The work in this thesis will attempt to cover these gaps by varying more process parameters and measuring resistivity over a large temperature range.

3.4.2. Resistivity of 316L Stainless Steel

Numerous material datasheets gave values for resistivity of cast and wrought 316L stainless steel, but only at room temperature. These values are presented in Table 10. P. Pichler *et al.* reported the resistivity of 316L stainless steel from 500 K – 2800 K using ohmic pulse heating [139]. They presented two sets of resistivity values, one using the initial geometry of the specimen, and another corrected for volume expansion. Both values are presented in Figure 17. Although the resistivity increases with temperature for both geometries, when corrected for volumetric expansion the sample slightly decreases in resistivity around 1900 K.

Table 10: Resistivity values of 316L stainless steel found from various datasheets. All values were taken at 20°C

Source	Value (µΩm)
United performance metals datasheet [140]	0.74
AZO Materials datasheet [141]	0.74
Thyssenkrupp datasheet [142]	0.75
Aalco datasheet [143]	0.74
Aerospace Specification Metals Inc datasheet [144]	0.74

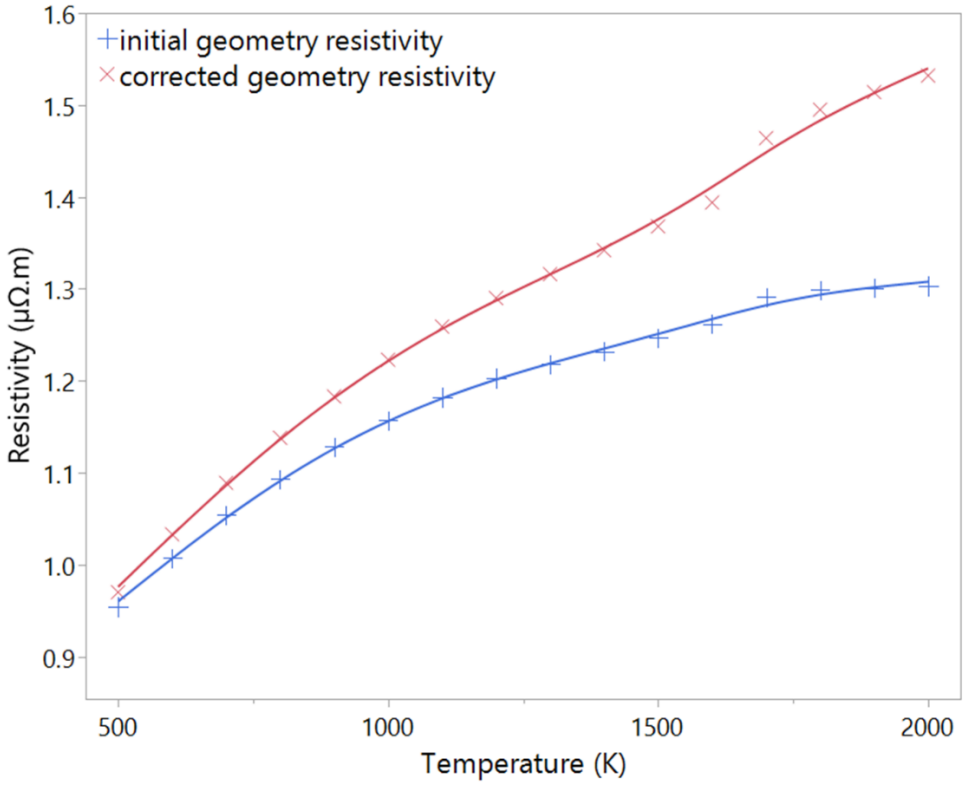

Figure 17: 316L SS resistivity values by P. Pichler *et al.*[139].

3.4.3. Summary

Both the resistivities of additively manufactured pure copper and alloys were shown to vary with build angle, though the reasons for the variation differed. For pure copper, it was because of porosity variations between build angles while for AlSi10Mg it was because of variations in size of silicon rich dendritic boundaries. Similar dendritic features are reported in SLM 316L stainless steel, but potential effects on resistivity are unknown. No studies reported resistivity of SLM metals at elevated temperatures. The resistivity of cast 316L SS is reported to vary between approximately 0.9 µΩm – 1.3 µΩm between expected resistojet service temperatures of 500 K – 1400 K.

4. Methodology

In this chapter, the methodology and instrumentation used to carry out the various experiments needed for this investigation are detailed. First, an overview and rationale of the experiments is presented followed by a description of the Design of Experiments technique used. An overview of the SLM process and the emissivity and resistivity measurements are then given followed by descriptions of the area determination and roughness measurement techniques used. Finally, the chapter outlines the various material characterisation techniques used.

4.1. Overview

The overall goal of this investigation was to understand how the SLM process affected the emissivity and resistivity of as built 316L stainless steel. To do this, process parameters were varied to see how these changes affected surface and microstructural features on built parts and how these in turn affected the emissivity and resistivity. The literature review in the previous chapter detailed which input factors were chosen and why.

Given the large number of input factors a Design of Experiments (DOE) method, particularly a definitive screening design, was used to explore the influence of each of these factors on the chosen output factors (responses) in as few tests as possible. The input factors and responses are detailed in Figure 18.

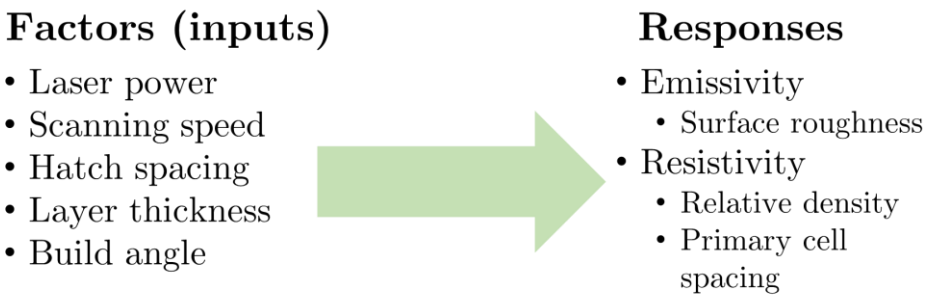

Figure 18: Input factors and responses chosen for this investigation

To thoroughly investigate each of the responses, numerous experimental tests were needed. The tests chosen are detailed in Table 11.

Table 11: Table detailing the different measurement and characterisation techniques used in this investigation

Response	NDE	Measurement method/ Technique	Standard	Note
resistivity	Destructive	Four probe	ASTM B193-16[145]	Measured alongside emissivity
emissivity	Destructive	Calorimetric method	ASTM C835-06 [146]	Sample size set by standard
primary cell spacing	Destructive	Scanning electron microscope/Area method and Image analysis	ASTM E112-10 [147]	-
surface texture	Non-destructive	Focus variation microscope	-	Sa, Sq, Ssk, Sku and Sdq
relative density	Destructive	Archimedes method and CT scanning/image analysis	ASTM B962-08 [148]	-
surface topography	Non-destructive	Scanning electron microscope	-	-

As seen in Table 11, some tests were destructive and so three samples were built for the processing condition specified in each DoE run. A summary of the samples used for each test is given in Figure 19, with further details on specimen dimensions and processing to follow.

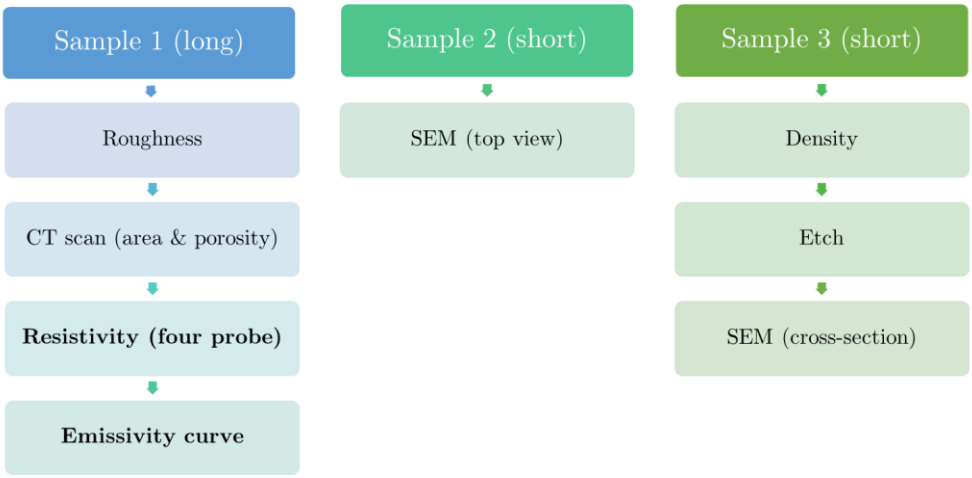

Figure 19: Chart detailing how each the tests were divided amongst the three samples produced for each build run

4.2. Selective Laser Melting

4.2.1. Overview

Selective Laser Melting (SLM) was chosen to additively manufacture the samples for this investigation. Parameters affecting volumetric energy density (laser power, scanning speed, hatch spacing, layer thickness) and build orientation were chosen as the DoE input variables due to the large reported influence on final part density, microstructural and surface features. This section details the build process including the range of the inputs and the rationale behind these choices.

4.2.2. Powder

The powder used was CL 20 ES, a 316L (1.4404) stainless steel powder supplied by Concept Laser. The particle size fractions specified by the supplier were $d_{10} = 20.29$ µm, $d_{50} = 30.98$ µm and $d_{90} = 45.55$ µm. The specified particle size distribution ranged from approximately 9 µm to 73 µm. The specified volume cumulative distribution (Q_3) and distribution density (q^3) are shown in Figure 20 [149]. The specified chemical composition of the powder is given in Table 18 [149].

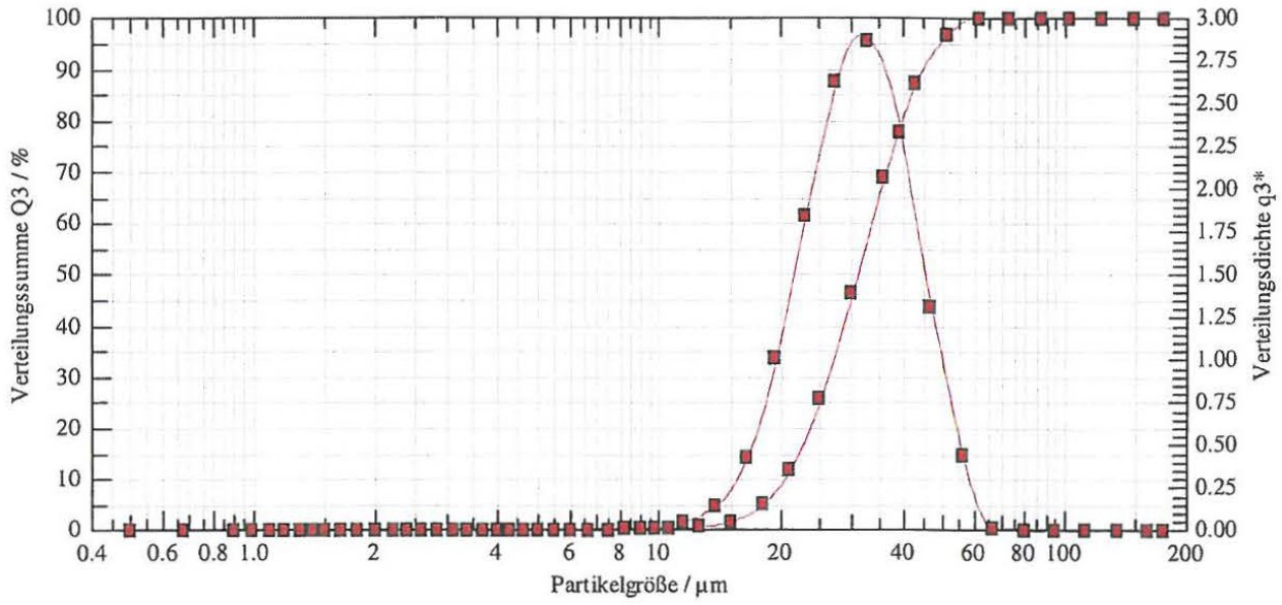

Figure 20: Particle size distribution of the CL 20ES powder used to build the parts for this investigation [149]. Provided by supplier.

Table 12: Elemental composition of the CL 20ES 316L stainless steel powder [149]

Element	Fe	C	Mo	Ni	Si	Mn	Cr	P	S
Wt. %	Balance	≤ 0.03	2 - 3	10 - 14	≤1	≤ 2	16.5 - 18.5	≤ 0.045	≤ 0.03

4.2.3. Metal printer

The machine used to build the parts was a Concept Laser M2 Cusing machine and was operated by the technicians at the Engineering and Design Manufacturing Centre (EDMC) at the University of Southampton. The main properties of this machine are shown in Table 13.

Table 13: Main properties of the Concept Laser M2 Cusing machine

Property	Value ranges
Build volume (x*y*z) (mm)	250*250*280
Layer thickness (µm)	20 - 80
Laser power (rated) (W)	200
Focus diameter (µm)	50
Gas supply	N_2

The parts were directly built onto a stainless-steel build plate using the island scanning strategy. Islands were 5 mm * 5 mm, and the scan direction was rotated by 45° between each build layer. After the builds were completed, parts were removed from the build plate by wire-cut electrical discharge machining (EDM).

4.2.4. Process Parameters

Design of Experiment

Following the literature review, the input parameters chosen to vary were:

- Laser power
- Scanning speed
- Hatch spacing
- Layer thickness
- Build orientation

By varying the values of these input parameters, their effect on the responses could be determined. However as there were many input parameters, traditional experimental methods such as trial and error or one factor at a time (OFAT) were not considered. OFAT would have resulted in many builds to study each parameter combination and would also have missed out on interactions between samples (how the level of one parameter affected the impact of another).

Design of Experiments (DoE) was chosen over OFAT to study the effects of each input factor on the responses with a fewer number of build runs, reducing build time and costs. It also allowed for modelling the behaviour of the responses as a function of the input factors and to use this to optimise the responses in future studies [150]. A Definitive Screening DoE was selected as it is suitable for early-stage experiments when there are many input factors to identify which factors have the greatest effect on the response [151]. Definitive screening designs are ideal when there are four or more factors, when most of these factors are continuous and when there are expected interactions between the factors [151].

Process Parameter selection

Definitive screening designs require each of the continuous input factors to be varied across three levels: low, middle, and high. Following a literature review of process parameters used to build 316L stainless steel parts seen in section 3.1.3, the following ranges of parameters were chosen as shown in Table 14.

Table 14: Table showing the range of process parameters chosen

	Laser Power (W)	Scanning Speed (mm/s)	Hatch Spacing (mm)	Layer Thickness (µm)	Build orientation (°)
Low	150	500	0.05	20	0
Middle	170	750	0.075	30	45
High	190	1000	0.1	40	90

The main criteria for this literature review were parameters for thin-walled 316L specimens and those that resulted in high density (>99%) parts. Energy densities from literature that resulted in high density parts varied from 33.3 J/mm^3 – 214.3 J/mm^3. For thin-walled parts an energy density of 59.52 J/mm^3 reportedly produced accurate parts (maximum 20 µm deviation from nominal). These were used as the basis for the middle values and then extremes were chosen on either side from values that resulted in up to 15% lower density values. Build orientation values were chosen to cover the widest possible range.

The software Minitab was used to build the different parameter combinations. The result was seventeen runs of different parameter combinations, as shown in Table 15.

As previously mentioned, the build angle describes the angle that the part was built relative to the build plate. An angle of 0° was parallel to the build plate, 45° was diagonal and 90° was perpendicular, as shown in Figure 21.

Table 15: Build parameter combinations for the definitive screening design

Build Run	Laser Power (W)	Scanning Speed (mm/s)	Layer Thickness (mm)	Hatch Spacing (mm)	Build Angle (°)	Energy Density (J/mm³)
1	170	1000	0.04	0.1	90	42.5
2	190	500	0.04	0.1	0	95
3	190	750	0.04	0.05	90	126.67
4	150	500	0.04	0.1	90	75
5	190	1000	0.04	0.075	0	63.33
6	150	500	0.04	0.05	0	150
7	150	1000	0.04	0.05	45	75
8	190	500	0.03	0.05	90	253.33
9	170	750	0.03	0.075	45	100.74
10	150	1000	0.03	0.1	0	50
11	190	500	0.02	0.1	45	190
12	150	500	0.02	0.075	90	200
13	170	500	0.02	0.05	0	340
14	190	1000	0.02	0.05	0	190
15	190	1000	0.02	0.1	90	95
16	150	1000	0.02	0.05	90	150
17	150	750	0.02	0.1	0	100

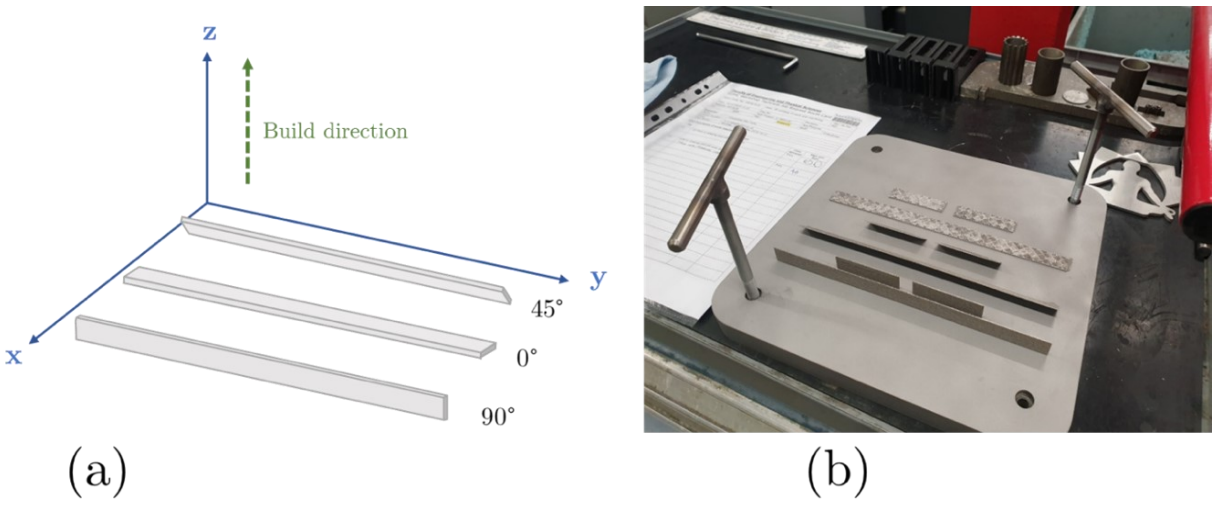

Figure 21: a) Diagram showing the build direction of the samples relative to the axes of the build chamber and (b) a batch of samples after they were removed from the build chamber

4.2.1. Sample Geometry

The samples for emissivity and resistivity measurements were built following the emissivity standard ASTM C835-06. This standard recommended samples being 250 mm in length, 13 mm in width and 250 µm in thickness. However, the build geometry of the Concept Laser M2 Cusing was limited to a recommended length of 200 mm, and so this shorter dimension was adopted. The samples to be used for other tests to characterise microstructure and surface morphology, noted in Figure 19 as samples 2 and 3, were only built to 50 mm length to save on build time and space on the build plate. The thickness and width dimensions however were kept the same. Figure 21 shows some of these samples after they were removed from the build chamber. As the island scanning strategy was used, the shorter samples would not affect the length of the scans. Also, the shorter length should not have affected the local heat transfer into the base plate or cooling rate, which were important factors for the resulting microstructures.

4.3. Emissivity and Resistivity Measurements

4.3.1. Emissivity Measurement – Calorimetric Method

Overview

The calorimetric method was chosen to measure the total hemispherical emissivity of the SLM parts. This was done following the standard ASTM C835-06 [146]. Generally, this required resistive heating of a printed test specimen suspended within an evacuated chamber until steady state conditions were reached. The temperature on the walls of the chamber as well as the temperature and power dissipated over a small central region on the test strip were continuously measured and the whole process was automated using a LabVIEW script. This was repeated over several steps until a maximum current input and corresponding maximum temperature was reached. Equating the power dissipated to the radiative heat transfer to the surrounding environment and knowing the temperatures, the emissivity of the sample was calculated using the Stefan-Boltzmann equation, shown as equation [10].

$$\varepsilon = \frac{Q}{\sigma A_1 (T_1^4 - T_2^4)} \quad [10]$$

Where Q (W) is the power generated in the specimen over the central test section length and A_1 (m^2) is the total radiating surface area of the central test section length. The Stefan-Boltzmann constant, σ, is equal to 5.669×10^{-8} $W/m^2 \cdot K^4$ and T_1 (K) and T_2 (K) are the temperatures of the test strip and the vacuum chamber wall respectively. The power generated in the specimen was calculated through equation [11].

$$Q = IV \quad [11]$$

Where I (A) is the current supplied to the test strip and V (V) is the voltage measured over the central test section length. For a rectangular specimen, the radiating surface area was calculated through equation [12].

$$A_1 = 2L(w + t) \quad [12]$$

Where L (m) is the length of the central test section, w (m) is the width of the test strip and t (m) is the thickness. The standard recommends a sample that is as long as possible to reduce conduction losses from the sample holders and recommends 250 mm for stainless steel, however only 200 mm lengths could be manufactured given equipment constraints noted about.

Other deviations from the standard necessitated by equipment limitations included the thickness of the thermocouple wires, the vacuum pressure and cooling of the chamber walls. Some of these differences as well as other sources of error were considered when calculating the emissivity and are detailed later in this section.

Vacuum Chamber

To avoid heat loss from the test strip by convection or conduction, emissivity experiments were conducted in the hatch chamber of a larger vacuum chamber facility in the David Fearn Electric Propulsion Laboratory at the University of Southampton. The dimensions of this hatch chamber were 0.75 m diameter x 0.7 length and had a view port on the door side to allow for visual inspection during testing. This chamber was equipped with an Edwards XDS 35i roughing pump and a Leybold TURBOVAC MAG W 700 iP and pressure in the chamber was constantly monitored by Pfeiffer Vacuum PKR 251 gauge. This vacuum chamber is shown in Figure 22.

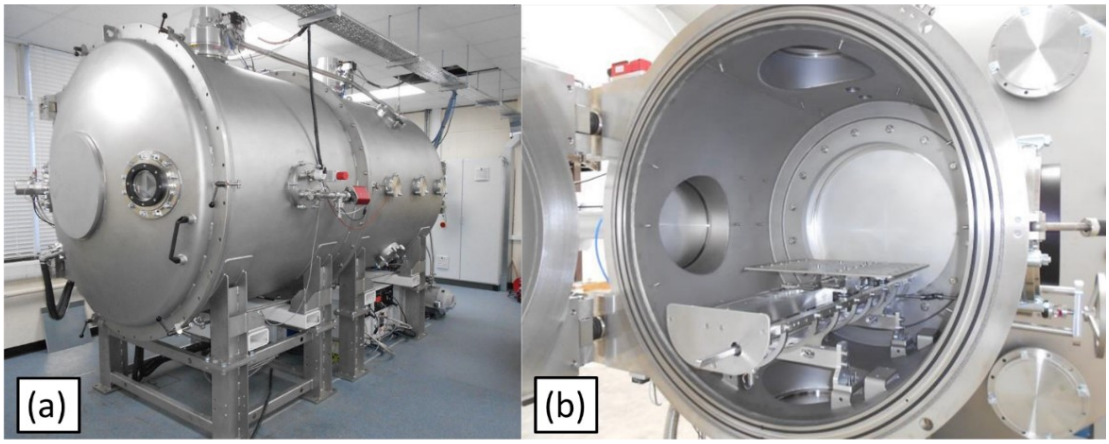

Figure 22: Photographs of (a) The main vacuum chamber and (b) The hatch vacuum chamber

The test required that the enclosure presented a blackbody environment to the test specimen. To achieve this the ASTM standard requires that the vacuum chamber enclosure and test strip meet the condition in equation [13].

$$\frac{1}{\varepsilon_1} \gg \frac{A_1}{A_2}\left(\frac{1}{\varepsilon_2} - 1\right) \qquad [13]$$

Where A_2 and ε_2 are the total internal surface area and the emissivity of the vacuum enclosure, respectively. The total internal surface area of the vacuum chamber hatch was approximately 2.53 m^2, whilst the surface area of the central test section, calculated using equation [12] (L = 0.075 m w = 0.013 mm, t = 0.00025 m), was approximately 1.99×10^{-3} m^2. Thus, the ratio of the central test section of the test strip to the surface area of the vacuum chamber was approximately 7.86×10^{-4}. This, when combined with the fact that the inner walls of the vacuum chamber hatch were lined with a black coloured thermal shroud, giving it a high emissivity greater than 0.8 (as required by the standard) ensured that the chamber satisfied equation [13].

Experimental setup

Metal tabs made from 316L stainless steel were clamped to the top and bottom of the sample test strip to supply electrical power for heating the sample. The top was fixed to a specimen holder and the bottom tab was free to allow for thermal expansion without flexing of the sample. Electrical connection to the tabs was made using copper rods connected to a feedthrough port on the vacuum chamber. To electrically isolate the test strip from the rest of the sample holder, the metal tabs at the top of the test strip

were sandwiched between ceramic tabs made from Machor machinable ceramic. During experiments, the test strip was suspended within the vacuum chamber hatch from a sample holder manufactured from aluminium extrusion, the bottom of which was fastened to the baseplate of the vacuum chamber hatch. This setup is shown in Figure 23.

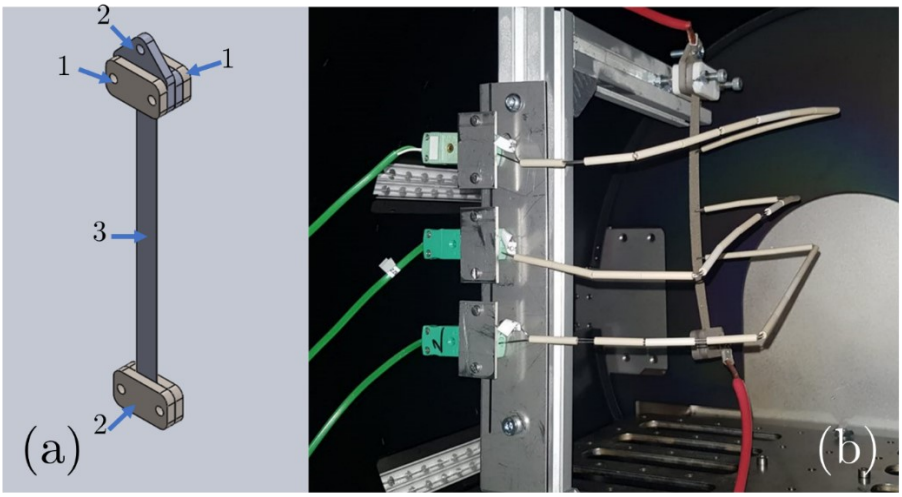

Figure 23: (a) CAD model of the SLM test strip in the test assembly showing 1-the Machor ceramic tabs, 2 - the metal tabs and 3 - the SLM sample and (b) a photo of the test assembly in the hatch vacuum chamber

Temperatures along the test strip were measured using three K-type thermocouples (model TC Direct 406-645) and were attached to the sample surface by spot-welding. These were mineral insulated thermocouples to prevent ground loops. These thermocouples were spot-welded on to the test strip approximately 37.5 mm apart resulting in a central test section 75 mm in length as recommended by the standard. A further three thermocouples were attached to the vacuum chamber enclosure using Kapton tape: two on opposite walls of the chamber and a third on the baseplate. Datalogging of the temperature measurements was achieved using a National Instruments NI-9213 module in an NI cDAQ-1988XT CompactDAQ chassis.

Electrical power to the test strip was supplied by a Kikusui PWX1500L power supply unit (PSU) operated in a current controlled mode. Voltage was measured across the two outermost thermocouples by using a Keysight 34401A digital multimeter. Voltage leads were attached to the thermocouple feedthroughs on the vacuum chamber door. A diagram of the entire experimental setup is detailed in Figure 24.

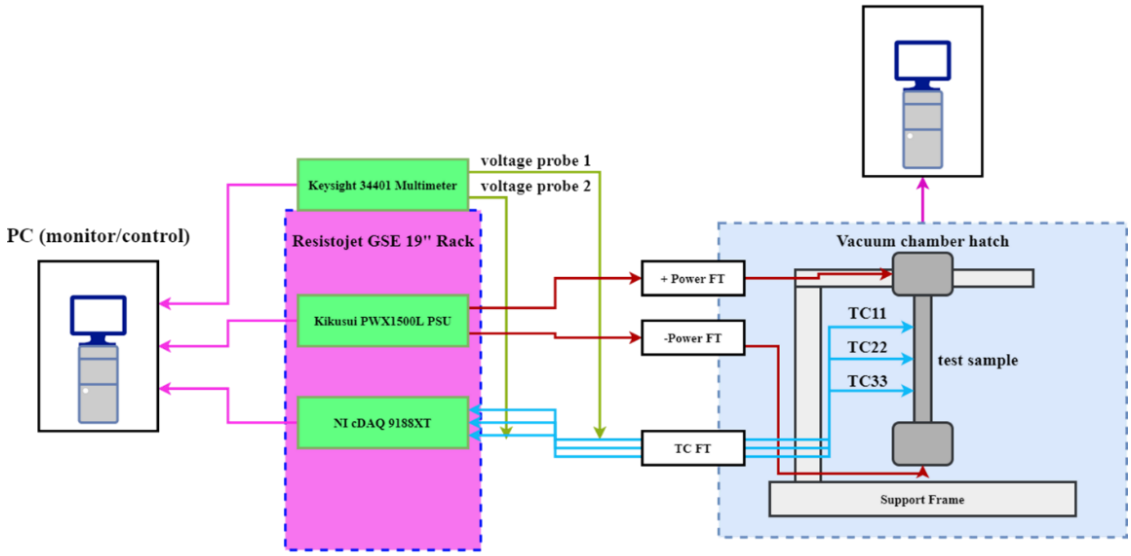

Figure 24: Schematic of emissivity/resistivity test setup. Purple: data connection; green: voltage probes; red: power supply; blue: thermocouple measurement

Experimental Procedure

Due to the unique surface features on additively manufactured parts, it was difficult to accurately measure the dimensions of the test strips using callipers, as recommended in the standard. As an alternative, each of the test strips were CT scanned over a length of approximately 15 mm in the centre of the test strips. Details of these scans and the image analysis used to calculate the area are given in section 4.4.

The samples were always handled whilst wearing gloves. Prior to testing, the sample test strip was rinsed with IPA to remove any contaminants. After spot-welding the thermocouples to the specimen, it was clamped into the sample holder and inserted into the vacuum chamber hatch. The electrical leads were then attached, the chamber door closed, and the chamber evacuated. Once the chamber reached a pressure of at least 10^{-5} mbar, heating of the test specimen began. Heating of the test specimen was controlled and monitored by the software LabVIEW. This software increased the current supplied to the specimen in intervals of 8 A over 10 steps, resulting in a maximum current of 80 A. This maximum current was chosen as it reached near the recommended current limit of the wires used to supply power to the samples. For each interval the current was held for 200 seconds to allow for the temperature and voltage readings to reach steady state conditions. Details of how this step length was chosen are discussed in section 6.2.

Emissivity losses

According to T. Fu *et al.*, equation [10] does not take into account different sources of error [152]. These sources are heat loss through residual gas in the vacuum chamber, conductive losses from the thermocouple wires, conductive losses from the investigated region to the rest of the test strip and error from the grey body assumption. Each of these losses are shown below in Figure 25.

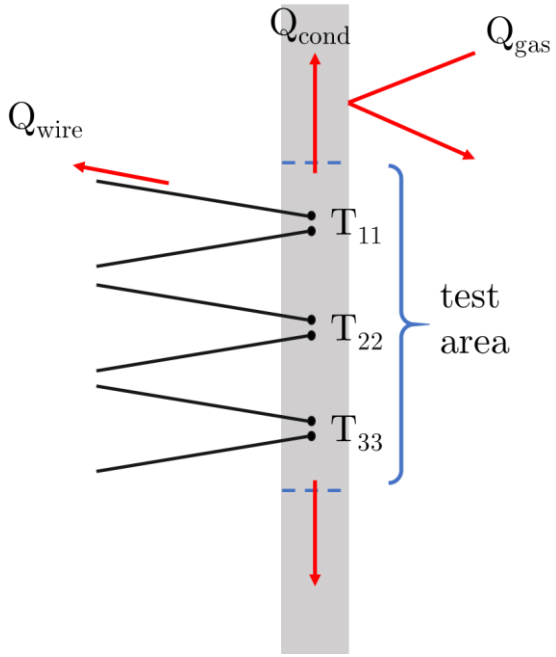

Figure 25: Diagram showing all the sources of heat loss from the emissivity test specimen. The thermocouples are labelled as T11, T22 and T33. Heat loss is indicated through the red arrows

Thermocouple wires

The thermocouples used in this investigation were approximately 0.5 mm in diameter, notably thicker than the 0.13 mm diameter recommended in the standard to minimise conduction heat losses. These were chosen for ease of attachment, as thinner thermocouples could not be successfully spot-welded to the specimens. To account for the conduction losses from the thermocouple wires, the expression in equation [14] was used [152].

$$\boldsymbol{Q_{wire} = \pi\{0.1\sigma \cdot \lambda_\omega \cdot \varepsilon_\omega \cdot d_\omega^3 \cdot [(T_1^5 - T_C^5) - 5T_2^4(T_1 - T_C)]\}^{0.5}} \quad [14]$$

Where T_c (K) was the end of the thermocouple wire near the vacuum chamber enclosure. For this investigation, this was estimated to be T_2, the temperature of the chamber wall. λ_ω is the thermal conductivity of the thermocouple (W m^{-1} K^{-1}), ε_ω is the

emissivity of the thermocouple wire and d_ω is the wire diameter (m). Only conduction losses on the central investigated portion of the test strip matter. It can be assumed that half of the conduction losses on the outer two thermocouples go to the rest of the test strip. Thus, for three thermocouples the total conductive heat loss can be calculated through equation [15].

$$\sum \boldsymbol{Q_{wire}} = \mathbf{2} \cdot \left(\boldsymbol{Q_{wire,1}} + \boldsymbol{Q_{wire,2}}\right) \qquad [15]$$

Residual Gas

Equation [10] assumes that the only heat lost from the sample was by radiation. The standard test method states that to ensure this, the tests must be carried out under a minimum vacuum of 1.3×10^{-5}mbar (1.3mPa). However due to issues with the chamber it was only possible to achieve a vacuum of $8 - 9 \times 10^{-5}$mbar. Thus, residual gas in the chamber after evacuation may have caused heat losses from the test specimen. In order to estimate heat loss through residual gas, the expression in equation [16] was used [152].

$$\boldsymbol{Q_{gas}} = \boldsymbol{A_1 m_r \lambda_0 p_{\mu b}} \cdot \boldsymbol{(273.2/T_2)^{0.5}} \cdot \boldsymbol{(T_1 - T_2)} \qquad [16]$$

Where m_r is the accommodation factor, λ_0 is the thermal conductivity of the gas molecules at 0°C equal to 0.164 (W $m^{-2}°C^{-1}mmHg^{-1}$) [152] and $p_{\mu b}$ is the pressure in the vacuum chamber (mmHg). The accommodation factor characterises the amount of thermal energy a gas molecule loses after a collision with a solid, and ranges from 0 to 1. A value of 1 means the gas molecules average temperature is the same as it the solid after the collision and a value of 0 means it is unchanged [153]. For this work it was estimated as 0.85 [153].

Conductive losses to the rest of the strip

Emissivity is only measured over a small central region of the test strip where the temperature is assumed to be constant. Conduction losses from this central region to the rest of the test strip need to be taken into account [152]. These losses are calculated through equation [17].

$$\boldsymbol{Q_{cond}} = \boldsymbol{A} \cdot \boldsymbol{\lambda}(\boldsymbol{T_{11} - T_{33}}) \qquad [17]$$

Where λ is the thermal conductivity of the test strip and T_{11} and T_{33} are the temperature readings of the outermost thermocouples. The placement of these thermocouples is shown in Figure 25.

Relative error

By considering the different losses given in equations[18][19][20][21], the relative error of emissivity for each of the error sources can be defined through the following equations.

$$(\Delta\boldsymbol{\varepsilon}/\boldsymbol{\varepsilon})_{\boldsymbol{non-grey}} = \frac{(\boldsymbol{T_2}/\boldsymbol{T_1})^{\boldsymbol{4}}}{\boldsymbol{1-\left(\frac{T_2}{T_1}\right)^{4.5}}} \cdot \left(\boldsymbol{1-\sqrt{T_2/T_1}}\right) \quad [18]$$

$$(\Delta\varepsilon/\varepsilon)_{gas} = Q_{gas}/Q_{UI} \quad [19]$$

$$(\Delta\varepsilon/\varepsilon)_{wire} = \sum Q_{wire}/Q_{UI} \quad [20]$$

$$(\Delta\varepsilon/\varepsilon)_{cond} = Q_{cond}/Q_{UI} \quad [21]$$

Chamber Wall Cooling

Depending on the lowest temperature intended to be measured and the maximum natural heat dissipation of the vacuum chamber, the test standard states that cooling of the walls may be necessary. To achieve the accuracy as stated in the standard, it recommends maintaining at least a 100°C temperature difference between the specimen and the chamber walls. Although the vacuum chamber used in this investigation did possess a thermal shroud, cooling of the shroud was not installed at the time these experiments were carried out.

Sources of error

Care was taken to ensure that the test procedure was as similar as possible between each sample. However, there were potential sources of human error when conducting these experiments. The standard recommended that the distance between the thermocouple leads be 75 mm. Handling difficulties when spot-welding the samples however meant that the distance of the thermocouples varied for some of the samples. The distance between thermocouples was measured using callipers and is presented in the results section of this thesis.

4.3.2. Resistivity Measurement – Four probe method

Overview

The four probe method was adapted from the ASTM standard B193-16, as well as numerous reports from the literature, to measure the resistivity of the SLM samples [145]. Generally, it involved placing four probes onto the surface of the test specimen. Across the outer two of these a current was passed, whilst across the inner two the voltage across the sample was measured. By measuring these values, and knowing the geometry of the sample, the resistivity was calculated using equation [22].

$$\rho = \frac{RA}{L} \qquad [22]$$

Where R (Ω) is the resistance of the sample, A (m^2) is the cross-sectional area and L (m) the distance between the voltage leads. By knowing the input current and measuring the voltage across the sample, the resistance was calculated using equation [23].

$$R = \frac{V}{I} \qquad [23]$$

Current was passed through the samples using the metal 316L end tabs and the voltage across the samples was measured through the outer two thermocouples spot-welded to the surface. Cross sectional areas of the specimens were measured using X-ray CT scanning, as will be detailed in section 4.4.

Deviations from the standard/sources of error

As this method was adapted to suit both the emissivity and resistivity measurements, some aspects of the experiment deviated from the standard.

Sample size

The standard recommended that samples have a test length of at least 1 ft or 300 mm. Although no specific reason was given for this sample length, it may have been to ensure that the resistivity measurement is not largely affected by unintended irregularities in the crystal lattice (such as cracks or impurities). However due to manufacturing constraints 200 mm length specimens were used instead and as detailed in section 4.3.1 the resistance measurement was taken over a 75 mm section in the

middle of the samples as required by the emissivity standard [146]. A 75 mm length was considered an appropriate length to measure the voltage over for the emissivity as stated by the standard and so was assumed to also be appropriate for the resistance measurement. Although it was outside the scope of this work, it could be worth in future printing samples of different lengths to see if there is a notable difference in resistivity measurements.

Contact Resistance

The metal tabs that supply power to the sample and the test specimen are not in perfect contact with one another. This is due to the roughness of the test specimen and the metal tabs restricting contact. This can also be exacerbated by the presence of a film such as an oxide layer on the surface of the test specimen reducing the actual contact area between the sample and electrical contacts. These restrictions can cause increase the resistance measured and as a result alter the resistivity measurement and are known collectively as the contact resistance. Lead resistance refers to the resistance of the electrical leads used to measure the sample properties [154]–[156]. Steps were taken to reduce these additional resistances, including conducting the test under vacuum to prevent oxidation, using the four probe method [156] and constructing the metal tabs out of the same material as the test specimen [154]

The standard also recommended reversing the flow of current through the sample either through the instrumentation or by physically flipping the sample [145]. This however was not performed due to the additional time it would have taken to remove and replace the sample in the test equipment.

4.3.3. Instrument uncertainty analysis

For both the emissivity and resistivity, the uncertainty was first calculated for the different instruments used in the experiments. These were then used to calculate the uncertainty for the emissivity and resistivity. The largest values of uncertainty were used to define error bars.

Instrument uncertainty

Voltage

Voltage was measured with the 34401A Digital multimeter. The uncertainty calculation was taken from the data sheet supplied with the multimeter which was given as % of reading + % for ranges of measured values in the hundreds of millivolts taken over 1 year, given as 0.005 + 0.0035 [157]. Thus, the absolute uncertainty was calculated through equation [24].

$$u_{voltage} = reading * \left(\frac{0.005}{100}\right) + reading * \left(\frac{0.0035}{100}\right) \quad [24]$$

Power Supply

Current was measured using the Kikusui PWX1500L power supply [158]. The uncertainty was taken from the data sheet supplied with the power supply. For the output current, this was given as ±(0.5% of set + 0.1% of rating). The output current was rated as 150 A. Thus, the absolute uncertainty calculated through equation [25].

$$u_{current} = current * 0.005 + 150 * 0.001 \quad [25]$$

Thermocouples

Temperature was measured using model TC Direct 406-645 Type K thermocouples. The uncertainty of these thermocouples was taken from a datasheet supplied by TC Direct and varied depending on the temperature range [159]. For temperatures between -40 °C to 333 °C, the absolute uncertainty was ± 2.5 °C. However, between 333 °C to 1200 °C, the absolute uncertainty was given through equation [29], Where T is the measured temperature.

$$u_T = \pm 0.0075 \cdot T \quad [26]$$

X-Ray CT

Surface determination is the process of defining the surface of a scanned object by estimating the location of the boundary between the air and material [160]. Defining the objects surface can influence the dimension measurements such as cross-sectional area

and thus accurate determination was important for calculating the emissivity and resistivity. In this work the uncertainty of the surface determination was taken as the uncertainty of the X-Ray CT measurements.

Surface determination was accomplished using the ISO50 method. For a mono-material object (such as the samples studied in this work), a histogram of the grey values of the CT dataset shows two peaks representing the air and material respectively. Using the ISO50 method the surface grey value (known as the ISO50 threshold value) is taken as the value halfway between the modal values of the air and materials peaks [160]. According to J.J Lifton *et al.*, when the air and material peaks follow Gaussian distributions, the grey values one standard deviation from the ISO50 threshold value can be taken as upper and lower bounds of the surface [160]. Thus measurements (such as cross-sectional area) calculated using these upper and lower values for the ISO50 threshold can be used to calculate the standard uncertainty due to the surface determination (u_{SD}) following equation [27]. Where x_u is the measurement calculated using the upper threshold and x_l is the measurement calculated using the lower threshold.

$$\boldsymbol{u_{SD} = \frac{|x_u - x_l|}{2}} \qquad [27]$$

However for air and material peaks that follow non-Gaussian distributions such as was seen in this work, rather than using the standard deviation the 68% dispersion for the air and materials peaks were recommended. These were measured by calculating the cumulative distribution functions for each peak and then determining the grey values at 16% and 84% distribution probabilities. These were then used to calculate the upper and lower bound threshold values which were then used in measurements (such as the cross-sectional areas). These measurements were then used to calculate the upper and lower bounds of the uncertainty, as seen in equation [30]. Where u_{SD_u} is the upper uncertainty bound, u_{SD_l} is the lower uncertainty bound, x_{84} is a measurement calculated using the grey value at the 84% distribution probability, x_{16} the grey value at the 16% distribution probability and x_{ISO50} the ISO50 threshold value.

A more in-depth description of the exact process followed can be found in the paper by J. J. Lifton *et al.* [160]

$$u_{SD_u} = |x_{84} - x_{ISO50}|$$
$$u_{SD_l} = |x_{16} - x_{ISO50}| \qquad [28]$$

Callipers

Uncertainty was taken from Mitutoyo E12021 callipers product guide [161]. The absolute uncertainty was given as ± 0.02 mm.

Methods uncertainty

Emissivity measurements

Emissivity uncertainty estimates were based on results from a paper by T. Fu *et al.* [152]. Following equation [29], the total hemispherical emissivity was a function of five independent variables. These variables were the surface area of the test specimen, the surface temperatures of the sample and vacuum chamber enclosure, the input current and the voltage drop over the specimen. These are shown below in equation [29]

$$\varepsilon = F_1(A_1, T_1, T_2, I, V) \qquad [29]$$

From J. P. Holman *et al.* [162] the uncertainty of the total hemispherical emissivity, $\Delta\varepsilon_1/\varepsilon$, can be calculated through equation [30]. This required knowing the uncertainty of the individual variables, taken as the instrumental uncertainties.

$$\frac{\Delta\varepsilon_1}{\varepsilon_1} = \left[\left(\frac{\delta \ln F}{\delta A_1}\right)^2 (\Delta A_1)^2 + \left(\frac{\delta \ln F}{\delta T_1}\right)^2 (\Delta T_1)^2 + \left(\frac{\delta \ln F}{\delta T_2}\right)^2 (\Delta T_2)^2 + \left(\frac{\delta \ln F}{\delta I}\right)^2 (\Delta I)^2 + \left(\frac{\delta \ln F}{\delta V}\right)^2 (\Delta V)^2\right]^{1/2} \qquad [30]$$

Resistivity measurements

Resistivity was calculated through equation [22] as the product of three independent variables. These variables are the resistance, the cross-sectional area and the length of the specimen. There are shown below in equation [31].

$$\rho = F_2(R, A, L) \qquad [31]$$

The resistance is the calculated by dividing the voltage by the current. The uncertainty of the resistance can thus be calculated through equation [32].

$$\frac{\Delta R}{R} = \left[\left(\frac{\delta V}{V}\right)^2 + \left(\frac{\delta I}{I}\right)^2\right]^{1/2} \qquad [32]$$

Thus, by knowing the uncertainty of the resistance, the uncertainty of the resistivity can be calculated through equation [33].

$$\frac{\Delta \rho}{\rho} = \left[\left(\frac{\delta \ln F}{\delta R}\right)^2 (\Delta R)^2 + \left(\frac{\delta \ln F}{\delta A}\right)^2 (\Delta A)^2 + \left(\frac{\delta \ln F}{\delta L}\right)^2 (\Delta L)^2\right]^{1/2} \qquad [33]$$

4.4. Area Determination

4.4.1. Overview

Both the emissivity and resistivity measurements required accurate values of the sample geometries. Both standards recommended using callipers to measure the sample dimensions and whilst the resolution of the callipers (± 0.02mm) was on the micron scale, they could not capture the effect of surface features that increased the area of the samples. Instead, X-Ray Computed Tomography (CT) scanning was used to capture cross-sectional images of the specimens, which were then analysed using image processing software. The perimeters of the cross-sectioned images were multiplied by the length between the outermost thermocouples (L in equation [12]) to calculate the emissive area (A_1 in equation [12]). The mean cross-sectional areas were used as the parameter A in equation [22] to calculate the resistivity. The overall process is shown in Figure 26. This section presents an overview of these two techniques. X-ray CT scanning was chosen over other methods because it was a non-destructive method of imaging the actual emissivity and resistivity samples. Other methods such as optical microscopy would have required destroying the sample to properly image the cross-sectional area.

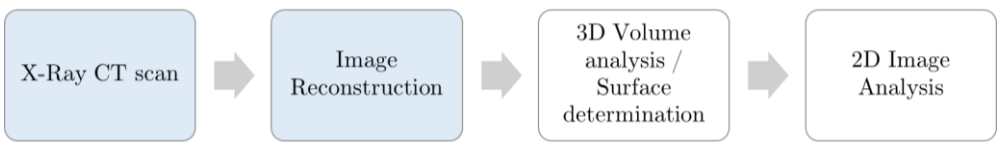

Figure 26: Flow chart detailing the X-Ray CT scanning process. Processes highlighted in blue were performed by the muvis team at the University of Southampton

4.4.2. X-Ray Computed Tomography

Experimental Procedure

All CT scans were performed at the µ-VIS X-Ray imaging centre at the University of Southampton on all seventeen sample 1 (long) specimens as shown in Table 16. Due to equipment availability, six of the scans were performed on a Zeiss 160 kVp Versa 510 whilst the remaining eleven were scanned on a custom 450/225 kVp Hutch CT. The different machines had different characteristics and resulted in different scanned section lengths and different spatial resolutions achieved, as presented in Table 16.

A small length over the middle of the sample, rather than the full length, was imaged. This was 15 mm for the samples scanned on the Versa and a smaller length of 10 mm - 11 mm for samples scanned on the Hutch CT system. The spatial resolution was determined by the voxel size. As seen in Table 16, the voxel size varied between 5 µm – 7.5 µm, smaller than the metal powder particle size range used for SLM processing. Due to deviations from the nominal width and thickness, some of the samples scanned using the Hutch CT system were imaged with a larger voxel size to fit the entire specimen width within the field of view. Samples scanned on the Versa could only be scanned over a 5 mm portion of the full width. As a result, the edges of the specimen were cut off in the resulting reconstructed images as shown for the 90° sample 8 in Figure 27. Thus, estimates for the full specimen perimeter required extrapolation as detailed in the next section.

4.4.1. Image Analysis

As detailed in Figure 26, after the parts were CT scanned, the resulting projections were reconstructed into 2D images. CT scanning and reconstructions were performed by colleagues at the µ-VIS X-Ray imaging centre. For Hutch and HMX scans, the CTPro3D and CTAgent software (Nikon Metrology, UK) was used. These used filtered back-projection algorithms to reconstruct the projection data into 32-bit float volumes. These were down-sampled to 8 bit to reduce processing time For Versa scans, the Zeiss XM Reconstructor software (Carl Zeiss Microscopy GmbH, Germany) was used to

reconstruct the images into 16-bit TXM files, and these were subsequently converted to 16-bit raw volumes.

Surface determination

After image reconstruction the resulting images consisted of pixels of varying grey-scale values. The values of these pixels and their variation in the image represented how the attenuation coefficient of the X-Ray beam changed as it passed through the samples and thus the density of the samples [163]. Surface extraction or determination was accomplished differently for samples scanned on the Hutch or the Versa machines.

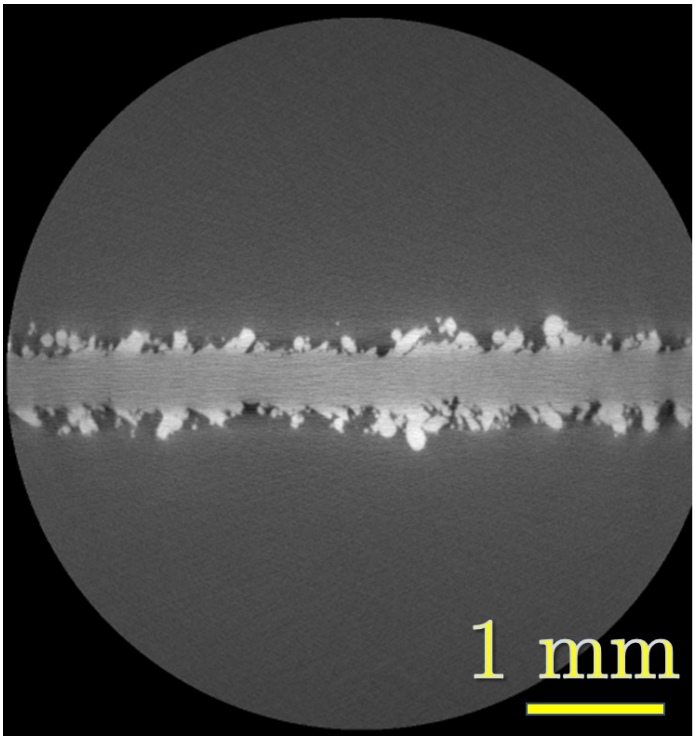

Figure 27: CT image reconstruction of the 90° sample 8, captured on the Versa showing the limited 5 mm field of view

Hutch images

Surface determination was performed automatically using the software VG StudioMax to implement the ISO50 method. The greyscale histogram of the CT volumes consisted of two peaks, one representing the background (air) and another representing the foreground (material). The ISO50 threshold value for the surface is halfway between these two peaks [160]. The associated uncertainty was calculated using the process shown in section 4.3.3.

Table 16: Table showing a summary of the different parameters used to scan the SLM samples

Sample	Machine	Length scanned (mm)	Voxel size (µm)	Volume x,y,z (voxel)	Volume(mm^3)	Angular step (°)	Voltage (kV)	Current (A)	Number of projections
5, 6, 13, 14	450/225 kVp Hutch CT	10 - 11	7*7*7	2000*500*2000	14*3.5*14	0.115	200	65 - 69	3142
4, 12, 15, 16, 17	450/225 kVp Hutch CT	10 - 11	7.5*7.5*7.5	2000*500*2000	14*3.5*14	0.115	200	65 - 69	3142
7, 11	450/225 kVp Hutch CT	10 - 11	7.5*7.5*7.5	2000*700*2000	14*3.75*14	0.115	200	65 - 69	3142
1, 2, 3, 8, 9, 10	Zeiss 160 kVp Versa 510	15	5*5*5	950*1007*4198	4.75*5.04*21	-	-	-	-

After surface determination, analysis techniques to calculate the perimeter, cross-sectional area, and relative density of the parts were implemented using the software ImageJ. Image stacks from XCT scans were imported and converted into 8-bit images. A threshold was then applied to binarize the images [164]. To calculate both the cross-sectional area and the perimeter, the 'analyse particles' tool in the software was used. This worked by scanning the image until finding the edge of an object, then outlining the object using the wand tool and finally measuring the resulting area or perimeter of the object [165]. Protruding features on the surface of parts, if they varied in the z-axis of the scan could appear differently in each scan slice. This is shown in Figure 28.

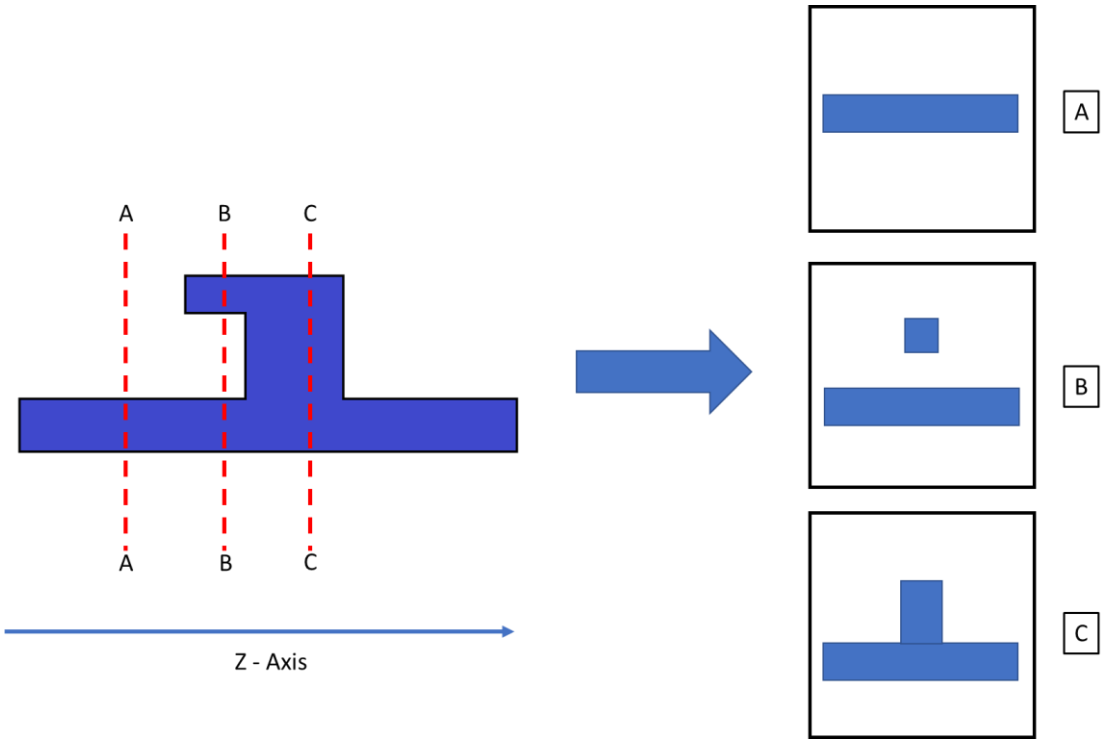

Figure 28: Image detailing how protruding features on the AM parts may have altered the perimeter and cross-sectional area determinations over different scan slices

Steps were taken to account for this. For the cross-sectional area, the area of every object in each scan slice was measured. The sum of these areas was then taken as cross-sectional area for each scan slice. The mean area of every scan slice was then taken as the cross-sectional area of the sample. This same principle was used to calculate the perimeter. When calculating the perimeter, to ensure that a continuous surface was measured the "fill holes" tool in ImageJ was used. This is shown in Figure 29.

Figure 29: A thresholded image before and after flood-filling the holes up to the isosurface

Versa images

The images taken on the Versa could not be imported into VG StudioMax, and so the isosurfaces were determined manually following the ISO50 method. A histogram of the grey values was determined using ImageJ, two peaks corresponding to the air and material were identified, the mid-point value between the peaks was calculated and then used as a threshold value to binarise the image.

As previously mentioned, samples scanned on the Versa system could only be scanned over a 5 mm portion of the full width. As a result, the edges of the specimen were cut off in the resulting reconstructed images. Thus, estimates for the full specimen perimeter required extrapolation using equation [36], which scales the perimeter measured over the limited 5 mm field of view to the full width of the specimen measured using callipers. This extrapolation assumes that the surface texture of the sample and the thickness was the same throughout the width of the sample. The method to calculate the uncertainty is given in the next section.

$$\boldsymbol{perimeter} = \frac{\boldsymbol{Versa\ perimeter} * \boldsymbol{calliper\ width}}{\mathbf{5}} \qquad [34]$$

4.4.2. Uncertainty Analysis

Uncertainty of the area obtained through surface determination was calculated by the process detailed in section 4.3.3. To obtain the uncertainty on the perimeter of the samples measured using the Versa, equation [35] is used. Where $\left(\frac{\delta X}{X}\right)^2$ is the percentage

uncertainty from the X-ray CT surface determination (detailed in section 4.3.3) and $\left(\frac{\delta C}{C}\right)^2$ is the percentage callipers uncertainty.

$$\frac{\Delta \mathbf{Versa}}{\boldsymbol{Versa}} = \left[\left(\frac{\boldsymbol{\delta X}}{\boldsymbol{X}}\right)^2 + \left(\frac{\boldsymbol{\delta C}}{\boldsymbol{C}}\right)^2\right]^{1/2} \quad [35]$$

4.5. Roughness Characterisation

Surface roughness was expected to have a large effect on emissivity and so several surface texture parameters of the AM surfaces were measured using Focus Variation Microscopy (FVM). Here, the basic principles of this technique are outlined as well as the exact steps taken when measuring the roughness of the samples.

4.5.1. Focus Variation Microscopy

Experimental Procedure

Roughness was measured at five different locations on each sample. It was measured on both the upskin and downskin sides for the samples printed at 90° and 45° relative to the build plate. Samples printed at 0° were only measured on the upskin side, as the downskin side was EDM cut from the build plate and were thus not representative of as-built AM surfaces.

To ensure that the same 5 locations were measured on every sample, a plastic sample holder denoting measurement locations was 3D printed. The CAD model of this with the corresponding distances along the holder is shown in Figure 30. The distance between each of the locations demarked on the sample holder was 33.3 mm. The measurement procedure involved several steps, which are outlined in Figure 31.

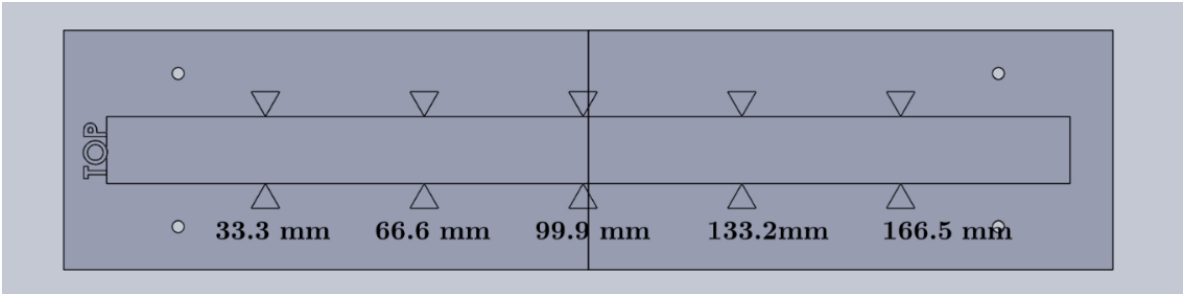

Figure 30: CAD model of the sample holder used to ensure roughness measurements taken at similar locations

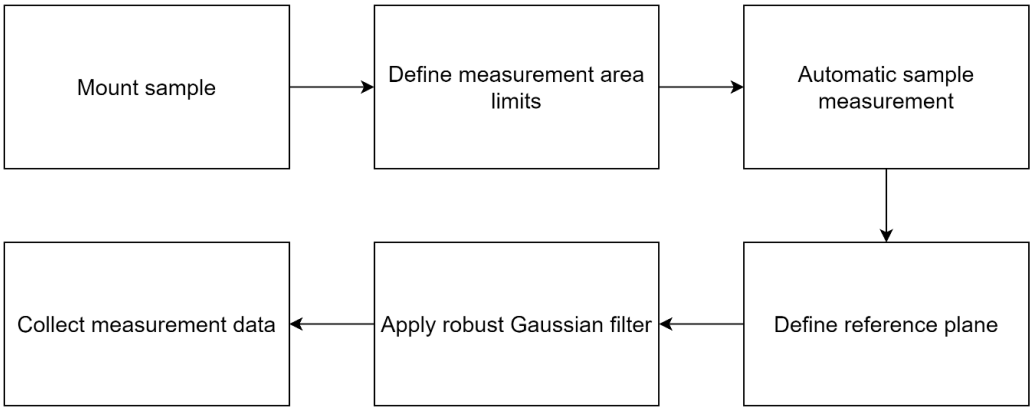

Figure 31: Flow diagram detailing the roughness measurement process

After mounting the sample onto the microscope, measurement area limits in the x and y axes were first determined. This area was approximately 2.5 mm by 2.5 mm as deemed appropriate by A. Triantaphyllou *et al.* [47]. The limits in the z-axis were set by moving the microscope up and down until the sample was out of focus. While the x and y limits were constant, the z-axis limit varied depending on the height of the peaks and depth of the valleys. The measurement itself was done automatically by the microscope. After the image was captured a reference plane was applied using a best fit method, a 2.5 mm L-filter was applied using a robust Gaussian filter, and the different surface texture parameters were collected. A summary of the different settings used are shown in Table 17.

Table 17: Summary of the different parameters used for the Focus Variation Microscope

Vertical resolution (nm)	Lateral resolution (µm)	Magnification	XYZ (mm)	Sampling distance (µm)	L-filter (mm)
800	8	10 x	2.693*3.824* (0.86-1.01)	883.51*883.51	2.5

4.5.2. Uncertainty Analysis

No information was available from the supplier of the microscope for uncertainty values for the high roughness values that were expected to be seen on the as-built AM samples. Instead, the repeatability of the measurement was taken as the uncertainty of the instrument. This was done once at the beginning on a single sample and generalised to all measurements. To measure the repeatability, at a single location on a sample

identical measurements of the different surface texture parameters were captured ten times. It was assumed that the variation of this sample would be representative of the full sample set. This was considered adequate for a screening experiment. The standard deviation of the mean of these values was then taken as the uncertainty of the roughness measurements.

4.6. Materials Characterisation

To assess the microstructure and overall surface geometry of the as-built AM parts, various materials characterisation techniques were used. This section will present an overview of these characterisation techniques as well as the various methods in which samples were prepared for the techniques and how microstructural analysis was done.

4.6.1. Sample Preparation

Cutting

Samples were cut to reveal the cross-sections for microstructural analysis. The planes that were cut varied depending on the build orientation of the parts. The samples were cut using an abrasive cutter. The samples built at 0° were cut along the x-z and y-z planes. The samples build at 90° were cut along the x-y and x-z planes. The samples built at 45° were cut at angles 45° to the x-y plane and 45° to the x-z plane. These are visualised in Figure 32.

The samples were cut along these different axes because these were easiest to mount in the cutting machine. Microstructural differences between the samples because of these different cutting planes will be discussed in the results section.

Mounting

After cutting, the samples were mounted in conductive Bakelite for grinding and imaging in the Scanning Electron Microscope. Samples were held upright using ring sample holders and mounted using a hydraulic press OPAL 410 machine which heated the samples for 6 minutes at 180°C.

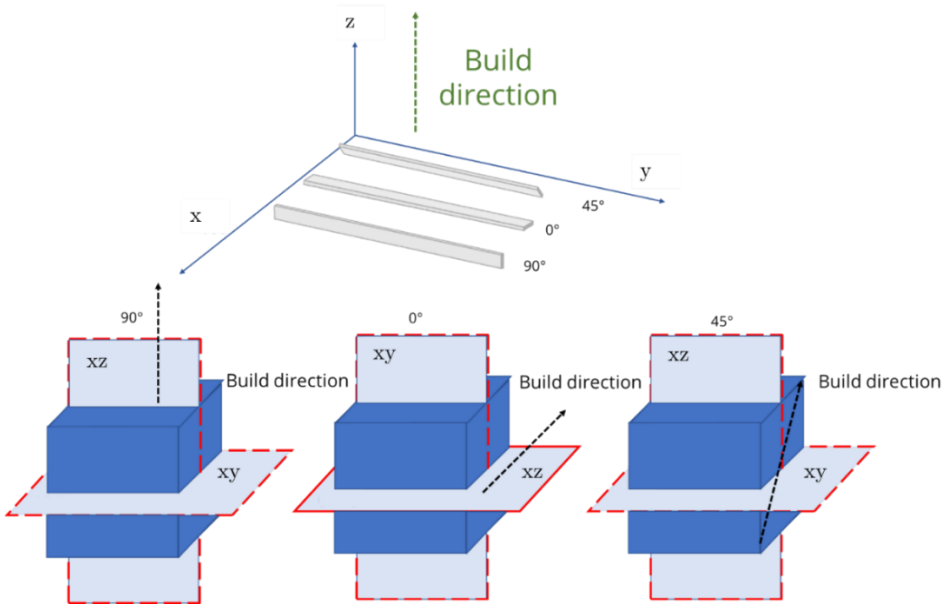

Figure 32: Diagrams showing the orientation of samples on the build plate and the different cross-section planes that dendrite spacing was measured on for each sample.

Grinding and Polishing

To remove abrasive marks from the cutting process and to make the samples level for imaging they were first ground and then polished. They were ground using 800 and 4000 grit abrasive papers before being polished using a polishing cloth and 6 µm and 1 µm diamond paste to achieve mirror-like surface finishes.

Etching

To reveal the microstructures samples were etched using Kalling's No.2 reagent, made up of 60 mL of hydrochloric acid, 40 mL of ethanol and 40 g copper chloride to make up 100 mL of etchant. Samples were immersed in the etchant for 7-8 seconds before being rinsed using tap water to stop the etch and methanol to dry the surface.

4.6.2. Scanning Electron Microscopy

Scanning Electron Microscopy (SEM) was used to view the microstructure of the cross-sectioned samples as well as the surface topography of the as-built samples. Image analysis was carried out on the resulting images to measure the primary cell spacing. Energy dispersive X-Ray spectroscopy (EDS) was attempted to gain information about the elemental composition of the samples.

Experimental Procedure

SEM analysis was performed in the Biomedical Imaging Unit at the University Hospital Southampton. One of two machines was used depending on availability. For EDS and secondary electron (SE) imaging a FEI Quanta 200 Scanning Electron Microscope was used. EDS analysis was performed using the Oxford Instruments Aztec software. A second machine, an FEI Quanta 250 Scanning Electron Microscope with Gatan 3view2XP serial block face imaging was used for SE imaging alone. The properties of the SEM used to image the samples are shown in Table 18.

Table 18: Table showing a summary of the SEM properties.

Sample	Region of Interest	Working Distance (mm)	Accelerating Voltage (kV)	Magnification range
2	Surface topography	8 - 10	10 - 15	50x, 100x ,200x,500x
3	Microstructure	8 - 10	-	200x - 12000x

4.6.3. Microstructural Characterisation

Primary Dendrite spacing

Two methods were used and compared to measure the primary dendrite spacing of the SEM images. The first was using the image analysis software ImageJ. Firstly, images were blurred using the Gaussian blur filter, and the contrast enhanced automatically using the "Enhance contrast" tool to better separate between the cell interiors and boundaries. The image was then converted into a binary black image and segmented using the 'find maxima' tool in ImageJ. Finally, the average area of the particles was calculated using the particle size analysis tool. These steps are illustrated in Figure 33.

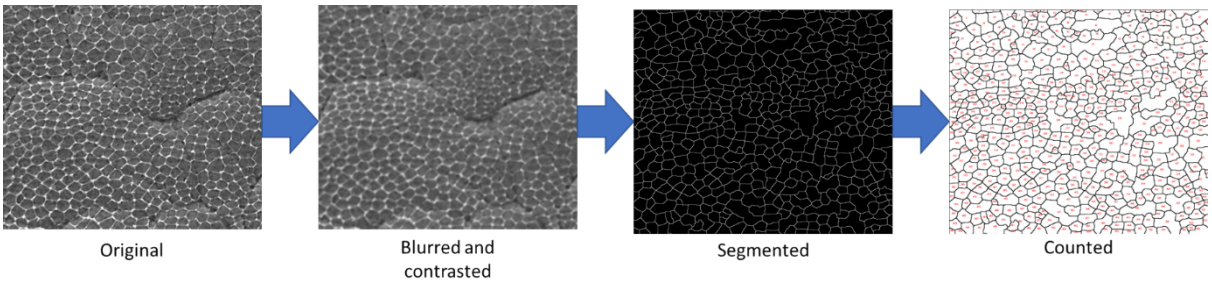

Figure 33: Diagram showing the steps taken to calculate the primary cell spacing in ImageJ

The second method was the area method as reported by M. Ma *et al.* [74], [166]. The equation for this method is shown below in equation [36]

$$\boldsymbol{\delta = \left(\frac{A}{N}\right)^{\frac{1}{2}}} \qquad [36]$$

Where δ is the primary dendrite spacing in microns, N is the number of (manually counted) cells in the targeted area and A is the area of the region of interest in square microns. This was repeated on different images of the same samples to obtain an average value. The dendrite area using this technique, A/N, was compared with the average area calculated from the image analysis technique.

4.7. Density Measurements

4.7.1. Archimedes method

The Archimedes method for density measurements was performed based on ASTM standard B962-17 [148]. Generally, this required measuring the mass of the sample in air and the mass of the sample when it was immersed in fluid. By knowing these masses and the density of the air and the density of the fluid, the density of the sample could be calculated. Whilst an equation to calculate this was given in the ASTM standard, a slightly modified version presented by A. P. Spierings *et al.* which took into account the buoyancy of the part in air was used [167]. This is shown below in equation [37].

$$\boldsymbol{\rho_p = \left(\rho_{fl} - \rho_{air}\right) \cdot \frac{m_a}{m_a - m_{fl}} \cdot \rho_{fl}} \qquad [37]$$

Where ρ_p is the density of the sample, ρ_{fl} is the density of the fluid, ρ_{air} the density of the air, m_a the mass of the sample in air and m_{fl} the density of the sample in the fluid. The fluid used was acetone which has a density of 0.791 g/ml. The density of air was taken as 0.01225 g/cm^3. For mass measurements a balance was used which could measure up to 5-digits (0.1 mg) as required by the standard for samples less than 10 g. The sample was suspended from a metal bracket which was submerged into the fluid. Each mass measurement was taken at least five times. To account for the evaporation rate of the acetone which would alter mass measurements, the mass change of the fluid

was measured over 10 seconds. This was measured five times and the average value of this was added to the mass of the sample in fluid in equation [37].

4.7.2. Image Analysis

Relative density measurements were also taken from the 2D Image slices obtained after image reconstruction and surface determination of the CT scans, as described in section 4.4. This was done using the software ImageJ and adapted from a procedure described by A. B. Spierings *et al.* [167]. First images were converted into binary following the procedure outlined in section 4.4.1 (although the images were not flood filled to preserve the internal porosity). The images were then cropped to remove the surface and focus solely on the internal porosity. Using the particle size analysis tool, the fraction of the image that was black (corresponding to air) was measured, which was taken as the relative density of the part. This process is illustrated in Figure 34.

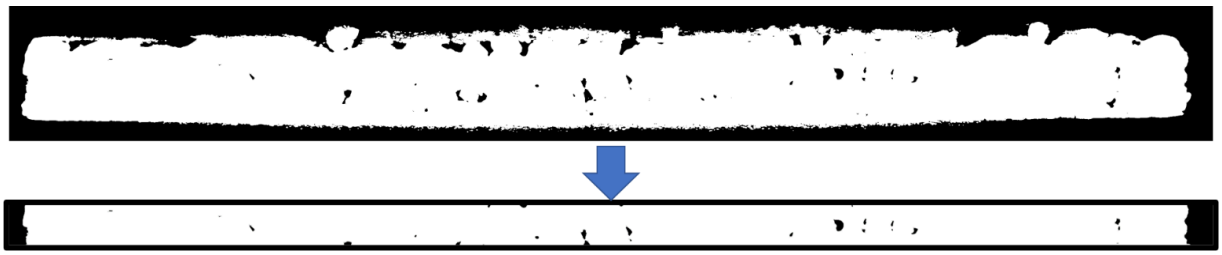

Figure 34: Images showing a sample after having a threshold applied and after the surface has been cropped to focus solely on the internal porosity.

5. Results and Discussion – Surface texture and morphology

5.1. Overview

As previously described, surface texture is deviation of a surface from its ideal shape after the underlying form of a part has been removed [42]. Surface texture can be further split into long wavelength deviations, known as waviness, and short wavelength deviations, known as roughness. Roughness is known as a key factor that influences the emissivity of a surface, however the rapid cooling and layer-by layer nature of SLM can cause unique features which increase the roughness of as-built surfaces. As the goal of this work was to understand how the SLM process influenced the emissivity, it was important to first understand how it affected the roughness of the parts produced.

In this section results of the surface texture measurements are presented. This includes a general look at the data before discussing how the different input parameters may have affected the results. Multiple linear regression models were created to determine not only which input factors affected the different texture parameters but also order them in terms of significance. Attempts were then made to correlate these to physical characteristics observed on the different samples, as well as to explain the physical reasons why changing the input parameters had the effects they did on the different texture parameters.

Using focus variation microscopy, the surface roughness of the parts was measured on seventeen samples and characterised through surface texture parameters. Each sample corresponded to a different combination of input parameters (laser power, scanning speed, hatch spacing, layer thickness and build angle) varied to obtain a range of different surface textures. The samples were measured at five equally spaced locations

along each sample on both the upskin and downskin sides. The surface texture parameters measured, and their definitions are shown in Table 19. Going forward in the text, when referring to roughness it is referring to these texture parameters (unless otherwise stated).

Table 19: Summary of the different areal surface texture parameters measured for this thesis

Texture Parameter (µm)	Definition	Physical meaning
Sa	Arithmetic mean of the absolute of the ordinate values	Average height deviation from a mean plane
Sq	Root mean square value of the ordinate values	
Ssk	Quotient of the mean cube value of the ordinate values	Measure of symmetry of roughness profile about mean plane
Sku	Quotient of the mean quartic value of the ordinate values	How closely roughness profile matches Gaussian distribution
Sdq	Root mean square of the surface gradient	Average slope of the surface

5.1.1. Overview of data

Roughness measurements were taken at the same 5 locations on each sample, 33.3 mm apart. Figure 35 shows box plot diagrams of the ranges for all the samples. The samples are split by build angle, which were defined relative to the build plate as shown in Figure 36. They are also split by the side measured, upskin and downskin. Upskin refers to the uppermost, visible surface of a part while downskin refers to surfaces facing down towards the build plate. However, it is important to note that because the 90° samples were built perpendicular to the build plate that both sides have the same orientation and that neither side is upskin or downskin. The sides have been labelled as such in Figure 35 only to separate them and for consistency with the other samples. Because the downskin of the 0° samples were removed from the build plate using electrical discharge machining (EDM) wire cutting, they were not representative of surfaces affected by the SLM process parameters and have been omitted.

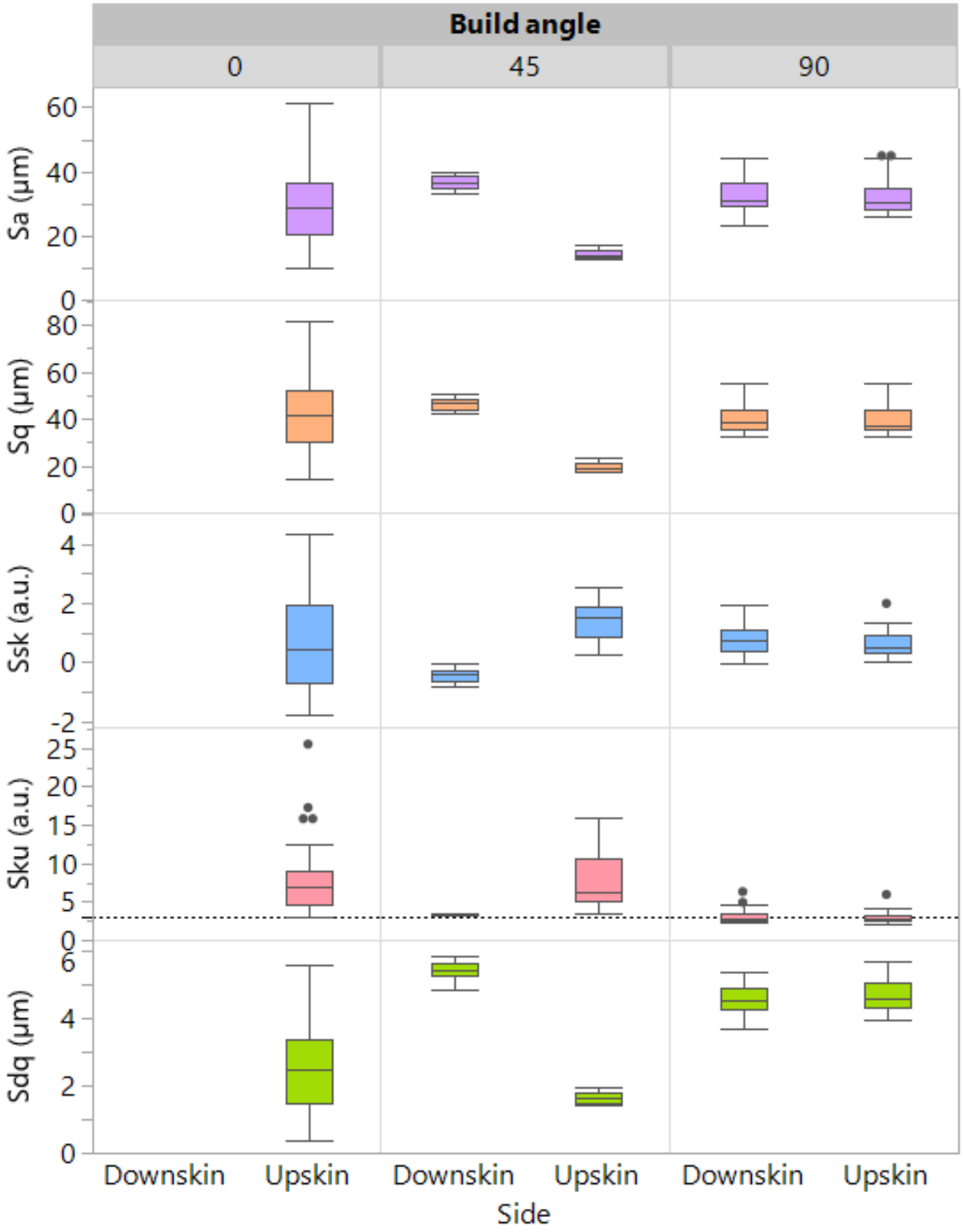

Figure 35: Box plot diagrams showing the ranges of the different texture parameters measured for the different build angles, split by side (upskin and downskin)

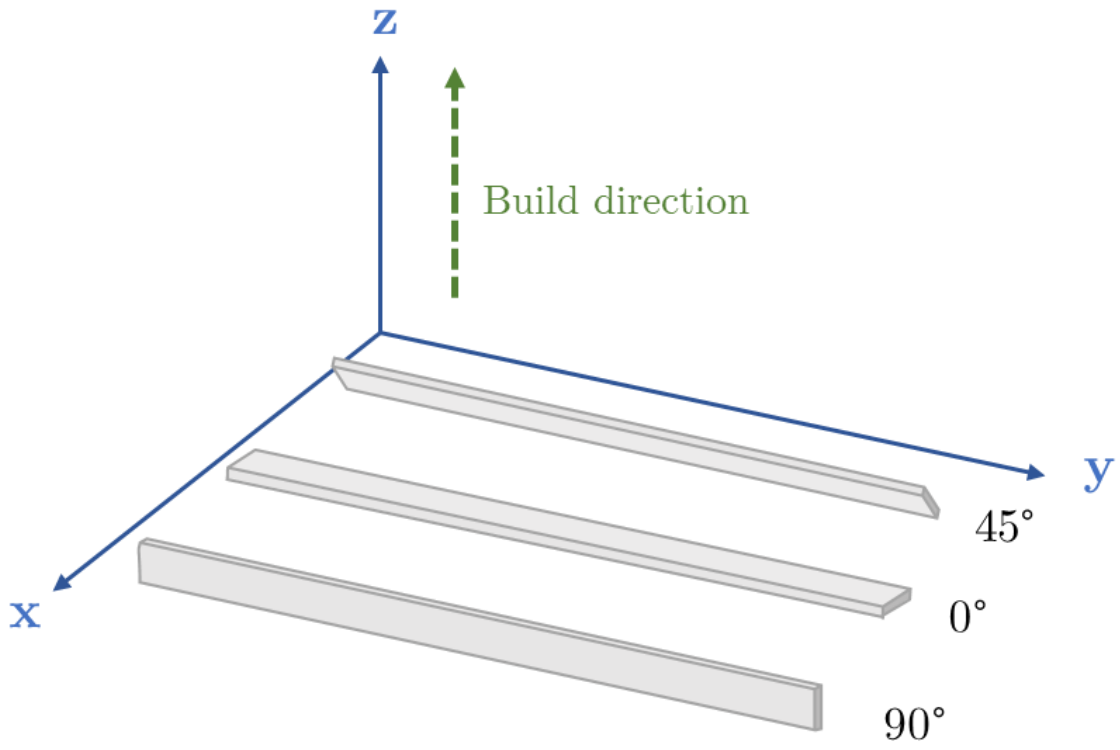

Figure 36: Diagram showing the build angle of the different samples built relative to the axes of the build chamber. 0° samples are parallel to the build plate, 90° samples are perpendicular, and 45° samples are in-between the two.

For each of the build orientations, Sa and Sq have similar trends, as expected since these are both measures of the average height of the sample surface deviation. It is interesting that Sdq, a measure of the average surface slope also has a similar trend to Sa and Sq. Of all the build angles, the 0° samples have the widest ranges for every texture parameter while the 90° samples are consistently the most similar on each side for each of the texture parameters. For each of the texture parameters, the upskin and downskin sides of the 45° samples are consistently very different from each other. This difference has been reported in the literature elsewhere and was expected due to the different thermal conduction pathways between the upskin and downskin surfaces. While the upskin surface had the previously solidified layers directly connected to the build plate as a thermal conduction path, the downskin was supported only by unbound powder which was poor at conducting away heat. Higher amounts of thermal energy led to the melt pools growing and sinking into the powder due to gravity causing the large differences in surface texture parameters seen in Figure 35. These differences will be

explored in greater detail later in this chapter. Finally, The Sku value for both sides of the 90° samples and the downskin of the 45° samples was consistently near three for both sides, showing that they had mostly normal distributions.

This overview of the data shows that the input parameters did influence the surface texture values, validating the need for an investigation to explore the relationship between them. From looking at the ranges of the samples some general trends can already be identified between the texture parameters, build angles and sides.

Before going into further detail about the relationships between the surface texture parameters, process parameters and physical surface features, it is important to first check the consistencies and ranges of the results for the individual samples. Given that the process parameters for each sample were the same across their length, it was assumed that the surface texture values would also be consistent. However, for certain samples there were notable changes to the surface texture values. When designing the experiment, it was assumed that only the five controlled process parameters would largely affect the surface texture and could thus be related to the emissivity. From reviewing the literature other factors not accounted for, such as the position of the samples on the build plate, may have affected the local heat transfer and thus the surface roughness. The next section will explore the extent of the variation seen in the samples, attempt to determine the reason why it occurred and how it can be accounted for when relating to the process parameters.

5.2. Consistency of measurements

As previously discussed in section 3.2.5, the orientation of parts with respect to the direction of the gas flow or the laser incidence angle has been shown to affect the roughness of parts. The gas can affect the cooling rate and rheology of melt pools while the laser incidence angle can affect the amount of energy absorbed from the laser [108], [168]. However, these factors were not considered when designing the experiments. These effects were investigated for each sample by looking at the range of values of the different texture parameters and trends in the values along the lengths of the samples.

5.3. Ranges of values

As the process parameters used to build the samples were consistent along their lengths, it was expected for the texture parameters to also be consistent (and have low ranges). Figure 37 shows bar charts of the ranges of the different texture parameters measured on each of the seventeen samples. These samples are split by side, with the shaded columns representing downskin surfaces.

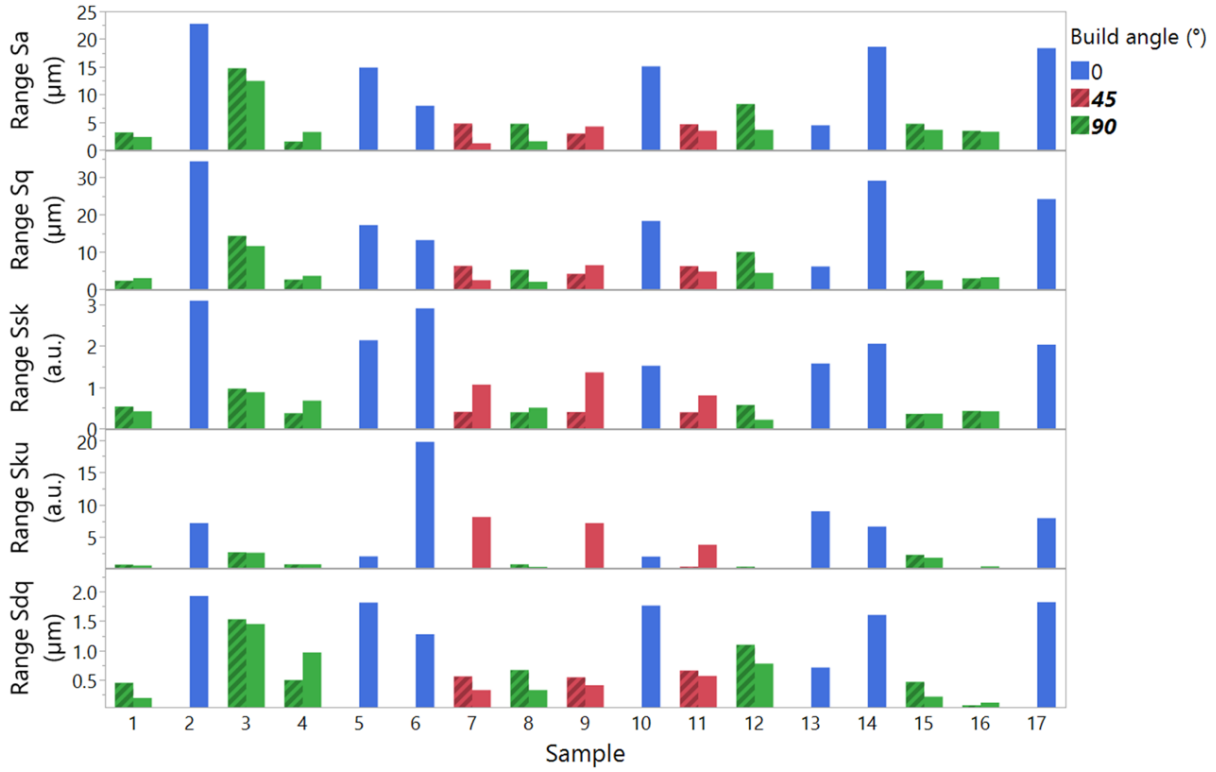

Figure 37: Bar chart showing the ranges of values for the different surface texture parameters for all 17 samples. Each plot is coloured by build angle and separated by side. The shaded plots are the downskin surfaces

The most notable observations are not only that the ranges of the samples differ, but that some ranges are much larger than others. If the results showed ranges that were homogeneous across all the samples, variation could be explained as a consistent error. The fact that the samples all have different ranges suggests that there may have been a factor (or factors) that affected the results beyond the random measurement error. Each of the texture parameters seem to follow the same general trends. The 0° samples have the largest ranges while the ranges of the 45° and 90° sample are lower. This indicates that the 0° samples were less homogeneous than the other build angles.

5.3.1. Trends in sample measurement

As previously mentioned, roughness was measured at five equally spaced (33.3 mm) points across each sample. This was ensured by using a sample holder, a rendering of which along with the corresponding distances along the sample is shown in Figure 30. To reiterate, given that the process parameters were supposedly consistent along the length of each sample, if the surface texture parameter values changed with length it could indicate an unaccounted-for factor that influenced the results such as the position of the parts on the build plate. To check this surface texture parameter values were plotted against the sample length. An example of this is shown in Figure 38 for the Sa values of the 90° samples 3 and 4.

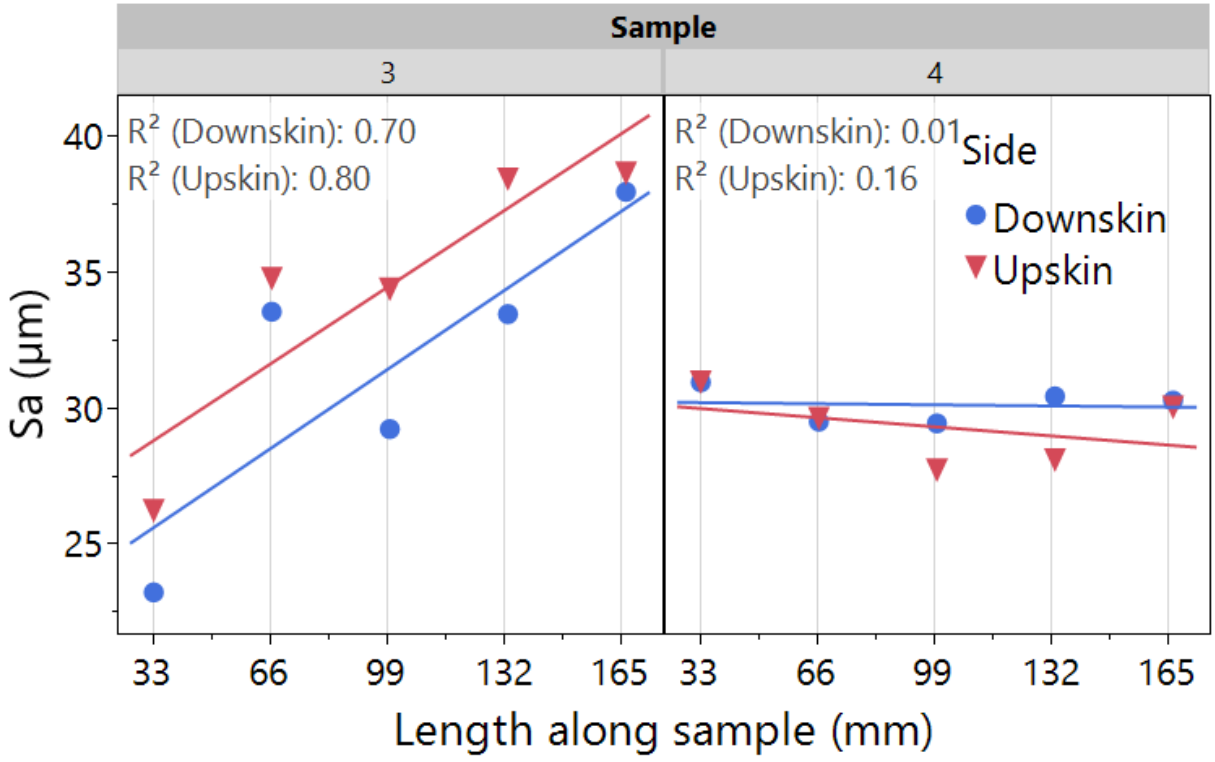

Figure 38: Sa values vs measurement number for samples 3 and 4 for both upskin and downskin sides (both printed at 90°)

A linear fit and R^2 values have been added to each data set. The data for each sample is not always linear but adding these fits can be used to clearly show trends especially for large volumes of data. The R^2 value here is used as an indicator for how strong a trend there is between Sa value and length along the sample. The higher the R^2 value, the stronger the trend. The R^2 value however does not show the direction of

the trend. The Sa values for Samples 3 and 4 are shown because they each demonstrate a clear trend or lack thereof. For sample 3, the Sa values clearly increase with length along the sample for both sides, demonstrated by the high R^2 values of 0.7 and 0.8. Sample 4 however shows no clear trend with increasing measurement number, given by the low R^2 values of 0.01 and 0.16. Figure 37 shows that sample 3 had one of largest ranges of all the samples, while sample 4 had one of the lowest.

Together the results of Figure 37 and Figure 38 suggest that there was an unaccounted factor(s) that influenced the results along the length of sample 3 but not sample 4. Thus the results of Figure 37 and Figure 38 when plotted against each other can be used as an indicator for samples that may have been influenced by an unaccounted for factor along their length, as shown in Figure 39. Although only Sa is shown here, plots were done for all the texture parameters and similar trends were found.

Samples that had a large range and strong trend (indicated by a high R^2 value) may have been influenced by external factors that affected the results along the length of the sample. This is equivalent to the top right corner of plot and was only seen for sample 3. As this influence was only seen for sample 3, it is difficult to draw strong conclusions from a single data point as the positional effects on roughness were not initially considered when designing the experiment. New samples, with the specific purpose of investigating positional effects on roughness would need to be built.

It is also interesting that only the 0° samples have high ranges of values but weak trends along the lengths of the samples. This again suggests that the surface textures are inhomogeneous along the lengths of the 0° samples and will be discussed in greater detail later in this chapter.

The reason why roughness was studied in such detail is that surface roughness directly affects the emissivity of parts. In this thesis an average emissivity was measured over an area of each sample. However, roughness was measured at discrete locations, with the assumption that roughness would be consistent across the sample as the build parameters for each sample were constant. If the roughness range was small (consistent across the sample), it would be easy to correlate roughness to emissivity. Because the

roughness varied, it is harder to directly link individual roughness values or the physical features corresponding to those values to emissivity. Understanding what the cause of the inconsistences was may be useful in future experiments to try and improve the consistency.

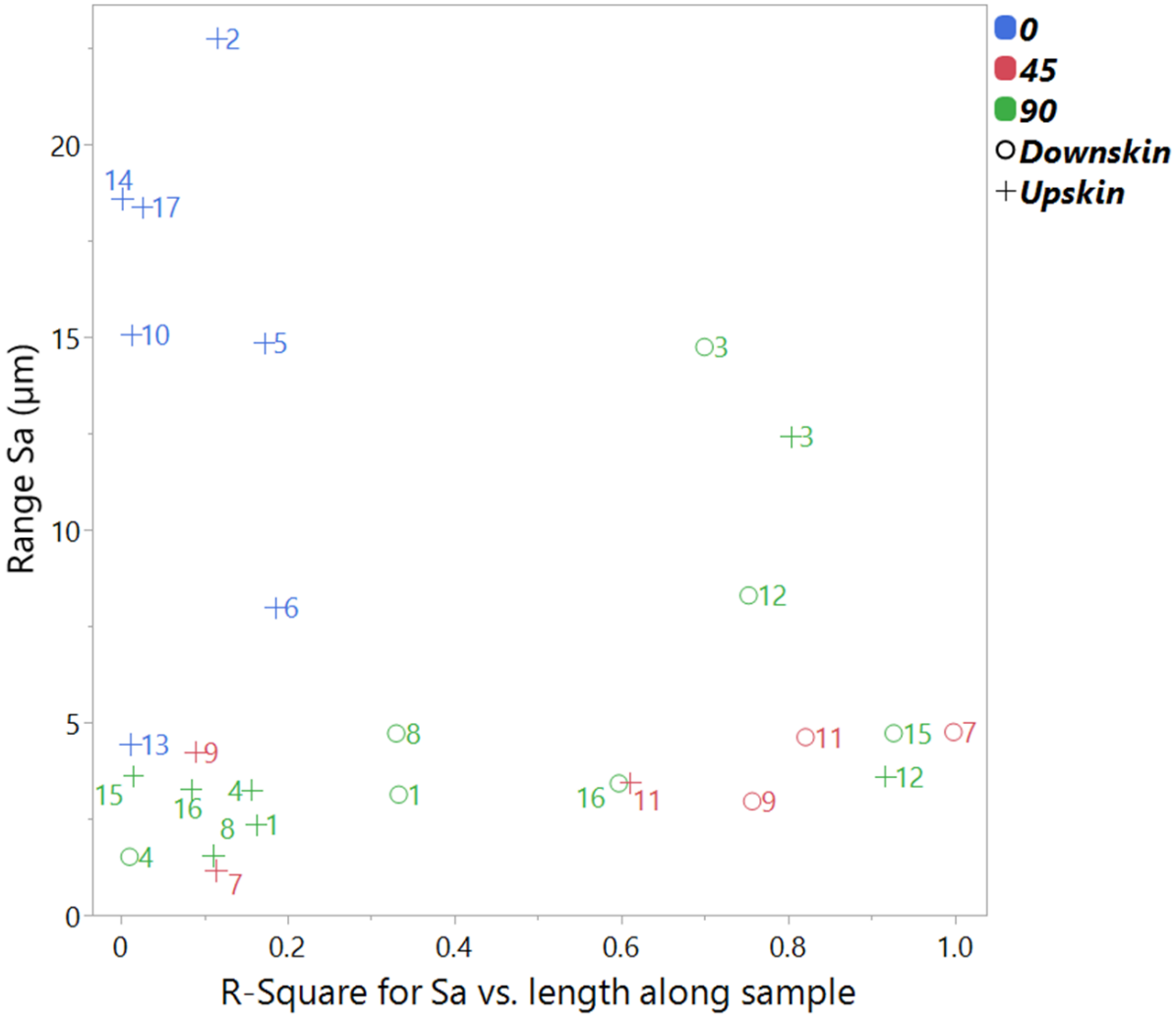

Figure 39: Plot of the range of Sa values against the R-square value for Sa vs. length along the sample for all 17 samples. Samples are coloured by build angle and split by side (upskin and downskin)

This inconsistency in roughness may affect the model as the same input parameters may now be expected to give very different values of the texture parameters. If this was a known issue before designing the experiment, more input parameters could have been measured to account for this. Given the available data, the most appropriate method of correcting for this may be to use average values of texture parameters as the responses to avoid biasing the model towards outliers.

5.4. Texture parameter and SEM image analysis

Table 19 details the physical definitions of each of the texture parameters. However just knowing the definitions does not give insight into what physical characteristics the parameters mean for the SLM surfaces. This section will look at the measured values of the texture parameters and link these to physical features seen on the sample surfaces seen in SEM images. The next section, which contains the model describing the relationship between the input parameters and the surface texture parameters, will attempt to explain how the inputs caused these physical features.

It is worth noting that the nominal geometries of samples used for roughness measurements (sample 1 in Figure 19) were different from the samples used for SEM imaging (sample 2 in Figure 19). Both sets of samples had identical thicknesses (250 µm) and widths (13 mm), but the lengths of the samples used for roughness measurements were 200 mm while the samples used for SEM imaging were 50 mm. The build parameters used to build both sets of samples were identical, and the shorter length of the SEM samples should not have affected the heat transfer to the baseplate or the cooling rate, which would have affected the roughness.

5.4.1. Physical meaning of Sa and Sq

Figure 40 shows the mean values of Sa and Sq for all seventeen samples. The error bars for each point corresponds to the standard deviation of the means. Each sample number corresponds to different build parameters used to build the sample, detailed in Table 15. The samples are coloured by build angle and split by side (upskin and downskin).

The overall trends of samples with Sa and Sq are nearly identical, which is unsurprising given that they are both measures of the average height deviation from a mean plane. The values of the 90° and 45° samples are consistent between samples, with the Sa for most of the 90° samples varying between 27 µm – 34 µm (both sides). For the 45° samples, the upskin Sa varies between only 13 µm – 15 µm and the downskin between 35 µm – 38 µm.

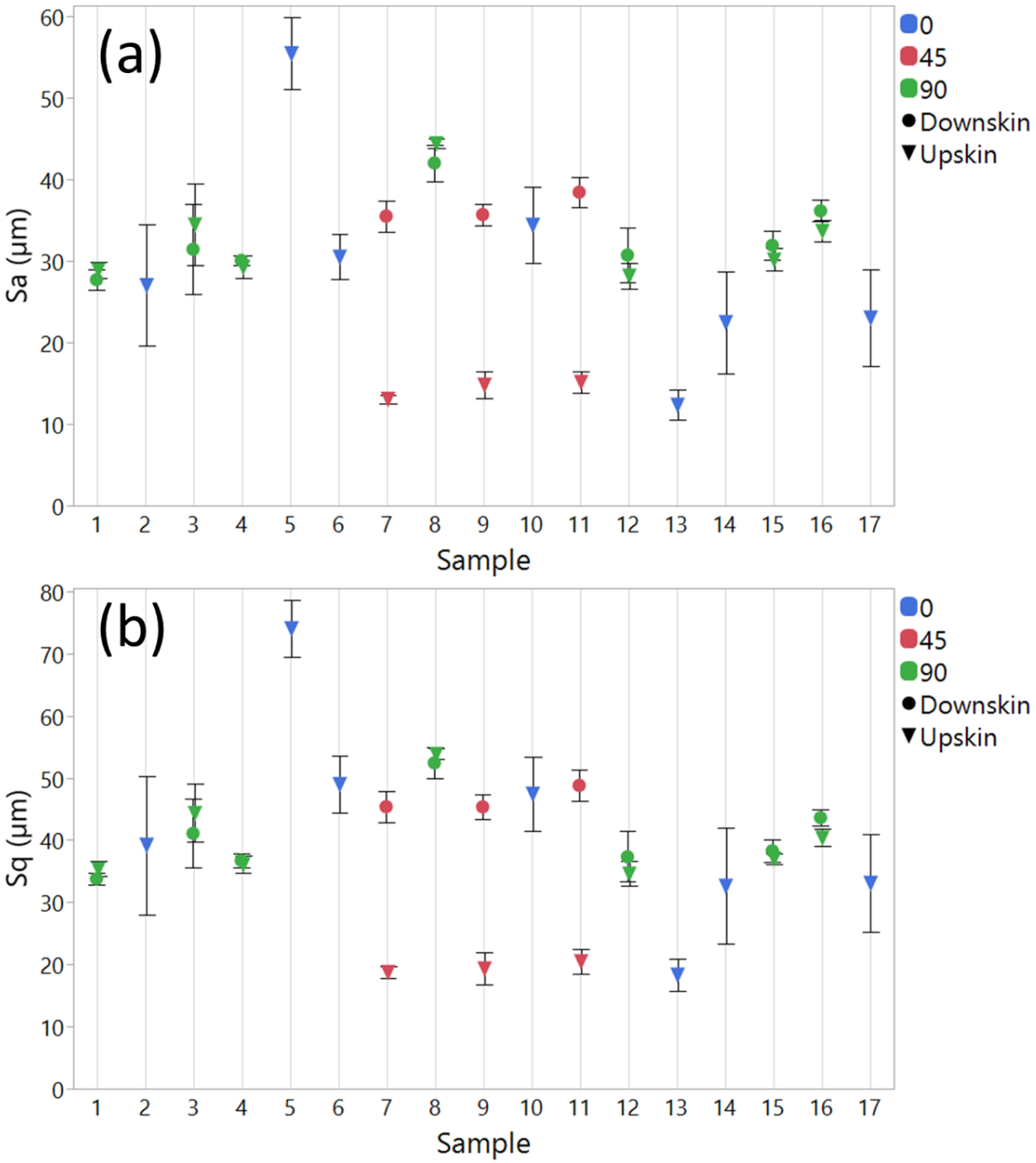

Figure 40: Plots showing the surface texture parameters vs. sample number for (a) Sa (b) Sq

These consistent values are reflected in similar physical characteristics seen in the SEM images as shown in Figure 41. Samples 1 in Figure 41(a) and 4 in Figure 41(b) are representative examples of the 90° surfaces and have mean values of 28.3 µm and 29.7 µm respectively. The surfaces are covered with agglomerated particles, the average height of which likely corresponds to the Sa as they are slightly larger than the average diameter of the raw powder used to build that samples, which was measured to be 18.1

µm ±8.1 µm (calculated over 5 SEM images, each measuring roughly 2000 particles). Samples 9 in Figure 41(c) and 11 in Figure 41(d) are representative examples of the upskin 45° surfaces that have mean Sa values of 14.8 µm and 15.1 µm respectively. Both SEM images show scan tracks left by the laser and on top of these are discontinuities in the scan tracks caused by balling and half-melted or agglomerated particles. These particles appear to be mostly arranged in vertical lines, corresponding to the edges of each build step.

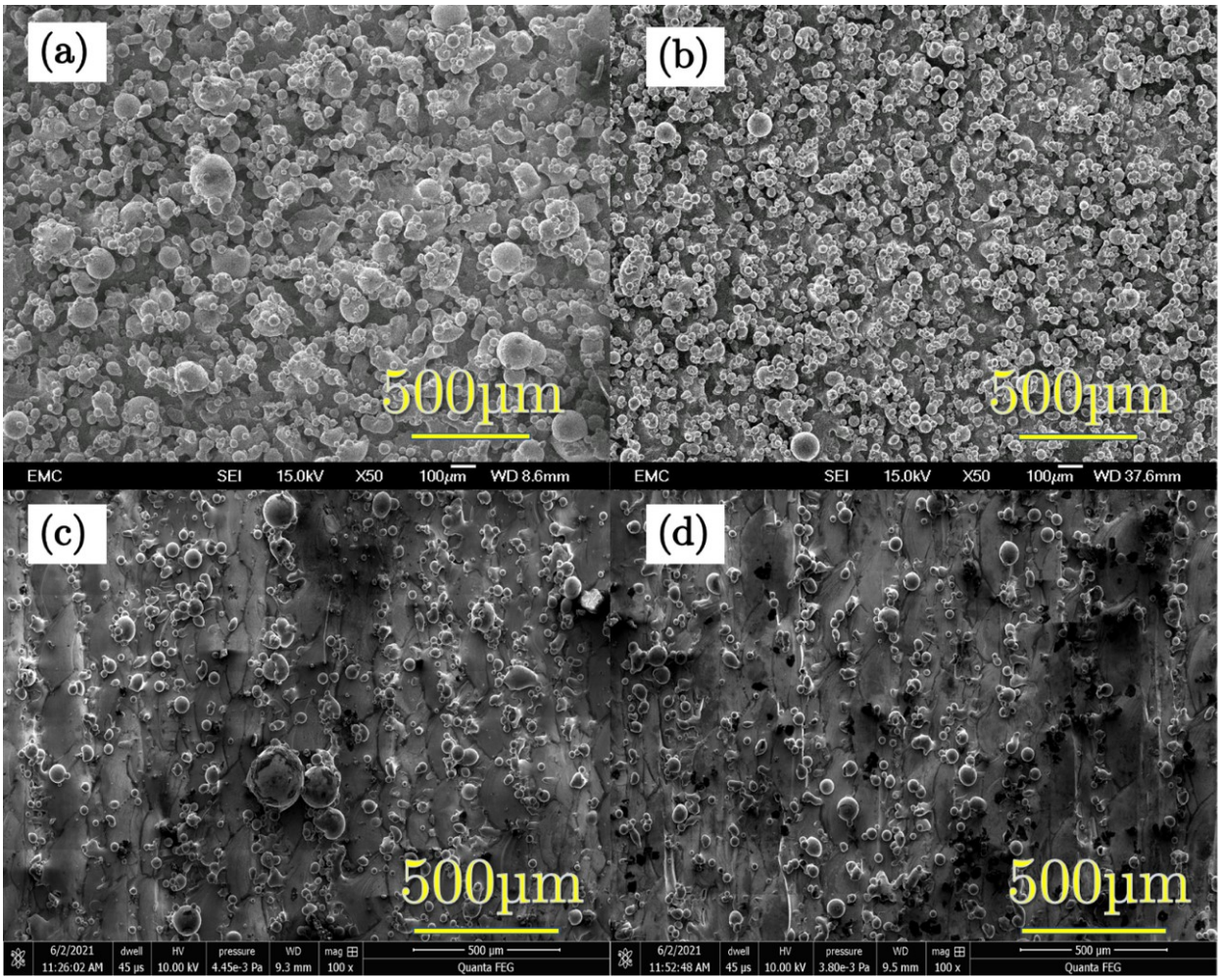

Figure 41: SEM images showing 50x magnification of the 90° (a) Sample 1 and (b) Sample 4 and 100x magnification of the 45° (c) upskin of Sample 9 and (d) upskin of Sample 11

However, not all samples with similar surface texture values had similar physical features. This was particularly true when comparing samples built at different angles. Both Sa and Sq show the average height deviation of a surface from a mean plane. However, this is a very limited description of a surface, and lacks detail such as whether

the deviation is above or below the mean plane or the shape of the deviation. Good examples of this are the 0° samples 6 and 10. Both of which have similar mean values of Sa and Sq for their upskin surfaces (30.5 µm and 34.4 µm Sa respectively). However as seen in Figure 42 the actual surfaces of samples 6 in Figure 42(a) and 10 in Figure 42(b) are very different. Although the scan tracks can clearly be seen in both images, there are clear discontinuities in the surface of sample 10 leading to numerous pores of varying size. The surface of sample 6 in contrast does not appear to have any porosity but does have several agglomerated particles of varying size adhered to its surface.

The SEM images suggest that samples 6 (Figure 42(a)) has mostly peaks on the surface, while sample 10 (Figure 42(b)) has mostly sub-surface pores. Rather than Sa or Sq, these are more clearly measured using Ssk (a measure of the symmetry of the roughness profile about the mean plane). Sample 6 skews positive (above 0) with a value of 2.57 while sample 10 skews negative (below 0) with a value of -0.89. (Ssk is discussed in more detail in section 5.4.2).

Sa, Sq and Ssk still only give limited information about the surface, not capturing the shapes or distributions of the surface features. For example, the 0° sample 10 in Figure 42(b) and the downskin of the 45° sample 11 in Figure 42(c) both have similar values for Sa (34.4 µm and 38.4 µm respectively) and are both negatively skewed. However, Figure 42(c) shows that the downskin surface of the 45° sample 11 is very different from sample 10. The surface of sample 11 is almost entirely covered in agglomerated particles and looks closer to the surfaces of the 90° samples 1 and 4 seen in Figure 41(a) and Figure 41(b). However despite appearing similar in the SEM images, the mean Sa of the downskin of the 45° sample 11 is notably higher (38.4 µm) than both 90° samples (28.3 µm and 29.7 µm).

The parameter Sdq, the average slope of the surface, helps to further distinguish the 0° sample 10 (Figure 42(b)) and downskin of the 45° sample 11 Figure 42(c). The Sdq of the downskin of sample 11 is notably higher (5.28 µm) than sample 10 (3.57 µm) due to the numerous adhered particles increasing the overall slope of the sample. Sdq is discussed in more detail in section 5.4.3

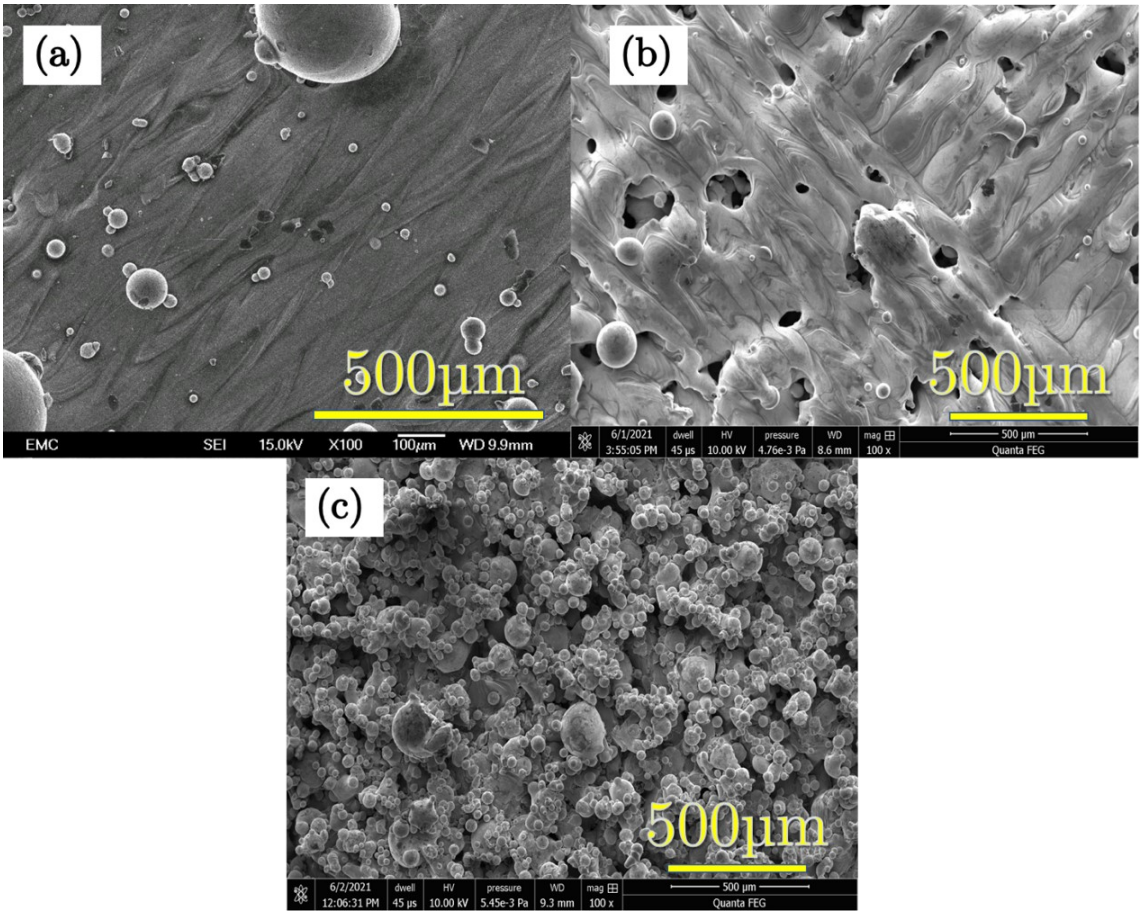

Figure 42: 100x magnification SEM images of (a) 0° sample 6 (b) 0° sample 10 and (c) the downskin of the 45° sample 11

Overall, it is apparent that while some of the samples have similar values for surface texture parameters, such as the Sa values of the 0° samples 6 and 10, the corresponding physical surfaces are actually very different. Similarly, the reverse was also found to be true, such as for the downskin surface of the 45° sample 11 which in SEM images appeared like the surfaces of the 90° samples 1 and 4 but had much higher values for Sa. Relying on only texture parameters or SEM images gives an incomplete description of the sample surfaces. It is possible that samples may have similar values for surface texture parameters but may each cause different amounts of internal reflections of radiation depending on how cavernous the surface features are leading to different values for emissivity. It is important to understand the physical features to which these parameters correspond in order to better understand how the emissivity may differ. This will be considered and explored in greater detail when discussing the emissivity results.

5.4.2. Physical meaning of Ssk and Sku

Figure 43 shows plots of the Ssk (a) and Sku (b) for all seventeen samples. The zero line has been denoted on the Ssk plot in Figure 43(a) to show the separation between positive and negative skew. On the Sku plot the red line denotes a value of 3, equivalent to a Gaussian distribution.

As previously mentioned, A. Triantaphyllou *et al.* [47], found that Ssk could be used to distinguish between upskin and downskin surfaces. Positive Ssk corresponded to a greater number of peaks on the surface and negative corresponded to a greater number of valleys, pores, and sub-surface porosity. R. Leach *et al.* described Kurtosis as a measure of the spread of the surface height distribution and as a method of identifying outliers [42]. A value of 3, which corresponds to a surface having a normal distribution was said to have an equal spread of soft and sharp peaks and valleys. Sku < 3 was said to correspond to mainly squashed peaks and valleys with large edge radii and Sku > 3 corresponds to sharp peaks and valleys with small edge radii.

As seen in image Figure 43(a) the 45° samples are clear examples of surfaces with different values for Ssk. The upskin surfaces are all positively skewed (>0) with a mean of 1.402 while the downskin surfaces are all negatively skewed (<0) with a mean of -0.44. As previously discussed, downskin surfaces of overhanging parts tend to have higher surface roughness. This is because during the build process these downskin surfaces only have unmelted powder to support them, causing heat to dissipate more slowly due to the lack of a conductive pathway to the baseplate. This causes the melt pools to grow large and sink into the powder due to gravity leading to the formation of valleys. Figure 44 shows the upskin (images (a), (c) and (e)) and downskin (images of (b), (d) and (f)) surfaces of the 45° samples 7, 9 and 11. The upskin surfaces appear free from porosity and are mostly dominated by balling, agglomerations and half-melted particles which likely correspond to the peaks. From the SEM images alone it appears that the downskin surfaces are also mostly dominated by half-melted particles, but underneath these can be seen numerous valleys, pits, and pores.

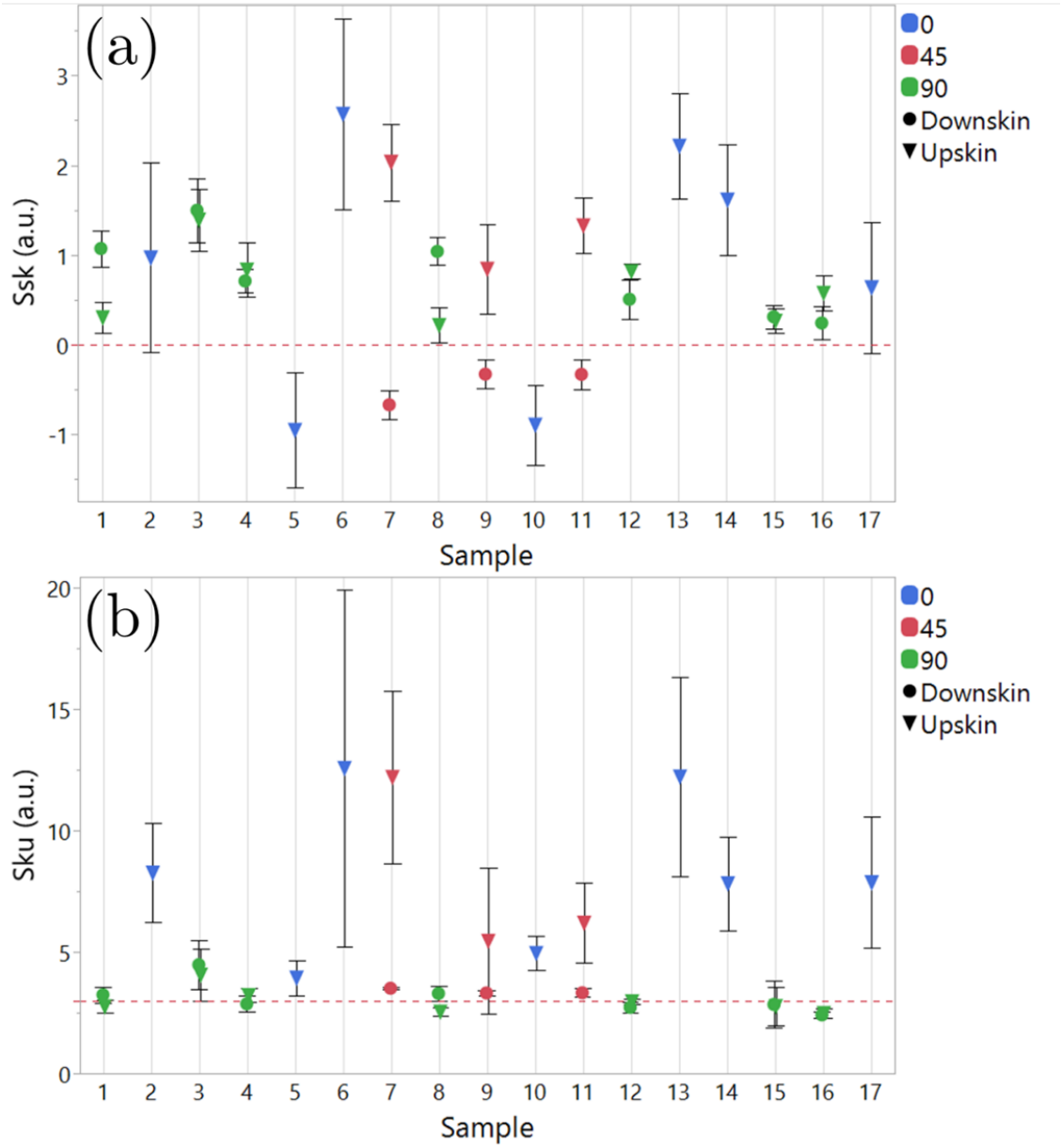

Figure 43: Plots showing the surface texture parameters vs. sample number for (a) Ssk (b) Sku. The red line on image (a) is at a value of 0, showing separating positive and negative skew. The red line on image (b) is at a value of 3, showing values with a Gaussian distribution

Zhu *et al.* studied the suitability of focus variation microscopy (FVM) on measuring various areal texture parameters including Ssk and Sku on 90° and 0° samples [169]. They used a similar method to this work, measuring areas 2 mm^2 at five different locations on both upskin and downskin surfaces, although they did not give values for the lateral resolution or L-filter. It should be noted that their results are not directly comparable to the work in this thesis as they investigated polyamide-12 manufactured using high speed sintering, but as they also used FVM general comparisons can be made.

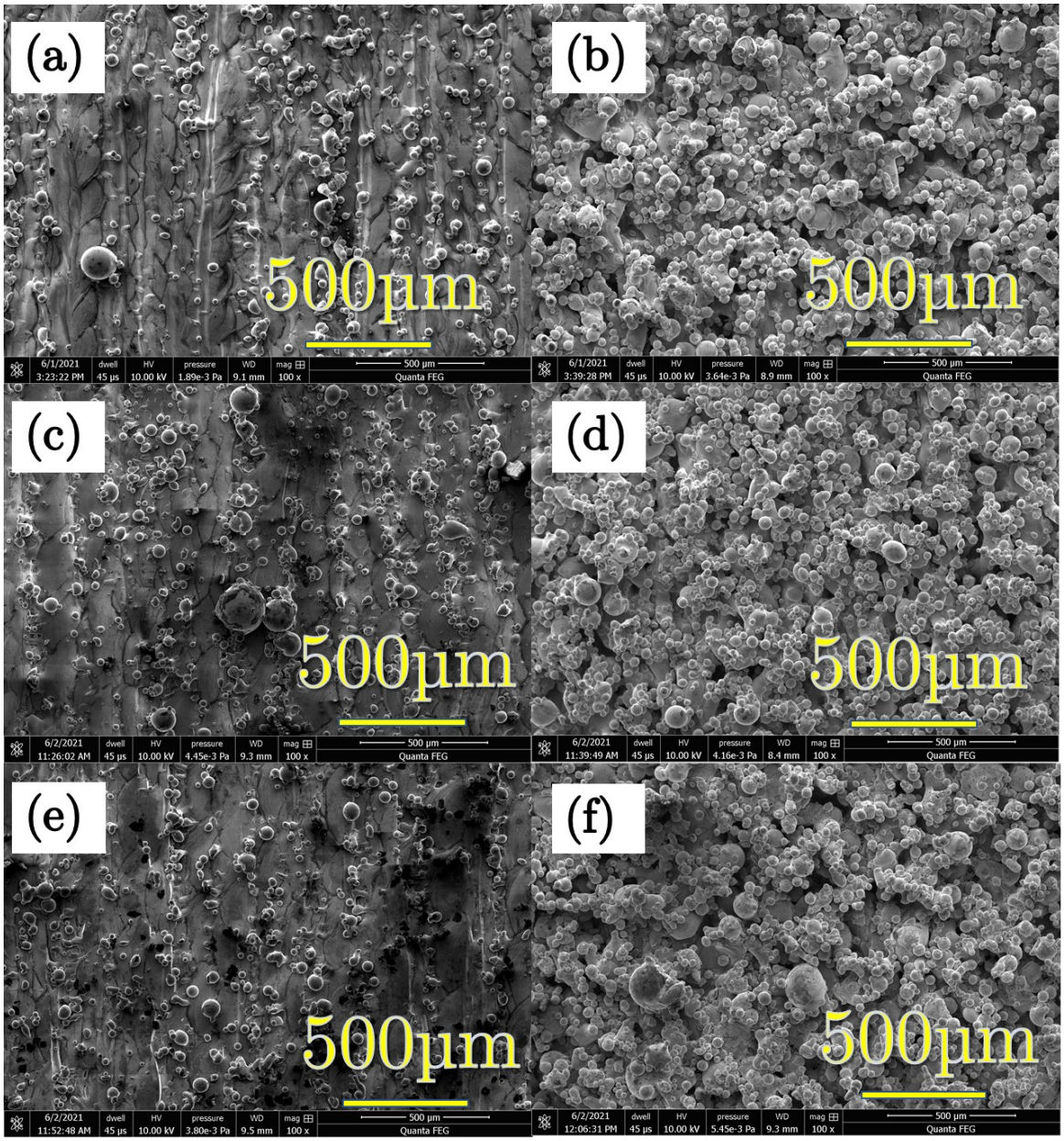

Figure 44: 100x Magnification SEM images of the upskin and downskin respectively of the 45° (a) and (b) sample 7 (c) and (d) sample 9 (e) and (f) sample 11

For the 0° samples they also found that Ssk was useful for distinguishing between upskin and downskin surfaces, although they found downskin surfaces were more dominated by peaks and upskin by valleys. This may be due to the different fabrication method used to build their samples. Interestingly they did not measure Ssk and Sku on 90° surfaces as they found that re-entrant features on such surfaces were not detectable using FVM due to line-of-sight restrictions limiting the amount of light reflected to the microscope, which increased measurement discrepancies for Ssk and Sku (although they did not give exact values). Re-entrant features may cause large amounts of internal

reflections of radiation, leading to higher values of emissivity. Thus these are important to be able to measure for understanding and correlating with emissivity. As seen in Figure 43(a) all the 90° samples are skewed positive, however given the surfaces are dominated by adhered half-melted and agglomerated particles, it was expected for the surfaces to be mostly peaks and thus skew positive. Looking at the SEM images and the Ssk results, Ssk was capable of distinguishing between peaks and valleys, although from this data it is not clear how suitable it was at capturing re-entrants for any build angle. Zhu *et al.* mentioned X-ray CT as a technique to better capture re-entrants and although it was not used in this work to measure areal texture parameters, X-ray CT was used to accurately measure the perimeter and cross-sectional areas of the samples. Comparisons between the X-ray CT measurements and the surface texture parameters are discussed in detail when discussing the impact of surface roughness on emissivity in section 6 of this thesis.

As seen in Figure 43 the 90° sample 12 and 0° sample 13 are good examples of opposite extreme values of Sku. The mean Sku values for both sides of sample 12 are 2.72 and 2.96 (very close to a Gaussian distribution of 3), while for sample 13 upskin it is much higher at 12.2. What these values mean physically can be seen in Figure 45. Figure 45(a) shows the surface of the 90° sample 12 which is dominated by half melted and agglomerated particles of varying size. From the value of Sku, it is known that the range of these sizes correspond to a roughly normal distribution. In contrast the surface of sample 13 shown in Figure 45(b) appears to be mostly flat

However in Figure 45(b) there can clearly be seen a very large, agglomerated particle with a diameter of approximately 326 µm, significantly larger than the average particle diameter of the raw powder used to build the samples which was measured to be roughly 18.1 µm ±8.1 µm. Although Figure 45(b) is only a single image of the surface of sample 13, if it is representative it may explain the very high values for Sku seen for sample 13 and others. Such large values of Sku may correspond to surfaces dominated by outliers.

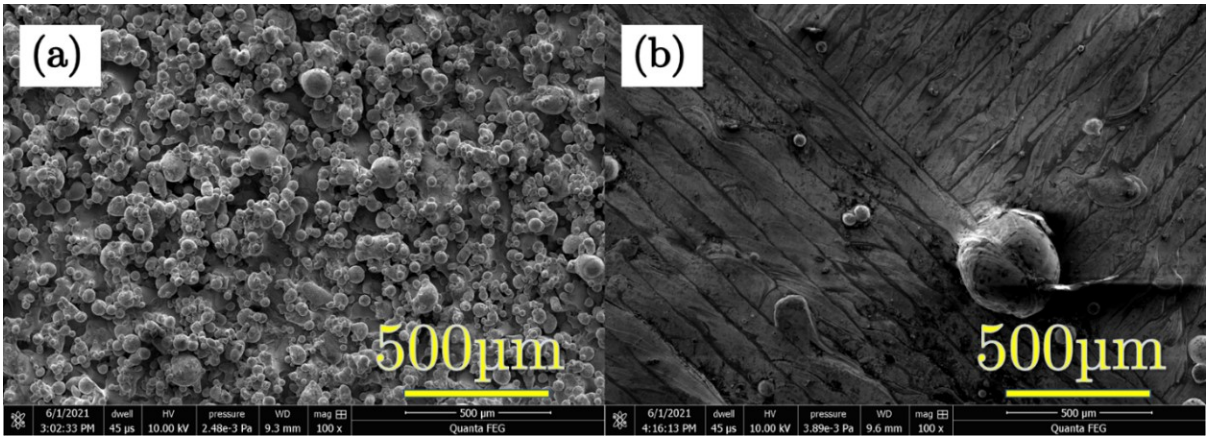

Figure 45: 100x magnification SEM images of (a) 90° sample 12 and (b) 0° sample 13

5.4.3. Physical meaning of Sdq

Sdq represents the root mean square slope of the surface. This is easy to understand for relatively flat surfaces or surfaces with well-defined peaks such as the examples shown in Figure 46. In Figure 46(a) there is no change in the slope of the surface, resulting in an Sdq of 0 while Figure 46 (b), the peaks are at 45° angles causing the change in height to be equal to change in position along the surface, giving the surface an average slope of 1.

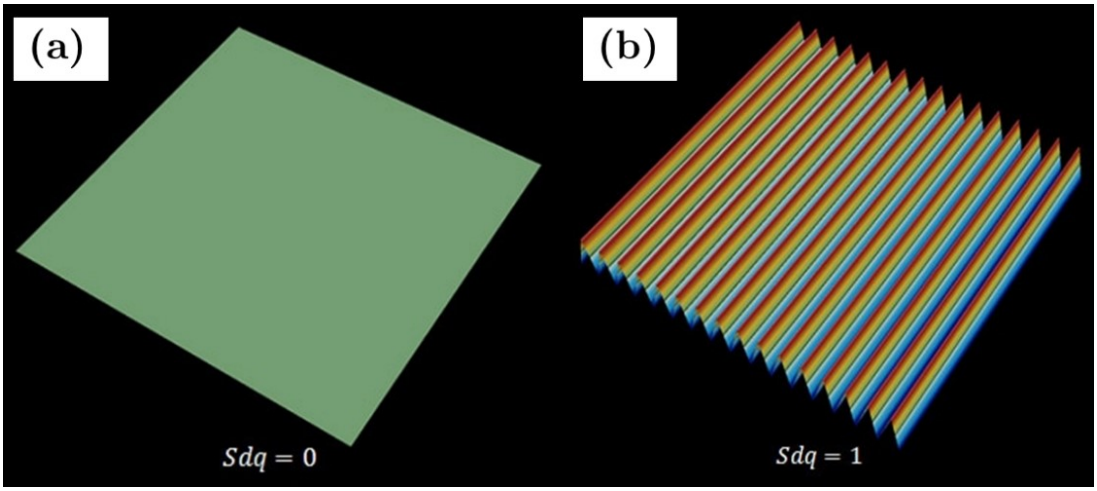

Figure 46: Images showing idealised surfaces with (a) an Sdq of 0 and (b) and Sdq of 1. This image is originally from Keyence [170]

However, such definitions are less suited for AM surfaces due to their aperiodic nature or features such as spherical particles. Figure 47 shows a plot of the mean values of Sdq against sample number for all seventeen samples. The SLM surfaces generated a wide range of average slopes which correspond to very different physical features. The

upskin of the 0° sample 13 shown in Figure 45(b) is a good example of a flat surface with a low value for Sdq (there is a large particle in this image, but as previously discussed this is likely an outlier).

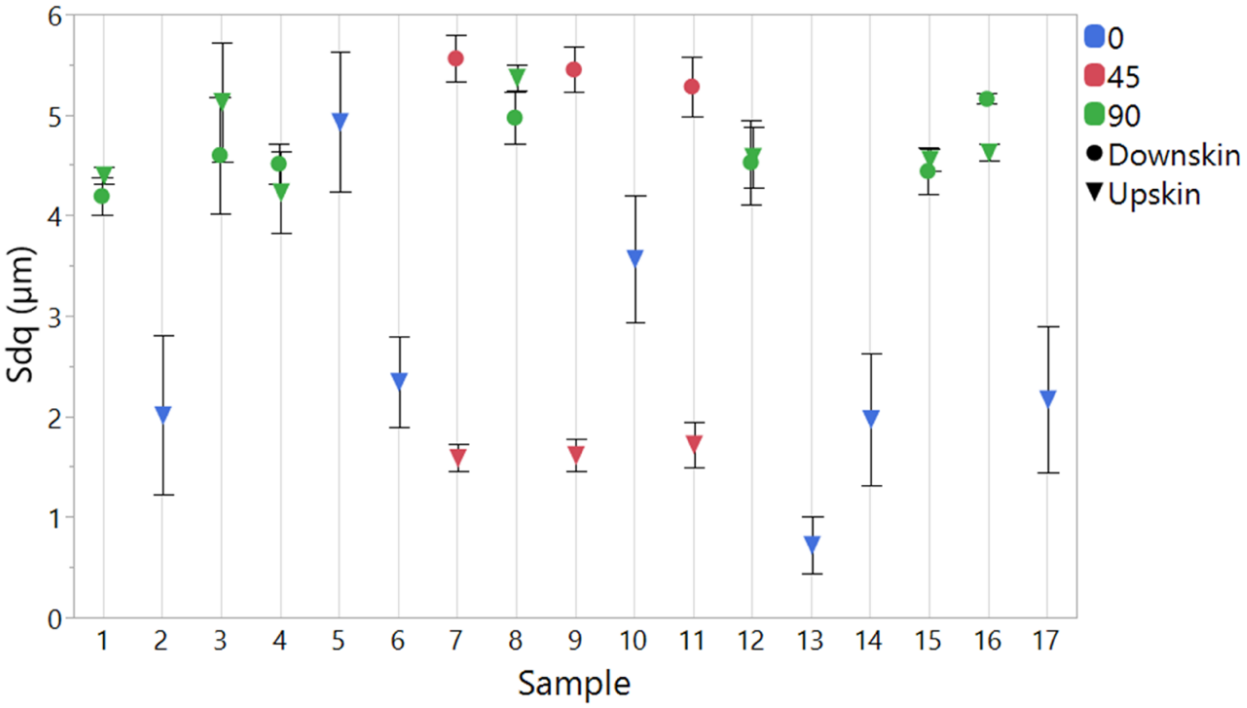

Figure 47: Plot showing the surface texture parameter Sdq vs. sample number

All the 90° samples in Figure 47 have relatively high values of Sdq (with means of 4.58 µm and 4.72 µm for the downskins and upskins respectively) and as previously discussed all share similar physical features, primarily many half-melted or agglomerated particles on the surface. These spherical or semi-spherical particles likely are the reason for the high slope values seen. Sdq, like Sa and Sq, only gives information on the magnitude of the slope and not the direction (whether there are more peaks or valleys). The 0° sample 5 is an example of a surface with high Sdq (4.93 µm), but negative skew, the surface of which is shown in Figure 48(a). The high Sdq of sample 5 likely corresponds to the steep sides of the numerous pores seen in the Figure 48(a). This is corroborated by the Sku value of 3.91 which because it is greater than 3 indicates features with steep sides.

It is worth comparing sample 5 against sample 10, the surface of which is shown in Figure 48(b). Sample 10 was also built at 0° and has a highly porous surface but has

a lower mean value of Sdq at 3.57 µm. It is difficult to state definitively which surface contains greater amounts of porosity just comparing SEM images, although sample 5 does seem to contain more unmelted particles which may have contributed to the higher slope. However, comparing Sa and Sq values shows that the magnitude to sample 5's surface deviations were much greater than sample 10. Sample 5 had a mean Sa of 55.5 µm while sample 10 had a value of 34.4 µm. Given that they have similar values for skewness (Ssk), it is likely that the average size of the pores on sample 5 were greater compared to sample 10 which may have caused the large difference in Sdq.

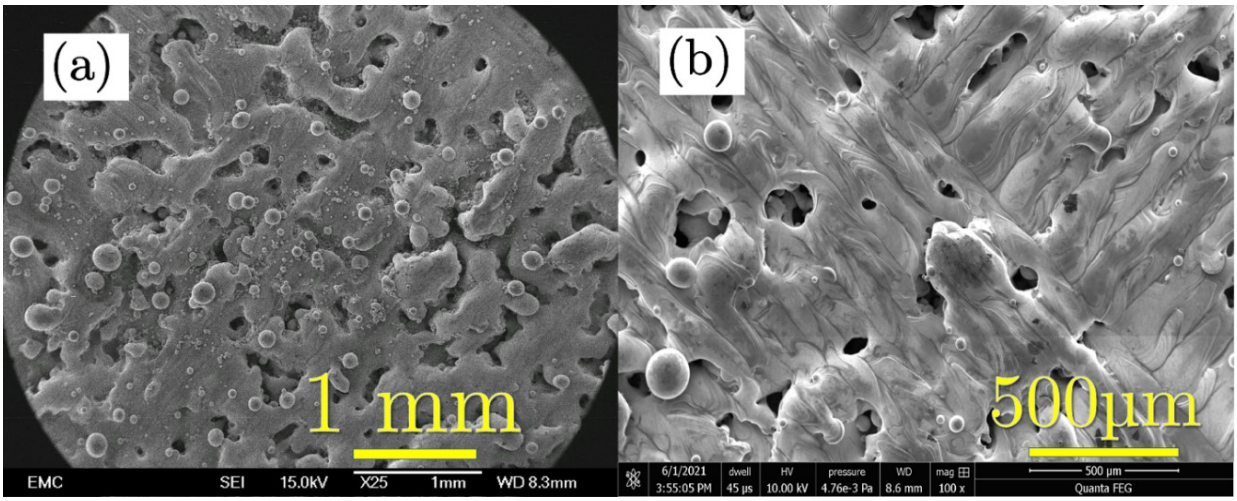

Figure 48: SEM images of the upskin surfaces of the 0° (a) sample 5 and (b) sample 10

The downskin surfaces of the 45° samples generally have the highest values for Sdq, with a mean value of 5.43 µm. SEM images of these surfaces are seen in Figure 44(b), (d) and (f). This may be because the physical features of these surfaces are combinations of large numbers of half-melted and agglomerated particles and large amounts of sub-surface pores with steep slopes.

5.5. Models linking process and surface texture parameters

The previous sections looked at the raw data, and how this data could be interpreted physically. This next section will look at modelling input parameters with roughness and how these relate to physical features.

5.5.1. Overview

The overall purpose was to model the relationship between inputs, the process parameters varied, and the surface texture parameters as outputs. A regression model was used, which describes the relationship between input factors (also known as predictors) and outputs (also known as responses). Regression describes a general collection of techniques used in modelling outputs as functions of input factors. When more than one input factor is used this is known as multiple linear regression, as used in this analysis.

Regression models can be written as linear equations, where they describe how the observed values of y (the outputs) change with given values of x (the inputs). The general form of this is shown in equation [38] where, for $i = n$ observations:

$$\boldsymbol{y_i = \beta_0 + \beta_1 x_{i1} + \cdots + \beta_p x_{ip} + \epsilon} \qquad [38]$$

Each input factor in the model has a slope coefficient, β_p. These coefficients represent the average increase in the output for a unit increase in each input factor if the other inputs are held constant. The term ϵ in the equation represents the random variation in the model. A new model was created for each of the texture parameters as the output (y), with each of the process parameters included as input factors (laser power, scanning speed, hatch spacing, layer thickness and build angle).

The regression models were calculated by the software JMP using the following methodology. To estimate the values of the model coefficients, the method of the sum of least squares was used. At first a model was generated including every input parameter up to the second order polynomial (each input parameter squared) and up to second order interactions (each parameter crossed with every other parameter). Higher order terms were not included because this was a screening experiment, and so the purpose was to determine the significance of inputs on the outputs, rather than generating a higher order model that more accurately describes outputs without necessarily providing more insight.

One of the input parameters that was used in this model was the side of the sample measured, corresponding to either the upskin or downskin surface. However, the roughness of the downskin 0° samples was not measured because they were removed from the built plate using EDM wire cutting. To account for this regression models were produced assuming that the texture parameter for upskin and downskin sides were the same for the 0° samples. As a result, the model assumes that side has no effect on the 0° samples, so no conclusions about downskin surfaces for 0° samples can be drawn. Future work might consider producing 0° samples with the downskin not directly connected to the baseplate, to study how process parameters influence the roughness.

Once the model had been generated the software also automatically calculated p-values for each of the terms in the model. The p-value is a measure of the probability that the null hypothesis is correct and that there is no relationship between the input parameters and the output. Using a typical threshold value of 0.05, any p-value lower than this threshold was deemed as significant and the corresponding term was deemed to have an impact on the model. The lower the p-value, the larger the impact the corresponding term had on the model.

To make sure that the model was not overfitted, terms were systematically removed from the model. This began with the term that had the highest p-value (and thus the lowest impact on the model) and continued until only terms with p-values lower than the threshold were left. Table 20 shows key values used to determine the significance of each of the models generated for each surface texture parameter.

The Root Mean Square Error (RMSE) is a measure of the unexplained variation in the model. The lower the value, the more precise the predicted values of the model. All the models in Table 20 have low values for the RMSE.

The Root Mean Square Error (RMSE) is a measure of the unexplained variation in the model. The lower the value, the more precise the predicted values of the model. All the models in Table 20 have low values for the RMSE. When describing the fit of linear models, a commonly used term is the R^2 value which in this instance is a measure of the strength of the correlation between the predicted and experimental results. The

models of each of the surface texture parameters seen in Table 20 have high R^2 values of 0.89 or above, indicating that each of the models can explain 89% or more of the variability in the data.

Table 20: Table showing key parameters for the models generated for each of the texture parameters

	Mean Sa (µm)	Mean Sdq (µm)	Mean Sku (a.u.)	Mean Sq (µm)	Mean Ssk (a.u.)
Mean of Response	30.53	3.67	5.39	40.15	0.65
Root Mean Square Error	3.42	0.228	0.624	3.865	0.3
R^2	0.894	0.978	0.963	0.916	0.907
F ratio	85.53	363.6	216.43	110.52	98.27
p-value	<.0001	<.0001	<.0001	<.0001	<.0001

As well as the p-value, a method of determining the significance of the model is the F-ratio. The F-ratio is the ratio of the variation explained by the model to the unexplained variation. The larger the F-ratio, the more of the variation that can be explained by the model. Each of the models have large values for the F-ratio and very low values for the p-values, showing that these models can explain much of the variation and are statistically significant. Although the values in Table 20 show that the models overall are reliable, they do not give information on which of the input factors are significant to the models which is the key purpose of the models. The plots shown in Figure 49 detail the significance of each of the input parameters and their interactions, for each of the different texture parameters. The more significant an input parameter, the greater the effect it had on the texture parameter. The plots are the LogWorth versus the source (input terms). The LogWorth is the negative log of the p-values, which more easily visualise the significance of each term. The blue line in the diagrams corresponds to a LogWorth value of 2 which is equivalent to a p-value of 0.01. This is to clearly show that any value greater than this is significant to the model. Most input parameters in Figure 49 have LogWorth values greater than 2, indicating they are significant to each of their models. Input parameters that are not significant have interactions with other terms that are significant and cannot be removed from the model.

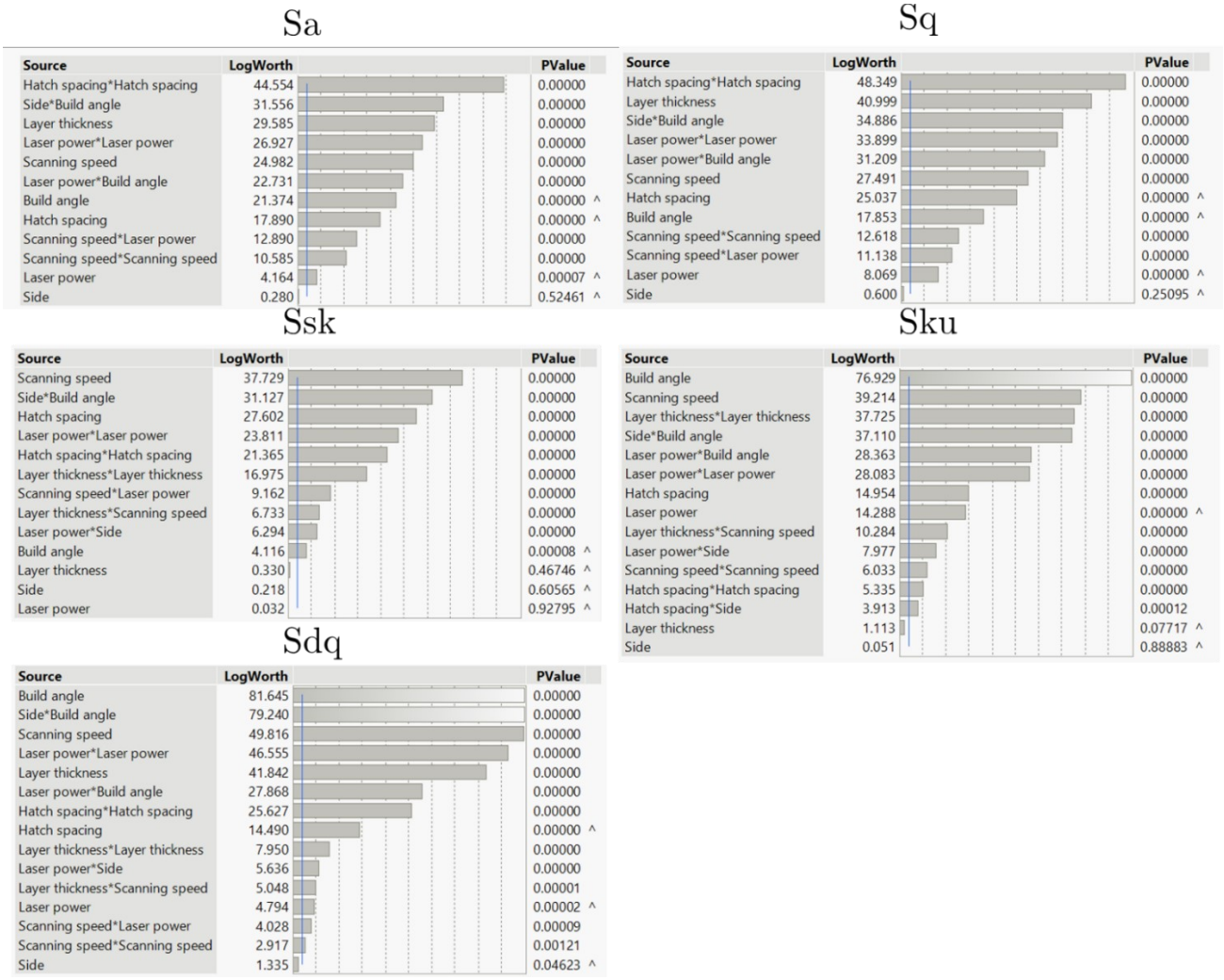

Figure 49: Plots showing the LogWorth vs. the source for the different texture parameters

5.5.2. LogWorth vs. source and main effects plots

Figure 50 shows plots of the model predicted responses on all the different texture parameters for each of the input parameters. As shown in Figure 49 the models for both Sa and Sq found the same input parameters significant. The square of hatch spacing had the largest impact on both models. Both low (0.05 mm) and high (0.1 mm) values produced low values of Sa and Sq (roughly 21 µm and 29 µm respectively), while middle (0.075 mm) values produced high values (roughly 38 µm and 49 µm respectively). non-linear effect occurs regardless of the level of any of the other input parameters.

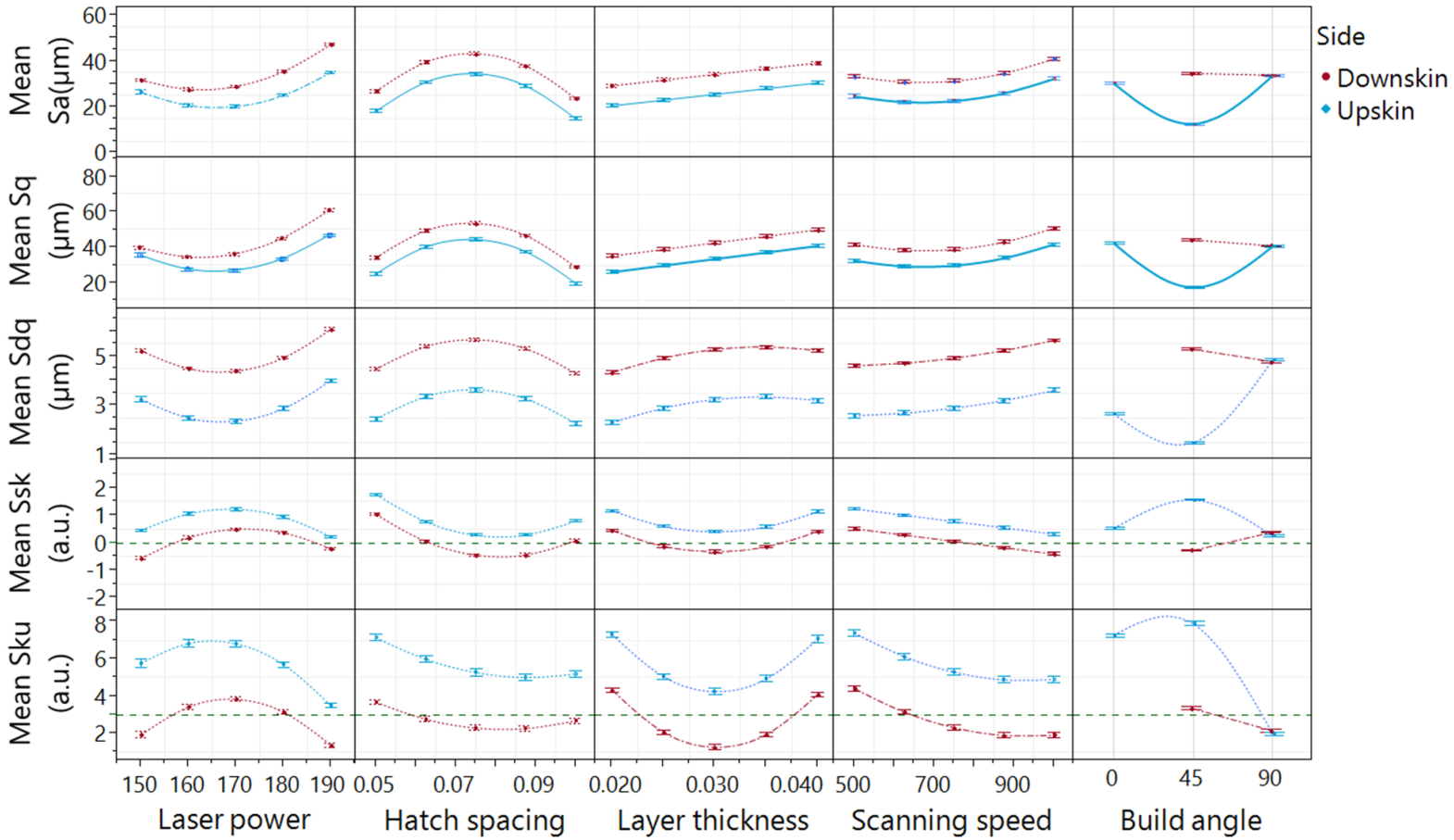

Figure 50: Main effects plots showing the model predicted responses on the different texture parameters for laser power, hatch spacing, layer thickness, scanning speed and build angle. Each plot is split by side (upskin and downskin. The green lines on Ssk plots are at a value of 0, showing separating positive and negative skews. The green lines on the Sku plots are at a value of 3, showing values representing a Gaussian distribution

This indicates that level of hatch spacing has a curved effect on both Sa and Sq as seen in Figure 50. It is important to note as only three levels of hatch spacing were studied that this does not mean that the relationship is necessarily parabolic, only that it is not linear. Hatch spacing also does not have any interactions with any other term, so this non-linear effect occurs regardless of the level of any other input parameters.

Because all the process parameters were changed simultaneously in this work, it is difficult to know the physical effects that changing a single parameter had on the surfaces. Instead, previous studies from the literature may help to explain the shape of the responses seen in Figure 50 and how they relate to physical features. Dong *et al.* also studied the effect of hatch spacing on the surface roughness of SLM 316L with process parameter ranges similar to those in this thesis [171]. They varied hatch spacing between 75 µm – 200 µm while keeping the laser power (200 W), layer thickness (50 µm), scanning speed (400 mm/s) constant. However, it should be noted that they gave no information on the build angle of their samples and only gave values of surface roughness in microns without detailing what texture parameter they were measuring. They found the significance of hatch spacing on roughness was because it determined the overlap rate and heat accumulation between adjacent tracks. At lower hatch spacings, there was sufficient heat accumulation to allow for neighbouring sections to combine into dense, flat regions. Though the lowest value of hatch spacing (0.075 mm) resulted in a slightly higher roughness than the next value (0.1 mm). At higher hatch spacings (0.15 – 0.25 mm) there was significantly less overlap between adjacent scan tracks, resulting in regions of insufficient melting and pores which caused increases in the surface roughness. Dong *et al.* concluded that a hatch spacing of 100 µm produced parts with the lowest values of surface roughness which matches the model predictions for lowest Sa and Sq in Figure 50. However, over the hatch spacing values they studied, the middle values produced the lowest values of roughness, which is the opposite of the trend seen in Figure 50. This may be because the range of hatch spacings differed as 100 µm was the maximum value used in this thesis while Dong *et al.* went up to values of 250 µm. Tian *et al.* also studied the effect of hatch spacing on surface

roughness (Ra) with different layer thicknesses [172]. They kept scanning speed (1900 mm/s) and laser power (370 W) constant while varying the hatch spacing (0.05 mm – 0.13 mm) and layer thickness (20 µm and 40 µm). However, they studied Hastelloy X alloy, so only overall trends can be compared with this thesis rather than specific values. They found that generally increasing hatch spacing decreased the Ra values for both levels of layer thickness. Large overlap caused by low hatch spacings increased the energy absorbed, causing a bigger heat affected zone which in turn caused more particles to be stuck to the surface and increasing the roughness [172]. Determining the exact reason behind why hatch spacing has a curved response on the Sa and Sq was beyond the scope of this experiment. However now that this has been identified as a critical influence on these texture parameters, future experiments could be designed to investigate this further.

For both models of Sa and Sq shown in Figure 49, the layer thickness and the interaction between build angle and side were the next most significant terms. In Figure 50 as the layer thickness increased so did the Sa and Sq. The significance of the interaction between build angle and side is likely because of the large difference in values of Sa and Sq between the upskin and downskin surfaces of the 45° samples. As shown in the plots of Sa and Sq in Figure 40 the side measured (upskin or downskin) had little effect on the values for the 90° samples, and no effect on the 0° samples because only upskin was measured. However, there was a large difference in values between the upskin and downskin sides of the 45° samples due to the previously discussed poor thermal conduction pathways of the downskin surfaces. Y. Liu *et al.* used a Response Surface Method to investigate what parameters had the largest effect on the surface roughness (Ra) of 90° samples of thin walled 316L SLM. They varied laser power (70 W – 170 W), scanning speed (65 mm/s – 235 mm/s) and layer thickness (0.0215 mm – 0.0385 mm) and found that layer thickness was the most significant term, although they gave no physical explanation. They also found that interactions between layer thickness, laser power and scanning speed had significant effects on the roughness while layer thickness had no interactions in the models of this thesis.

However, it should be noted that they studied single track samples, and so hatch spacing was not included in their model. Strano *et al.* investigated how build angle affected surface roughness of SLM 316L parts, varying build angle between 0 ° - 90° while keeping all other process parameters constant. At low build angles the stair step effect was the main impact on surface roughness, when the particle diameter was of comparable size to the layer thickness [91]. However, in this thesis models of both Sa and Sq did not have enough information to include the interaction between build angle and layer thickness and so understanding this interaction would require further investigation in future work.

The shapes of the model predicted responses for Sdq in Figure 50 are very similar to those for Sa and Sq, particularly for laser power, scanning speed and hatch spacing. This may be because as features on the surfaces get larger, such as agglomerated particles or sub-surface pores, the slopes of these features generally also increase. Thus, parameters that increase or decrease the Sa and Sq would have the same effect on the Sdq. A notable difference between the model predicted responses for Sa, Sq and Sdq is that for upskin surfaces Sdq increases notably between 45° and 90°. Build angle was the most significant term on the model for Sdq seen in Figure 49 and the shape of the response is reflected in the values of Sdq seen in Figure 47, where the 90° samples had the highest values of Sdq (mean of 4.65 µm) due to the numerous agglomerated particles on their surfaces while the upskin 45° and 0° samples were much lower (means of 1.642 µm and 2.53 µm respectively).

Ssk and Sku give information about the distribution of the surface features, rather than physical information. The shapes of the model predicted responses for Ssk and Sku in Figure 50 are generally opposite to the shapes for Sa, Sq and Sdq. For example, the middle value of laser power (170 W) produces the lowest responses for Sa, Sq and Sdq but the highest response for Ssk and Sku. Similarly, the highest scanning speed produces the highest Sa, Sq and Sdq but lowest Ssk and Sku. For both Ssk and Sku, scanning speed was a significant term to the models as seen in Figure 49 and both texture parameters generally decreased as the scanning speed increased. However as

discussed in section 5.4.2 because multiple parameters were changed simultaneously it is difficult to know the exact physical features these trends correspond to. This is illustrated in Figure 51 which shows the Sku and Ssk values for each sample number, coloured by scanning speed.

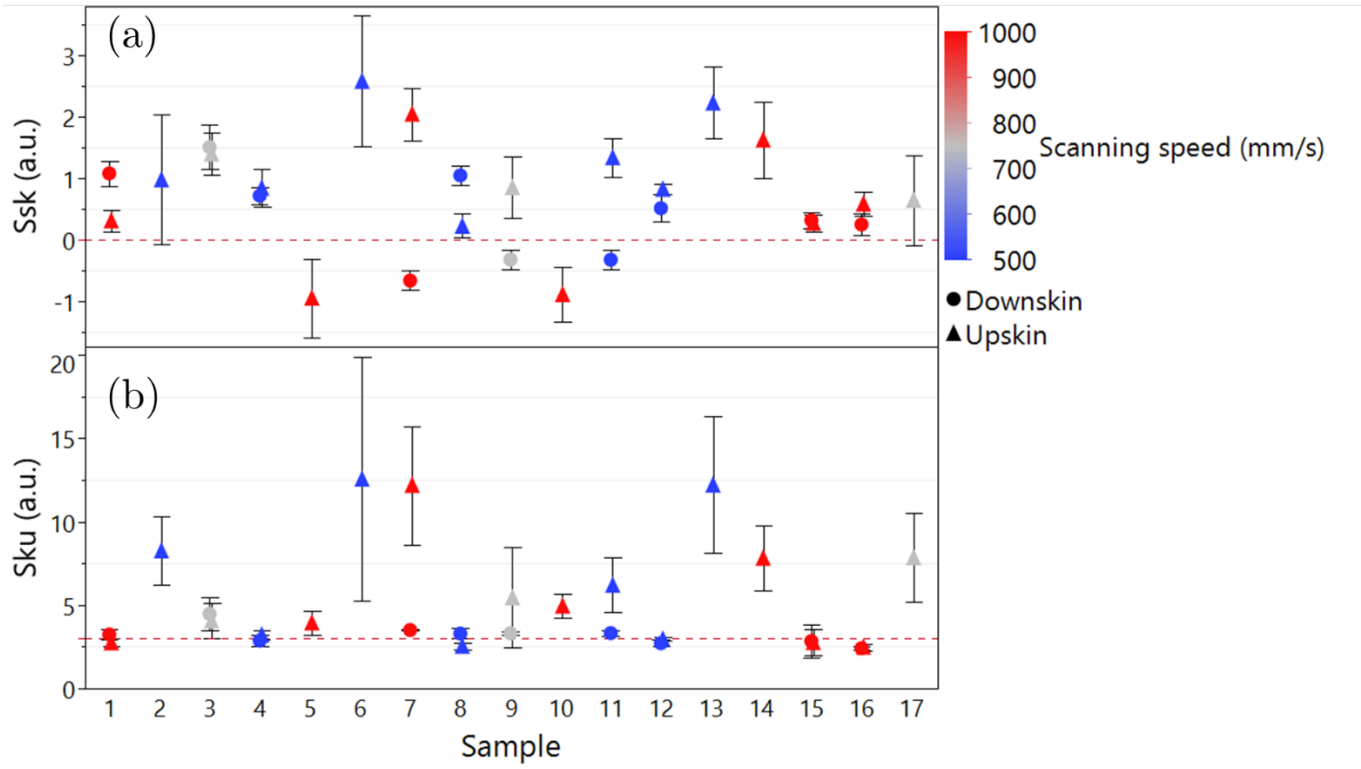

Figure 51: Plots showing the surface texture parameters vs. sample number for (a) Ssk (b) Sku. Both images are coloured by scanning speed. The red line on image (a) is at a value of 0, showing separating positive and negative skew. The red line on image (b) is at a value of 3, showing values with a Gaussian distribution

The same values for scanning speed give very different values for the texture parameters. For example, in Figure 51(a) both the 0° sample 5 and the 90° sample 14 were produced with scanning speeds of 1000 mm/s, but the Ssk of sample 5 is -0.952 while sample 14 is 1.615. Similarly, in Figure 51(b) both the 90° samples 4 and 0° sample 6 were produced with the lowest scanning speed of 500 mm/s, but sample 4 has a mean Sku of 3.37 while sample 6 has a much higher mean value of 12.56. Hypotheses can be made to explain the shapes of the model predicted responses seen in Figure 50. For example, low scanning speeds may have led to more thermal energy absorbed by the powder, leading to defects such as spattering which could cause an overall positive Ssk due to ejected particles on the surface or a high Sku if such particles

were outliers on an otherwise flat surface. High scanning speeds may have led to too little thermal energy being absorbed, causing lack of fusion and sub-surface porosity which would correlate to negative (or lower) values of Ssk. However further work would be required to better understand what exactly causes these response shapes.

5.6. Energy Density

Overall, the models provide valuable information on which of the input parameters have significant effects on the texture parameters. The complex nature of the relationships meant that with this one screening experiment they could not be deconvoluted to fully explain how they altered the physical surfaces. Energy density is an alternate way of relating the input parameters to physical changes on the samples.

5.6.1. Sa, Sq and Sdq

Figure 52 shows the relationship between energy density and Sa for the 90° and 0° samples. Similar relationships were found for the parameters Sq and Sdq and so those plots have been omitted.

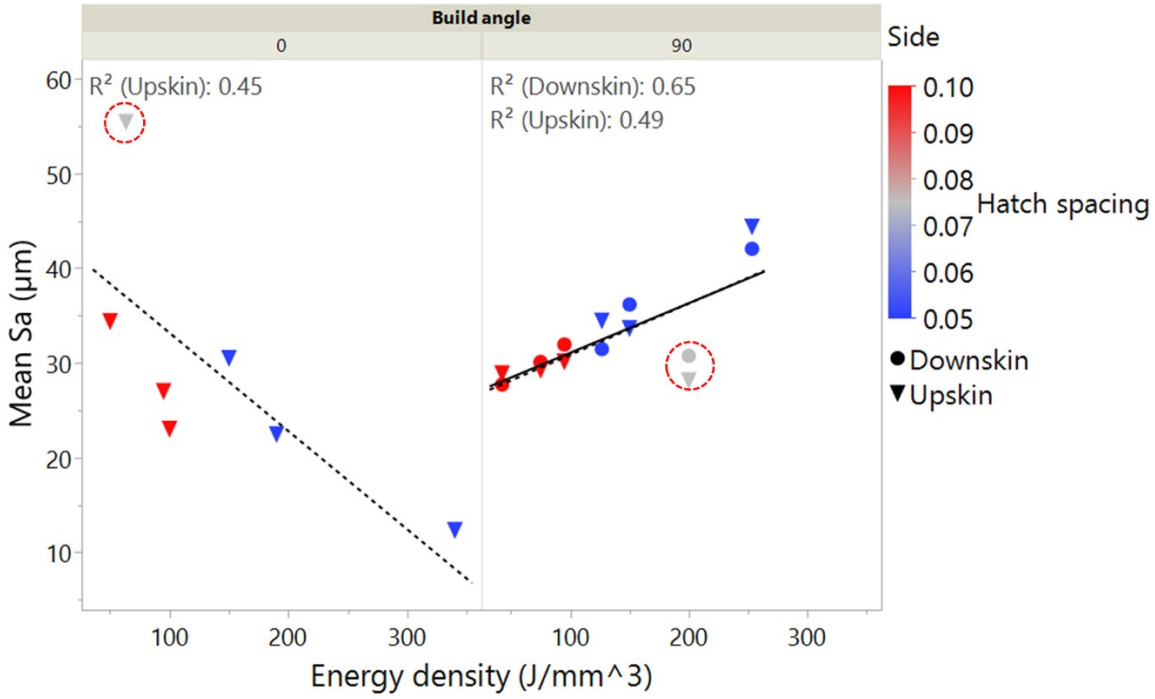

Figure 52: Graphs showing the mean Sa vs. Energy density for 90° samples and 0° samples. The samples are split by side (upskin and downskin) and coloured by hatch spacing. Outliers are highlighted in red circles.

As there were only three data points for the 45° samples this was not enough data to draw strong conclusions between energy density and surface texture and so these samples have been omitted. The graphs in Figure 52 clearly show trends for both build angles. For the 90° samples as energy density increases so does Sa. For the 0° sample the opposite is true, Sa decreases as the energy density increases.

There are notable outliers of these trends for both the 90° and 0° samples, both of which are highlighted in red circles on the graphs. For 90° it is sample 12, which has a considerably lower values for Sa and Sq while for 0° it is sample 5 which has considerably higher values of Sa and Sq. It is interesting to note that both outliers used the mid value of hatch spacing, 0.075 mm. These outliers agree with the trend between hatch spacing and Sa and Sq seen previously in the models and highlights the need for further investigation to understand exactly why this is occurring. Particularly because this goes against the trend between hatch spacing and roughness reported by other authors. Other papers have looked at the relationship between energy density and surface roughness and seen similar trends to those seen here.

0° samples

D. Wang *et al.* studied the Ra of the top surfaces of SLM 316L cuboid samples, which are equivalent to the upskin surfaces of the 0° samples produced for this thesis [107]. They varied the laser power (100 W – 150 W), scanning speed (250 mm/s – 1300 mm/s) and hatch spacing (60 µm – 100 µm). They divided energy densities into three distinct zones based on the magnitude of the energy density and the resultant physical features: Low, middle, and high.

- At low energy values (< 75 J/mm^3), the energy density is insufficient to completely melt the powder resulting in unformed track patterns and raw or partially melted powder on the surface.
- At medium values (75 J/mm^3 - 120 J/mm^3), there was significant balling as the wettability of the melting track was not enough.
- At high values (120 J/mm^3 – 180 J/mm^3), the laser can melt the powder and form a continuous smooth track.

Observations in this thesis did correspond to each of these zones, although the ranges of energy density for the zones were slightly higher than those reported by D. Wang *et al.* Figure 53 shows SEM images of 0° samples representative of each of these zones.

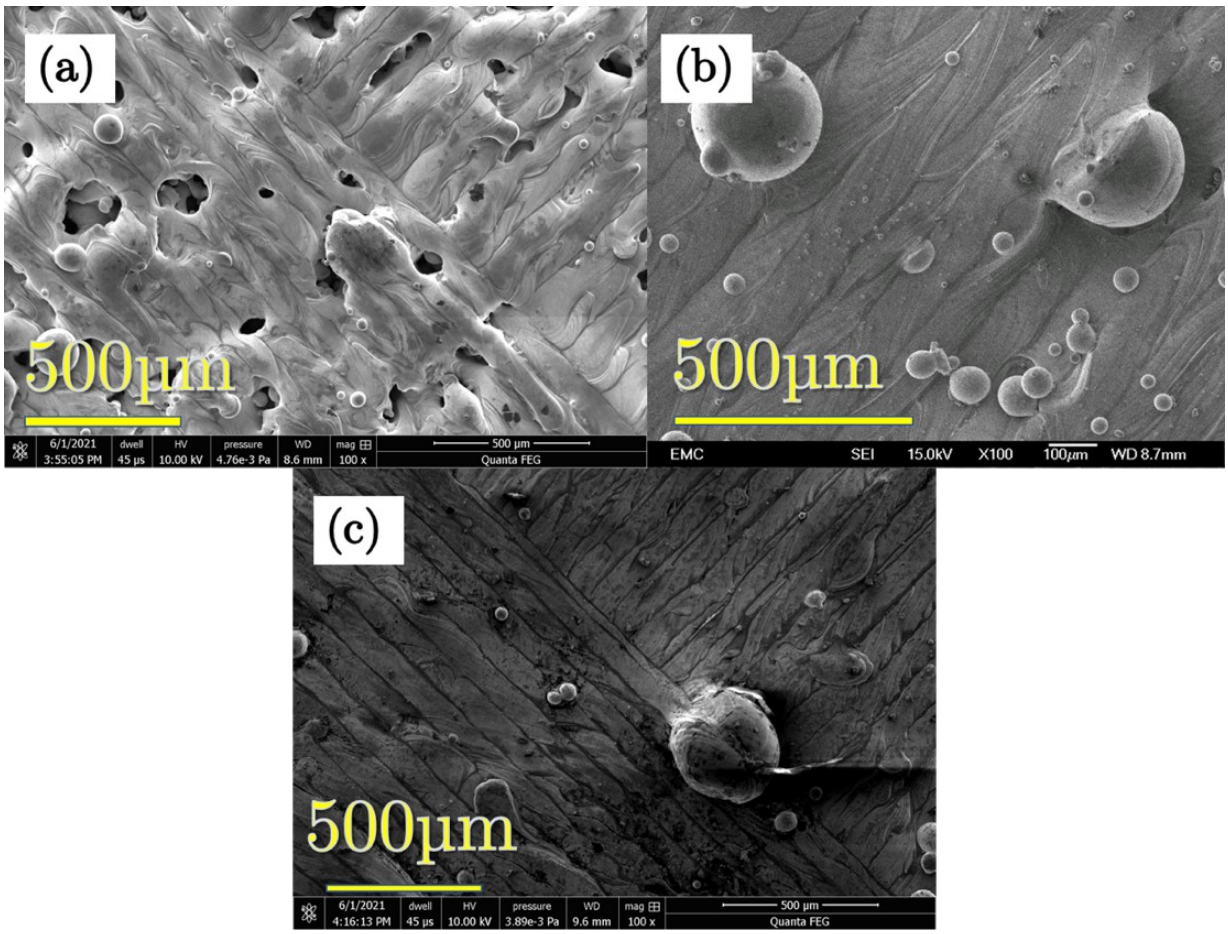

Figure 53: SEM images of the 0° samples (a) sample 10 – 50 J/mm³ (b) sample 2 – 95 J/mm³ and (c) sample 13 – 340 J/mm³

Figure 53(a) shows sample 10 which had a low value of energy density of 50 J/mm³. High amounts of porosity, raw and half-melted powder can clearly be seen on this surface which corresponded to an Sa of 34.42 µm. Figure 53(b) shows sample 2 which had an energy density of 95 J/mm³. Agglomerates and discontinuities in the weld tracks caused by balling can clearly be seen but it had a lower Sa than sample 10 at 27.03 µm. Figure 53(c) is the surface of sample 13 which was produced with a high energy density of 340 J/mm³. Although some agglomerations are on the surface, overall it appears much flatter and more continuous than the other two surfaces and has the lowest Sa of 12.37 µm.

D. Wang *et al.* also described a fourth zone, above 180 J/mm^3 where, because the processing temperature is so high, spattering or powder material loss occurs resulting in an increase in Ra. However, despite going to higher energy densities this was not seen in the experimental results herein. P. Wüst *et al.* also studied the effects of energy density on the Sa of top facing (0°) surfaces of cuboid samples. They varied laser power (200 W – 350 W), scanning speed (300 mm/s – 1400 mm/s) and hatch spacing (0.12 mm – 0.2 mm) while keeping layer thickness constant (50 µm). However, their results are not directly comparable with this thesis or the work of D. Wang *et al.* because they studied Maraging steel. However, the general trends of their results may help to explain some of the trends seen in this thesis. Generally, P. Wüst *et al.* found that, like D. Wang *et al.*, at low values of energy density there was balling and lack of melting which caused high values of Sa. However, they found that Sa only decreased as energy density increased. This was because the underlying solidified material dissipated heat well enough and never reached the temperatures to cause evaporation.

Generally, it has been reported that the surface texture of top surfaces is caused by rippling effects due to surface tension exerting shear forces on the melt pool liquid surface as it cools. These are caused by the temperature gradient between the laser and the solidifying zone of the surface. Mumtaz *et al.* investigated how scanning speed and hatch spacing affected the melt pool dynamics and surface roughness of thin walled Inconel 625 specimens [40]. High energy densities caused by low scanning speeds and low hatch spacing gives the melt pool time for gravity and surface curvature to counteract the thermally induced shear forces allowing them to flatten before solidification, reducing the Ra.

This is equivalent to the high energy density zone (120 J/mm^3 – 180 J/mm^3) described by D. Wang *et al.* and sample 13 of this investigation seen in Figure 52 which had the lowest value of Sa. Sample 13 had a middle value for laser power and low values for scanning speed, layer thickness and hatch spacing which resulted in a high energy density. However low scanning speeds and low hatch spacing also widen and increase the volume of liquid within the melt pool. As a result, the thermal properties

of the melt pool vary, leading to a variation in surface tension which causes balling as the melt pool breaks off into smaller entities to reduce the surface tension differences. These breakoffs solidify at the edge of the melt pool and increase the Ra. This may also explain the balling seen in the middle energy density zone as described by D. Wang *et al.*

90° samples

As seen in Figure 52, the Sa of the 90° samples followed the opposite trend of the 0° samples, increasing in value as energy density increased. P. Wüst *et al.* investigated the relationship between energy density and the Sa of 90° surfaces [173]. These were also for Maraging steel rather than 316L and the 90° surfaces built by P. Wüst *et al.* were built with single scanning tracks, and so hatch spacing was not considered and energy density was measured in J/mm^2 rather than J/mm^3. Thus, the values of energy density that they used are not directly comparable with those seen in this thesis, only general trends.

Similar to what D. Wang *et al.* found for top surfaces, P. Wüst *et al.* found that for 90° surfaces Sa had a parabolic relationship with energy density. Low energy densities caused unstable tracks with lack of melting and balling, and too much energy caused evaporation which led to high Sa values. This parabolic trend was not seen in the results of this thesis. Instead, the Sa of the 90° samples only increased in value as energy density increased. D. Wang *et al.* stated that the reason for low surface roughness at lower energy densities for 90° surfaces was because it encouraged quicker melt pool solidification and minimised the volume of liquid within the melt pool [107]. This in turn causes less thermal variation within the melt pool making them less likely to suffer from balling as there are less thermally induced surface tension forces. At higher energy densities the 90° surfaces are surrounded by raw powder which conducts heat poorly compared with solid material.

Ssk and Sku

Figure 54 shows the relationship between the mean values of Ssk and Sku against energy density for the 0° and 90° samples (45° samples have again been omitted due to

a lack of data). Both texture parameters show identical trends for both build angles. The texture parameters increase with energy density for the 0° samples and show no trend with the 90° samples.

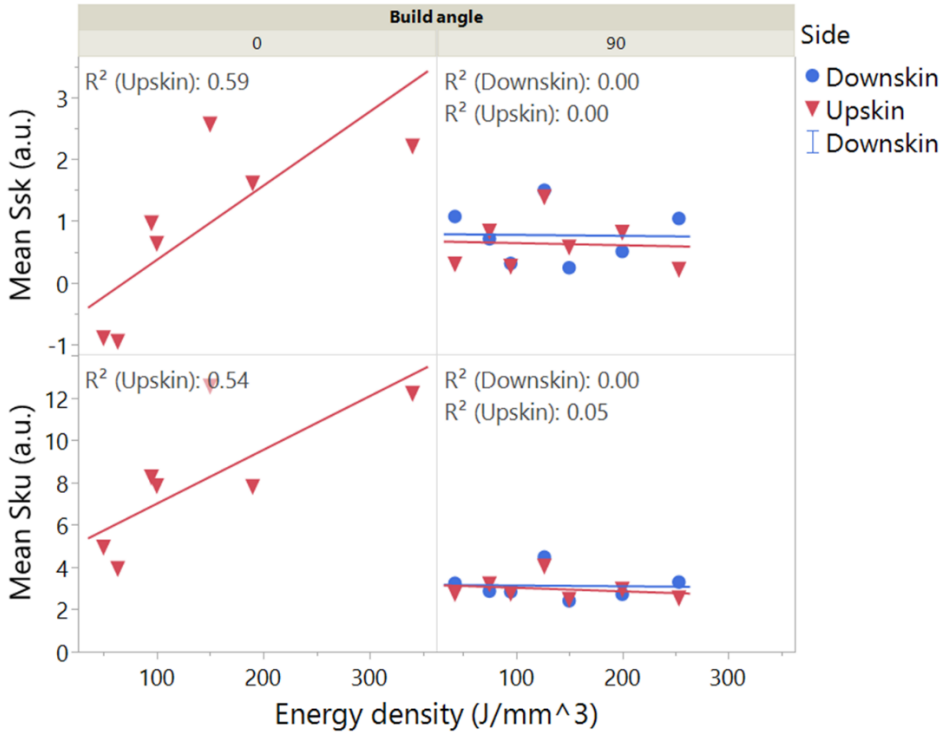

Figure 54: Graphs showing the mean Ssk and Sku vs. Energy density for 90° samples and 0° samples. The samples are split by side (upskin and downskin)

For the 0° samples low energy densities corresponded to lack of fusion and higher numbers of sub-surface pores, which would have a negative skew. Sample 10 which had an Ssk of -0.9 and an energy density of 50 J/mm^3 is an example of this, seen in Figure 53(a.) As energy density increased, samples flattened out, reducing sub-surface pores, and gaining more peaks, increasing the skew. Sample 13 is an example of this seen in Figure 53(c) , with an Ssk of 2.22 and energy density of 340 J/mm^3, For the 90° samples, regardless of energy density samples were dominated by half-melted and agglomerated particles, so their skewness remained constant.

The Sku of the 0° samples was close to Gaussian distribution at low energy densities. As energy density increased, samples became generally flatter with more notable outliers, which increased the Sku. For the 90° samples regardless of the energy density, the particles adhered to the surface resulted in a Gaussian distribution.

5.7. Conclusions

Roughness values were found to change along the length of some samples, possibly due to factors not considered when initially designing the experiment such as position of the parts relative to the gas flow direction within the build chamber. Average surface texture parameters for each sample were used in subsequent analysis to correct for this.

A wide range of surface texture parameters were measured across all seventeen samples. The 90° samples had consistent values on both sides of the samples, covered with half-melted and agglomerated particles that corresponded to positive skew, high values for Sa and Sq and high average surface slope. The 45° samples were very split by side, the upskin surfaces being generally flat with correspondingly low values for all the surface texture parameters while the downskin sides were covered with valleys and half melted particles that corresponded to very negative skew, high average slopes and high Sa and Sq. The 0° samples were only measured on the upskin surfaces because they were removed from the build plate using EDM wire cutting on the downskin side. They were the least homogeneous, having the sample with the lowest value for Sa (90° sample 13) with a very flat surface, and the highest Sa (0° sample 5) which was covered with surface pores.

Statistically significant multiple linear regression models were created for each of the surface texture parameters linking them to the input parameters. Notably although the square of hatch spacing was identified as the most significant input factor for both Sa and Sq, the shape of the response was the opposite to what was commonly reported in the literature. The middle value corresponded to a high value for the texture parameters and because this was only a screening experiment it is not clear exactly why this response shape was seen. For Sa and Sq the 90° samples had a positive correlation with energy density, and the 0° samples a negative correlation. Low energy density reduced balling effects for the 90° samples but corresponded to lack of fusion for the 0° samples. High energy density caused spattering for the 90° samples but flattened the melt pools for the 0° samples.

6. Results and Discussion – Emissivity

6.1. Overview

The previous section looked at surface texture of the different samples, and how these were affected by the input process parameters. This section will build on those results, but also looking at the emissivity of the samples and understanding how the surface texture of the samples affected it. First the results of the experiments done to determine the step length for each steady state emissivity measurement are presented, followed by a discussion on the different techniques used to measure the surface area of the samples. Next a general overview of the data is presented, before discussing the relationships found between emissivity and surface texture and surface area. Attempts are made to explain how physical changes seen on the sample surfaces relate to the emissivity values measured. Finally, multiple linear regression models between the input parameters and emissivity and the input parameters and surface area are presented and discussed.

Emissivity was measured using the calorimetric method taken from the ASTM standard C 835-06 [174]. This involved resistively heating test coupons under vacuum whilst measuring the surface temperature of the sample and enclosure walls. By knowing the power dissipated over a central region of the sample and equating it to the radiative heat transfer to the surroundings, emissivity was calculated using the Stefan-Boltzmann equation, shown in equation [39]

$$\varepsilon = \frac{Q}{\sigma A_1 (T_1^4 - T_2^4)} \qquad [39]$$

6.2. Determination of hold time for input current steps

Before testing could begin in earnest, a series of preliminary tests were performed to determine the minimum time to reach steady state during each step of the test. As stated in the standard, the temperature of the samples needed to be in the steady state condition for the emissivity calculation to be valid. However as experimental time was limited, a balance needed to be found between allowing enough time for samples to reach steady state, but short enough that all samples could be tested in the available time.

As it would take samples the longest time to reach steady state at low temperatures a single sample was heated with low input currents 8 A and 16 A. The temperature and time (t) were recorded and the temperature difference between subsequent time points t(t) and t(t+1) recorded. When this temperature difference (ΔT) first reached 0, the sample was considered to have reached steady state. A graph of the average temperatures of the three thermocouples against time is shown in Figure 55.

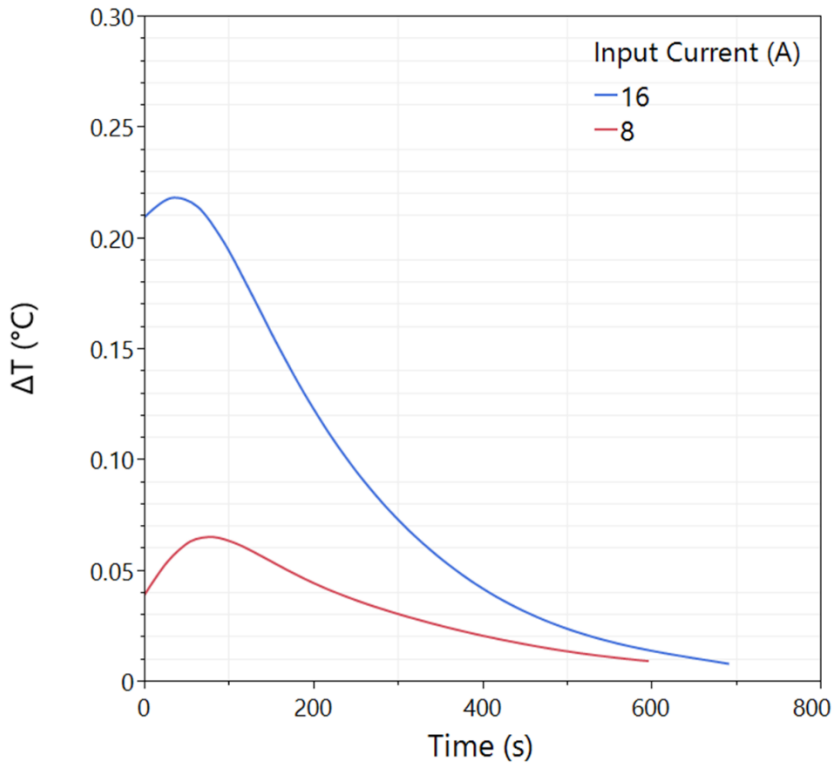

Figure 55: Graph of average temperature difference against time for input currents of 8A and 16A

From Figure 55 for both 8 A and 16 A, the sample appeared to reach steady state at a temperature difference of $\Delta T \cong 0.01°C$ after approximately 600 seconds. However, 600 seconds was deemed to be too long, as this would have resulted in a test time of nearly 2 hours. A second test was run, going from 8 A up to the full 80 A, to determine how long it would take to reach steady state at higher temperatures. The results of this are shown in Figure 56.

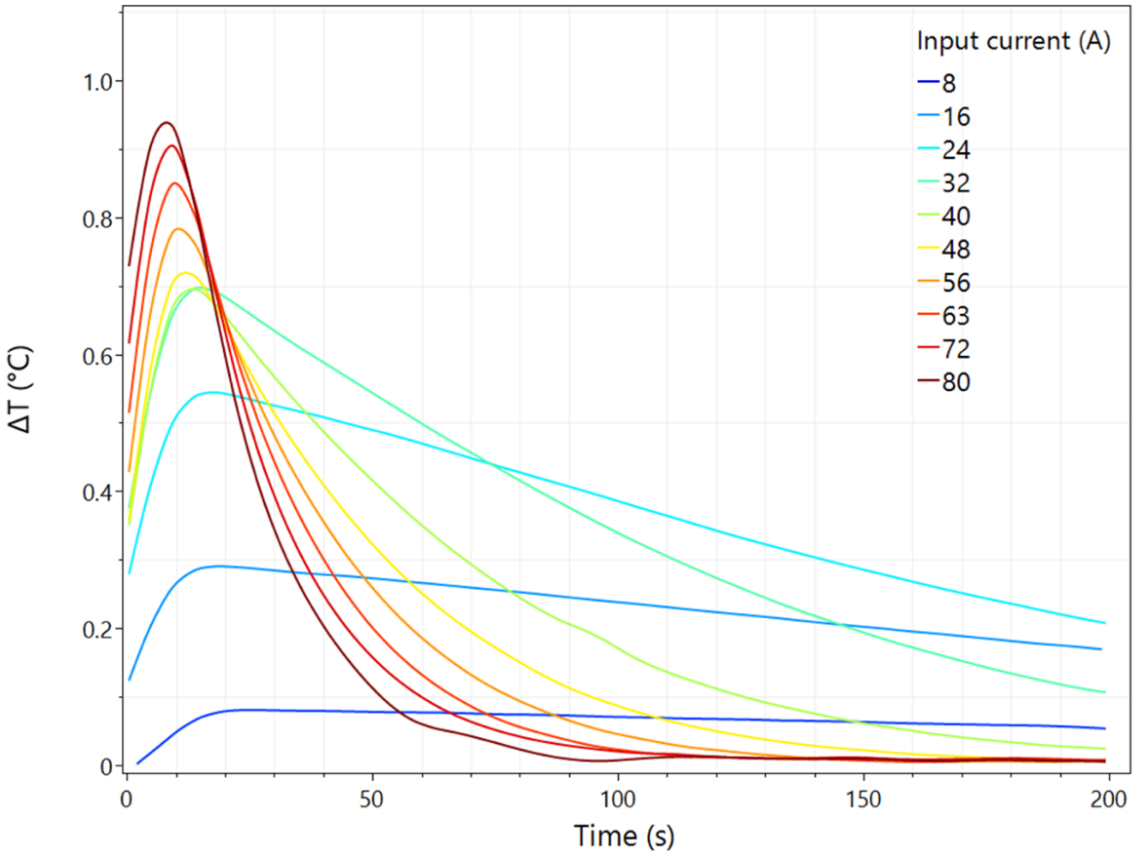

Figure 56: Graph of average temperature difference against time for input currents ranging from 8A to 80A

From Figure 56 as the input current (and thus temperature of the sample) increases, the time taken for the sample to reach steady state conditions decreases. Given the motivation of this work by STAR resistojet applications, high temperature values were of greater interest than low temperatures. Priority was given to a test time that would ensure steady state conditions at higher temperatures whilst allowing for a reasonable test duration. From 40 A and above it took approximately 200 seconds for the temperature to reach steady state conditions ($\Delta T \cong 0.01°C$ or less) for each input current.

Table 21: Table showing the average temperatures and emissivity values at 200s and 600s for 8A and 16A current inputs

Current (A)	Time (s)	Average temperature (K)	Emissivity (a.u)
8	200	336.1	0.41
	600	347.7	0.30
16	200	387.1	0.53
	600	417.3	0.35

Table 21 shows a comparison of the average temperatures and emissivity reached at 200 seconds and 600 seconds for both 8 A and 16 A input currents. At an input current of 8 A, the temperature difference is approximately 3% and at 16 A is approximately 7%. These appear to be small differences, but as shown in Table 21 emissivity values are significantly higher when the temperature has not reached steady state. If the emissivity values calculated at 600 s are taken as steady state conditions (based on the results of Figure 55), there was a roughly 31% difference between the 200 s and 600 s emissivity values at 8 A and a 41% difference for the values at 16 A. These are significant errors in emissivity. The change in temperature ΔT was calculated for each of the seventeen tested samples and the values of emissivity calculated before the sample reached steady state (determined when $\Delta T = 0.01$ °C or less) have been omitted when discussing the emissivity of the samples. Emissivity at high temperatures is relevant for STAR resistojet applications. If of interest, future work could consider low temperature emissivity measurements by allowing more time to reach steady state.

6.3. Overview of data – surface area

Accurate measurement of the emissive surface area, equivalent to A_1 in equations [10] and [12], is important to calculating the emissivity. The standard on which these tests were based recommended measuring the surface area using nominal dimensions from callipers, with a resolution of 0.025 mm. However, this standard was not intended for AM surfaces which, as discussed in section 5 can have re-entrant features or pores which increase the surface area but would not be captured by the nominal dimensions from callipers. For example, the average diameter of the powder used to build the parts

was measured as approximately 18 µm. To overcome this limitation the surface area of the samples was also determined using by X-ray CT scanning and image analysis, as detailed in section 4.4. Depending on the machine used, the X-ray CT scans were able to capture a resolution between 5 µm – 7.5 µm A summary of the results of the surface area determination are detailed in this section.

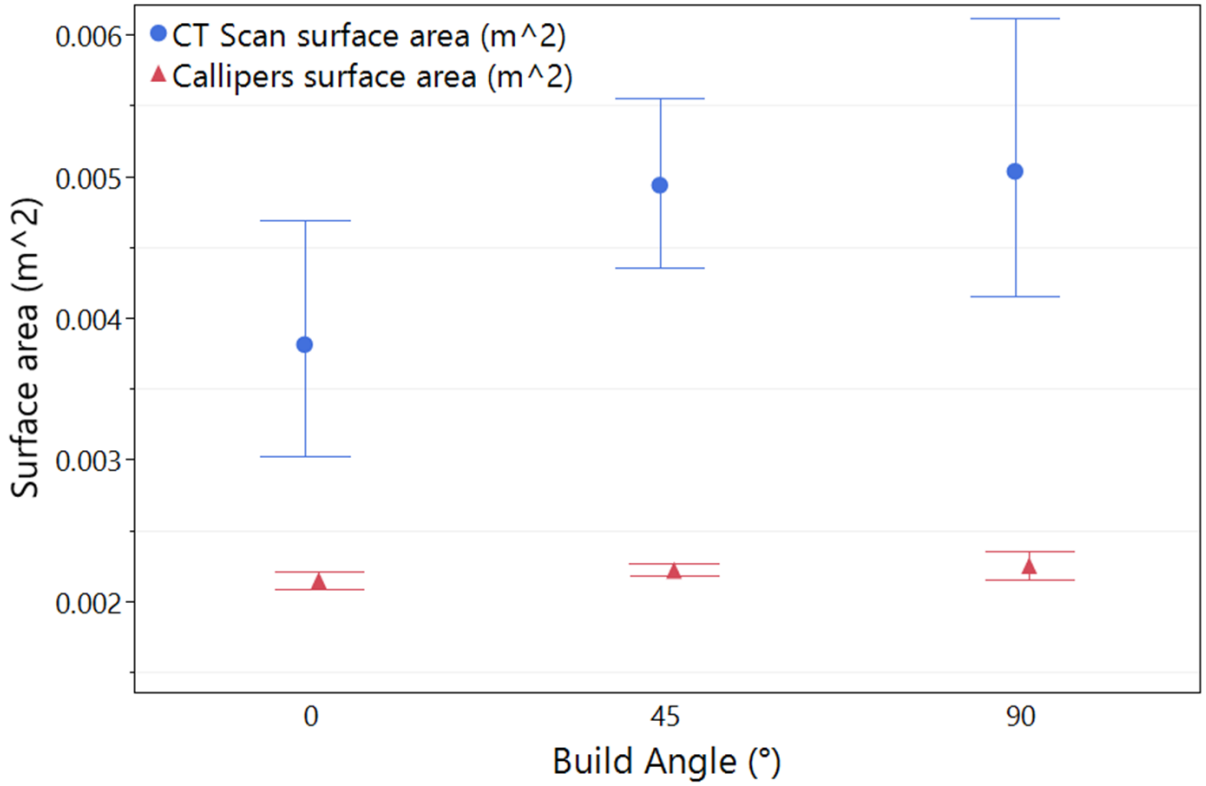

Figure 57: Plot showing the mean values of the surface area of the samples separated by build angle as determined by CT measurement and callipers. The bars on each point correspond to the range of values measured for each build angle

Figure 57 shows a plot of the mean values of the surface areas of each of the samples calculated by either CT measurement or callipers, separated by build angle. The bars on each point represent the range of values measured for each build angle. The calliper determined areas are much lower than the CT surface areas. The largest calliper surface area was a 90° sample with a value of 0.0024 m^2, which was less than the smallest CT surface area of a 0° sample with a value of 0.003 m^2, as expected due to re-entrant features or pores that wouldn't be able to be captured by the flat surface of the callipers.

The overall trends of data between the CT measured surface area and calliper surface area are however similar. For both measurement techniques, the 0° samples generally have the lowest surface areas (calliper area has a mean of 0.0021 m^2 and CT area has a mean on 0.0038 m^2), while the 90° and 45° samples have similar means and cover similar ranges of values. In both, however there are outlier values of the 90° samples.

Because the 0° samples were removed from the build plate using EDM wire cutting, the downskin wire cut sides had significantly lower roughness and an overall smoother surface compared to the upskin side lowering the overall surface area. Despite the similar overall ranges of surface area between the two measurement techniques, the trends of individual samples vary between the two. The 90° sample 1 has the highest surface area when measured using CT scanning (0.0061 m^2), but it is amongst the lower surface areas for the 90° samples when measured using callipers (0.0022 m^2). Most of the surface area is from re-entrant features which could not be captured by callipers. For callipers, surface area would have been mostly influenced by the overall width and average thickness.

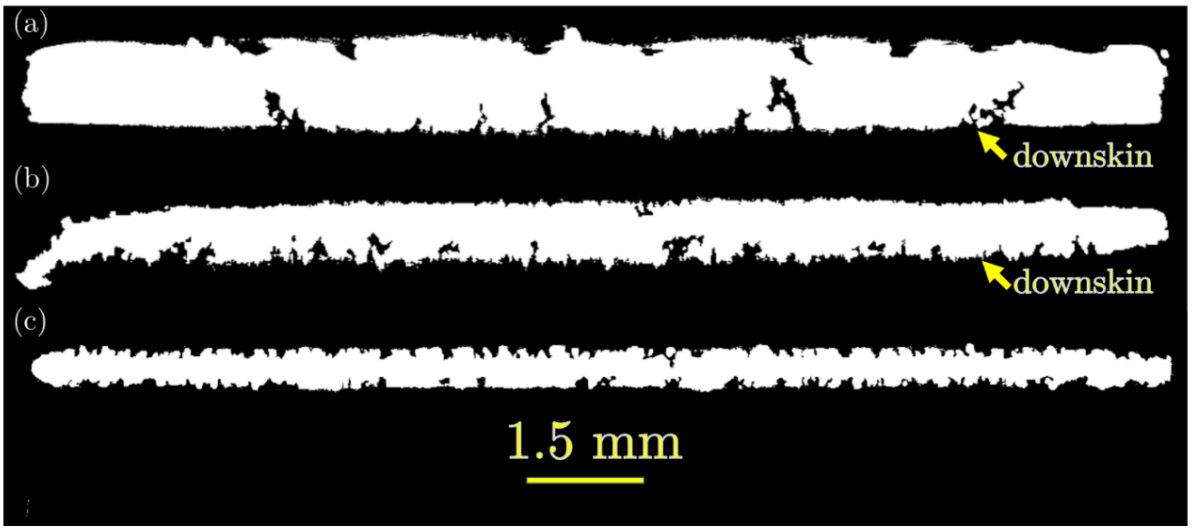

Figure 58: Image processed CT scans showing cross sections of (a) 0° sample 5 (b) 45° sample 7 and (c) 90° sample 4

Figure 58 shows CT scans of 0°, 45° and 90° samples after image processing has been done to remove internal porosity, as described in section 0. From these scan images the physical features on each sample that caused the differences in surface area

can be seen. The downskin surfaces of Figure 58(a) and (b) are labelled on the image. For the 0° sample in Figure 58(a) the downskin (EDM cut) surface is significantly smoother and less tortuous than the upskin surface. The opposite is true for the 45° sample in Figure 58(b) as the upskin surface is significantly smoother than the downskin surface. Reasons for this difference in surface texture have previously been described in section 5.4

Given how the 45° samples have one smooth side and one rough side, it was expected for them to generally have smaller surface areas compared to the 90° samples that are rough on both sides. Instead, they cover a similar range of surface areas as the 90° samples. There are a few possible explanations for this. While the upskin surface of the 45° samples may appear relatively smooth from Figure 58(b), SEM image analysis and roughness measurements detail otherwise. The upskin surfaces contain ridges due to the stair-step effect, along which are balling and half melted particles which may have contributed to increasing the surface area. The high surface area of the 90° samples was due to the large numbers of partially melted particles stuck to the surfaces of the samples. The downskin 45° samples were also covered in part melted particles, but also had many valleys, as indicated by the negatively skewed Ssk results of the roughness measurements seen in section 5.4.2. This may have led to larger surface areas than just the half-melted particles alone. When combined with the features on the upskin side, this may have led to similar surface areas to the 90° samples. Overall, despite showing similar trends CT scans and image analysis more accurately captured surface areas than the calliper measurements.

6.4. Overview of data – emissivity

Figure 59 shows the emissivity of all seventeen samples, calculated using surface area determined either by CT measurement or by callipers, each plotted against temperature. Samples are split by build angle and labelled by sample number. Sample number corresponds to the set of process parameters used to build the sample and are detailed in Table 15.

The error bars were determined using the methods detailed in section 4.3. and correspond to the instrument uncertainty which was the largest uncertainty.

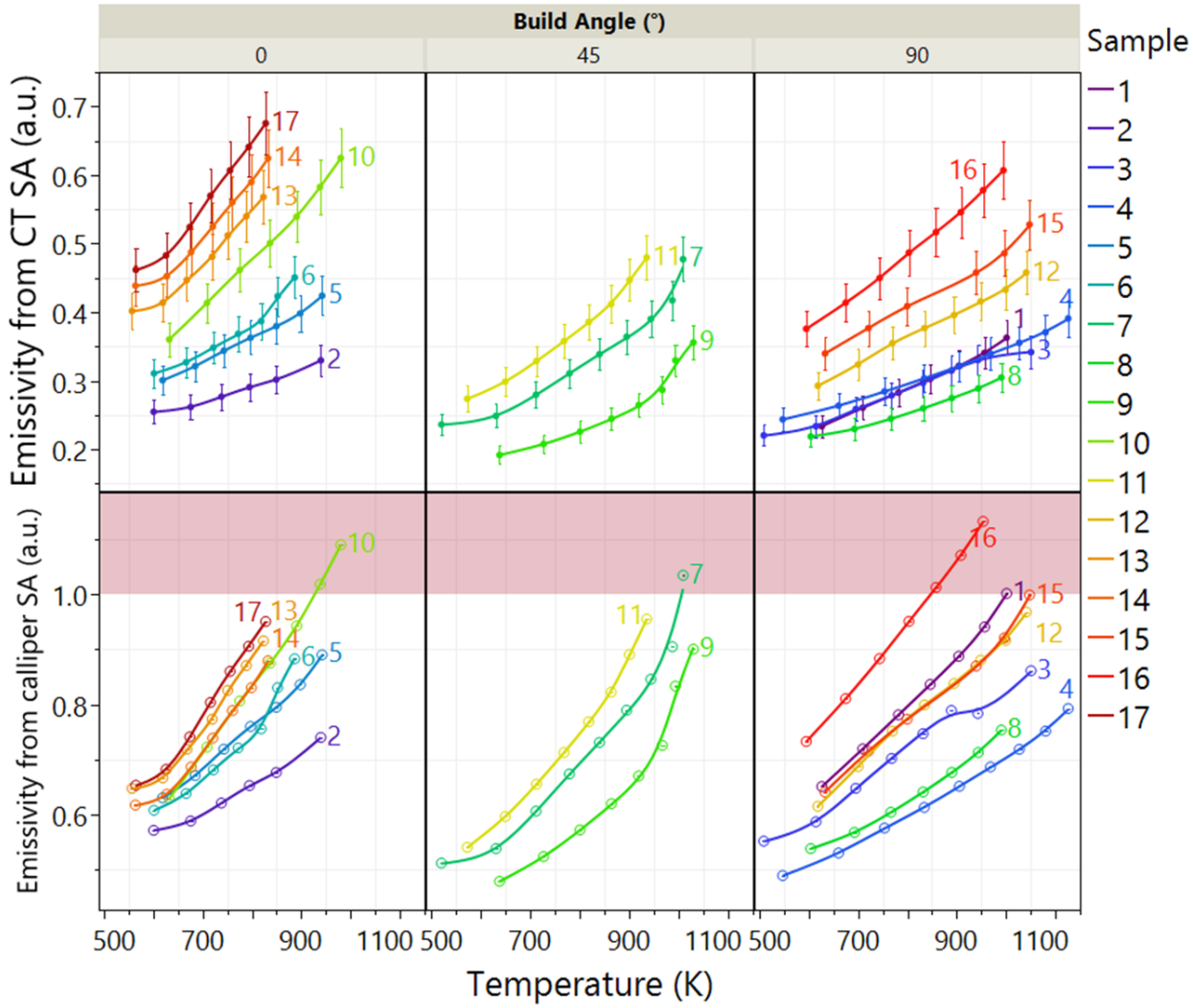

Figure 59: Plots showing the emissivity vs. temperature of all the samples, with surface area determined by both CT and callipers, with non-steady state points at lower temperatures removed. Samples are coloured and labelled by sample number. The red band details the emissivity values. Error bars correspond to instrument uncertainty.

In Figure 59 for all samples as the temperature increases so does the emissivity which was expected given the discussion of emissive power in section 2.3. While trends and temperature ranges of individual samples appear to be similar for both CT and calliper emissivity values, the emissivity ranges are very different between the two methods. The calliper emissivity values, considering all temperatures and samples, covered a range from 0.48 to 1.13. The CT emissivity values covered a much lower range from 0.19 to 0.68. The calliper emissivity values for samples 7, 10 and 16 have

values over 1 which are impossible as that would mean they have a greater emissivity than a blackbody. These unrealistically high values for emissivity are likely attributable to the low surface area measured by callipers and inaccurate representation of the emissive surface area. The fact that these values were impossibly high likely indicates that none of the emissivity values determined using callipers are accurate for the AM surfaces. Going forward, this chapter will focus on emissivity results obtained using CT measurements, unless otherwise stated.

For the CT determined emissivity values, considering all temperatures and samples, both the 0° and 90° samples covered an emissivity range of approximately 0.4. The emissivity values covered by the 0° samples were slightly higher, ranging from 0.26 to 0.68 while the 90° samples ranged from 0.21 to 0.61. The majority of 0° samples reached higher values of emissivity compared to the 90° samples. The 45° samples covered a slightly smaller range of approximately 0.3, varying from 0.19 to 0.48, however they also had fewer data points as there were only three 45° samples. Most emissivity values fall within the range 0.20 to 0.45 which covers the majority of datapoints for the 90° and 45° samples.

Even though the 0° samples reached the highest emissivity values, they also covered the smallest temperature range, with no sample reaching above 950 K. The 45° and 90° samples covered similar temperature ranges, although the 90° sample, sample 4, reached the highest temperature of any of the samples at 1126 K and an emissivity of 0.39. The CT determined emissivity values are compared against values for cast 316L of different roughness and temperature by Hunnewell *et al.* in Figure 60 [120].

Generally, the cast samples covered a range of emissivity from 0.25 to 0.47 which was similar to the range covered by most of the 90° and 45° SLM sample measured in this thesis. However, the SLM samples reached greater extremes with 45° and 90° samples generally having lower values of emissivity at lower temperatures and the 0° samples reaching higher maximum emissivity values. It should be noted that the cast samples all had much lower emissive surface areas than the SLM samples, with a

maximum area of 1.68×10^{-6} m^2. Apart from the as-received cast sample, the emissivity of the cast samples decreased with increasing surface area. The relationship between surface area and emissivity will be discussed in section 6.6 of this chapter.

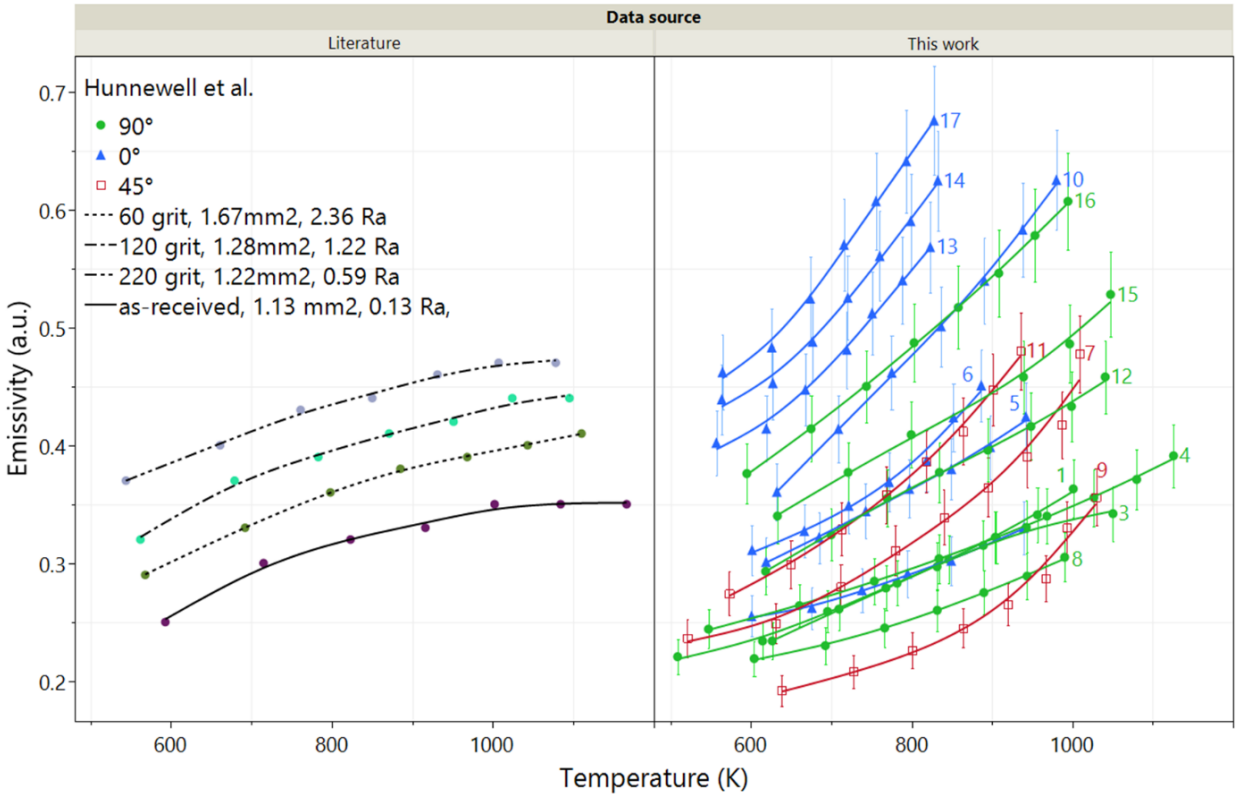

Figure 60: Plot comparing the CT determined emissivity values (coloured by build angle and labelled by sample number) against emissivity values for cast 316L roughened by different grits by Hunnewell *et al.* [120] Error bars correspond to instrument uncertainty.

The cast sample with the highest Ra and surface area has the second lowest emissivity only above the as-received sample. Instead the sample roughened by the highest grit has the highest emissivity which was explained as having a surface that produced the highest number of internal reflections [120]. This is surprising as other literature sources found strong correlations between Ra and emissivity. The differences in emissivity between the SLM samples built at different build angles can be explained by the differences in physical characteristics of the sample surfaces. These will be discussed in the next section.

6.5. Surface texture and emissivity

6.5.1. Overview

Emissivity is a surface phenomenon and is greatly affected by the topography of a surface. When considering roughness on a similar length scale to the wavelengths of thermal radiation, the relationship between physical features on a surface and emissivity is determined by the number of reflections a ray of light undergoes before leaving a surface. The greater the number of reflections, the greater the absorptivity and thus emissivity according to Kirchhoff's law. Surface texture is often used to quantify the topography of a surface and the relationship between physical features on a surface and emissivity. A commonly used texture parameter related to emissivity is Ra, a measure of the average absolute deviation of a surface from a mean line over an evaluation length.

Generally, as discussed in section 2.3, as Ra increases so does emissivity at any temperature. However for metal SLM surfaces, specifically 316 stainless steel, S. Taylor *et al.* found that Ra alone is a poor link between surface texture and emissivity [60]. This was reportedly because the irregularity of AM surfaces could lead to similar values for Ra but correspond to different physical features and thus different emissivity. A similar lack of consistency for Sa was found between the samples produced as part of this thesis, as reported in section 5.4.1. Instead, S. Taylor *et al.* said valley angle was the most important factor between surface features and emissivity, rather than just the height of the features, as angle is what determined internal reflections [60]. The product of root mean square slope and average absolute height (Ra×Rdq) reportedly had the strongest correlation to emissivity. This was considered when designing the experiments of this thesis and resulted in choosing the five different surface texture parameters: Sa, Sq, Ssk, Sku, and Sdq. These were chosen as it was believed they could capture more information about SLM surfaces than just Sa alone. The physical meaning behind each of these parameters has been previously described in section 2.2. It should be noted that, while profile and surface texture parameters are not directly comparable, they should still reveal similar trends [48].

6.5.2. Individual surface texture parameter correlations

The previous chapter 5 detailed how the surface texture parameters varied for each sample, and how the upskin or downskin side significantly influenced the roughness. The calorimetric method measures emissivity based on the temperature of an emitting surface area. However the thickness of the samples was not large enough for there to be a notable temperature gradient, and so the temperature measured on the samples was uniform across the sample (as required by the standard [146]). Thus, the emissivity measured was the average emissivity over the entire emissive surface area which included both sides of the samples. Thus, combined average values of both the upskin and downskin surface texture parameters were used when discussing the relationship between surface texture and emissivity.

Figure 61 shows a plot of emissivity determined using CT scanning surface areas against the average Sa for all seventeen samples, coloured by build angle. S. Taylor *et al.* demonstrated that quadratic fits match well when describing the relationship between emissivity and surface texture parameters [60]. As a result, quadratic fits were also used in this work. However even when using linear fits, the R^2 values were very similar. Each vertical column of points in Figure 60 represents a single sample, the different points corresponding to increasing temperatures

The low coefficient of determination for the quadratic fit in Figure 61 ($R^2 = 0.08$) indicates a lack of strong correlation between emissivity and Sa. Even when separated by build angle, the 0°, 45° and 90° samples only had R^2 values of 0.14, 0.31 and 0.27 respectively. The results in Figure 61 are convoluted with temperature. To compare at specific temperatures, the emissivity values as functions of temperature were fitted using quadratic equations for each specimen, in order to enable isothermal comparison of emissivity across samples (since heat input was controlled in emissivity tests for each sample, not temperature directly). An example of this is shown in Figure 62 for sample 8, where the linear fit is in blue and the quadratic fit is in red.

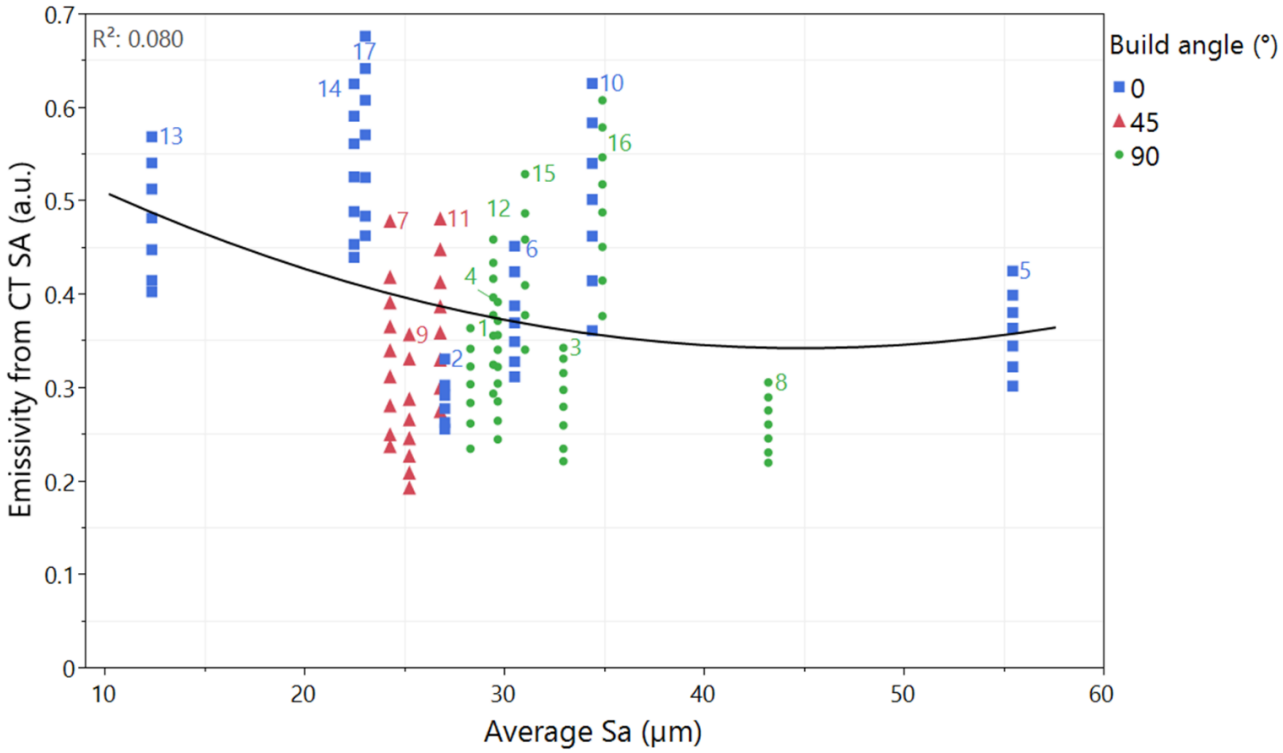

Figure 61: Plot showing emissivity determined using CT measurements against average Sa for all 17 samples, coloured by build angle

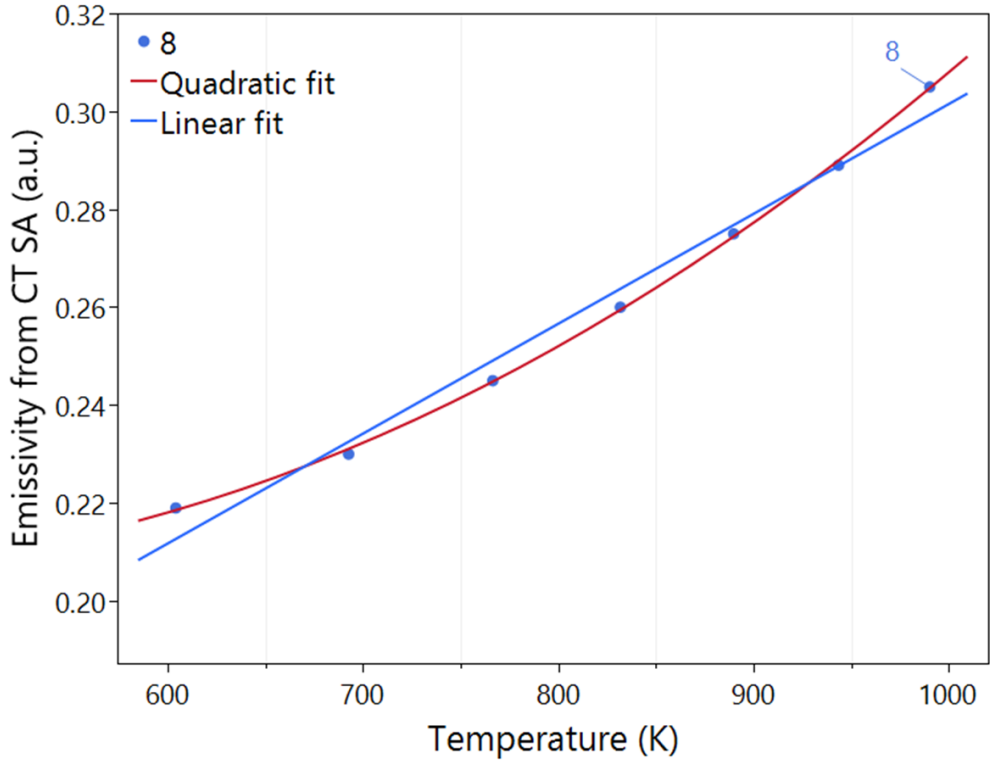

Figure 62: Plot showing emissivity against temperature for the 90° sample 8, with a linear fit in blue and a quadratic fit in red

The quadratic fit has an R^2 value of 0.99 compared to 0.981 of the linear fit. Emissivity values at specific temperatures were interpolated using quadratic fits for all the samples, as shown in Figure 63 for temperatures of 500, 700, 900, and 1000 K.

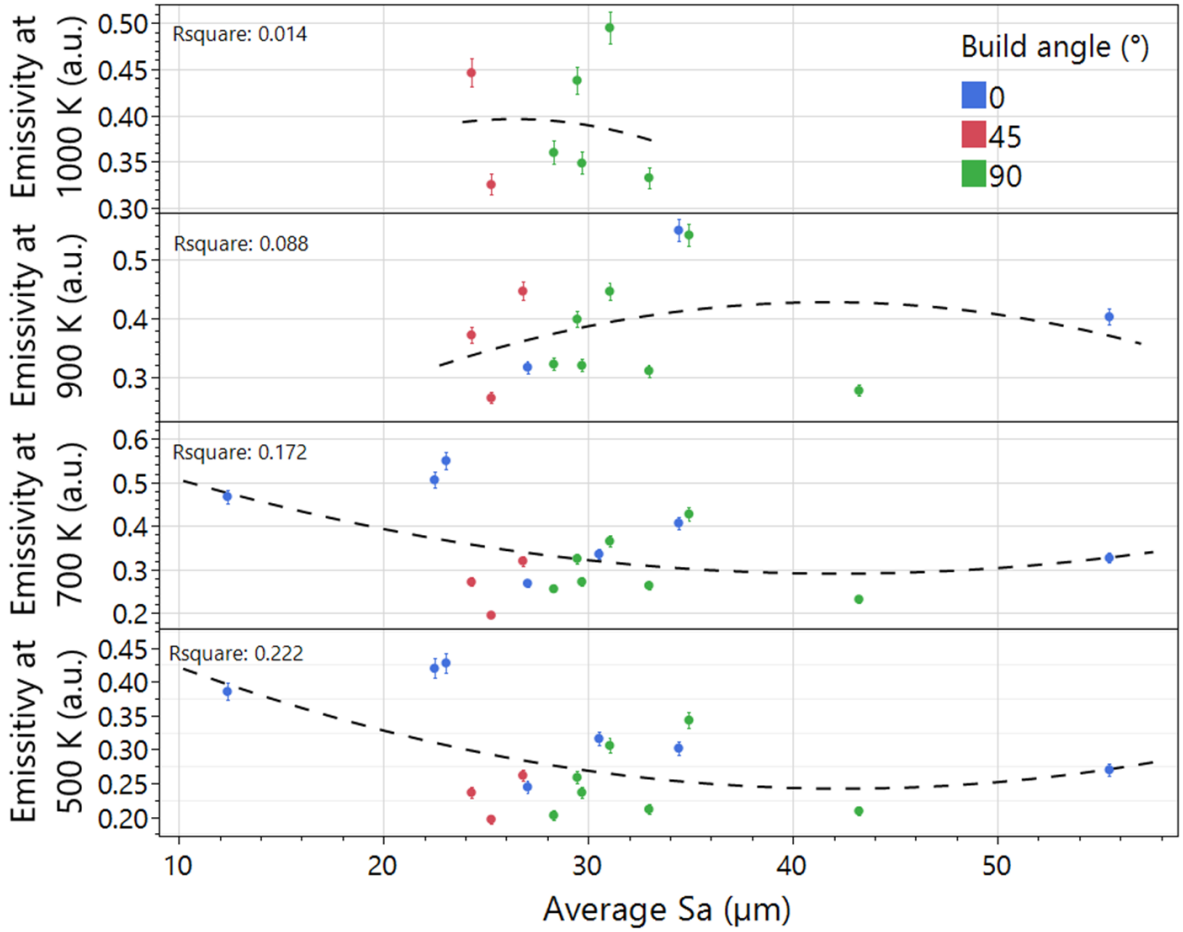

Figure 63: Plot showing interpolated emissivity values for all seventeen samples at 500K, 700K, 900K and 1000K against average Sa. The trends are shown using quadratic fits. Error bars correspond to instrument uncertainty.

Even when separated along isotherms, the trend of emissivity with average Sa appears weak at each temperature in Figure 63. The plot of emissivity at 500 K has the highest R^2 value at only 0.22. As previously discussed in section 5.4.1 and as mentioned by S. Taylor *et al.* [60], because Sa is only a measure of the average absolute height deviation, different samples can have similar values but vastly different physical features. Sa alone appears to be a poor indicator of the type of surface that will produce multiple internal reflections.

While only plots for Sa have been shown here, similar analysis was done for all the different texture parameters. Table 22 shows the R^2 values for the quadratic fits

of emissivity against each of the texture parameters at all measured temperatures. It must be noted that R^2 is not an absolute measure of the quality of the data and does not consider things such as lack of data points which may skew results. However, it is a useful tool to generally compare correlations.

Table 22: Table showing the R^2 values for all the different texture parameters against emissivity for all the samples at different temperatures

Texture Parameter	R^2 value				
	Overall	500 K	700 K	900 K	1000 K
Sa	0.08	0.225	0.176	0.09	0.012
Sq	0.055	0.128	0.106	0.068	0.144
Ssk	0.041	0.137	0.075	0.276	0.175
Sku	0.069	0.253	0.153	0.011	0.628
Sdq	0.14	0.414	0.309	0.045	0.069

Table 22 shows that generally, none of the texture parameters correlated strongly with emissivity at any temperature. The only notable exception to this is Sku at 1000 K, the only parameter to have an R^2 value above 0.5. This plot is shown in Figure 64. This trend is skewed by the Sku of the 45° sample 7 that has a value of 7.8. There is not enough data at this temperature to make strong conclusions about the trend seen.

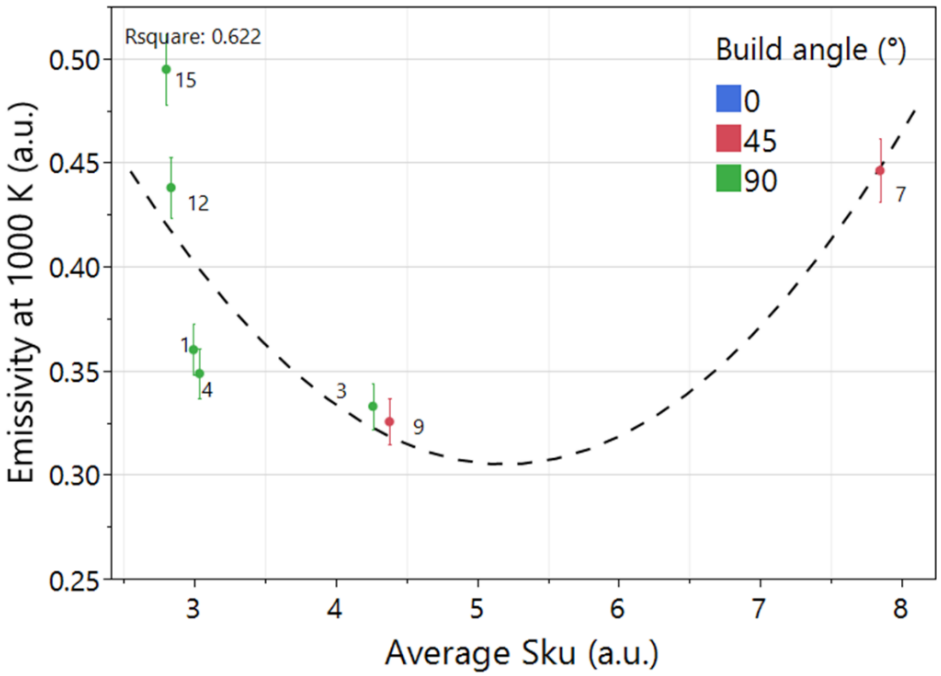

Figure 64: Plot showing the interpolated emissivity at 1000 K against the average Sku. Points are coloured by build angle. Error bars correspond to instrument uncertainty.

Variation of trends with temperature may be due to other factors that affect emissivity that have not been considered here. These may include changes to the surface composition, such as whether the samples have oxidised at higher temperatures or changes to the microstructure which might have affected the amount of energy absorbed by the samples.

6.5.3. Limitations of Focus Variation Microscopy

No single surface texture parameter considered in this study (Sa, Sq, Ssk, Sku and Sdq) correlated strongly with the CT determined emissivity regardless of temperature or build angle. Generally, this is contrary to what has been reported in literature which saw emissivity increasing with surface texture parameters, specifically Ra and Rdq.

This may be due to the limitations of focus variation microscopy (FVM) which was used to capture the surface texture parameters. As previously discussed FVM is an optical measurement technique that relies on contrast between neighbouring pixels to generate topographical information. As such FVM can struggle with regions that are overly dark or bright [169], [175]. Such regions can include recesses and re-entrant features due to either a lack of or multiple reflections of light. However, these reasons that make such features difficult to capture by FVM are also likely to increase the emissivity of the samples. The SEM images of the sample surfaces shown in section 5.4 and the CT micrographs in Figure 58 demonstrated that many of the samples have recesses and re-entrant features. Thus, if FVM was unable to capture such features accurately in the texture parameters they may not represent the resultant emissivity values of the samples. Zhu *et al.* stated that X-ray CT (XCT) may be better at capturing re-entrant features than FVM for AM surfaces [169]. W. Liu *et al.* did a study comparing measurements of the surface texture parameters Sa, Sq, Ssk and Sku using FVM and X-ray CT (XCT) on the top surfaces (equivalent to 0° in this work) of cuboids of Ti-6Al-4V [175]. For the FVM they used the same microscope and similar measurement settings to this work, although they did not give the L-filter they used and measured generally lower values for the texture parameters compared to the 0°

samples in this thesis (a maximum Sa of 7.15 µm). While they did note specifically that FVM had difficulty in measuring re-entrant features that XCT did not, the measured differences between the texture parameters for the two techniques were small—maximum difference of approximately 1 µm was reported between the two techniques for Sa, Sq, Ssk and Sku. Further work would be required to see if this trend still holds for the higher areal texture parameter values seen in this thesis.

There are other factors with the FVM measurement setup that need to be considered. FVM measures sample topography from directly above and so may not have been able to accurately capture shadowed regions. As previously discussed in section 2.2, measurement settings are known to influence the accuracy of FVM texture parameter measurements. Literature sources highlighted illumination, and lateral resolution in particular, as responsible for the contrast on surfaces and the resolution of the minimum feature size respectively [100], [175]. Co-axial illumination was used in this thesis because it was reported to produce a lower number of missed points for 90° surfaces. However at 10× magnification it may have caused higher than actual Sa values [48]. A lateral resolution of 8 µm was used. Although initially it was believed to be suitable because it was lower than the expected minimum feature size, it may have had a smoothing effect and led to erroneous values for the texture parameters [175]. However, thorough studies by L. Newton *et al.* and W. Liu *et al.* showed that variation in illumination, vertical and lateral resolution had minimal effects on Sa, Sq, Ssk and Sku values [48], [175]. L. Newton *et al.* studied the effect of varying magnification, illumination type, lateral and vertical resolutions on the top and side surfaces (equivalent to 0° and 90° in this thesis respectively) of Al-Si-10Mg, Inconel 718 and Ti-6Al-4V cuboids manufactured using SLM. They used the same microscope (an Alicona Infinite Focus) and similar ranges of measurement settings as used in the work presented herein. The ranges of Sa values they measured (e.g., 0° Ti-6Al-4V from 33.9 µm – 34.1 µm, 90° Ti-6Al-4V from 25.7 µm – 26.6 µm) were similar to this work (mean Sa of 0° was 30.4 µm and for 90° was 32.8 µm). Overall, they found that variations produced at most a 5% difference in Sa values. W. Liu *et al.* found at most an increase

of 10% in Ssk values when using coaxial rather than ring illumination. The variation of all other texture parameters was less than 5%. However, as previously stated, the ranges of the texture parameters W. Liu *et al.* measured were less than seen in this thesis. While non-ideal measurement settings may have been used in this work, they likely had a small effect on the values of the texture parameters.

6.5.4. Product surface texture parameter correlations

Another factor that could have affected the results is that AM surfaces are too complex to be accurately captured by single surface texture parameters. Surface texture parameters were originally intended for cast or machined surfaces and are meant to represent periodic displacements of the surface, such as cuts or grooves. As shown in section 4.7.2 metal AM surfaces are very irregular. Single texture parameters can be applied to a variety of different structures. For example, surface slopes can be represented by features such as pores, surfaces of half-melted and agglomerated particles or ridges due to the stair-step effect. Each of these may result in similar values for Sdq but cause different amounts of internal reflections. It may be that the types of surface variation that surface texture parameters were intended to describe are too broad to describe the kinds of features seen in SLM surfaces. S. Taylor *et al.* came to a similar conclusion about Ra, as surfaces could have the same Ra value but different shapes [60].

The roughness results chapter showed that no single texture parameter gave enough information to describe the variety of features seen on the surfaces in the SEM images. Surfaces were best described when using multiple texture parameters. The results in section 6.5.2 seem to show the same result, that no single texture parameter correlates well with emissivity. Instead, combinations of parameters may work better. As previously stated, S. Taylor *et al.* found that the product of Ra and Rdq showed the strongest correlation between emissivity and build angle for SLM 316L stainless steel [60]. This was reportedly because it was indicative of surface shapes that produce the Mendenhall wedge effect where a steeper and taller structures result in a greater number of internal reflections [114]. Figure 65 shows a plot of the emissivity values

against the product of the average Sa and average Sdq values at all measured temperatures, while Figure 66 shows the interpolated emissivity values along specific isotherms.

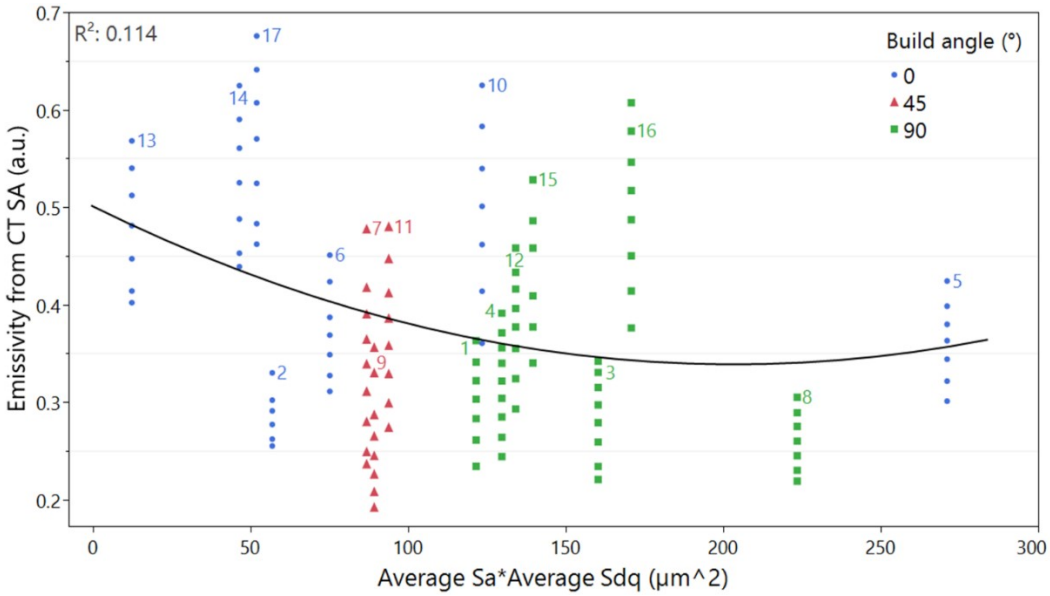

Figure 65: Plot of CT determined emissivity against the product of Average Sa and Average Sdq. Points are coloured by build angle

Although S. Taylor *et al.* reported that this showed a stronger correlation with emissivity, the plots in Figure 65 and Figure 66 have lower R^2 values than Sdq against emissivity both overall and at every isotherm as can be seen in Table 22. It is worth noting that S. Taylor *et al.* only studied emissivity at room temperature while the results presented in Figure 66 only begin at 500 K due to previously discussed issues with steady state measurements at lower temperatures. While these trends would be expected to hold true at lower temperatures because there should be no change to the physical surface, the R^2 values in Table 23 do change with temperature indicating that there may be another factor other than surface texture that is influencing the roughness at different temperatures such as changes to the surface composition. Further work would be required to investigate this fully and compare with the room temperature work of S. Taylor *et al.* Similar analysis was done for all the different surface texture parameter combinations. Table 23 shows the R^2 values for the quadratic fits of the emissivity interpolated at specific temperature against the products of the different texture parameters.

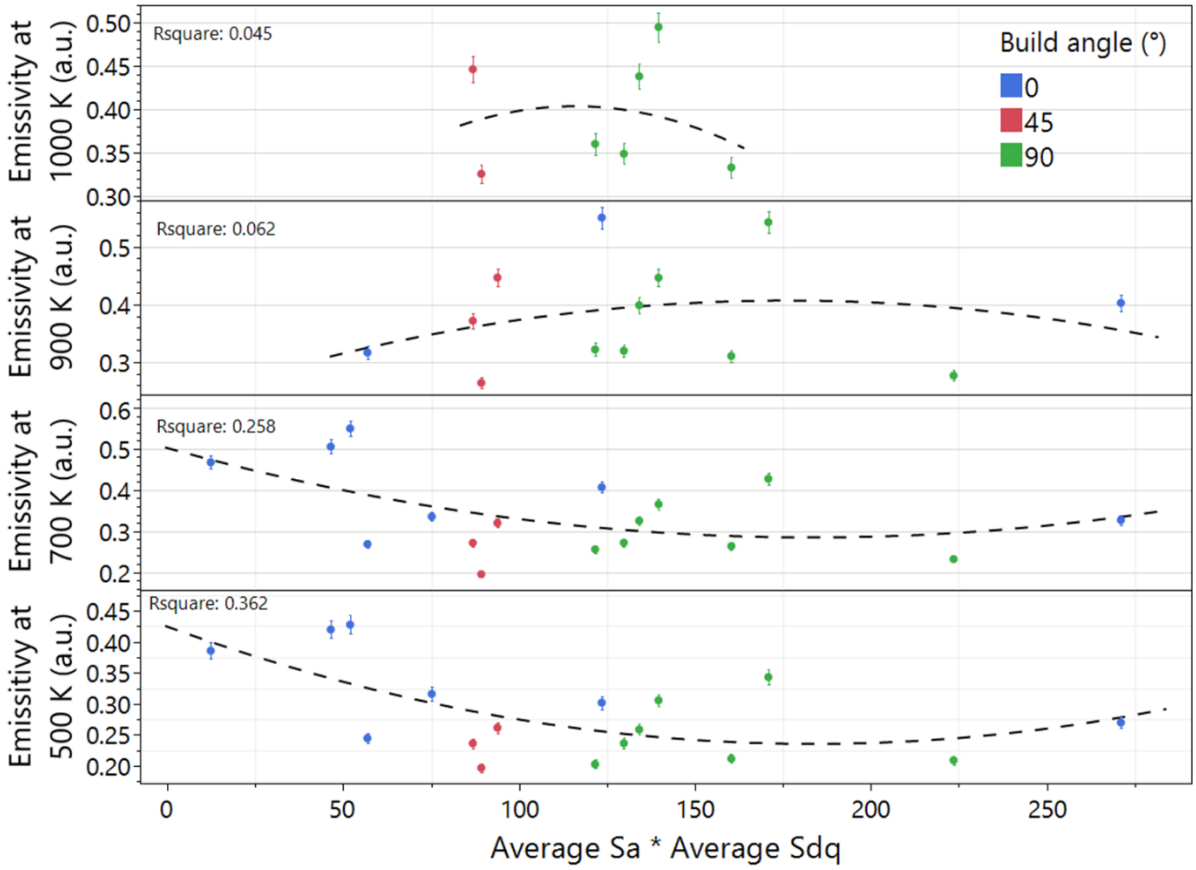

Figure 66: Plot showing interpolated emissivity values for all the samples at different temperatures against average Sa*average Sdq. Error bars correspond to instrument uncertainty.

Table 23: Table showing the R^2 values for all the different texture parameter products against emissivity for all the samples at different temperatures

Surface texture product	R^2 value			
	500 K	700 K	900 K	1000 K
Sa*Sq	0.147	0.116	0.05	0.082
Sa*Ssk	0.006	0.003	0.269	0.187
Sa*Sku	0.08	0.063	0.009	0.524
Sa*Sdq	0.362	0.258	0.062	0.045
Sq*Ssk	0.017	0.001	0.271	0.178
Sq*Sku	0.122	0.095	0.003	0.538
Sq*Sdq	0.343	0.251	0.065	0.119
Ssk*Sku	0.163	0.07	0.275	0.016
Ssk*Sdq	0.039	0.049	0.221	0.187
Sku*Sdq	0.015	0.021	0.022	0.536

Of the different product combinations shown in Table 23 only three have R^2 values greater than 0.5, all of which occur at a temperature of 1000 K and all of which involve the surface texture parameter Sku. Plots of these surface texture products against emissivity at 1000 K are shown in Figure 67.

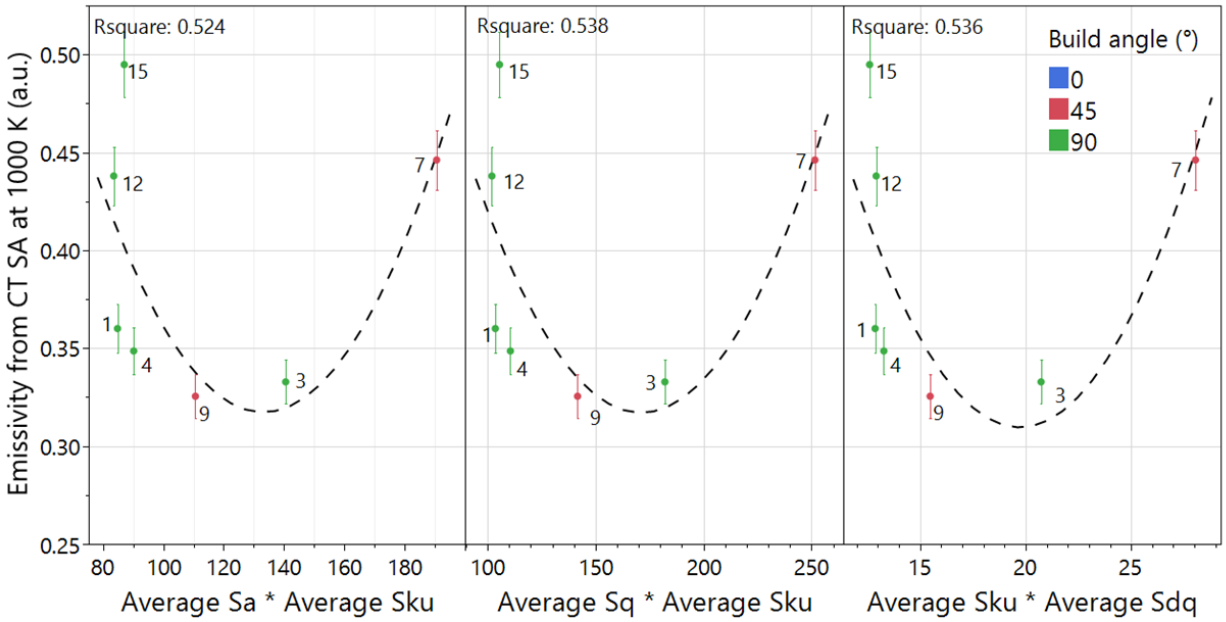

Figure 67: Plot showing the interpolated emissivity at 1000 K against the products of the average Sa and average Sku, average Sq and average Sku, and average Sdq and average Sku. Points are coloured by build angle

Like Figure 64, each of the plots shown in Figure 67 are skewed by the 45° sample 7 which causes the high R^2 values. There is not enough data at this temperature to make strong conclusions about the trends seen. Overall, the results in this section show that the areal texture parameters, even when taken as a product, do not correlate strongly with emissivity over the measured temperature ranges. This may be due to limitations of FVM, or because the surface texture parameters are not capable of accurately describing the complexity of AM surfaces.

At the time of writing, no reported work has been found linking areal surface texture parameters to emissivity. Only the work of S. Taylor *et al.* was found that investigated the emissivity of SLM surfaces using profile measurements and although they found strong correlations between emissivity and profile texture parameters such strong links could not be replicated in this work. These results may show that areal parameters are not well suited for linking surface texture and emissivity, despite their

advantages in describing AM surfaces compared to profile measurements. A direct comparison between areal and profile measurements on how well they trend with emissivity could be investigated as future work.

When looking at specific isotherms, especially at higher temperatures, there are instances where there is not enough data to draw strong conclusions. For example, the plot of emissivity at 1000 K against Sku in Figure 64, the R^2 value is skewed by the 45° sample 7. The shape of this trend could be better defined if there were more samples with different values of Sku that reached this temperature. This plot is also missing any 0° samples, more of which could help reveal if there are any notable trends with build angle. The next section will continue to discuss the relationship between the physical features of the samples and emissivity, looking at the trends of the CT determined surface area.

6.6. Surface area and emissivity

6.6.1. Surface area and Temperature

Another way of linking emissivity physically to the samples was with the emissive surface area. Figure 68 shows a plot of emissivity against surface area determined using CT measurements. The most immediate trend that can be seen from this plot is that as the surface area of the samples increases, the emissivity decreases. Although the extremes of surface area are tied to specific build angles, this trend appears to be true regardless of build angle. Samples with similar surface areas built at different build angles appear to have similar values for emissivity. Examples of this are the 0° sample 6 and the 90° sample 15, both highlighted on Figure 68. Overall, this has a strong trend when not separated by build angle, with an R^2 value of 0.576 using a quadratic fit (a linear fit gives a very similar value of 0.559). Figure 69 shows the interpolated emissivity against surface area along specific isotherms. Fits in these plots were quadratic because they more closely match the datapoints than linear fits. When separated along isotherms, the trend of emissivity decreasing with increasing surface area becomes much stronger, which holds true for all temperatures. This is evidenced by the high R^2 values for each of the trendlines.

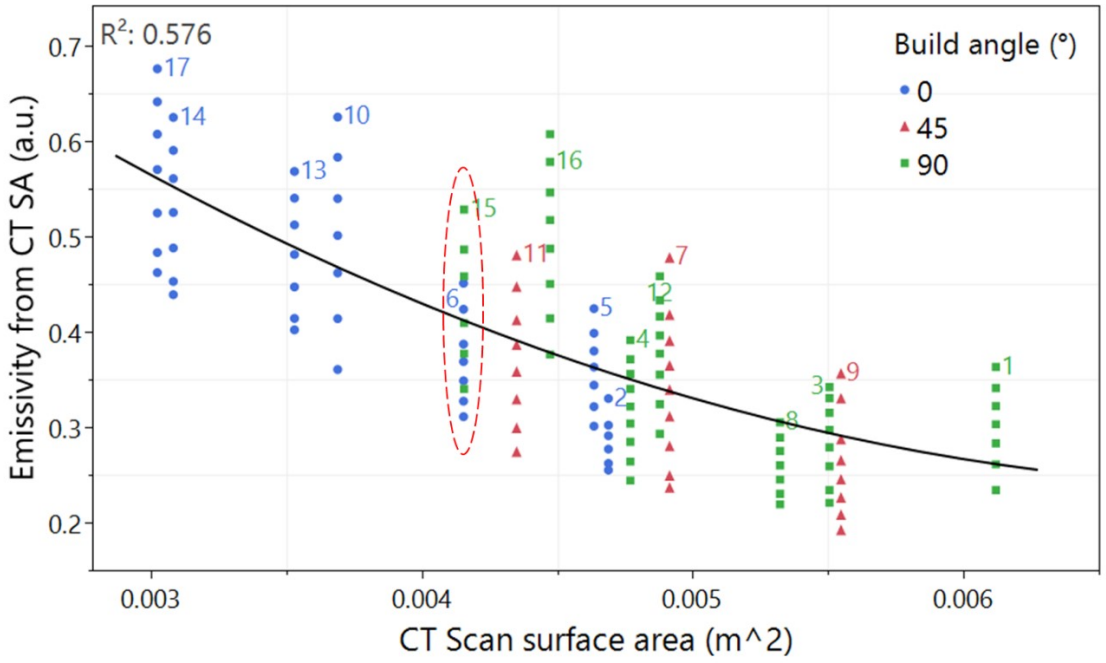

Figure 68: Plot showing the emissivity against surface area, both determined by CT scanning. Points are coloured by build angle

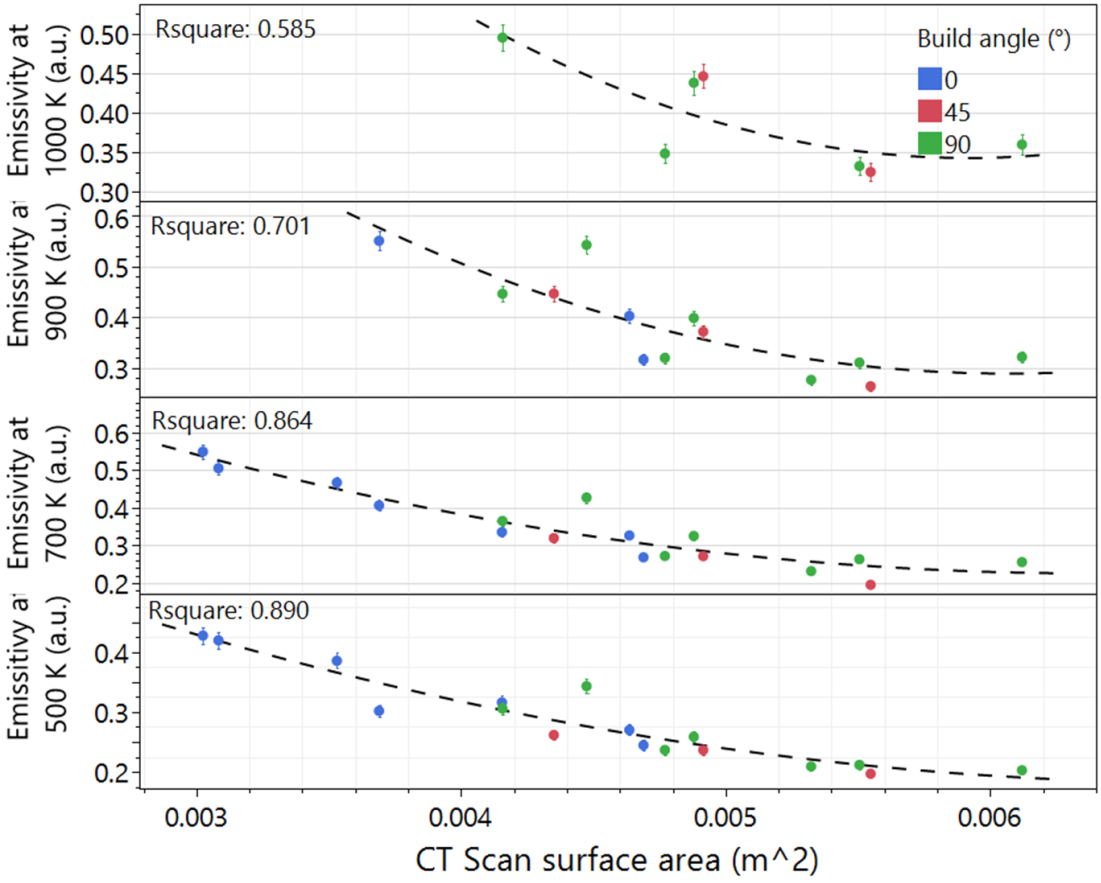

Figure 69: Plot showing interpolated emissivity values for all the samples at different temperatures against CT measured surface area. Error bars correspond to instrument uncertainty.

6.6.2. Surface area and power

Following the calorimetric emissivity equation in equation [39], it can generally be said that to reach the same temperature, samples with different surface areas require different emissive powers. As previously stated in section 2.3, emissive power is equivalent to the energy emitted by a surface per unit area and per unit time. To reach the same temperature, samples with larger surface areas will have to emit less energy per unit area and per unit time compared with smaller surface areas. Thus, their emissive power relative to a blackbody at the same temperature will decrease and so the emissivity will decrease. This same logic can be applied when considering constant emissive power, as shown in Figure 70 for emissive power of 50 W. For this specific emissive power, as the emissivity increases the temperature decreases. Similarly, as the surface area increases, the temperature increases.

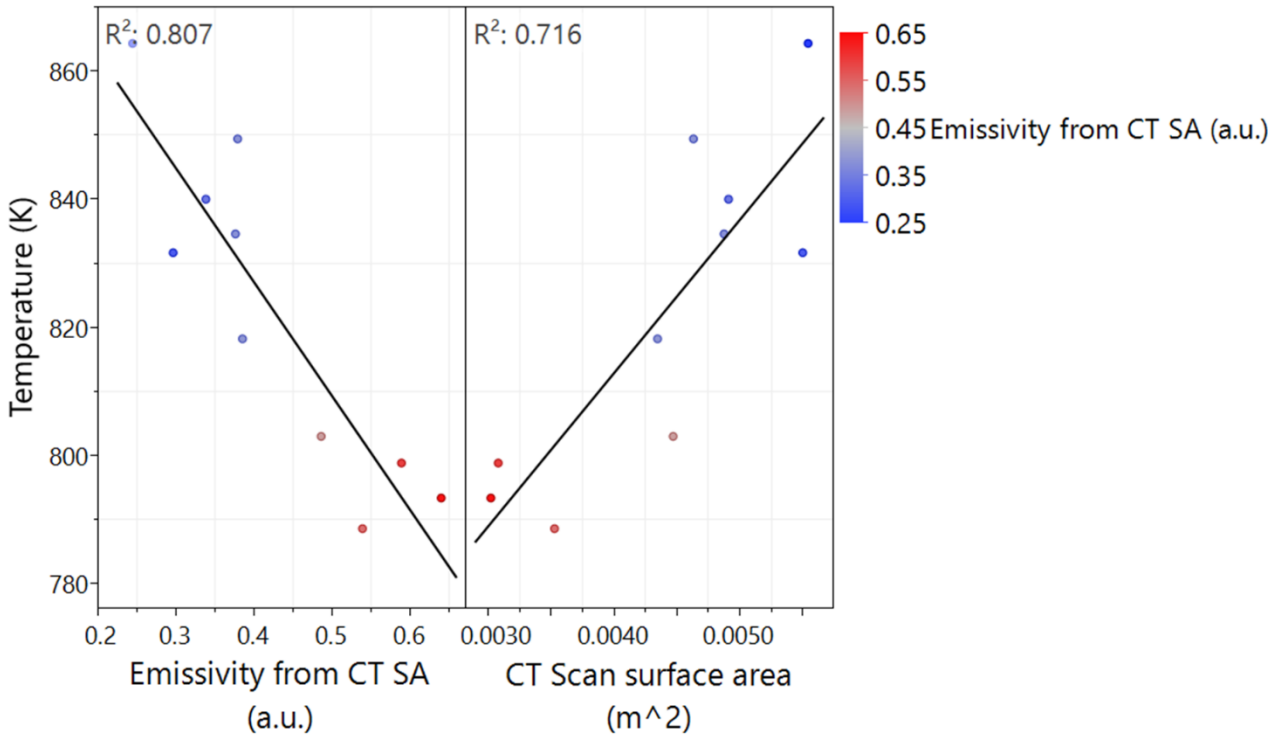

Figure 70: Plots of temperature against CT determined emissivity and CT determined surface area at an emissive power of 50 W

Samples with larger surface areas will have to emit less energy per unit area compared to smaller surface areas to have the same overall emissive power. By decreasing the amount of energy emitted per unit area and time, they have decreased relative to a blackbody as well and so the emissivity must also decrease. According to

the emissivity equation, the emissive power is equivalent to the power supplied to the sample. There are losses that can be considered such as conduction and convection, but as stated in the standard and as demonstrated previously these losses are small enough that they can be neglected. This is an important example as it can be directly related to actual scenarios such as the resistojet thruster on which this work is based. The thruster will operate under a constant input power. As shown in Figure 68, surface area varies strongly depending on the build angle. Thus, despite having the same input power, because different sections of the thruster may have different surface areas due to different build angle, they will also have different emissivity values and thus reach different temperatures.

Overall, the results in section 6.6.1 and 6.6.2 show that, for metal AM samples, emissivity is negatively correlated to surface area, regardless of temperature or emissive power. These are like the trend observed by Hunnewell *et al.* shown in Figure 60 [120]. Possible explanations for this are discussed in section 6.7.

6.7. Surface area, physical features, and surface texture

Because emissivity increases with surfaces that result in more internal reflections, which S. Taylor *et al.* characterised by the product Ra*Rdq [60], the trend of emissivity decreasing with increasing surface area initially appears counterintuitive. This relationship between emissivity and internal reflections was originally proposed by C. Mendenhall [114]. They stated that for a given reflectivity, as a valley on a surface gets narrower, radiated photons will undergo more internal reflections within the valley and thus the emissivity will be greater [114]. This was quantified through equation [40].

$$\boldsymbol{\varepsilon \approx \alpha = 1 - \rho^{\frac{180}{\theta}}} \qquad [40]$$

Where ϑ is the internal wedge angle in degrees, α is the absorptivity and ρ is the reflectivity. From equation [40] it can be seen that, as the internal angle of the wedge decreases, the emissivity increases. It was assumed that the narrower the valley angle, the more valleys could be fit onto the surface which would cause an increase in surface

area. This implies that increasing surface area would lead to an *increase* in emissivity. This is supported by Lam *et al.*, who stated that surface area is determined by the size and density of features in a geometric area [176]. To maximise the surface area would need a factor that maximises both size and density. This might explain why S. Taylor *et al.* found that the product of Ra and Rdq had the strongest trend with emissivity. Ra corresponded to the size of features while Rdq corresponded to the slope. The higher the Rdq, the steeper the slopes and thus the narrower the valley angle. Thus, an increase in Ra*Rdq might correlate well with increasing surface area and emissivity.

However, an increase in surface area does not necessarily have to correspond to an increase in the types of features that would result in more internal reflections. Valleys as described by C. Mendenhall [114] are an idealised feature that rely on at least two features in close proximity to form a wedge between them. However as shown in the SEM images of the SLM samples, real SLM surfaces do not often match this description. For example, the distance between features can be large enough that there is an appreciable increase in the overall surface area compared to flatter surfaces, but too large a distance to cause the wedge like effect necessary to increase internal reflections. Similarly, the shape of features, even when near each other, may not lend themselves to increasing internal reflections. This is seen in features such as surface pores or half-melted or agglomerated particles. They can increase the surface area without creating a wedge like shape.

This may explain the trend seen in Figure 68 and Figure 69. As the sample surfaces increase in complexity, they increase in surface area. However, the more complex surfaces do not generate more internal reflections than the less complex surfaces due to factors such as shape of the features or distance between them causing similar or less energy to be radiated over increasingly larger surface areas, resulting in decreasing emissivity. Another possible explanation is that, if the complexity of the surface has no impact on the number of internal reflections generated, that changes in emissivity from internal reflections saturates above a certain level. Thus, increasing the surface area above this level only reduces the emissivity.

From reviewing the literature, few sources were found discussing the variation of emissivity with surface area. Figure 68 shows the trend of emissivity decreasing with increasing surface area; which was also previously reported by T. S. Hunnewell *et al.* [120]. They measured the emissivity of cast 316L in the as-received condition and increasingly roughened with sandblasting from 60 grit up to 220 grit over a similar temperature range used in this thesis. They reported roughness in Ra so the results cannot be directly compared to the results presented herein, but the general trends can be. They also found no strong correlation between Ra and emissivity although they did not offer an explanation why. The surface areas of their samples were significantly lower than those in this thesis, from 1.22×10^{-6} m^2 - 1.67×10^{-6} m^2. However, it is worth noting that T. S. Hunnewell *et al.* measured four samples, and the trend of decreasing emissivity with increasing surface area was only for three of those samples (not the as received which had the lowest surface area). They also did not state how they measured surface area or the resolution of those measurements If the resolution of the measurement instrument was larger than the smallest feature on the surface, it could have caused smoothing effect and measured the area as being smaller than it was, resulting in emissivity values higher than they should have been. In this thesis, the X-ray CT achieved a resolution between 5 µm – 7.5 µm which is small relative to the average diameter of the powder particles used to build the parts (~18 µm).

B. P. Keller *et al.* did an identical investigation to T. S. Hunnewell *et al.* but for cast Inconel 718 [126]. Like T. S. Hunnewell *et al.* their surface areas were much lower than those measured in this thesis, ranging from 1.52×10^{-5} m^2 - 1.74×10^{-5} m^2. Although they also found no correlation between Ra and emissivity for surface area (and did not explain why), they found the opposite trend to this thesis for surface area. As surface area increased so did emissivity. However, it is again worth noting that they also did not report how they measured surface area and only measured four samples, and so it is hard to draw strong conclusions from this data. These sources show that the trend of emissivity with surface area is not yet well documented, and the available information is conflicting.

Table 24 shows a table of the R^2 values of quadratic fits for plots of the CT determined surface area against the five areal surface texture parameters. This shows that areal surface texture also does not correlate strongly with surface area.

Table 24: Table showing the R^2 values of quadratic fits for plots of CT determined surface area against average areal surface texture parameters

Areal surface texture parameter	R^2
Sa	0.181
Sq	0.084
Ssk	0.141
Sku	0.299
Sdq	0.412

The work presented here has shown that, for the metal SLM surfaces investigated, accurate surface area measurements are a better predictor of emissivity than surface texture measurements. However, the surface area measurements performed as part of this investigation were expensive in terms of both cost and labour and involved specialised equipment for X-ray CT scanning that may not be widely available. The standard on which this work was based recommended measuring the surface area of the samples using callipers and most studies found in the literature also used callipers. While these were for machined and cast samples, callipers in general are easier to obtain and significantly less labour intensive compared to the CT scanning and image analysis techniques used in this thesis. While determining surface area with CT scanning may obtain more accurate results for emissivity of AM samples, this may not always be possible to do. It may be useful in future to investigate alternate, less labour intensive but equally accurate methods for determining surface area of samples rather than CT measurements or if other methods of determining areal surface texture parameters, such as X-Ray CT scanning, correlate better with surface area and emissivity.

Overall, these results show surface area correlates strongly with emissivity regardless of temperature or emissive power. This is likely because, as emissivity is a

measure of the emissive power per unit area and time, as the area increases while other factors are fixed, the emissive power will decrease and thus so will the emissivity. While emissivity increases with surfaces that produce more internal reflections, this is not necessarily counter to decreasing with increasing surface area. SLM surfaces can include features which increase the overall surface area, whilst not increasing the number of internal reflections. The next section will focus on modelling the relationship between emissivity and the input process parameters used to build the AM parts.

6.8. Models linking process parameters, emissivity, and surface area

One of the objectives of this thesis was to understand how the SLM process affected the emissivity of the parts produced. Key to this was understanding how the input process parameters varied in this study (laser power, scanning speed, hatch spacing, layer thickness and build angle) influenced the emissivity of the resultant parts. To achieve this, like the model for roughness presented in section 5.5, multiple linear regression models were created using the software JMP.

The purpose of the models was to determine which process parameters affected emissivity the most, and to rank the process parameters in order of significance on emissivity. The relationship between temperature and emissivity is well-known and widely reported in the literature as discussed in section 2.3. Rather than create models that were convoluted with this non-linear relationship, linear regression models were developed for emissivity at specific isotherms. Models could not be generated for temperatures over 700 K, as there were not enough data points from this study. Future studies could ensure that more samples reach higher temperatures to build more high temperature models. Given the strong correlation seen between surface area and emissivity in the previous section 6.6, a model was also made to understand what input process parameters affected the surface area. The method used to create the models was identical to that presented in section 5.5. Table 25 shows the key values used to determine the significance of the models generated.

Table 25: Table showing key parameters for the models generated for emissivity and surface area

	Emissivity at 500 K	Emissivity at 700 K	Surface area (mm^2)
Mean of Response	0.28	0.34	0.0045
Root Mean Square Error	0.0089	0.009	0.00013
R^2	0.99	0.99	0.98
F ratio	651.86	1115.2	377.78
p-value	<.0001	<.0001	<.0001

The data in Table 25 shows that each of the models generated are reliable, as they have low values for RMSE, high R^2 values and F ratios and very low values for the p-values. The plots shown in Figure 71 detail the significance of each of the input parameters and their interactions for each of the different models.

The most notable trend of the plots shown in Figure 71 is that for all the models, layer thickness and build angle are the most significant terms. These models link emissivity to inputs that result in the physical changes to the samples surfaces.

Given the strong relationship between emissivity and surface area, it is not surprising that the input parameters that are significant to surface area are also significant to the emissivity at different temperatures. For all the models both laser power and the product of hatch spacing with itself were also significant terms.

The square of hatch spacing is of note because, as demonstrated in section 5.5, it was the term that had the most significance on both Sa and Sq. Although, as seen in Table 25 surface area does not correlate well with surface texture, the fact that surface area and texture share significant input factors indicates that surface texture may have a significant role in determining the overall surface area. Similarly, as shown in Figure 49 build angle was the most significant term in the models for Sdq and Sku. More work will need to be done to better understand the relationship between surface texture and surface area of metal AM parts.

Emissivity at 500 K

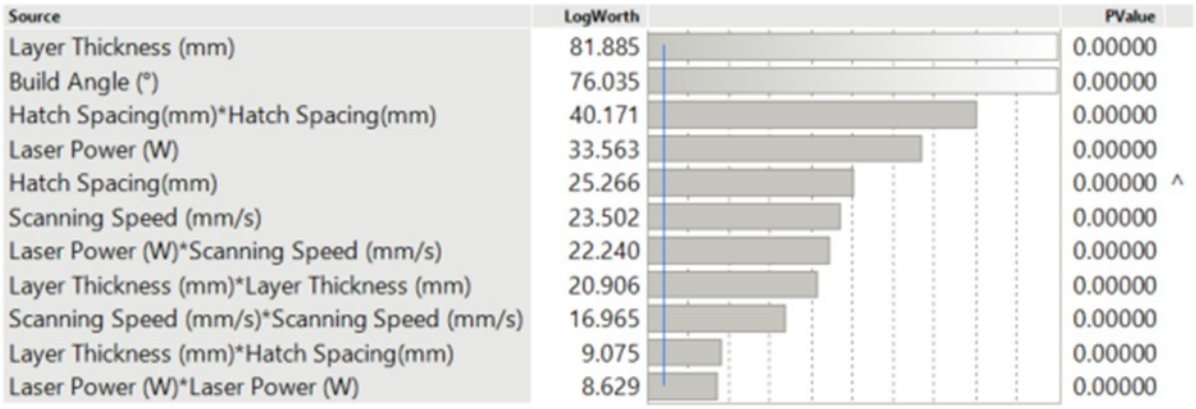

Source	LogWorth	PValue
Layer Thickness (mm)	81.885	0.00000
Build Angle (°)	76.035	0.00000
Hatch Spacing(mm)*Hatch Spacing(mm)	40.171	0.00000
Laser Power (W)	33.563	0.00000
Hatch Spacing(mm)	25.266	0.00000 ^
Scanning Speed (mm/s)	23.502	0.00000
Laser Power (W)*Scanning Speed (mm/s)	22.240	0.00000
Layer Thickness (mm)*Layer Thickness (mm)	20.906	0.00000
Scanning Speed (mm/s)*Scanning Speed (mm/s)	16.965	0.00000
Layer Thickness (mm)*Hatch Spacing(mm)	9.075	0.00000
Laser Power (W)*Laser Power (W)	8.629	0.00000

Emissivity at 700 K

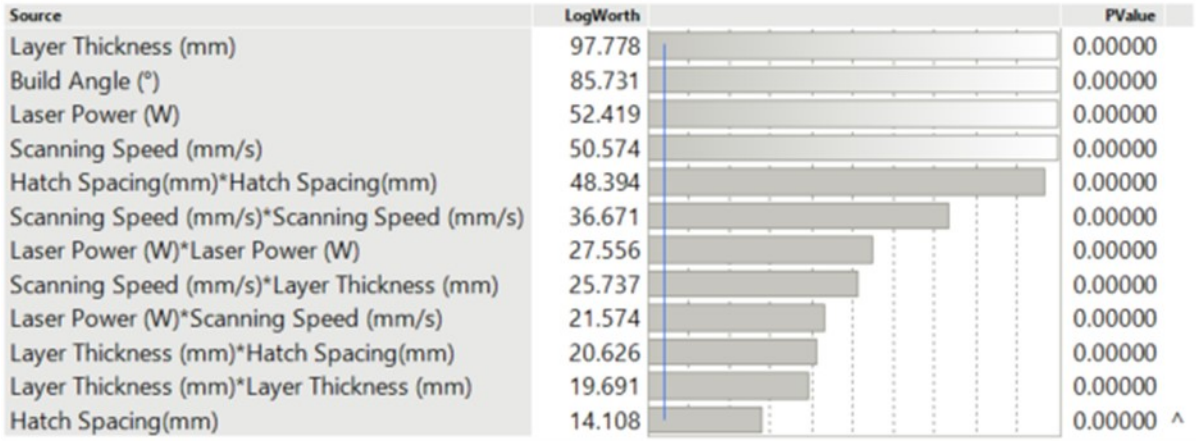

Source	LogWorth	PValue
Layer Thickness (mm)	97.778	0.00000
Build Angle (°)	85.731	0.00000
Laser Power (W)	52.419	0.00000
Scanning Speed (mm/s)	50.574	0.00000
Hatch Spacing(mm)*Hatch Spacing(mm)	48.394	0.00000
Scanning Speed (mm/s)*Scanning Speed (mm/s)	36.671	0.00000
Laser Power (W)*Laser Power (W)	27.556	0.00000
Scanning Speed (mm/s)*Layer Thickness (mm)	25.737	0.00000
Laser Power (W)*Scanning Speed (mm/s)	21.574	0.00000
Layer Thickness (mm)*Hatch Spacing(mm)	20.626	0.00000
Layer Thickness (mm)*Layer Thickness (mm)	19.691	0.00000
Hatch Spacing(mm)	14.108	0.00000 ^

CT Surface Area

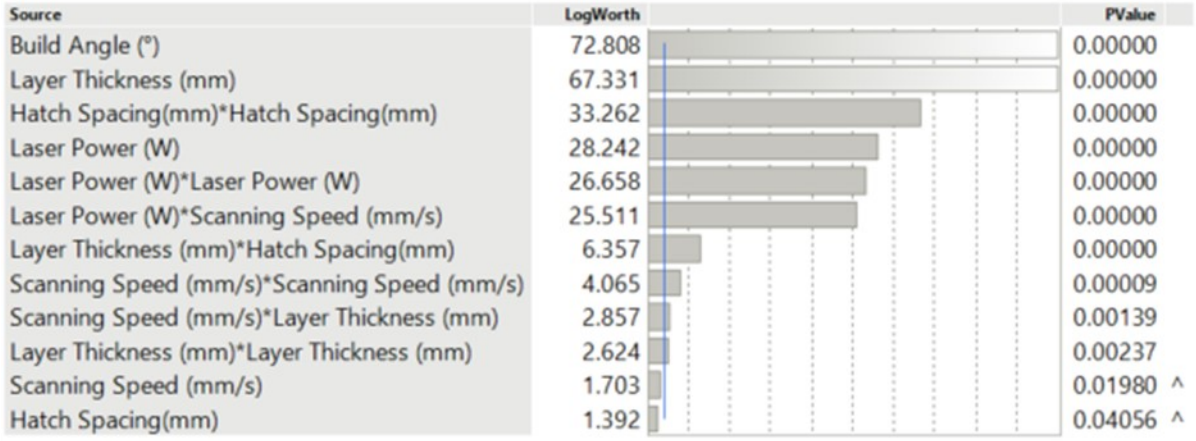

Source	LogWorth	PValue
Build Angle (°)	72.808	0.00000
Layer Thickness (mm)	67.331	0.00000
Hatch Spacing(mm)*Hatch Spacing(mm)	33.262	0.00000
Laser Power (W)	28.242	0.00000
Laser Power (W)*Laser Power (W)	26.658	0.00000
Laser Power (W)*Scanning Speed (mm/s)	25.511	0.00000
Layer Thickness (mm)*Hatch Spacing(mm)	6.357	0.00000
Scanning Speed (mm/s)*Scanning Speed (mm/s)	4.065	0.00009
Scanning Speed (mm/s)*Layer Thickness (mm)	2.857	0.00139
Layer Thickness (mm)*Layer Thickness (mm)	2.624	0.00237
Scanning Speed (mm/s)	1.703	0.01980 ^
Hatch Spacing(mm)	1.392	0.04056 ^

Figure 71: Plots showing the LogWorth vs. the source for the different models of emissivity and surface area

It is worth noting that some terms were more significant for some of the models than others. For example, hatch spacing on its own was significant for emissivity at

500 K, but was the least significant term for both surface area and emissivity at 700 K. This may indicate that there are other factors not accounted for in these models that are influencing the relationships. As previously mentioned, factors such as surface composition are known to affect emissivity, and changes to the composition may have occurred at different temperatures resulting in different relationships between emissivity and the input parameters.

As seen in Figure 58, the surface area of the samples is clearly different on different sides of the same sample (upskin and downskin). The 0° samples tend to have the lower surface areas compared to the 45° and 90° samples. This is because the 0° samples were removed from the build plate using EDM wire cutting. Thus, the downskin sides of the 0° samples were much flatter compared to the other samples, significantly reducing their overall surface area. Overall, this may explain why build angle is so significant to each of the models.

The fact that the 0° samples were removed from the plate using EDM wire cutting does not invalidate the results of the model. The measured surface area and emissivity values of the 0° samples are representative of samples with a surface removed from a build plate using wire cutting, and thus so are the models. These results are not however representative of 0° samples produced parallel to the build plate, but with the downskin not directly connected to the plate. Such samples were not originally considered when designing the experiment and could be investigated in future studies.

Figure 72 shows plots of the model predicted responses on the emissivity and surface area for the different input parameters. The error bars on each plot represents the standard error.

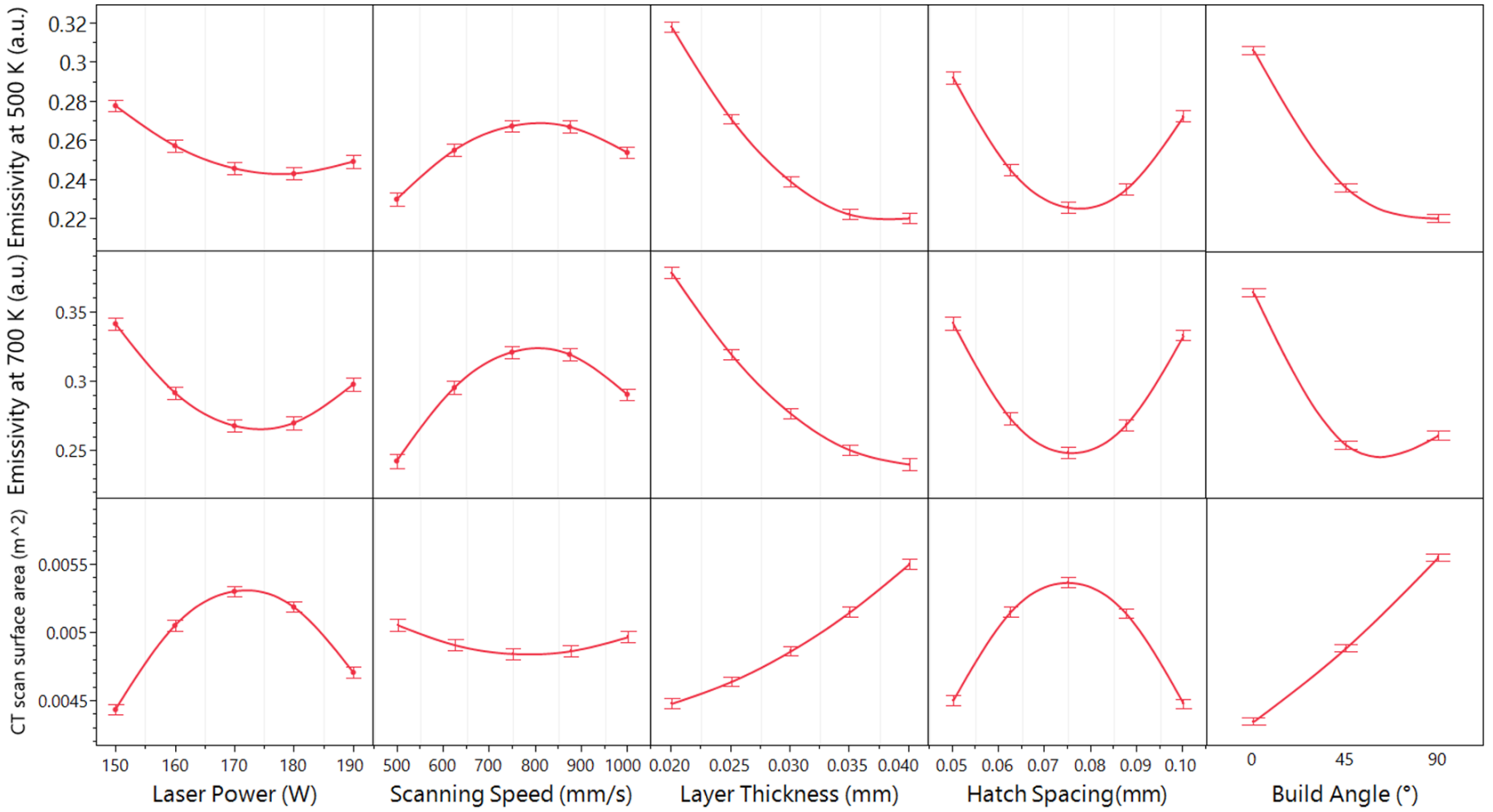

Figure 72: Main effects plots showing the model predicted responses on emissivity at 500 K and 700 K and surface area for the different input parameters. Error bars correspond to standard error.

The shape of the effects of layer thickness, build angle and laser power are nearly identical on emissivity at both 500 K and 700 K. None of the terms appear linear which was expected given that, except for build angle, each of the terms in the models have both square terms and interactions with other terms. However not enough information has been gathered to definitively state the shape of the response the inputs have. As previously stated, this was a screening experiment designed to identify what inputs had the greatest effect on the outputs. Now that these have been identified as critical factors, future experiments should focus on these factors and on developing an understanding of the response they produce.

The trends of these inputs with surface area appear to be nearly inverse compared with emissivity. This was expected, as the overall trend of surface area with emissivity is negatively correlated. Therefore, it is expected that changes to the input parameters that increase the surface area will also reduce the emissivity. The fact that the shapes of the responses are not the exact opposite of the emissivity response curves however does indicate that there are other factors that affect the responses that are not considered in these models.

6.9. Conclusions

Using the calorimetric method, the total hemispherical emissivity of all seventeen samples produced using different process parameters was measured up to input currents of 80 A. Steady state conditions were not reached for all samples at low input currents (generally up to 40 A) and temperatures, requiring these results to be omitted from further analysis.

When using surface areas measured with callipers, the emissivity values for some samples were greater than the theoretical maximum of 1 (equivalent to a blackbody) meaning that the results were likely incorrect, due to the callipers underestimating the surface areas. Emissivity determined using CT scan surface area varied from roughly 0.2 to 0.7 over 500 K to 1100 K, slightly higher than literature values for cast stainless steel. The 0° samples generally had the highest emissivity values, but the lowest maximum temperatures.

None of the surface texture parameters measured (Sa, Sq, Ssk, Sku and Sdq) or their products correlated strongly with emissivity. This may have been because focus variation microscopy was unable to capture recessed and re-entrant features, which would likely correspond to higher emissivity values.

Surface area, when measured using a combination of CT scanning and image analysis, trended very strongly with emissivity, regardless of temperature or power. This may have been because as surface area increased, this did not correspond to an increase in the types of surface features that generate internal reflections, but only increased the area over which energy was radiated, decreasing the emissive power and thus emissivity.

Multiple linear regression models were created linking the process parameters to the emissivity at 500 K, 700 K and CT determined surface area. These models shared significant input parameters, indicating that changes to the surface area likely affected the emissivity also.

7. Results and discussion - Resistivity

7.1. Introduction

As previously discussed in section 2.4, when considering metals, deviations from the periodicity of the crystal lattice increase the likelihood of scattering events for electrons which in turn increase the resistivity. These reductions in periodicity can be caused by substituted or interstitial atoms and imperfections in the crystal lattice. Such imperfections can include grain boundaries, dislocations, or vacancies. As a result, the microstructure of a metal plays a large part in determining the resistivity of a metal. This is particularly interesting for SLM metals, as the build process can result in microstructures that are very different compared to metals made through better understood processes such as casting.

Resistivity was measured using the four-probe method adapted from the ASTM standard B193-16. This involved placing four probes onto the surface of the samples, applying a current through the outer two probes and measuring the voltage across the inner two. By knowing the exact cross-sectional area (A) of the sample and length between the voltage probes (L) the resistivity could be calculated using equation [41] from the measured resistance (R) of the sample.

$$\boldsymbol{\rho = \frac{RA}{L}} \qquad [41]$$

This section will provide a look at how the microstructure of the SLM samples manufactured for this thesis varied before discussing how these changes affected the resistivity of the samples. First an overview of the resistivity data will be provided before discussing how the density and primary cell spacing affected the resistivity.

7.2. Resistivity

7.2.1. Overview of data

As previously described in section 4.3, the resistivity of all seventeen samples was measured using the four-probe method in the same setup used to measure emissivity. The standard did not recommend a specific method for obtaining the cross-sectional area, only that it was accurate within ±0.1%. This was achieved using a combination of CT scanning and image analysis, detailed in the methodology section of this thesis. Resistivity was measured up to approximately 1000 K. Figure 73 shows the resistivity of all seventeen samples, separated by build angle. The error bars were calculated through the method described in section 4.3. The error bars correspond to the instrument uncertainty which was the largest.

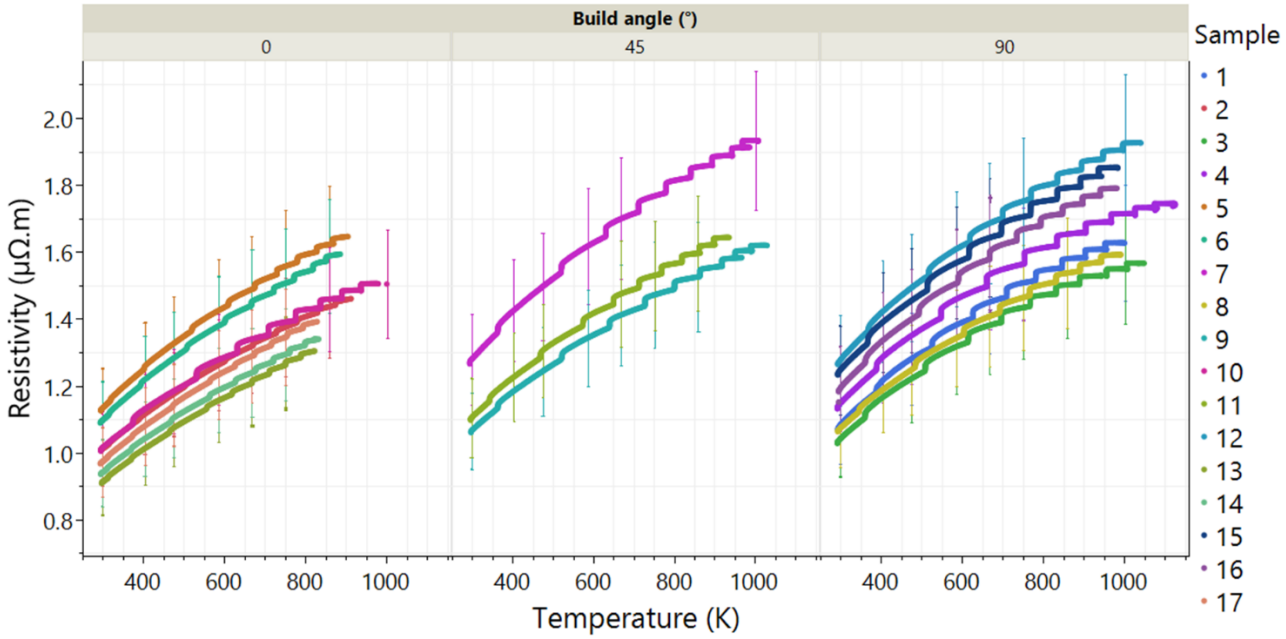

Figure 73: Plots showing the resistivity vs. temperature of all the samples, separated by build angle. Error bars correspond to instrument uncertainty

The most immediate trend that can be seen from Figure 73 is that, as the temperature increases so does the resistivity for all the samples. As previously discussed in 2.4, for metals resistivity is temperature dependent. As temperature increases, so does the vibration of atoms about their positions in the crystal lattice. This reduces the periodicity of the lattice and thus increases the resistivity.

All the curves in Figure 73 increase in discrete steps. Each of these steps correspond to an increase in the current supplied to the sample. When comparing the resistivity at similar temperatures, this plot shows that generally the 0° samples exhibited lower resistivity compared to the 45° and 90° samples. The 0° samples covered the lowest range of values, from approximately 0.91 µΩ.m to 1.65 µΩ.m giving them a total range of roughly 0.74 µΩ.m. The 45° and 90° samples covered higher ranges from approximately 1.03 µΩ.m to 1.93 µΩ.m giving them a total range of roughly 0.9 µΩ.m.

In Figure 74 this data is compared to the high-temperature resistivity of traditionally manufactured 316L as reported by P. Pichler *et al.* [139]. P. Pichler *et al.* demonstrated that thermal expansion at increasing temperatures change the overall specimen geometry and distance between the voltage probes can vary compared to room temperature values. If this change was not taken into account, it gave lower values for resistivity [177]. The corrected values in Figure 74 take this thermal expansion into account, resulting in higher resistivity compared to values based on the initial geometry.

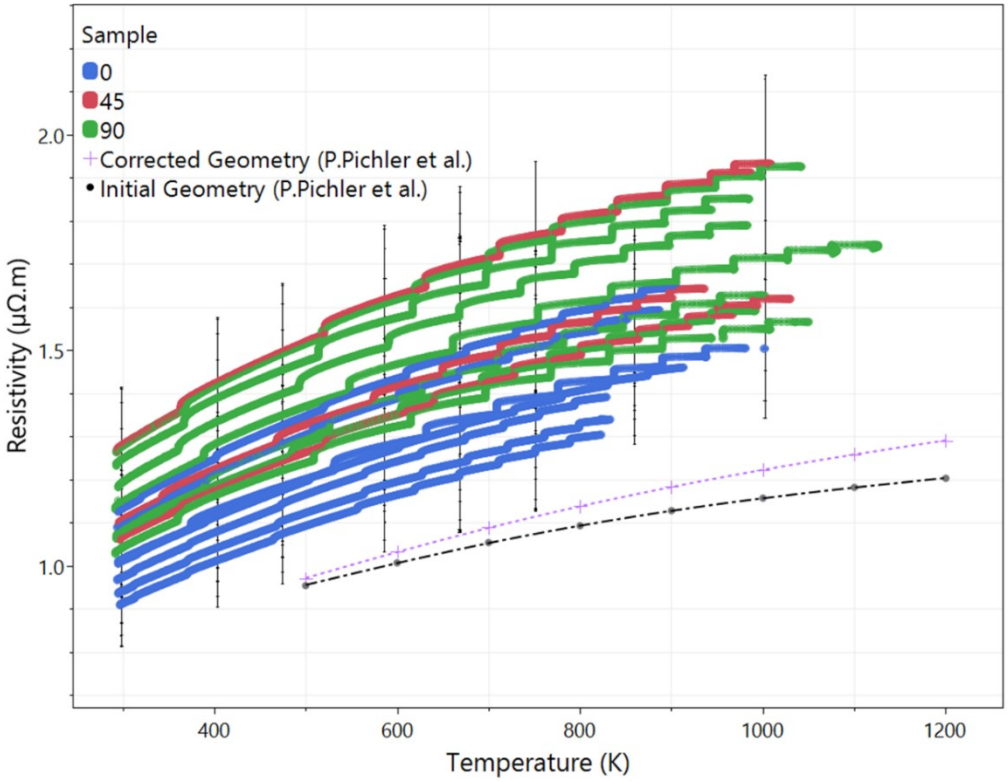

Figure 74: Graph comparing the resistivity values for all 17 samples of SLM 316L and coloured by build angle against literature values for cast 316L by P. Pichler *et al.*, separated by initial geometry and thermal expansion corrected geometry. Error bars correspond to instrument uncertainty [139]

P. Pichler *et al.* measured thermal expansion by capturing images of their samples as they expanded every 2.5 µs, [139] however replicating this was beyond the capabilities of the work for this thesis. Although there appears to be only a small difference in resistivity values between initial and corrected geometries up to the highest temperatures seen in this work, the work of P. Pichler *et al.* was conducted on traditionally manufactured 316L stainless steel, and it is unknown if the same trends would be seen in SLM 316L.

M. Yakout *et al.* studied the influence of process parameter variation on the coefficient of thermal expansion (CTE) of SLM 316L from 294 K – 1273 K [178]. They produced cubic samples with energy densities varying from 41.7 J/mm^3 – 156.3 J/mm^3) and found that the CTE of SLM 316L was analogous to wrought 316L with no significant changes. This suggests that the changes in resistivity seen by P. Pichler *et al.* for traditionally manufactured 316L would also be seen for SLM 316L. However further work would be required to determine the extent of the change in resistivity.

The main purpose of measuring the resistivity was to improve the models for the resistojet by accurately measuring resistivity at high temperatures. Taking thermal expansion into account may improve the accuracy of these resistivity measurements and the model of the resistojet. Thus, future work could strive to take this into account.

When comparing the data at similar temperatures, the SLM resistivity values are notably higher, regardless of the build angle, when compared to both initial and corrected values from P. Pichler *et al* for traditionally manufactured material. If SLM resistivity values were corrected for thermal expansion they would be expected to increase slightly more. Given the same designated composition of these 316L stainless steels, these differences between the SLM and cast are likely due to differences in the microstructure, and the differences between the SLM samples are likely because of the differences in the process parameters used to build them. These differences will be explored in greater detail throughout this chapter.

7.2.2. Model linking resistivity and SLM process parameters

As was done for both the roughness and emissivity, multiple linear regression models were created using the software JMP to assess the effect of process parameters on resistivity. Process parameters related to volumetric energy density (laser power, scanning speed, hatch spacing and layer thickness) and the build angle were explored. Resistivity values at specific temperatures (300 K, 500 K, 700 K and 800 K) were interpolated using quadratic fits for all the samples. Linear regression models were created using these interpolated resistivities to avoid convoluting the results with temperature. The method used to create the models was identical to that presented in section 5.5. Table 26 shows the key values used to determine the significance of the models generated. These results show that each of the models generated were reliable given the low values for RMSE, the high R^2 values and F ratios and very low p-values. Each of the models found the same parameters significant in the same order of significance. A plot of these values is shown in Figure 75.

Table 26: Table showing key parameters for the models generated for resistivity at different temperatures

	Resistivity at 300 K	Resistivity at 500 K	Resistivity at 700 K	Resistivity at 800 K
Mean of Response	1.10	1.30	1.47	1.53
Root Mean Square Error	0.02	0.02	0.02	0.02
R^2	0.98	0.98	0.98	0.98
F ratio	266158.06	315252.62	334339.98	334267.84
p-value	<.0001	<.0001	<.0001	<.0001

It was assumed that the input parameters affected the microstructure which in turn affected the resistivity. Figure 75 shows that as the temperature increased the input factors that affected the models and their significance stayed the same. This suggests that there were no changes to the microstructure caused by increasing the temperature that affected the resistivity within the bounds of this experiment. As shown in section 6.8, the significance of certain input parameters changed for the emissivity models at different temperatures.

Source	LogWorth	PValue
Build angle (°)	54052.46	0.00000
Laser Power*Laser Power	36991.98	0.00000
Laser Power	34444.09	0.00000 ^
Hatch spacing (mm)*Laser Power	30628.29	0.00000
Scanning speed (mm/s)*Laser Power	14495.39	0.00000
Scanning speed (mm/s)	14264.30	0.00000 ^
Layer thickness (mm)*Scanning speed (mm/s)	13359.22	0.00000
Layer thickness (mm)	5874.045	0.00000 ^
Hatch spacing (mm)*Hatch spacing (mm)	5647.680	0.00000
Layer thickness (mm)*Layer thickness (mm)	3865.893	0.00000
Scanning speed (mm/s)*Scanning speed (mm/s)	3359.681	0.00000
Hatch spacing (mm)	51.406	0.00000 ^

Figure 75: Plot showing the LogWorth vs. the source for the resistivity models

Build angle was found to be the most consistently influential factor on resistivity, which is evident in Figure 73 and Figure 74. While the results in Figure 75 do give information on how the process parameters affected the resistivity, they do not explain why they have the significance or effect that they do. To understand this, it was necessary to investigate how the microstructure of the SLM samples changed with process parameters and in turn relate this back to resistivity which is goal of the rest of this chapter. Focus was given to the relative density and the primary cell spacing of the parts because previous reports by C. Silbernagel *et al.* and Y. Shi *et al.* indicated that these had effects on the resistivity of SLM parts, as detailed in the section 3.4.1 [128], [131], [137].

7.3. Relative density

7.3.1. Introduction

Density in this thesis is described in terms of relative density, which compares the density of the samples to a theoretically ideal sample which is completely free of pores. This density was calculated using equation [42]

$$\rho_r = \frac{\rho_m}{\rho_{316L}} \cdot 100 \qquad [42]$$

Where ρ_r is the relative density of the parts, ρ_m the measured density and ρ_{316L} the pore free density of 316L stainless steel, which was taken as 8.05g/cm^3 [143]. Previous work by K. Ibrahim *et al.* showed that for AM 316L stainless steel, as the porosity increased from 5% to 40%, the resistivity increased by roughly 86% [138]. Porosity interrupts the crystal lattice, resulting in a more tortuous conduction path for the electrons. However, these results were reported for selective laser sintering rather than melting, which typically produces parts with higher porosity compared with SLM. The density of the seventeen samples in this thesis were measured to better determine the relationship with resistivity. The density of each of the samples was measured using both the Archimedes method and using a combination of CT scanning and image analysis, both of which have been establish for measuring the density of SLM samples [167].

Archimedes density measurements were not performed on the actual samples used to measure resistivity, but instead on smaller representative samples. There is confidence that these samples are representative as they were printed using identical build parameters and with the same width (13 mm) thickness (250 µm) but shorter length (50 mm instead of 200 mm). The shorter length should not have affected the heat transfer between the sample and the base plate, which is an important factor on the resultant microstructure. The 200 mm long samples used to measure resistivity were CT scanned to calculate surface area. These same scans were also used to calculate the density.

7.3.2. Comparison of measurement methods

The Archimedes method was carried out following the modified procedure of the ASTM standard as described by A. B. Spierings *et al.* [167]. It calculated density by measuring the volume of liquid displaced by the immersed samples, while the image analysis calculated the area fraction of binarized CT micrographs that was empty space. Detailed descriptions of these methods can be found in section 4.7. For reference the equation used to calculate the density in the Archimedes method is shown in equation [43].

$$\boldsymbol{\rho_p = (\rho_{fl} - \rho_{air}) \cdot \frac{m_a}{m_a - m_{fl}} \cdot \rho_{fl}} \qquad [43]$$

Where ρ_p is the density of the sample, ρ_{fl} is the density of the fluid, ρ_{air} the density of the air, m_a the mass of the sample in air and m_{fl} the density of the sample in the fluid. There were however issues when using the Archimedes method that may have affected the accuracy of the results.

The samples used by A. B. Spierings *et al.* and specified in the standard were cubic samples. The samples used in these experiments however were flat strips to be as representative of the larger samples used in resistivity and emissivity measurements as possible. While theoretically the dimensions of the sample should not have played a part in the density measurements, in practice the shape of these samples made them difficult to handle. The samples may have been too large for the container and may not have been properly suspended in the fluid. As a result, the mass measurements in the fluid (m_{fl}) may have been erroneously low causing the overall density values to be underestimated as seen in equation [43]. This is reflected in the values for the relative density calculated using the Archimedes method shown in Table 27 and Figure 76 where, except for sample 2, there is a large difference in density between the two methods for each sample. Generally, density measurements using the Archimedes method were significantly lower than those measured using CT scanning.

The lowest density measured using the Archimedes method was 46.5% while comparatively the lowest using CT scanning was much higher at 83.5%. For the CT determined density values, all the 90° and 45° samples achieved density greater than 98%. Only the 0° samples had lower density values (as in Figure 4). The Archimedes density values in Figure 76 also clearly decrease with increasing sample number. While this may be simply a coincidence as sample number does not correspond to any increasing build parameter, it does match the order in which the samples were measured. It may indicate that an error, possibly due to handling, worsened with increasing measurements.

Table 27: Table showing the relative density measurements for all 17 samples as determined by CT scanning/image analysis and the Archimedes method

Sample	CT density (%)	Archimedes density (%)
1	98.7	76.9
2	94.9	91.6
3	98.2	75.6
4	98.1	66.6
5	90.3	65.9
6	91.8	70.8
7	99.2	57.8
8	98.2	62.5
9	99.0	63.7
10	83.5	53.0
11	98.9	57.1
12	98.3	54.3
13	99.3	73.0
14	98.3	68.6
15	99.5	46.5
16	99.4	48.9
17	98.2	66.3

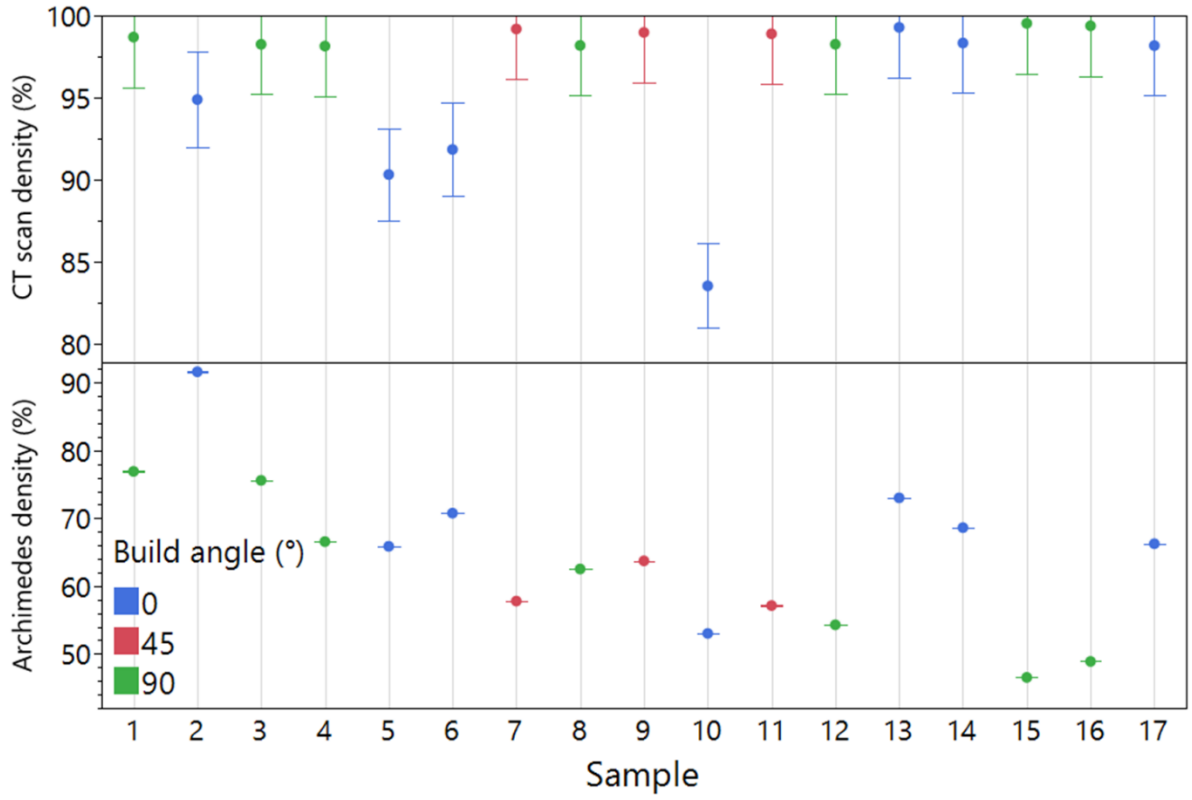

Figure 76: Plot showing the relative densities calculated using CT scanning/image analysis and the Archimedes method for each of the 17 samples, coloured by build angle

The density values calculated using CT scanning were much closer to what was expected given that the process parameters used to build the samples were chosen based on literature values that produced high density (>99%) parts. This method was adapted from a procedure described by A. B. Spierings *et al.* for micrographs of a cross section [167]. There were however also issues with this technique. For the image analysis used in this thesis to work, the CT image reconstructions were cropped to remove the surface and focus solely on a region of interest (ROI) of the internal porosity. Given how much the surface of some of the samples varied over all the micrographs, this was difficult to consistently achieve without occasionally also including some of the surface. As a result of this, the porosity may have occasionally been erroneously high. A sensitivity analysis was performed to understand how much the density varied by decreasing the area of the ROI. This was performed for the 0° sample 5, 45° sample 11 and the 90° sample 4. The results of this analysis are shown in Figure 77.

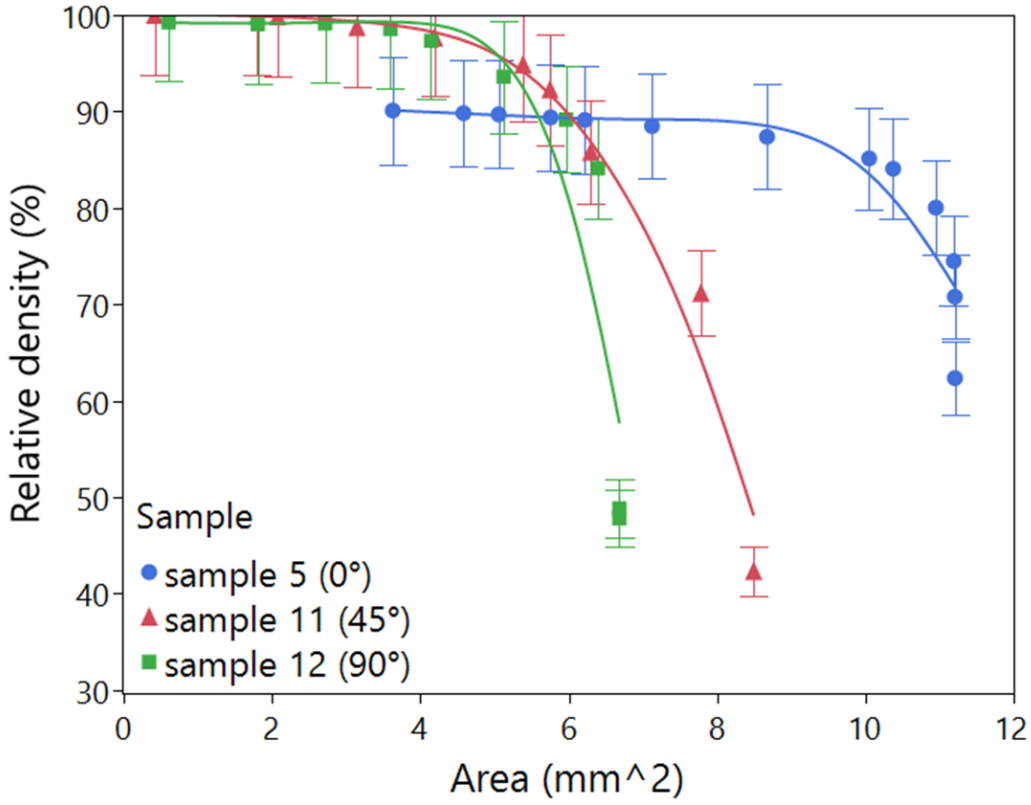

Figure 77: Graph showing relative density against area of the ROI measured as part of a sensitivity analysis

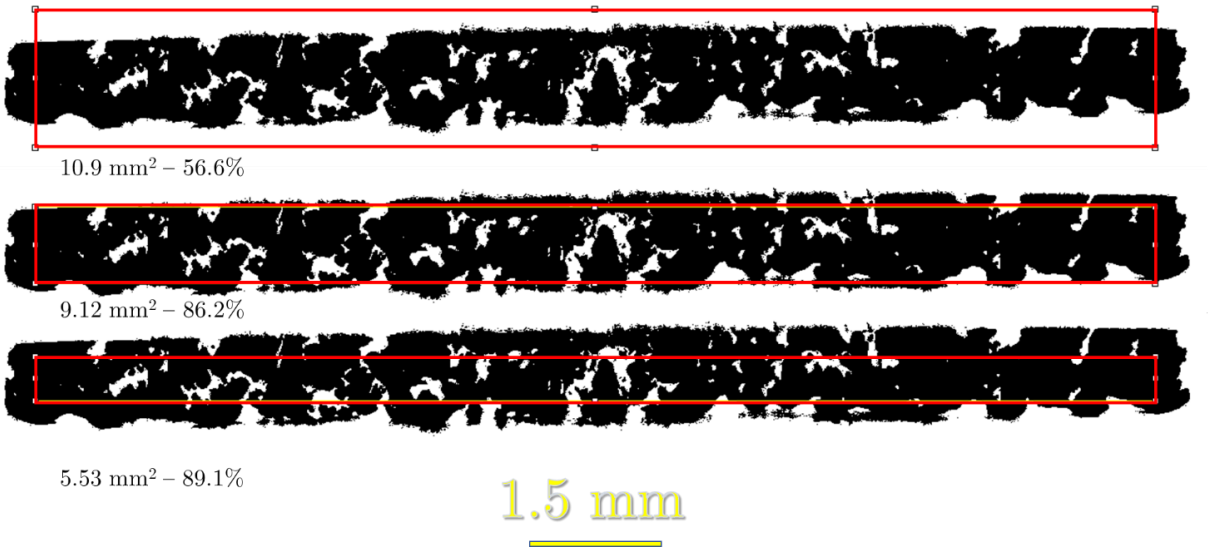

Figure 78: Examples of different ROIs and the resultant values of relative density for the 0° sample 5

The results of Figure 77 clearly show that for each of the samples, below a certain threshold of the ROI there is a minimal change in the relative density of the sample. For example, reducing the area of the 0° sample from 11.2 mm^2 to 8.27 mm^2 increased the relative density from 62.4% to 87.4%. However further reducing the area down to 3.63% only increased the density to 90.1%. It is also noteworthy that the smallest area of the ROI for the 0° sample still resulted in a notably lower density compared to the 90° and 45° samples. This suggests that for optimal results an area within the low sensitivity regime (smaller ROI) should be selected. Figure 78 shows that the beginning of the stable region for each sample was found to be easily identifiable when manually selecting the areas giving confidence that the relative densities measured were suitable. To gain confidence in the technique, measurements were repeated three times and an average value of the density was taken.

Without having a reference density sample to compare against, it is difficult to quantify the extent of the error in both density techniques. Visual inspection of the samples indicated that they were unlikely to correspond to the very low densities from the Archimedes method. When combined with the fact that the CT density values were much closer to what was expected, this indicated that the error in the Archimedes density values was likely greater than the CT density values. Going forward, these results will focus on density calculated using the CT scanning and image analysis

technique. However, in future studies samples with more suitable geometries for both techniques should be manufactured, and a comparison made against a reference to determine which method is the most suitable.

7.3.3. Relative density and energy density

Energy density has been referred to as one of the best predictors for parts relative density [7], [22]. Figure 79 shows the relationship between the density of the samples and energy density. The error bars were calculated using the method detailed in section 4.3 and corresponds to X-Ray CT scan uncertainty which was the largest. No fit has been assigned to this graph, as no justification for using a fit could be found in the literature.

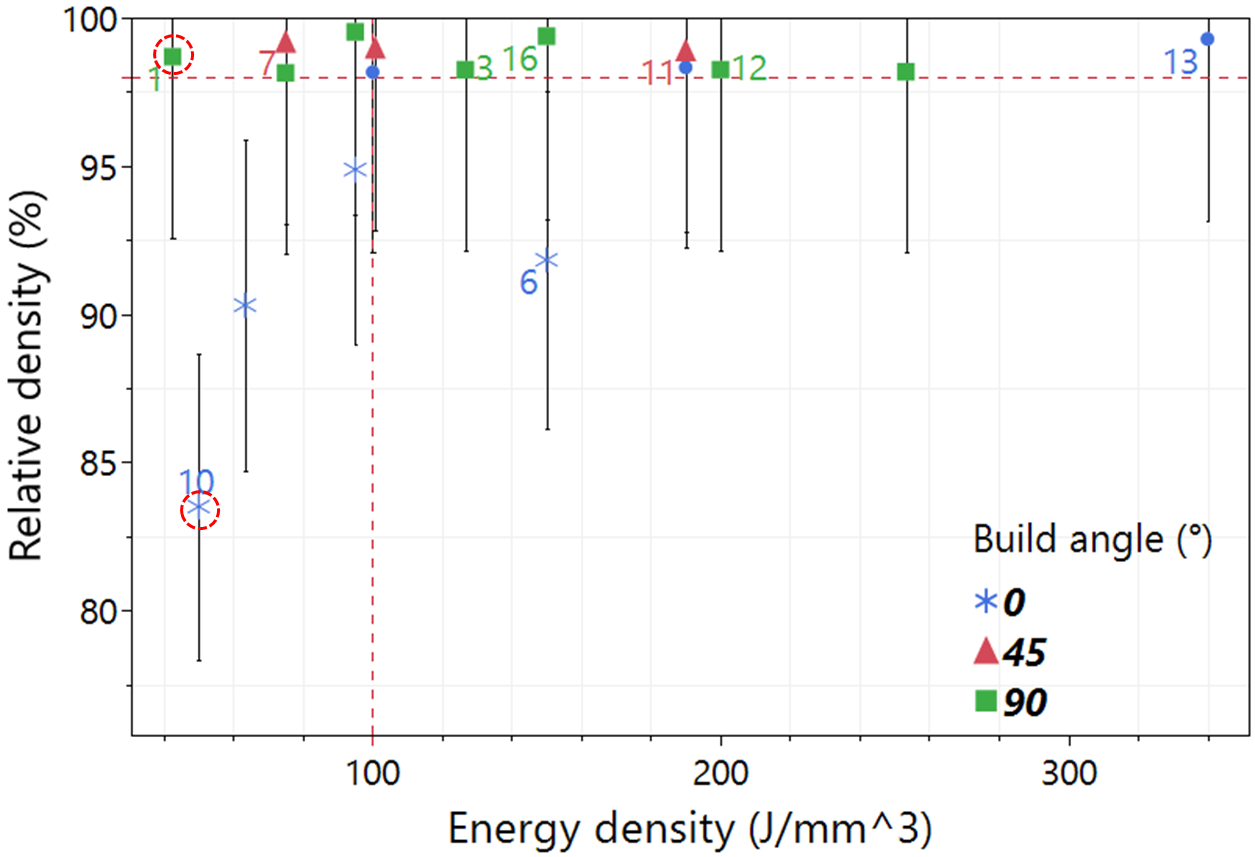

Figure 79: Graph showing the relationship between CT determined density and energy density. 98% relative density and 100 J/mm3 energy density are marked on the graph. Samples 1 and 10 are circled in red.* samples are the 0° samples with <98% relative density

Generally, there does not appear to be a clear relationship between the relative density of the parts and energy density. Samples with similar values of energy density

have very different values for relative density such as the 90° sample 1 and 0° sample 10, both marked on the graph (dashed red circles). Sample 10 had an energy density of 50 J/mm^3 and a relative density of 83.5% while sample 1 had a similar energy density of 42.5 J/mm^3 and a much higher relative density of 98.7%. This lack of a relationship between relative density and energy density remains true for the 90° and 45° samples. However, for the 0° samples, it could be argued that as the energy density increases, so does the density. In this regard, the low relative density of sample 6 (91.8%) would be considered an outlier as it does not follow this trend. It is notable that all the 90° and 45° samples had relative densities greater than 98% while the 0° samples had relative densities both above and below 98%. This indicates that, within the bounds of this experiment, build angle may have had a large effect on relative density.

E. Liverani *et al.* also investigated how energy density affected the relative density of SLM 316L and found that generally it was a good predictor of relative density [25]. The hatch spacing (0.05 and 0.07mm), build angle (0°, 45° and 90°) and scanning speed (700m/s) were similar to this work while the laser power (100 and 150 W) covered a lower range than the 150 W – 190 W studied here. However, they gave no information on the dimensions of the specimens they used for density measurements or about layer thickness used. While this lack of specific information makes direct comparison with their results difficult, the similarities in material and process parameter ranges may still allow for general comparison of trends [25]. They found that parts with a relative density greater than 98% could only be produced with energy densities of 100 J/mm^3 or greater. They determined this experimentally and gave no explanation as to why. While most points above 98% density in Figure 79 do occur above an energy density of 100 J/mm^3, there is also data below 100 J/mm^3 with density greater than 98% and data above 100 J/mm^3 with density less than 98%. E. Liverani *et al.* also stated that the relative density was unrelated to build angle, which is contrary to lower densities for 0° samples in Figure 79.

S. Greco *et al.* reported how process parameters affected the relative density of cubic SLM 316L samples [78] at constant energy densities of either 33.3 J/mm^3 or 119

J/mm^3. They varied laser power (30 W – 90 W), layer thickness (25 µm – 45 µm) and scanning speed while keeping hatch spacing (56 µm) constant. Again, their different sample dimensions and process parameter ranges make direct comparison with this work difficult but allows for comparison of general trends. However contrary to E. Liverani *et al.* they found that energy density was not a good predictor of relative part density. In general, similar to E. Liverani *et al.* they found that more dense samples were produced at higher energy densities. They explained this as an increase in energy density corresponded to an increase in the thermal energy delivered to the sample and thus a larger percentage of the material within that volume was heated above its melting point. However, they also found that part densities varied when input parameters changed, but the overall energy density was kept constant. For example, they found that as the laser power increased, so did the relative density regardless of energy density or other input parameters. This was reportedly due to an increase in the ratio between laser power and heat conduction as laser power was increased, resulting in more powder material being heated above its melting point [78]. This may explain the difference in relative density between samples 1 (laser power 170 W) and 10 (laser power 150 W).

Another hypothesis is that because the 45° and 90° samples are thin walled, the heat input was more concentrated causing more of the sample to be melted and leading to higher relative densities. The 0° samples had a wider area directly connected to the build plate and could dissipate heat through thermal conduction more rapidly. The relationships between the sample's relative densities and the process parameters will be discussed in detail in a later section, when discussing models for process parameters and density.

7.3.4. Relative density and resistivity

To avoid convoluting the results with temperature, interpolated resistivity values from quadratic fits were plotted against the relative density of the samples at 300 K, 500 K, 700 K, and 800 K. These results are shown in Figure 80.

When considering all the samples regardless of temperature, below approximately 98% density the resistivity generally increases as the density decreases, except for the 0°

sample 10 at 83.5% density. This increase in resistivity is still within the range of resistivity values seen for samples with greater than 98% density. According to K. Ibrahim *et al.,* this trend may be because porosity causes a more tortuous path conduction path for electrons [138]. This can be equated to a higher number of disruptions to the periodic lattice, which would result in a higher resistivity. Above 98% relative density it appears that there is no clear relationship between resistivity and density. This may indicate that there is another factor which has a stronger relationship with resistivity above this density threshold. Y. Shi *et al.* found a similar relationship between resistivity and density for a novel Al alloy manufactured through SLM [137]. They found that below 99.5% density, there was a linear relationship between resistivity and density. However above 99.5%, resistivity was primarily affected by the amount of solute in the solid solution.

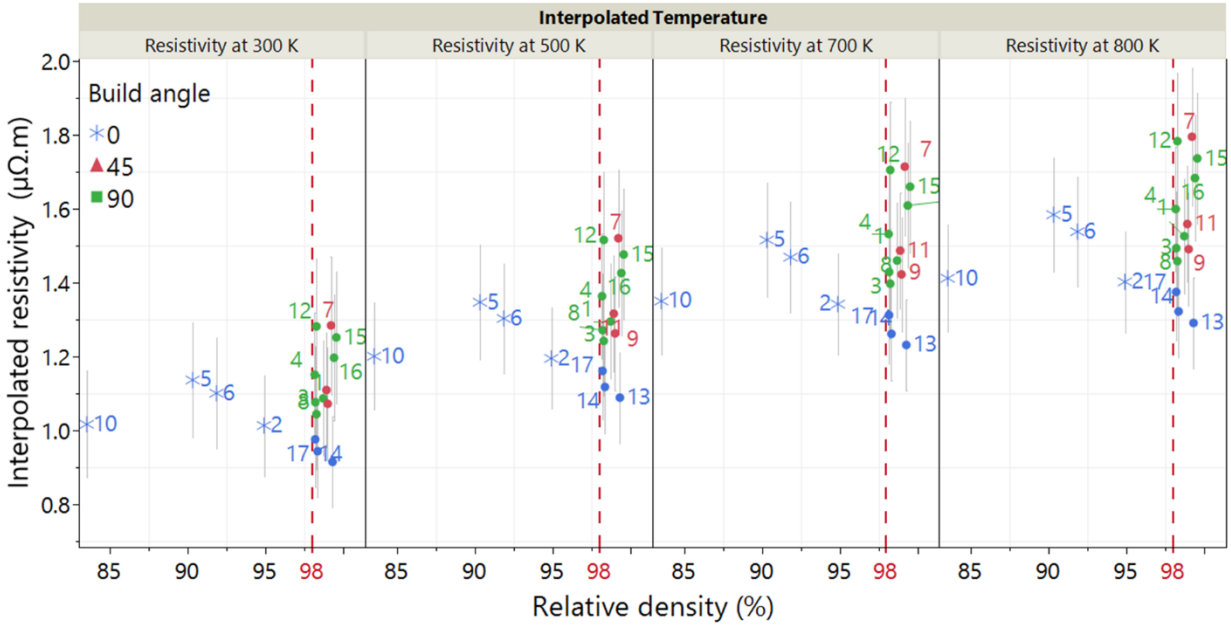

Figure 80: Plot showing the relationship between resistivity and relative density interpolated at 300 K, 500 K, 700 K and 800 K, separated by build angle. 0° samples with densities less than 98% are marked with *

It is worth noting that the linear relationship between density and resistivity below 98% density seen in Figure 80 only holds down to roughly 90% density. Below this, the low density of sample 10 appears to defy this trend by having a comparatively lower resistivity for each temperature. Given the large gap in densities between sample 10 and the next highest density, it is difficult to say for certain if this is part of a trend or an

outlier value. These density values are also much lower than reported by Y. Shi *et al.* Thus, the repeatability of this could be investigated in greater detail in a future study. When considering build angle, the 90° and 45° samples do not show any clear trends with resistivity and density while the 0° samples, apart from sample 10, show increasing resistivity with decreasing density both above and below 98% density. However as there are no 90° or 45° samples below 98% density it is difficult to say for certain if the trend of increasing resistivity with decreasing density would be observed for all the build angles.

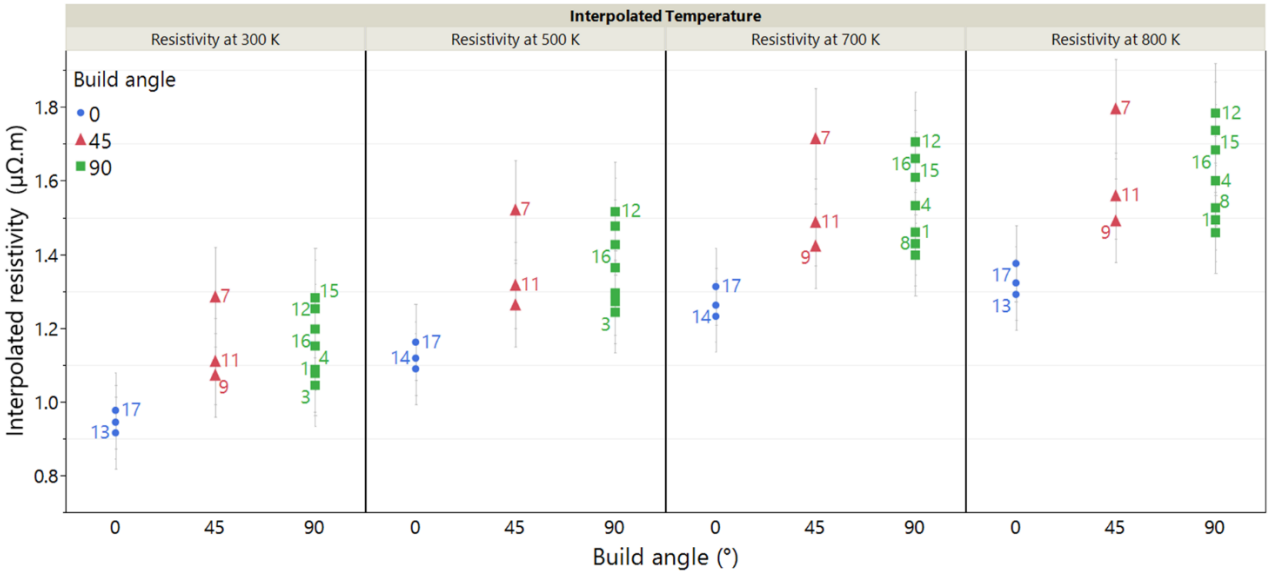

Figure 81: Plot showing the relationship between resistivity and build angle at specific temperatures for samples above 98% relative density

When considering only the samples above 98% relative density as shown in Figure 81, the relationships between resistivity and build angle also seems to be clearly separated by build angle. Figure 81 shows that generally, for the same temperatures, the 90° and 45° samples cover similar ranges of resistivity, while the 0° samples are consistently lower. As previously mentioned in section 2.4, C. Silbernagel *et al.* investigated the effect of build orientation on rectangular specimens of both pure copper and the alloy AlSi10Mg manufactured using SLM [128], [131]. In both instances they reported that resistivity was anisotropic and that build angle had a strong influence.

As shown in Figure 82, their 90° samples were built with the long axis along the z axis of the build chamber while in this work it was in the y axis. For the copper the

difference in resistivity was explained by differences in porosity distribution. Resistivity was measured along the long axis of the samples and there were more continuous build tracks free from porosity along the long axis of the 0° samples compared the 90° samples. This was attributed to a lack of interlayer fusion and intralayer defects that caused a more tortuous conduction path for the 90° samples, resulting in a higher resistivity. This is particularly interesting because a similar trend to this is seen in Figure 81; the 90° samples consistently have higher resistivities than the 0° samples. It is important to note however that there are only three 0° samples and 45° samples above 98% density. With so few data points for each build angle, it is difficult to say for certain if there are trends. Comparing the CT image reconstructions used to determine the porosity of the samples built for this thesis, there did not appear to be a notable difference in porosity distribution between the samples built at different build angles when their relative densities were over 98%. It is worth noting that C. Silbernagel *et al.* found this trend for a pure metal rather than an alloy, and only achieved a maximum density of 85.8%.

As previously mentioned, no 90° or 45° samples below 98% density were produced in this thesis and the direction of current flow was the same for all samples in this thesis (along the y-axis in Figure 82) but was different for each sample for C. Silbernagel *et al.* Thus, it is unknown if this trend between build angle and resistivity holds true at lower density values. Another factor that may have influenced the resistivity for the samples above 98% density was disruptions to the lattice caused by grain boundaries. These are discussed in detail in the next section.

7.3.5. Model linking relative density and SLM process parameters

Previous reports have found strong links between the process parameters that make up energy density and relative density. Given that this current work has found a link between relative density and resistivity of SLM 316L, understanding the relationship between process parameters and relative density would help to better understand the relationship between the SLM process parameters and resistivity.

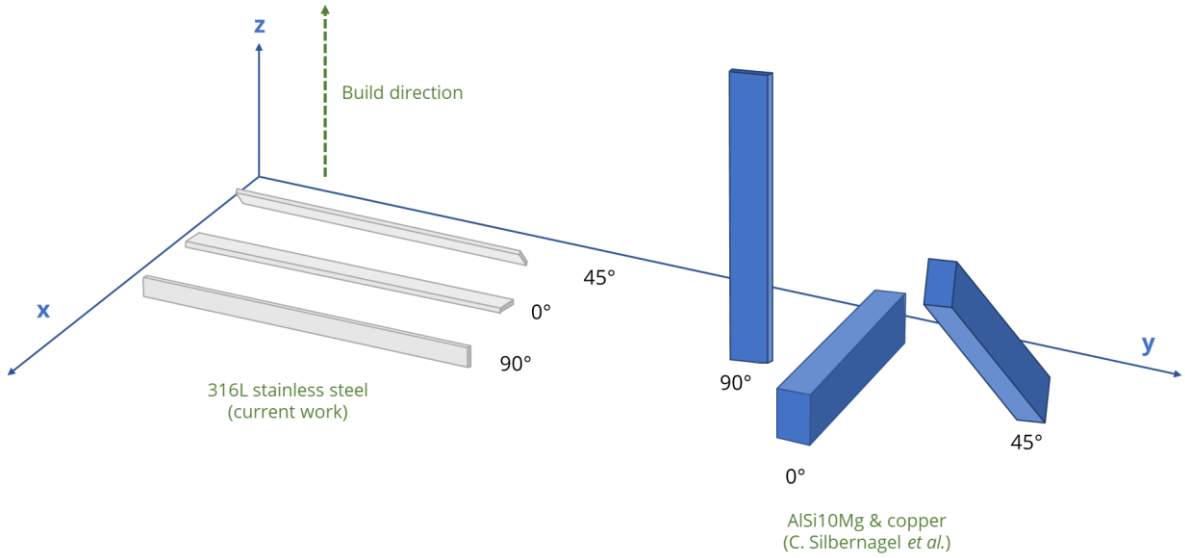

Figure 82: Diagram showing the difference in build orientation for the samples built as part of this thesis and the samples built by C. Silbernagel *et al.*[128], [131]

To do this, a multiple linear regression model was created with the purpose of finding out which of the input parameters most significantly contribute towards the relative density of the parts. In future this work can be used as a basis towards developing a deeper model to understand exactly why these factors produce the responses they do on relative density.

The process parameters investigated were those that make up volumetric energy density (laser power, scanning speed, hatch spacing and layer thickness) and the build angle of the parts relative to the build plate. The model was created using the same method presented in section 5.5 using the software JMP. Figure 79 shows that for similar ranges of energy density, only the 0° samples show notable variation in density. Process parameter variation within the range of values used in this work had little effect on the density values for the 45° and 90° samples. For this reason, the 45° and 90° samples were excluded from the model.

The key parameters for the model shown in Table 28 indicate that the model is reliable, given the low values for the root mean square error, very high R^2 and F ratio values and low p-value. The plot shown in Figure 83 details the significance of the process parameters and their interactions in the model.

Table 28: Table showing the key parameters for the multiple linear regression model generated for the relative density of the 0° samples

Mean of Response	93.9
Root Mean Square Error	4.25E-07
R^2	1
F ratio	7.64E+17
p-value	<.0001

Source	LogWorth	PValue
Laser Power*Laser Power	213061.3	0.00000
Laser Power	57696.69	0.00000
Scanning speed (mm/s)	48017.78	0.00000
Layer thickness (mm)	44403.54	0.00000
Scanning speed (mm/s)*Laser Power	31815.16	0.00000
Hatch spacing (mm)	21847.69	0.00000
Scanning speed (mm/s)*Scanning speed (mm/s)	1126.815	0.00000

Figure 83: Plots showing the LogWorth vs. the source for the model of relative density of the 0° samples

The square term of laser power and laser power alone are the most significant terms to the model. These are notable as these were also the most significant terms in the models for resistivity after build angle, as seen in Figure 75. That both models share these as most significant terms indicates that the relative density and resistivity are likely correlated with each other, further supporting the hypothesis that density has a significant impact on resistivity. This is also supported by the fact that these terms were significant in the resistivity model regardless of temperature and the relative density of the samples likely did not change with temperature. The shapes of the model predicted responses on the relative density for each of the input parameters are shown in Figure 84. Generally, as the process parameters change to increase the energy density (laser power increasing, scanning speed and layer thickness decreasing) the relative density increases. The exception to this trend is hatch spacing, which as it increases (corresponding to a decrease in energy density) the relative density also increases. Comparing these results to similar results from the literature may help to better understand them.

As previously mentioned, E. Liverani *et al.* also investigated how process parameter variation affected the relative density of SLM 316L specimens [25]. While their values of scanning speed (700 mm/s) and hatch spacing (0.05 mm and 0.07 mm) were similar to the ranges covered in this work, the laser power values (100 W and 150 W) were lower than this work (150 to 190 W) and they gave no information on layer thickness or part dimensions. It is also worth noting that their process parameters were based on a previous study that produced parts with >98% density.

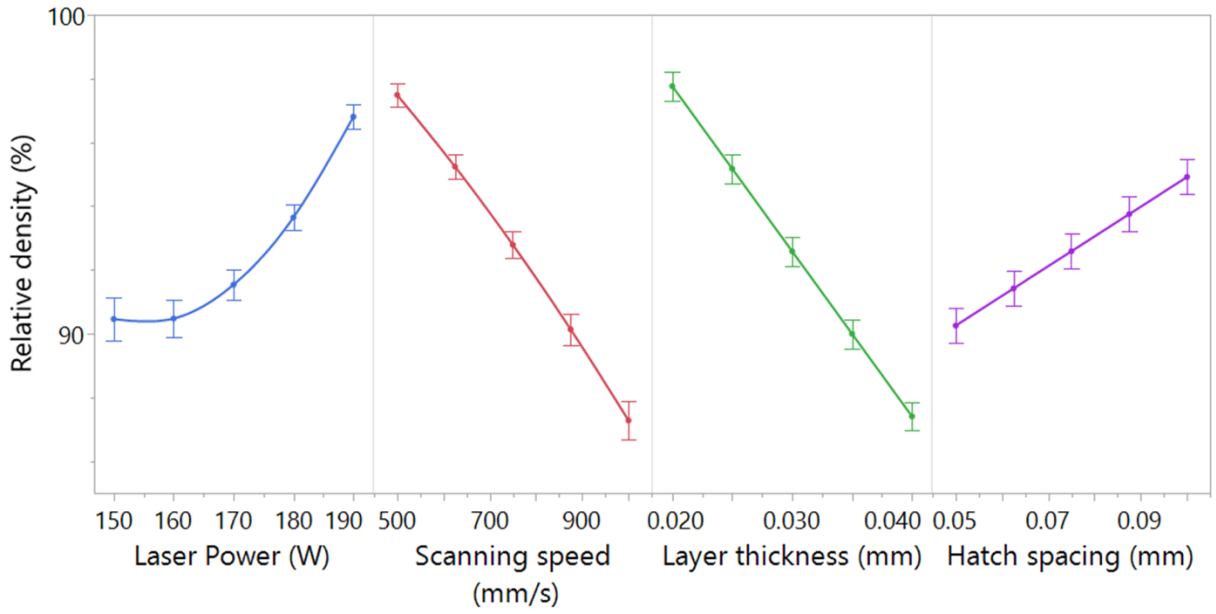

Figure 84: Main effects plots showing the model predicted responses on the relative density of the 0° samples for each of the input parameters

While E. Liverani *et al.* did not offer explanations for their results, they found that low laser power of 100 W produced the lowest density parts (98.4%) while a high laser power (150 W) produced the highest density parts (>99.9%). While the ranges are different, this is like the trend of laser power seen in Figure 84. E. Liverani *et al.* also varied hatch spacing and found it had minimal effect on the relative density of their parts, unlike the trend seen in Figure 84.

The findings of E. Liverani *et al.* were similar to the work of S. Greco *et al.* who looked at how varying process parameters but maintaining energy density affected the relative density of cubic SLM 316L samples [78]. In general they also found that increasing the laser power increased the relative density of their samples, regardless of other parameters. It should be noted that their range of laser powers (30 W – 90 W)

was much lower than used in this work. S. Greco *et al.* theorised that increasing the laser power corresponded to an increase in the energy density and amount of thermal energy being delivered to the part. This increased the amount of material being heated above its melting point, improving the density of the part. They also theorised that there was a limit to this beyond which further increasing the energy density would not increase the relative density, dependent on material properties such as thermal conductivity. While not directly comparable with the results in Figure 84 because of the lack of information on layer thickness and part dimensions, the trend that density increases with laser power was also seen in this work.

This relationship between thermal energy and relative density may also explain the responses of the other input parameters. S. Greco *et al.* also reported that increasing layer thickness resulted in a decrease in relative density at a constant energy density due to decreasing penetration of thermal energy from the laser into the powder layer. This resulted in insufficient melting of previous layers and raw powder, both of which were required to ensure proper adhesion of past and subsequent layers and resulted in an overall decrease in relative density. A decrease in relative density with increasing layer thickness was also seen in Figure 84. Based on the work of S. Greco *et al.*, an explanation for the scanning speed trend is that increasing scanning speed decreased the energy density and thus decreased the amount of thermal energy being delivered to the part. Thus, less of the material was heated above its melting point and lead to defects such as lack of fusion of particles that reduced the relative density.

The fact that density increases as hatch spacing increases is counter to what was expected, as previous work in section 5.5 showed that as the hatch spacing increased, overlap between adjacent tracks decreased resulting in an increase in porosity. It was assumed this would coincide with a decrease in the relative density. A. M. Khorasani *et al.* offered a possible explanation for this, stating that lower hatch spacing increased the energy density and energy absorbed within a certain area and increased the likelihood of defects such as keyholes [179]. Larger hatch spacing however increased the contact between the melt pool and the previous solidified layer, which increased the stability of

the melt pool and reduced the porosity. While the work of A. M. Khorasani *et al.* did look at how process parameters affected the relative density of parts, it was for the alloy Ti-6Al-4V rather than 316L. The results of their work offer a potential explanation for the trend seen in Figure 84, but different materials properties between the two metals may result in different behaviours. The purpose of the models in this work was to detail what terms are most significant to the relative density (and how these might also affect resistivity) rather than understand exactly why they produce the responses seen in Figure 84. Given that these models do indicate correlation with resistivity, it is worth investigating them in further detail to see if the explanation for the trends, such as given by A. M. Khorasani, are applicable.

7.4. Primary cell spacing

7.4.1. Introduction

Grain boundaries are interfaces between two different crystalline regions that have different orientations to each other. At this interface there is a disruption to the periodic crystal lattice that increases the resistivity of a material [64], [65]. SLM 316L stainless steel has columnar grains, within which are cellular structures with cells typically on the order of 0.5 µm-2 µm defined by sub-grain boundaries that separate the cells [66]. These cells are formed due to the fast-cooling rates during solidification forming dendrites and insufficient time for diffusion of heavier atoms such as molybdenum [66]. The cellular boundaries have also been associated with high concentrations of dislocations and residual stresses. A report by C. Silbernagel *et al.* showed that cellular structures on the same order of magnitude play a large part in determining the resistivity of the SLM alloy AlSi10Mg [131]. Generally, they found that the greater the number of these sub-grain boundaries along the conduction path, the higher the resistivity.

In this work the distances between the centres of neighbouring cells (also known as the primary cell spacing) were measured at different locations to give an indication of the number of sub-grain boundaries. Average values were taken for all seventeen samples to determine if they had a relationship with the measured resistivity values. As

these were destructive tests that required cross sectioning the samples, these measurements were not done on the same samples used to calculate resistivity. Instead, they were carried out on smaller representative samples, printed in the same batches using identical build parameters and the same width (13 mm) and thickness (250 µm) but different length (50 mm instead of 200 mm).

According to D. Wang *et al.*, the growth direction of cellular dendrites in SLM 316L vary within the melt pool and follow the highest thermal gradient, which is dictated by the laser and the path of laser scanning [74]. They observed this on tensile specimens built using similar ranges of process parameters as in this thesis, although they did not give information about the build angle. Dendrite orientation was also reportedly influenced by factors such as the preferred growth orientation of the crystal structure, which varied at different regions within the melt pool, and Marangoni flow which could change the heat flux direction and thus growth orientation. To capture dendrites in different orientations and obtain a better average value for the primary cell spacing, measurements were carried out on two planes of each sample. How these planes corresponded to the axes of the build chamber are shown in Figure 32.. Multiple images were taken of each plane.

7.4.2. Comparison of measurement methods

As reported by others [66], [67], [74], [75], cell spacing can vary within a single melt pool due to factors including Marangoni convection altering the heat flux direction and varying cell orientation which follows the maximum temperature gradient (e.g. towards the build plate near the bottom of the melt pool). This results in an expected heterogeneous distribution of cell spacing as shown by locations A and B in Figure 85. However, electrical resistance is a bulk property that depends on the volume average of potential microstructural factors like cell size. Therefore, cell spacing was measured and averaged at randomly sampled different positions in the cross-section micrographs with the area method and averaged over the full field of view with the image analysis method. The area method is based on the ISO standard 643:2020 and has heritage of being used specifically on SLM 316L stainless steel [74], [166], [180]. At least two micrographs were

imaged per sample, except for the 0° sample 5 due to poor image quality. The image analysis technique was developed specifically for this work and follows the same principle as the area method but measured the total number of cells within an image rather than randomly sampled positions. It was believed better accuracy could be achieved by measuring a greater number of cells but, to validate this, both methods were compared, the results of these are shown in Figure 86.

The error bars in Figure 86 are the standard deviations of the mean values and represent the spread of the results. There are no error bars for sample 5 because grains that could be clearly resolved could only be seen in one image.

To reiterate, multiple sources stated that primary cell spacing was dependent on the cooling rate, which itself was dependent on numerous factors including the dimensions of the specimen and the process parameters. Directly comparing the results of this work with literature values is difficult due to these many varying factors but gives an indication of the range of expected values. Various values found in the literature are presented in Table 29. Comparing these values with those from this work (Figure 86) shows that they are overlapping.

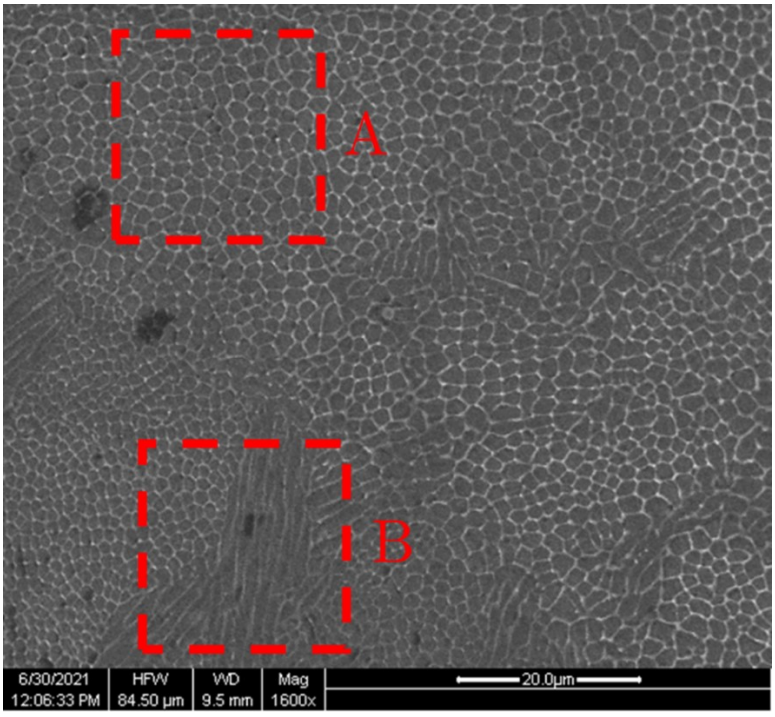

Figure 85: 1600x magnification SEM image of the 90° sample 8 showing the differences in size and orientation of the cellular microstructure seen in a single image

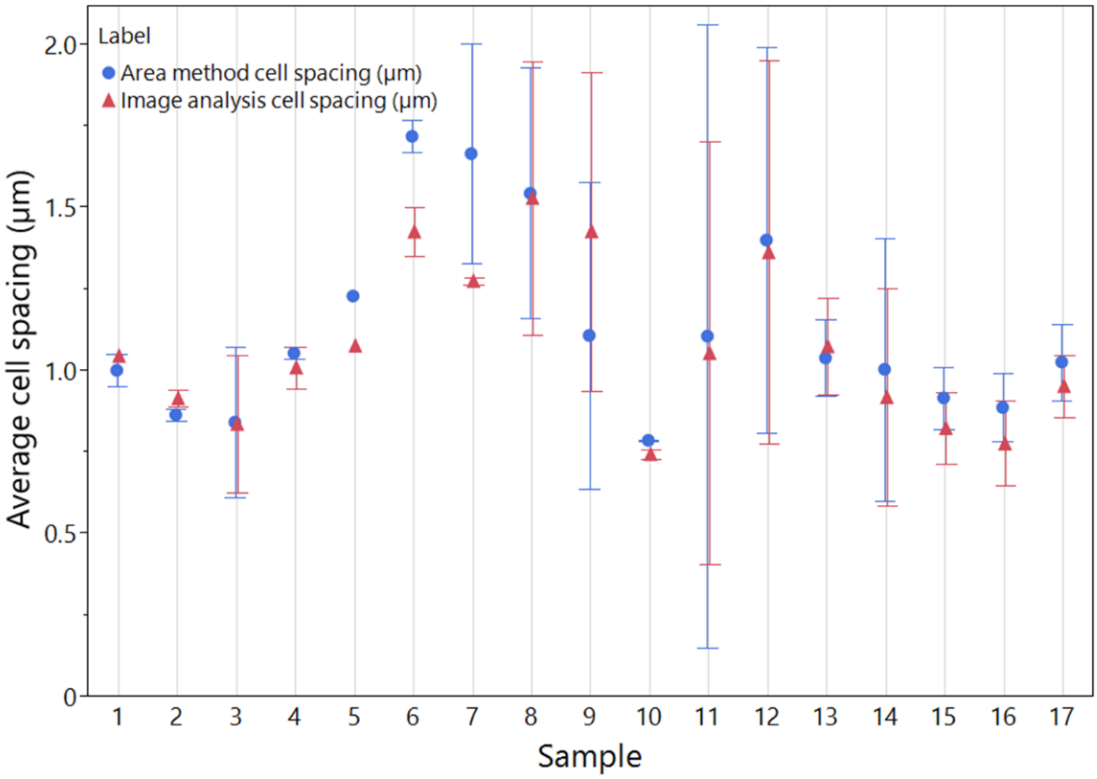

Figure 86: Plot showing the average primary cell area as determined by both image analysis and the area method for all 17 sample

Table 29: Table detailing the primary cell spacings and process parameters of 316L stainless steel samples found in literature

Author	Cell size (µm)	Laser power (W)	Scanning speed (mm/s)	Hatch spacing (mm)	Layer thickness (mm)	Build angle (°)	Sample shape
K. Saeidi. et al [66]	0.5	195	800	0.1	0.02	-	cuboid
D. Wang. et al [74]	0.74	300	700	0.08	0.03	-	tensile
	0.52	300	800	0.08	0.03	-	tensile
	0.35	300	1000	0.08	0.03	-	
	0.31	300	1200	0.08	0.03	-	
E. Liverani. et al [25]	>2	100,150	700	0.05,0.07	-	45, 90	tensile
I. Yadroitsev. et al [75]	0.4-1.2	50	80-280	N/A	0.08	-	single track
This work	0.74-1.71	150, 170, 190	500, 750, 1000	0.05, 0.075, 0.1	0.02, 0.03, 0.04	0, 45, 90	thin wall

For both measurement methods, most of the samples have similar mean values and standard deviations in Figure 86. Given that the area method is based on a standard, the fact that the image analysis results are very similar increases confidence for future

use. The image analysis method, if scripted, has the potential for faster analysis of multiple images which could be valuable for future work. While there are large standard deviations observed for some samples, that these are seen in both techniques indicates that these differences may be due to the sample inhomogeneity, rather than measurement error.

Although there was good agreement in general, some differences were further analysed. Samples 5, 6, 7, and 9 show notable differences between the mean values for each technique. A possible cause for this, as introduced previously, was the different sample sizes used. For a more direct comparison, the primary cell spacing was calculated on the exact same size area as shown in Figure 87 which shows an SEM image of the 0° sample 6. This sample was chosen because there was a notable difference between the primary cell spacing values calculated using the two methods as seen in Figure 86. Measurements were carried out on the area highlighted in red in Figure 87 for both methods, and the whole picture using the image analysis technique. The results of the different analysis techniques are presented in Table 30

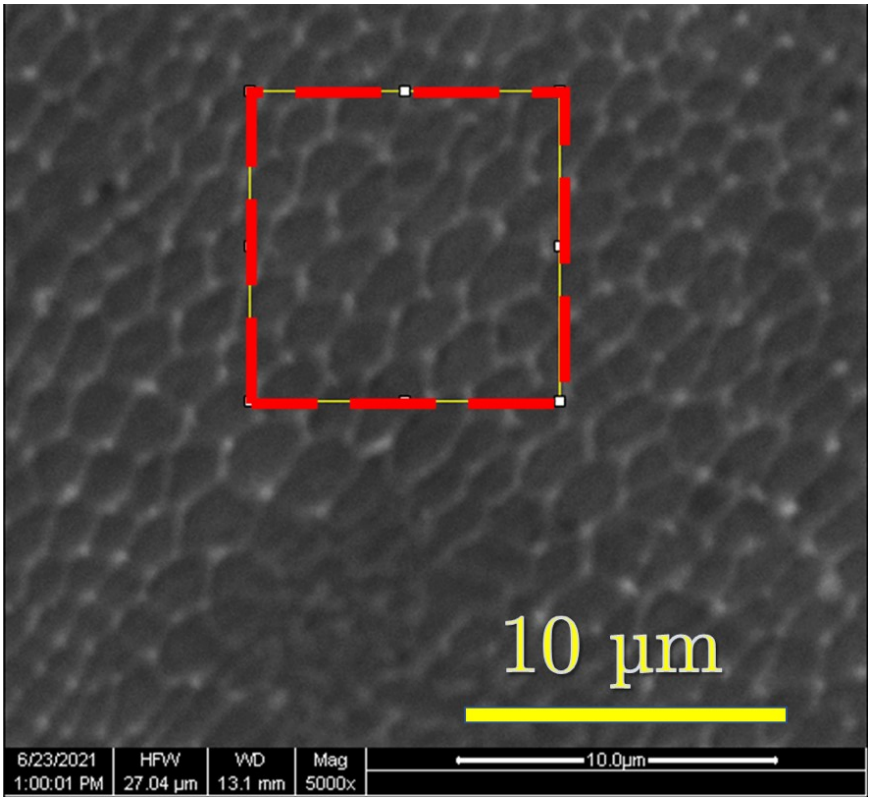

Figure 87: SEM image of 0° sample 6 with a highlighted area showing the region that was compared using both the area method and image analysis techniques

Table 30: Table comparing the primary cell spacing measured using the area method and image analysis on an area of the same size

Method	Primary cell spacing (µm)
Area analysis (square)	1.61
Image analysis (square)	1.59
Image analysis (full)	1.40

The values for the primary cell spacing for both methods are nearly identical when comparing an area of the same size. However, the dendrite spacing of the full image, calculated using the image analysis technique, is lower. This is hypothesised to be because the larger area can account for more cells and thus is more representative of the average cell spacing across the full sample. Both methods follow the same basic principle and provide comparable results for the same area. However given that the image analysis technique could look at more cells over a greater area and allow for faster analysis this was selected as the method for this thesis.

7.4.3. Primary cell spacing and energy density

Figure 88 shows the primary cell spacing, coloured by build angle, against energy density. Build angle may affect cell spacing as it may affect the heat transfer and cooling rates that ultimately control cell spacing. No clear trends can be seen for 0° and 45° samples, although there are only three data points for the 45° samples. For the 90° samples cell spacing appears to increase above an energy density of 150 J/mm^3. There are however only two samples above 150 J/mm^3, so it is difficult to know for certain if these points are part of a larger trend or are outliers.

Both D. Wang *et al.* and Yadroitsev *et al.* reported that primary cell spacing of SLM 316L was strongly influenced by energy density [74], [75]. D. Wang *et al.* produced tensile specimens and kept the laser power (300 W), layer thickness (30 µm) and hatch spacing (80 µm) constant while varying the scanning speed between 700 mm/s – 1200 mm/s. They gave no information about the build angle of their specimens. The ranges of these parameters are similar to those used in this work and the energy density range investigated was within, but smaller than, the range covered in this thesis.

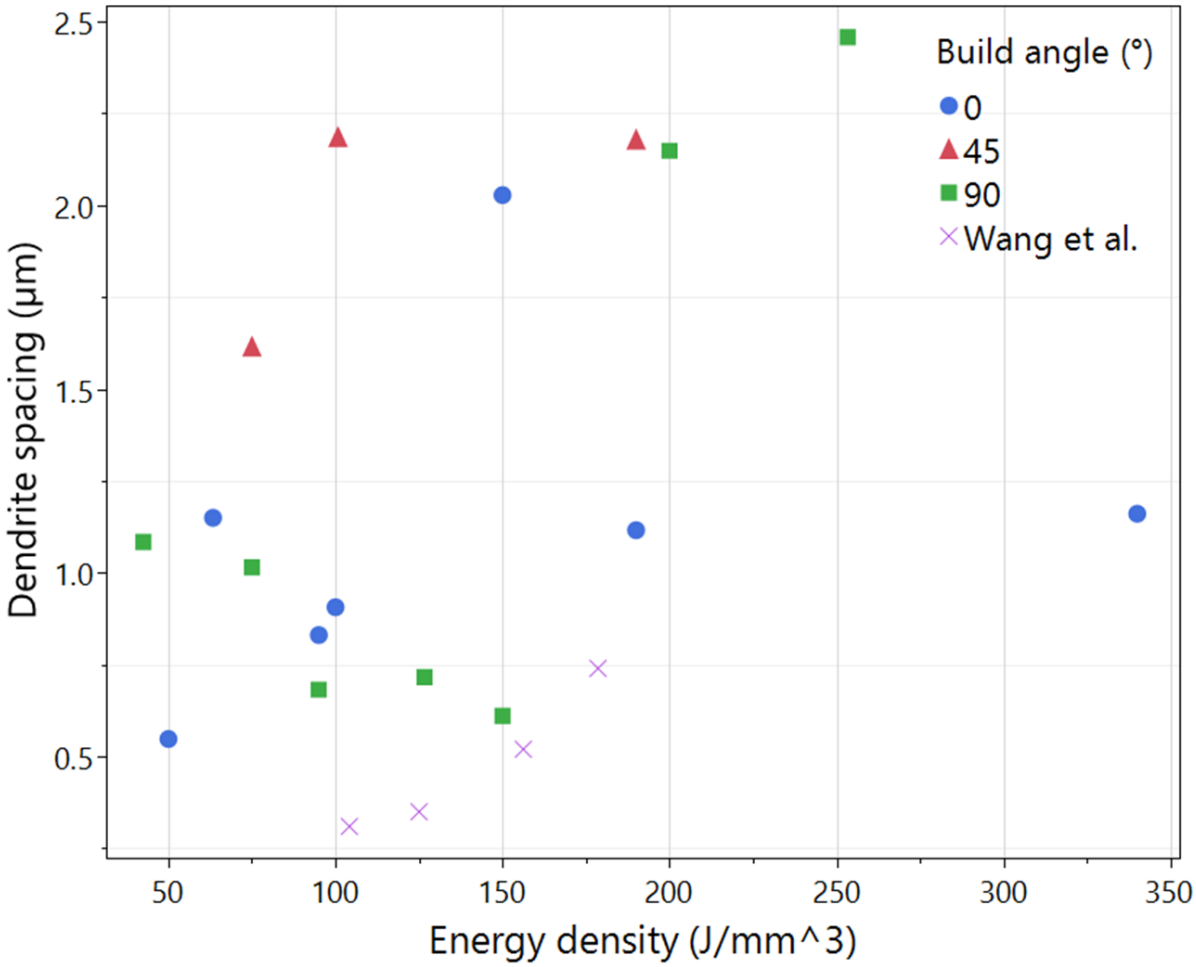

Figure 88: Graph showing the relationship between primary cell spacing and energy density for all 17 samples and the results by D. Wang *et al.*, coloured by build angle

As the dimensions and build angles are unknown, only general trends are compared. They found that as the energy density increased from 104.17 J/mm^3 to 178.57 J/mm^3 the primary cell spacing also increased from 0.31 µm to 0.74 µm. Generally, this was because increasing energy density resulted in higher temperatures which provided more energy for the growth of the cellular dendrites. It is worth noting that Yadroitsev *et al.* found that cell spacing varied significantly depending on where in the melt pool it was measured. For example, at scanning speeds of 800 mm/s the cell spacing at the bottom of the melt pool close to the fusion boundary was roughly 0.6 µm, but at the top of the melt pool (no less than 10 µm from the surface) it was roughly 1µm. Location within the melt pool was not considered when taking images of cells, although as the purpose was to measure an average cell size rather than at specific locations.

7.4.4. Primary cell spacing and resistivity

To assess the potential relationship between resistivity and the average primary cell spacing of the samples, these were plotted in Figure 89. To avoid convoluting the results with temperature, interpolated resistivity values from quadratic fits at specific temperatures (300 K, 500 K, 700 K and 1000 K) were used. The temperature at the top of each plot denotes the fitted temperature. It appears that, as the temperature increased, so did the resistivity. The reasoning for this trend was explained in section 7.2.1.

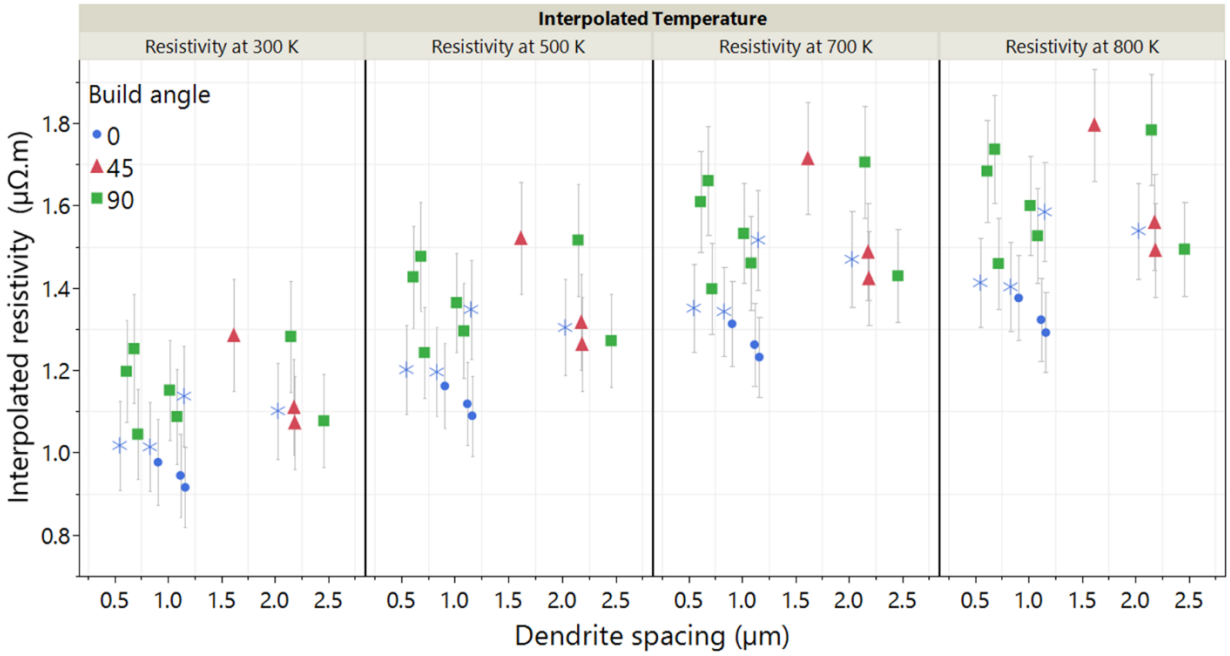

Figure 89: Graph showing resistivity against average primary cell spacing at 300 K, 500 K, 700 K and 800 K for all 17 samples, coloured by build angle. * points are the 0° samples with relative density below 98%

In Figure 89, it was expected that as the dendrite spacing increased, the resistivity would decrease. The mechanism for this expectation was that, as the average dendrite spacing increased, the number of sub-grain boundaries along the conduction path of the electrons would decrease and thus so would the number of deviations to the periodic lattice. Thus, the resistivity would also decrease. However, at each temperature there does not appear to be a strong trend between resistivity and the primary cell spacing. The previous section showed a strong correlation between relative density of a part and resistivity. Even when considering only the samples with a relative density greater than

98% there still does not appear to be a strong trend between resistivity and dendrite spacing. This lack of the expected trend may indicate that the grain boundaries did not contribute significantly to the resistivity of the samples. Although the resistivity of the 45° samples appears to decrease with increasing dendrite spacing, as there are only three data points this cannot be definitively stated as a trend.

To reiterate, C. Silbernagel *et al.* found strong trends between resistivity and build angle for the alloy AlSi10Mg manufactured using SLM [131] because of differences in primary cell orientation. The needle-like cellular dendrites were orientated towards the Z-axis build direction which for the 90° samples was parallel to the conductive pathway but for the 0° samples was perpendicular. Thus for the 0° samples electrons saw more of these boundaries and had a higher resistivity than the 90° samples. For this thesis the expected cell orientation was also in the Z-axis build direction, however for all build angles this was perpendicular to the conductive pathway in resistivity testing. Thus electrons would encounter similar amounts of cell boundaries regardless of build angle, which may explain the lack of any strong effect of build orientation on resistivity.

7.4.5. Model linking primary cell spacing and SLM process parameters

The previous section showed that there was not a strong link between primary dendrite spacing and resistivity within the bounds of this experiment, unlike results report by C. Silbernagel *et al.* for SLM AlSi10Mg. Nevertheless, in order to better understand the effect of process parameters on dendrite spacing, a multiple linear regression model was created for cell spacing and laser power, scanning speed, hatch spacing, layer thickness and build angle. This model was created using the same method shown in section 5.5. The data in Table 31 shows that the model generated is reliable, as it has a low value for the root mean square error, a high R^2 value and F ratio and a very low p-value. The purpose of this model was to show which input factors are most significant to the primary dendrite spacing, and the shape of the responses. The significance of the input parameters and their interactions are shown in Figure 90.

Table 31: Table showing the key parameters for the multiple linear regression model generated for the primary cell spacing

Mean of Response	1.34
Root Mean Square Error	0.25
R^2	0.84
F ratio	33154.78
p-value	<.0001

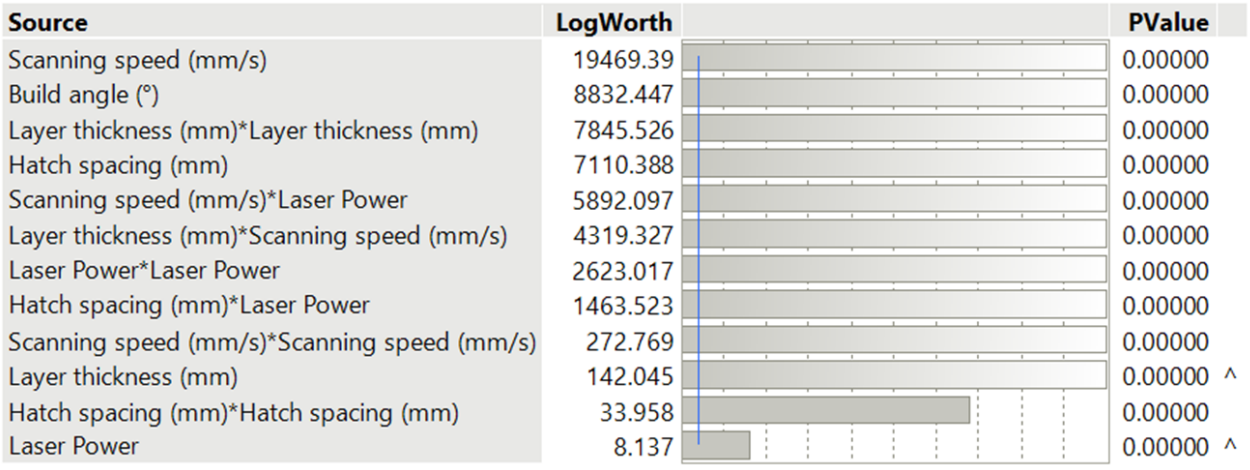

Source	LogWorth	PValue
Scanning speed (mm/s)	19469.39	0.00000
Build angle (°)	8832.447	0.00000
Layer thickness (mm)*Layer thickness (mm)	7845.526	0.00000
Hatch spacing (mm)	7110.388	0.00000
Scanning speed (mm/s)*Laser Power	5892.097	0.00000
Layer thickness (mm)*Scanning speed (mm/s)	4319.327	0.00000
Laser Power*Laser Power	2623.017	0.00000
Hatch spacing (mm)*Laser Power	1463.523	0.00000
Scanning speed (mm/s)*Scanning speed (mm/s)	272.769	0.00000
Layer thickness (mm)	142.045	0.00000 ^
Hatch spacing (mm)*Hatch spacing (mm)	33.958	0.00000
Laser Power	8.137	0.00000 ^

Figure 90: Plots showing the LogWorth vs. the source for the model of primary cell spacing

Scanning speed was identified as the input parameter that has the most significant impact on the primary dendrite spacing. Scanning speed also has interactions with both laser power and layer thickness. Although significant, scanning speed was not the most significant term in the resistivity models in Figure 75. Laser power was amongst the most significant terms to the resistivity model, yet is the least significant to the cell spacing model. If cell spacing and resistivity shared significant terms, it would be expected for one to correlate with the other. The fact that they do not further supports the observation that cell spacing does not strongly influence the resistivity within the range of parameters tested in this work.

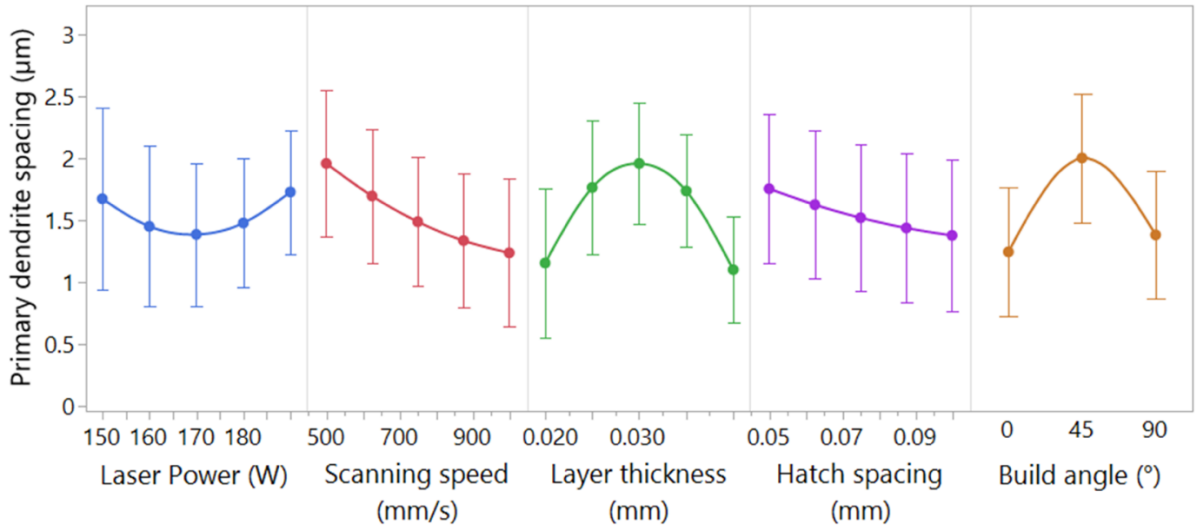

Figure 91: Main effects plots showing the model predicted responses on primary cell spacing for each of the input parameters

The model predicted responses for primary cell spacing at different input parameters are shown in Figure 91. The errors bars on each plot represent the standard error. The results show that as the scanning speed increases, the dendrite spacing decreases. This is similar to trends found by both D. Wang *et al.* and I. Yadroitsev *et al.* I. Yadroitsev *et al.* investigated how scanning speed and preheating temperature affected the primary cell spacing of single tracks of 316L stainless steel, using analysis of variance (ANOVA) to determine what effects were most significant [75]. The laser power (50 W), spot diameter (70 µm) and powder layer thickness (80 µm) were all kept constant while the preheating temperature was varied at either 80°C or 900°C and the scanning speed between 80 mm/s to 280 mm/s. These conditions and ranges were notably different than those used in this thesis. Particularly the scanning speeds, which in this work were much higher and varied from 500 mm/s – 1000 mm/s. However, given that it was the same material and process as used in this thesis, the trends of their results are worth comparing. Overall I. Yadroitsev *et al.* found that both scanning speed and preheating temperature significantly affected the primary cell spacing and that the cell spacing decreased by 25-40% as scanning speed was increased. This decrease was independent of the preheating temperature. This decrease in cell spacing was explained by a higher presumed cooling rate (the product of solidification rate R and the temperature gradient G) at higher scanning speeds.

This was expanded upon by D. Wang *et al.* who also investigated how process parameters affected the primary cell spacing of SLM 316L stainless steel [74]. In general D. Wang *et al.* also found that as the scanning speed increased, the primary cell spacing decreased. Increasing the scanning speed increased the solidification rate (R) in the melt pool, increasing the nucleation rate which refined the microstructure and decreased the cell spacing. On the other hand, decreasing the scanning speed increased the energy density, decreasing the cooling rate and increasing the cell spacing. M.-S. Kim *et al.* gave a similar explanation for the effect of hatch spacing on the cell spacing of the SLM AlSi10mg alloy [181]. The smaller the hatch spacing, the greater the overlap between adjacent tracks, which resulted in a higher energy density, lower cooling rate and thus higher cell spacing.

Although no reports were found in literature for the effects of other process parameters, this relationship between R*G and the primary cell spacing can also explain their responses on primary cell spacing. For example, the interaction between scanning speed and laser power (Figure 92) shows that as the laser power increases the impact of scanning speed on cell spacing decreases.

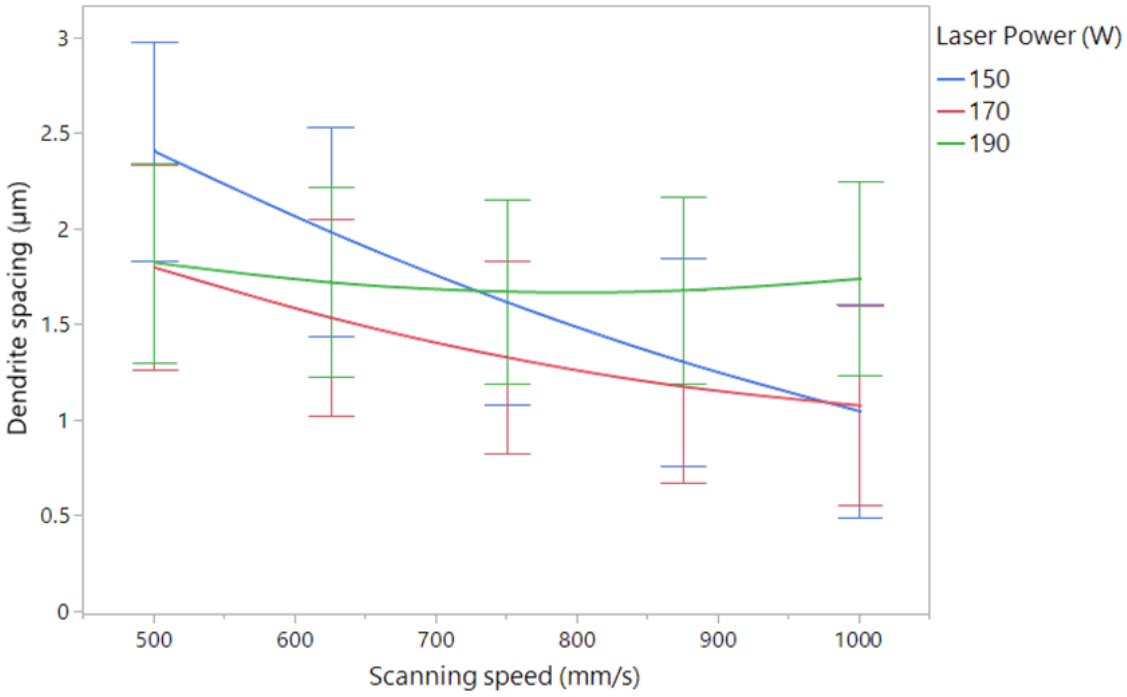

Figure 92: Graph showing the interaction between scanning speed and laser power on primary cell spacing

At low laser powers, the energy input by the laser is low and so the energy density is low and cooling rate is high. Thus, increases to the solidification rate caused by increased scanning speed have large effects on the primary cell spacing. However at high laser powers, the increase in solidification rate provided by increased scanning speed is offset by the increase in the energy density and the decrease in cooling rate, reducing the impact of scanning speed on cell spacing.

7.5. Conclusions

The resistivity of the SLM samples was higher than reported values for cast 316L over a similar temperature range. Samples oriented at 0° had slightly lower resistivity values than the 90° and 45° samples.

Only 45° and 90° samples had >98% relative density and showed no strong correlation with resistivity or energy density. Generally, the 0° samples relative density increased with energy density, and as the relative density increased the resistivity decreased. This was likely because increasing porosity decreased the lattice periodicity and increased the conduction paths of the electrons. An exception to this was sample 10, which had a low resistivity that defied the trend at a relative density of 83.5%. Multiple linear regression models for resistivity and relative density shared significant input factors, notably the square of the laser power suggesting that relative density and an effect on resistivity,

Despite literature reports to the contrary for the SLM alloy AlSi10Mg by C. Silbernagel *et al.*, no strong trend was found between primary cell spacing and resistivity for 316L stainless steel in this work.

8. Results and Discussion – Multiphysics modelling

8.1. Introduction

The motivation for this thesis came from the need for improved predictions from multiphysics simulations of the resistojet developed by F. Romei *et al.* [182]. They created a 3D model and used emissivity values for cast polished 316 steel found in literature for the surface emissivity of the SLM resistojet heat exchanger [183]. At steady state conditions, they predicted temperatures that differed by 5%-20% from experimental measurements with a root mean square error of roughly 10% [182]. They noted that the simulation results were particularly sensitive to the emissivity values used, and suggested this was likely due to the differences between the emissivity and resistivity of actual SLM materials properties and the values for cast materials available in the literature.

An aim of this thesis was therefore to obtain accurate values for the emissivity and resistivity of SLM 316L steel. This chapter presents computational models that simulate the experiments carried out in this thesis and that used the measured emissivity and resistivity values and sample geometries measured using different techniques (nominal CAD, callipers, and CT scanning/image analysis). The predicted temperature results from these models were compared with model predictions based on emissivity and resistivity for cast materials, and also with experimental values.

8.2. Background of COMSOL Multiphysics

8.2.1. Overview

The software chosen to model the experiment was COMSOL Multiphysics, the same software used by F. Romei *et al.* [184]. COMSOL is a finite-element analysis software that was used to simulate the resistojet as it is capable of modelling highly coupled physics that occur during the resistojet operation.

As stated by F. Romei *et al.*, there were three initial steps needed to run a simulation in COMSOL Multiphysics [184]. First, the space dimension of the problem was defined. This could be 3D, 2D axisymmetric, 2D, 1D axisymmetric, 1D or 0D. Within this space the geometry of the component that was studied was then either created using the tools within COMSOL or imported. In this work a 3D model of the experimental setup, imported from the software Solidworks, was used in the multiphysics simulation.

Every component of this geometry had both a domain representing the bulk volume and a boundary representing the surface, to which properties could be assigned. The physics modules of the problem were then selected and assigned to the relevant domains. It is these modules that contained the basic equations that are solved by the software. As this was a multiphysics software, multiple modules could be selected. The physics modules used to simulate the experimental test setup were the heat transfer in solids module and the electric current module. The equations that dictated how these models worked are detailed in the next section. The third step required deciding whether the study was stationary or time dependent. After the initial setup, details of the model needed to be added including applying materials and properties, assigning initial and boundary conditions on both domains and boundaries, and dividing the geometry with a mesh.

8.2.2. Heat transfer in solids module

The heat transfer in solids module was used to model the heat transfer by conduction and radiation. The basic equation solved for temperature by the heat transfer

module was equation [44]. This equation is based on the principle of the conservation of energy and that changes to the internal energy of a system are equal to the difference between heat added and work done by the system [185], [186].

$$\boldsymbol{\rho C_p\left(\frac{\delta T}{\delta t}+u_{trans}\cdot\nabla T\right)+\nabla\cdot(q+q_r)=-\alpha T:\frac{dS}{dt}+Q} \quad [44]$$

Where ρ (kg/m^3) is the density, C_p (J/(kg.K)) is the specific heat capacity at constant stress, T (K) is the absolute temperature, u_{trans} (m/s) is the velocity vector of the surrounding fluid media, q (W/m^2) is the heat flux by conduction, q_r (W/m^2) is the heat flux by radiation, α (1/K) is the coefficient of thermal expansion, S is the stress tensor and Q is additional heat sources. The second term on the left-hand side of equation [44] is the convection term in the equation. However, the run assuming vacuum conditions and so this term was removed. The stress tensor was also removed as it was assumed that the mechanical and thermal properties of the material were isotropic. Thus equation [44] could be rewritten as equation [45].

$$\boldsymbol{\rho C_p\frac{\delta T}{\delta t}\cdot\nabla T+\nabla\cdot(q+q_r)=Q} \quad [45]$$

The heat flux by conduction was described through Fourier's law of heat conduction, given in equation [46]

$$\boldsymbol{q=-\alpha\nabla T} \quad [46]$$

To keep the model as simple as possible, rather than modelling the hatch vacuum chamber that the experiment was conducted in, the boundary condition surface-to-ambient radiation was applied to all radiating surfaces. This assumed that the environment is a blackbody emitter at a constant uniform temperature, which matched an assumption made in the emissivity test standard upon which the experimental method was based [174]. The heat flux from surface to ambient radiation was calculated using equation [47].

$$\boldsymbol{q=\varepsilon\sigma\left(T_{amb}^4-T^4\right)} \quad [47]$$

Where ε is the surface emissivity, σ is the Stefan-Boltzmann constant and T_{amb} is the ambient temperature. For this model the ambient temperature was held at the default temperature of 293.15 K.

8.2.3. Electric current module

The electric current module was used to calculate the heat generated from joule heating which was the term Q in equation [45]. When considering stationary electric currents, heat generated from a current source is calculated through equations [48] and [49]

$$\boldsymbol{Q} = \nabla \cdot \boldsymbol{J} \quad [48]$$

$$\boldsymbol{J} = \sigma \boldsymbol{E} + \boldsymbol{J_e} \quad [49]$$

Where J (A/m^2) is the current density, J_e (A/m^2) is an externally generated current density, σ (S/m) is the electrical conductivity (and the reciprocal of the resistivity) and E is the electric field. Boundary conditions were applied to the model to establish the ground (E = 0) and input current. These were applied as shown in Figure 93. All other domains had the boundary condition of electrical insulation applied, equivalent to $n.J = 0$ meaning that no other electric current could flow into or through the boundaries [186]. For sake of ease this model also assumed that there was 100% contact between the different conducting surfaces.

8.2.4. Model Geometry

The model used to simulate the experimental setup was a 3D CAD model imported from the software Solidworks. This model was originally used for manufacturing the individual components. An exploded view of this model is shown in Figure 93. COMSOL contained a materials library from which materials and their properties could be applied to different domains and boundaries of the model. The material labelled 316L [solid, polished], was assigned to the metal tabs used to supply electrical power to the sample (label (b) in Figure 93) and the material MACOR was assigned to the ceramic tabs (labelled (a) in Figure 93).

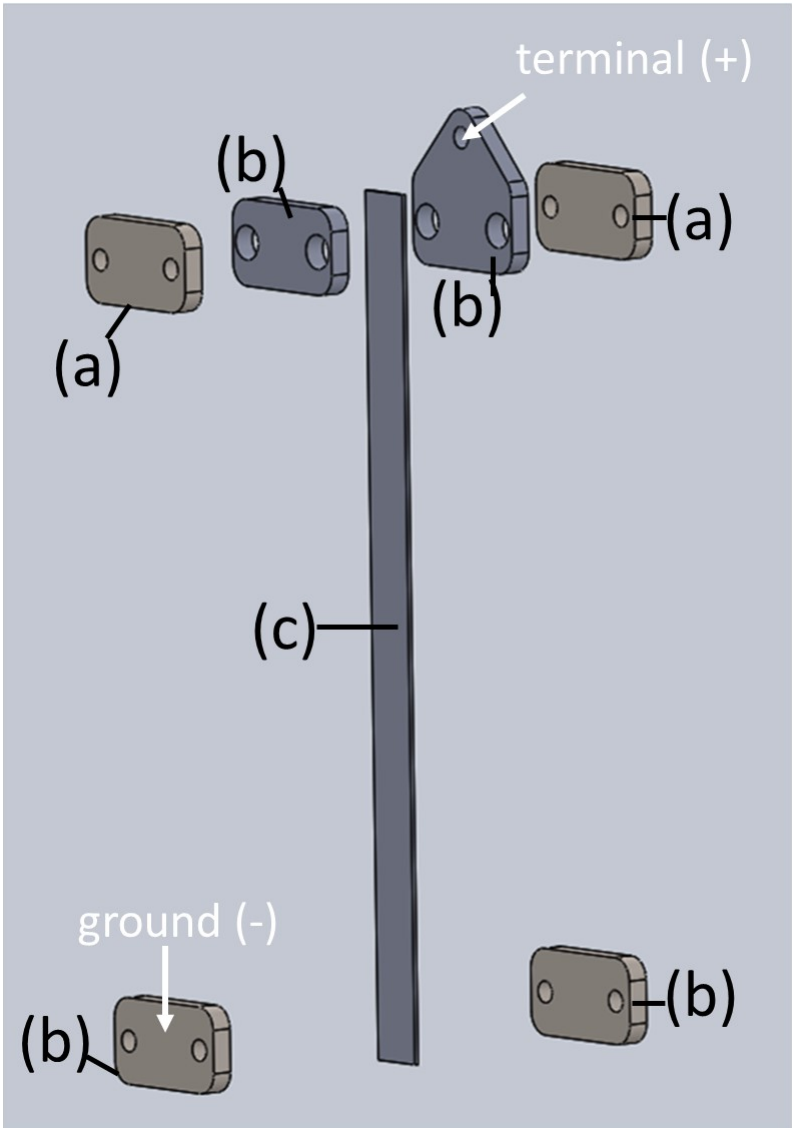

Figure 93: Picture showing an exploded view of the CAD model imported from Solidworks into COMSOL. The different components are (a) the ceramic Macor tabs (b) the cast 316L stainless steel tabs and (c) the SLM 316L test strip. The locations where the terminal and ground boundary conditions are labelled in the image

The test coupon (labelled (c) in Figure 93) was assigned the material 316L [solid, polished]. The properties for COMSOL materials library were taken from a paper by C. Isetti *et al.* for emissivity and papers by M. Rouby *et al.* and A.F. Clark *et al.* for the resistivity [187]–[189]. For later simulations, these properties were substituted with the measured values reported in this thesis. As found in section 5.4, the surface of the SLM samples was covered in peaks and valleys that increased the surface and cross-sectional areas significantly compared to the nominal CAD geometries on which the samples were

based. The dimensions of the test strip were changed to reflect either the nominal geometry in the CAD files used for additive manufacture, the geometry determined through calliper measurements, or the geometry determined from CT scanning.

A mesh was automatically generated by the COMSOL software that was adapted to the physics modules being used. The element size of the mesh was originally set to the finest size and the volume maximum temperature of the SLM sample domain measured. To reduce the computational time, coarser mesh element sizes were applied, and simulations were repeated. This coarsening was continued until the maximum surface temperature predicted on the coarse mesh was less than 0.99 of that on the finest mesh. This resulted in a coarsest mesh of tetrahedral elements, the number of elements for each geometry are shown below in Table 32. For each geometry the maximum element size was 11.9 mm, and the minimum was 0.867 mm.

Table 32: Table showing the different mesh elements generated for the different sample geometries modelled

Geometry	Domain elements	Boundary elements	Edge elements
Nominal geometry	79393	27536	2251
Calliper determined geometry	41864	14985	1759
CT scanning determined geometry	110136	39217	2343

8.3. Simulation overview

The goal of replicating the experimental setup in COMSOL was to validate the model by attaining similar temperature values to the experiments. Comparisons were also made against models using the literature values for emissivity and resistivity that F. Romei *et al.* had used when simulating the resistojet, to determine whether the SLM measured values yielded predictions in better agreement with experiments [182].

As the method used to measure the emissivity and resistivity was identical for all 17 samples, a single simulation of the 0° sample 13 is presented here as representative of all models of other samples. As previously discussed in section 6.2, due to experimental error, samples at lower input currents were not given enough time to reach steady state conditions resulting in incorrectly high emissivity values. For sample 13, this corresponded to input currents up to 32 A. Thus, only emissivity values above 32 A

were manually entered into the model, with emissivity values at lower input currents automatically extrapolated in the software using a linear fit. Stationary rather than time dependent studies were chosen for the models. A stationary study is one in which the variables do not change over time. Although in reality the experimental temperatures measured were time dependent, the steady state solution was equivalent to measuring the values of the experiment under steady state conditions, as required by the test standard [174]. An auxiliary sweep was applied to increase the input current of the model in equal steps after solving for the previous input current, rather than manually changing the values and re-solving every time. An initial input current of 8 A was used and increased in steps of 8 A until a final current of 80 A was reached. An example of the temperature field for a solved model is shown in Figure 94.

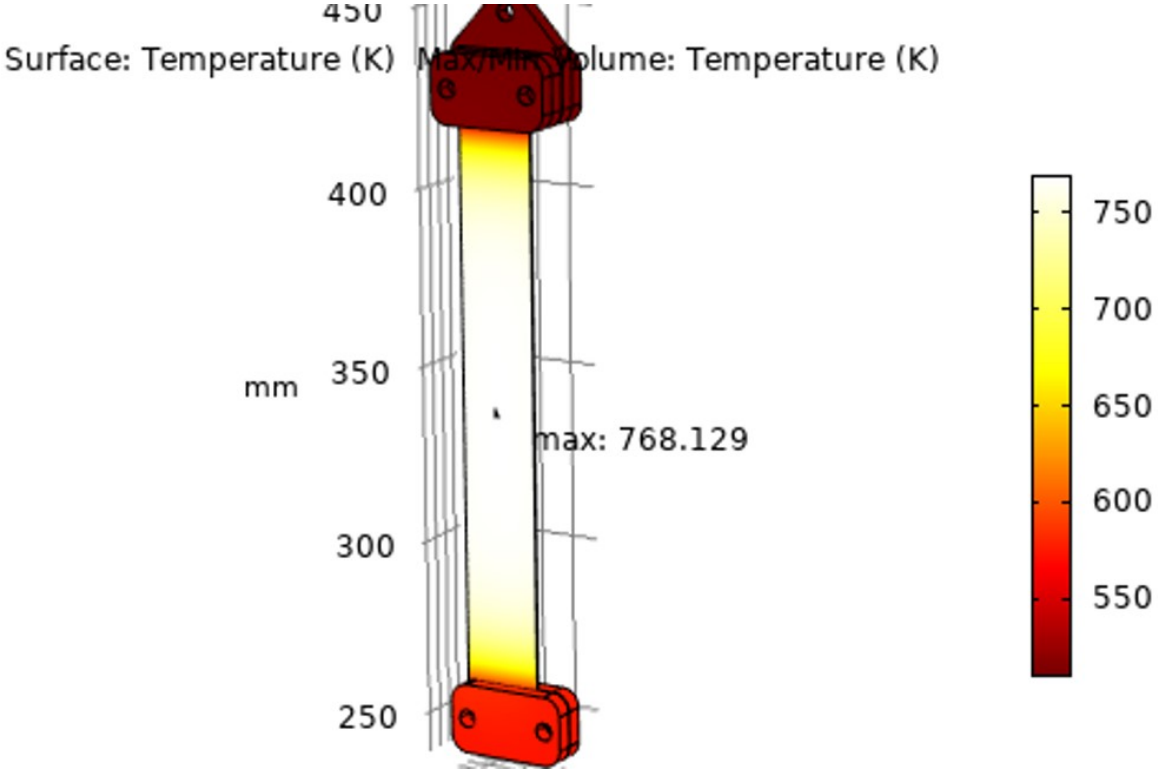

Figure 94: Temperature plot of a model using the CT determined geometry and values at an input current of 80 A

8.4. Summary of different simulations

Several different simulations were run to both validate the model and compare against simulations that used literature values. A summary of these different simulations is shown in Table 33.

Table 33: A table summarising the different simulations runs in terms of the emissivity and resistivity values used and the geometry of the test coupon

Simulation	Emissivity values	Resistivity values	Geometry
1	CT determined surface area	CT determined surface area	Nominal CAD
2	CT determined surface area	CT determined surface area	Calliper determined
3	CT determined surface area	CT determined surface area	CT scanning determined
4	F. Romei *et al.* [183]	COMSOL literature cast [188], [189]	CT scanning determined
5	COMSOL literature cast [187]	COMSOL literature cast [188], [189]	Nominal CAD
6	calliper determined surface area	calliper determined surface area	Calliper determined
7	F. Romei *et al.* [183]	COMSOL literature cast [188], [189]	Nominal CAD

Table 34: Dimensions of the different sample geometries used in simulations

Measurement method	Width (mm)	Thickness (mm)	Cross-sectional area (mm^2)
Nominal CAD	13.00	0.25	3.25
Callipers	13.22	1.05	13.83
CT scan/image analysis	22.48	0.56	12.49

The first tests done to validate the model used the experimentally determined values for emissivity and resistivity that were calculated using surface area determined by CT scanning and image analysis. Three different geometries were tested using these values because, as seen in equation [48], the geometry affected the heat contribution from joule heating and thus the overall results. The nominal CAD and calliper geometries, although less accurate than CT scanned geometries, were easier to obtain and may be more commonly used in future work that considers more complex geometries, such as the STAR resistojet. The dimensions of each of the geometries are shown in Table 34Table 34. The actual CT scan/image analysis geometry had numerous

peaks and valleys which could not be captured in the simple 3D models. Instead, an artificial thickness and width were selected to result in the same surface and cross-sectional areas as the actual samples. Simulations were also run using only the COMSOL literature values for emissivity and resistivity and the nominal CAD geometry as this represented the default settings as a baseline comparison.

As detailed in section 6.6, the surface area of the test strips was strongly correlated with the emissivity. Although the emissivity test standard recommended measuring the emissive area of the samples using callipers, these produced impossibly high values for the emissivity [146]. However the solution to this, measuring the surface area with CT scanning and image analysis techniques, was a labour-intensive process that may not be easy to replicate in future work potentially focused on alternate geometries.

F. Romei *et al.*, when simulating the resistojet, used literature values for polished 316L stainless steel taken from a Calex electronics datasheet and extrapolated the in-built resistivity values from 873 K to 1300 K [183]. These values were also used in simulations, to see if the measured SLM values produced more accurate temperature results. They also used emissivity values from T. S. Hunnewell *et al.* [120], although F. Romei *et al.* did not report which emissivity value they used (T. S. Hunnewell *et al.* report multiple values for different roughnesses and temperatures) nor did F. Romei *et al.* report the temperature values this model reached.

8.5. Temperature results comparison

8.5.1. Overview

A summary of the maximum temperature values for each input current obtained by each of the different simulations, as well as the experimental values, is shown in Figure 95. As previously mentioned, the experimental values for sample 13 up to 32 A were lower than they would have been under steady state conditions due to short test times.

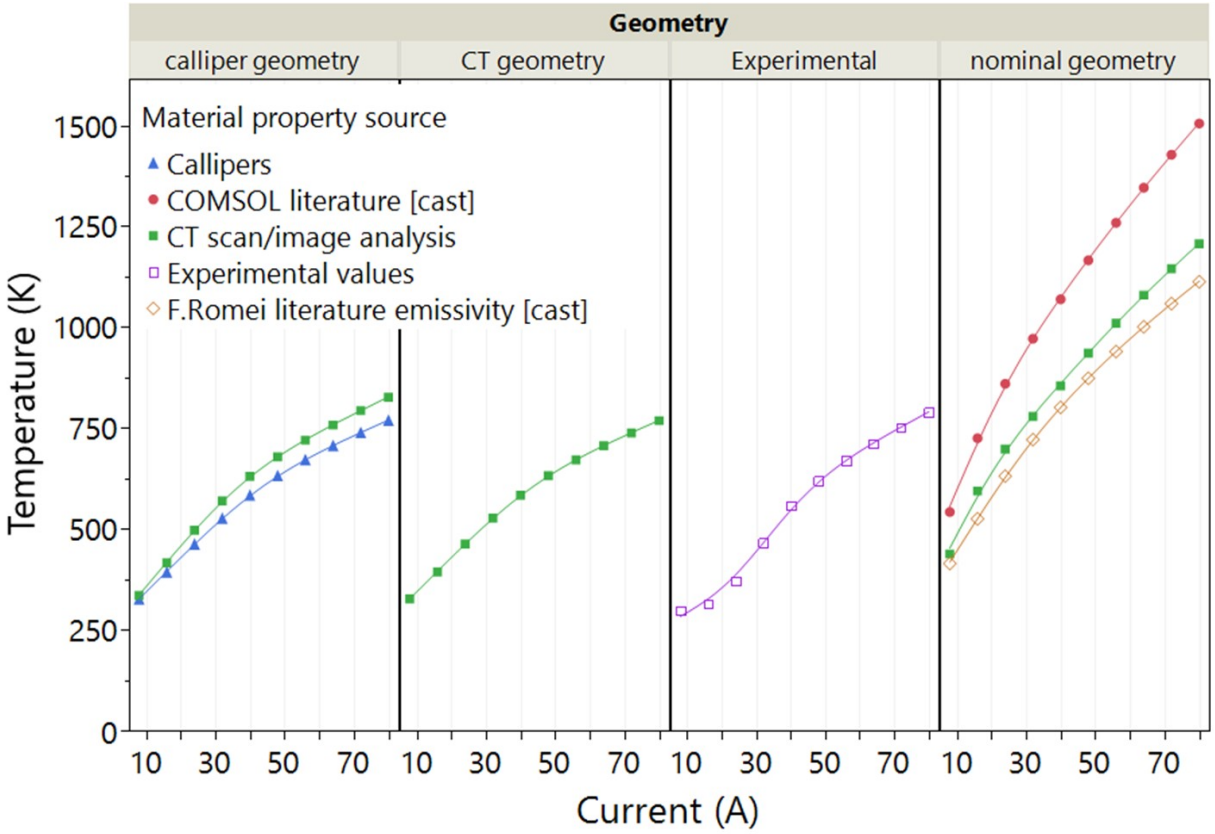

Figure 95: Plots of the maximum temperature against input current for each of the different models, and the experimental values

8.5.2. Nominal Geometry models

The simulations of the nominal geometry, regardless of the values used for emissivity and resistivity, all predicted notably higher temperatures at every input current compared with experimental results. The models had maximum differences between 28% - 91%. As shown in Table 34 the nominal geometry had a smaller cross-sectional area compared to the actual sample, which may have resulted in a higher current density and thus these models predicted more heat generation from joule heating. The nominal geometry with cast values for emissivity and resistivity had the largest difference from the experimental values. This simulation represented the default use case as it used original CAD geometry and software supplied values for emissivity and resistivity, which as previously discussed were only for cast metals. The simulation that used a nominal geometry with the literature values used by F. Romei *et al.* produced temperatures closer to the experimental values than the nominal geometry with cast values. However they were still notably higher than the experimental values, with the

difference between the two increasing as the temperature increases. It should be noted that this simulation produced lower temperature values than the simulation that used the nominal geometry with the CT determined emissivity/resistivity values. This may be because the emissivity value that F. Romei *et al.* used were higher than any of the CT determined emissivity values. Thus, given the same geometry, the higher emissivity value meant that more heat was emitted, reducing the surface temperature.

8.5.3. Calliper and CT determined geometries

As seen in Figure 95 the samples that used the calliper or CT scanning/image analysis determined geometries produced temperature results that were very close to the experimental values. The two simulations that were the closest to the experimental values were the CT determined geometry with CT determined emissivity/resistivity values and the calliper geometry with calliper determined emissivity/resistivity values. Each of these two models produced near identical results that, especially at currents of 40 A and above (for reasons previously explained) matched very closely with the experimental values. When considering the values at 40 A and above, compared with the experimental values these models had a maximum difference of roughly 25 K and a minimum difference of 5 K (equivalent to approximately 4% and 0.8% differences respectively). Given that the geometry and material property values most closely matched the actual experiment, it was expected for the model that used the CT determined geometry with CT determined values to match the experimental values most closely. However, it was not expected for the model that used the calliper geometry and calliper determined material properties to match so closely with experimental results given that these material property values were known to be incorrect (exceeding the emissivity of a blackbody in some cases, which is not physically possible).

Overall, best results were found when using the same area determination method for both materials properties and geometry (e.g. calliper determined emissivity and calliper geometry). This can be explained as the two parameters (emissive surface area and emissivity) are not independent in that the emissive surface area (A_1) is used to calculate the emissivity (ε). Equation [10] to calculate the emissivity in section 4.3.1

shows that the two are inversely correlated $\left(\varepsilon \propto {}^{1}/_{A_1}\right)$ and so the product of emissivity and emissive surface area is constant for a specific emissive power $(\varepsilon A_1 = k)$. Therefore while the calliper method provides unrealistically low surface area values, this is compensated by an unrealistically high emissivity. When both are substituted back into equation [10] the result is a constant in the form of temperature. It must be noted that this relationship is true only if the emissive surface area is used to calculate the emissivity.

The CT scan/image analysis geometry, while more representative of the actual sample, was difficult to translate into a CAD model. In future work it may be much easier to use calliper geometries callipers and callipers determined values for emissivity and resistivity given in this work.

A model using the CT determined geometry with the literature emissivity values used by F. Romei *et al.* (and the COMSOL material library resistivity values) was simulated and produced results very close to the experimental values, achieving a maximum difference of 2% at input currents above 40 A. However, this was likely a coincidence because the emissivity values used happened to closely match the actual emissivity values of sample 13. A comparison of the emissivity values is shown in Table 35. To investigate this further, a second sample was modelled. The 90° sample 3 was chosen because it had much lower emissivity values over a similar temperature range compared with sample 13. Two simulations were run: First the CT determined geometry and the CT determined emissivity/resistivity values, and the second using the CT determined geometry and the literature values for emissivity. The results of these are shown in Figure 96. The maximum temperature difference between the experimental results and the model that used the CT determined emissivity/resistivity values was roughly 8%, which was higher than for sample 13. However, the model that used the literature values of emissivity had a significantly higher maximum difference compared to the experimental values of roughly 36%. This shows that the measured values for emissivity and resistivity produce more accurate temperature results compared to cast values.

Table 35: Table showing the emissivity values for the cast 316L as used by F. Romei *et al.* and the measured emissivity values for samples 13 and 3. Emissivity values when the samples were not in steady state have been omitted

Calex Electronics datasheet [183]		Sample 13 (0°)		Sample 3 (90°)	
Temperature (K)	Emissivity (a.u.)	Temperature (K)	Emissivity (a.u.)	Temperature (K)	Emissivity (a.u.)
297	0.28	556.9	0.40	508.7	0.22
505	0.57	619.0	0.41	614.4	0.23
1222	0.66	667.7	0.45	695.3	0.26
-	-	719.3	0.48	767.9	0.28
-	-	750.7	0.51	831.6	0.30
-	-	788.5	0.54	889.1	0.32
-	-	823.1	0.57	942.6	0.33
-	-	-	-	1006.7	0.33
-	-	-	-	1050.5	0.34

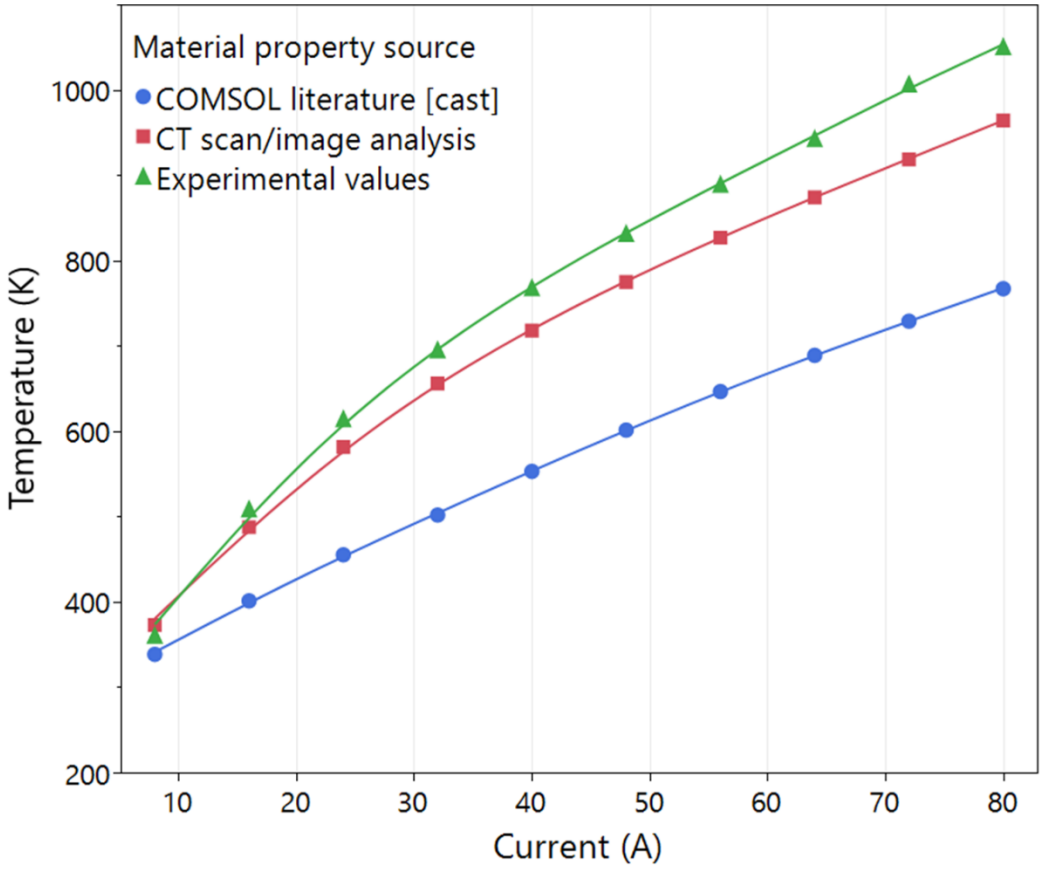

Figure 96: Plots of the maximum temperature against input current for the two different simulations of sample 3 (both CT determined geometries), and the experimental values

8.6. Conclusions

Using the software COMSOL Multiphysics, simulations of the emissivity and resistivity experiment were run with different combinations of sample geometries and materials properties to determine how closely the temperatures matched the experimental values.

Models that used CT scan geometry with the CT determined emissivity and resistivity had the best agreement with the experimental values, achieving a maximum difference of 4%. Models that used combinations of calliper geometries and calliper determined emissivity and resistivity achieved similar results, despite the emissivity values being incorrect (and in some cases in excess of a blackbody and thus physically impossible). This was because these emissivity and resistivity values were originally calculated using measured temperatures, and so the models that used these emissivity and resistivity values corresponded to the experimental temperature values. It was much less labour-intensive to measure sample geometries and calculate emissivity with callipers compared to CT scanning and image analysis. In future work calliper measured emissivity values, although physically invalid, might be useful for simulating the temperature of parts such as the STAR thruster using calliper measured dimensions.

9. Overall conclusions and future work

9.1. Overview of thesis

The overall goal of this thesis was to understand how the SLM process affected the surface topography and microstructure of 316L stainless steel parts and how these in turn affected the material properties emissivity and resistivity. This was motivated by the desire to not only understand the cause behind the temperature differences between simulations and experimental results of the Super high Temperature Additively-manufactured Resistojet (STAR) by F. Romei *et al*, but to also enable more accurate temperature simulations of the resistojet to improve performance estimations. Using a definitive screening design, the process parameters laser power, scanning speed, hatch spacing, layer thickness and build angle were varied over three levels to produce 17 samples with different surface features and microstructures to cover wide a design space. The emissivity and resistivity were measured in a custom-built rig that allowed for simultaneous measuring of both using the calorimetric and four-point probe methods respectively. Dimensional analysis, surface topography and microstructural measurements of the samples were carried out using a variety of different techniques that included CT scanning, focus variation microscopy, scanning electron microscopy and density measurements. Multiple linear regression models were created to determine the significance of the input parameters and their interactions on the different outputs used to characterise the emissivity and resistivity. Finally, the experimentally determined values for emissivity and resistivity were used in a multiphysics model to determine whether accurate temperature estimations could be obtained. These were compared against similar models that used cast values for the emissivity and resistivity.

This chapter outlines the main conclusions of the results sections in Chapters 5, 6, 7 and 8. These conclusions are then used as a basis for recommendations for future work to continue investigating the link between SLM process parameters, emissivity, and resistivity.

9.2. Conclusions

9.2.1. Effect of process parameter variation on surface topography

The rapid cooling and layer by layer nature of the SLM process caused unique surface features that were believed to be the reason behind the difference in emissivity between as-built SLM parts and cast 316L. A high number of pits and valleys with high aspect ratios, commonly seen on as-built SLM surfaces, may have increased the number of reflections incident radiation undergoes on a sample surface which would in turn increase the emissivity. The input process parameters were successfully varied to produce samples with a wide range of different surface textures to study this. Although surface texture studies have been done in the past, no other study was found that varied all the process parameters that make up volumetric energy density (laser power, scanning speed, hatch spacing, layer thickness) and build angle. Measurements of the surface texture parameters Sa, Sq, Ssk, Sku and Sdq were taken at the same five locations along all 17 samples that were used for emissivity and resistivity measurements. These parameters were chosen through literature review as they each described different physical features or trends of the surfaces that were thought to be useful when linking the surface topography to emissivity. It is worth emphasising that understanding how the SLM process parameters affected the surface texture was not the overall aim of this project but was instead an intermediary necessary to understand the effects of surface texture on emissivity for samples processed within the range of parameters varied.

Despite consistent build parameters for each sample, the values of surface texture parameters varied notably along the length of certain samples. This was particularly true for most of the 0° samples which consistently had the widest ranges of values and the downskin of the 45° samples which had low ranges but strong trends of increasing or decreasing values along the sample lengths. The 90° samples generally had the lowest ranges and little trends, with some exceptions. These variations were likely caused by factors that were not considered when initially planning the experiment, such as the position of the samples relative to the laser or gas flow direction which other literature

studies have reported having influenced the surface texture. To correct for this, average values of the texture parameters were used when describing the surface texture of each of the samples with emissivity.

SEM images of the samples were used to relate the surface texture parameters to physical features. Sa and Sq were measures of the average absolute height of the surfaces. Although there was some variation between the samples, individually the Sa and Sq values were generally large and consistent on both sides of the 90° samples, varying between 27.716 µm – 44.41 µm. These surfaces were dominated by half-melted and agglomerated particles. The downskin surfaces of the 45° samples appeared very similar in the SEM images and corresponded to similar ranges of Sa and Sq. The upskin surfaces however were much smoother with correspondingly lower Sa and Sq. The upskin SEM images showed scan tracks with discontinuities due to balling. These differences between sides for the 45° were because the downskin surfaces had poor thermal conduction which caused the melt pools to grow and sink into the powder and for particles to stick the surface. The 0° samples, both individually and overall had the widest ranges for Sa and Sq and these were reflected in how the different surfaces appeared in the SEM images. Sample 13 had the lowest mean values and the surface appeared overall smooth with few agglomerates. Sample 5 had the highest overall values and the surface appeared covered in large pores filled with unmelted powder.

The Ssk determined whether a surface was dominated more by peaks or valleys. The 45° samples were very clearly split by side, with the downskin surfaces having more valleys and the upskin more peaks. Despite similar appearances to the 45° downskin surfaces, the 90° samples generally had more peaks which corresponded to the particles adhered to the surfaces. Generally, there was no clear split by side for the 90° samples, which was expected given that the build conditions for these samples were the same on both sides. The 0° samples, like the Sa and Sq values, had the widest individual and overall ranges for Ssk. The surface pores of sample 5 resulted in the lowest mean Ssk at 0.952 µm, while sample 6 had the highest mean at 2.573 µm due to several large agglomerations.

Sdq, the average slope of a surface, was highest for the 90° and downskin 45° samples and seemingly corresponded to the numerous spherical or semi-spherical particles adhered to the surfaces. It was generally much lower for the 0° samples which had much fewer surface agglomerates with the exceptions of samples 5 and 10 with values of 4.93 µm and 3.568 µm respectively. Both samples had large amounts of surface porosity, with the high Sdq values likely corresponding to the slopes of the pores.

Sku was a measure of the spread of the surface height distribution with a value of 3 equivalent to a Gaussian distribution. While most samples had values around 3, some samples had values significantly higher, indicating the presence of outliers. Sample 13 had the second highest mean Sku of 12.21, despite also having the lowest mean Sa and Sq. SEM images of the surface reflected this, as it appeared mostly smooth with some large surface agglomerates.

Statistically significant multiple linear regression models were created for each of the texture parameters up to second degree polynomials. The purpose of these models was to identify the input factors that had the largest impacts on the different surface texture parameters, so that these could then be compared against similar models for emissivity and see if there were any similarities in terms of significant input factors. The models for Sa and Sq, as they were measures of the same physical features, had similar rankings for the input parameters in terms of significance. Both models found that the square of hatch spacing had the largest impact on the texture parameters. Hatch spacing had a curved response on Sa and Sq, where the middle value of hatch spacing corresponded to the high values for the texture parameters. Similar studies in literature also found that hatch spacing had the most significant effect on surface roughness, as it determined the overlap rate and heat accumulation between adjacent tracks which either resulted in dense, flat regions or insufficient melting and surface pores. However, rather than a curved response the literature studies generally found that roughness only increased with increasing hatch spacing. It should be noted that these studies in literature were more limited in scope than this work as they varied fewer process parameters. As this work was a screening experiment, the purpose was to identify which

factors had significant effects on the surface texture parameters. Not enough data was collected to definitively state the reason for the response hatch spacing had on Sa and Sq.

Volumetric energy density was instead used to relate the process parameters to the physical changes seen. When looking at the relationship between mean Sa and Sq with energy density, the 0° and 90° samples both showed clear trends. Sa generally increased with energy density for the 90° samples and decreased for the 0° samples. For the 90° samples low energy densities reduced balling effects and high energy densities caused spattering while for the 0° samples lower energy densities caused lack of fusion and balling while higher energy densities gave the melt pools time to flatten before solidifying. Notable outliers however were the samples made with the middle value of hatch spacing, the 90° sample had lower values for Sa and the 0° sample much higher. This again highlighted the need for further work to understand exactly why hatch spacing produced these outliers.

9.2.2. Effect of process parameter variation on emissivity

Using the calorimetric method, the total hemispherical emissivity of the seventeen samples produced with different process parameters were measured by resistively heating the samples under vacuum up to input currents of 80 A. This was directly linked to the roughness measurements as the goal was to understand how the process parameters affected the surface, and how this in turn affected the emissivity. This was a novel study as the literature review identified only one other paper by S. Taylor *et al.* that investigated the emissivity of SLM surfaces. The scope of that paper was different from this work, as they investigated emissivity as a function of wavelength rather than total hemispherical emissivity as was done in this work, and only at room temperature.

Due to time limitations, dwell time was insufficient to reach steady state conditions at lower input currents (for example, up to 40 A for sample 14). Given the known linear relationship between emissivity and temperature, this caused the samples to have significantly higher emissivity values than expected for these input currents. For sample 14 even small transient temperature changes of 0.05 °C/s at an input current of 8 A

resulted in errors in emissivity of 36% when compared against the same sample and input current at steady state. This highlighted the importance of ensuring samples reached steady state conditions. Emissivity values for samples not in steady state were omitted from further analysis.

Although the emissivity test standard recommended using callipers to measure the geometry of the samples, these produced impossibly high values of emissivity for certain samples. The callipers could not capture the recesses and re-entrant features on the surfaces that caused the emitting area to be much larger than was measured by callipers. Measuring the emitting area with a combination of CT scanning and image analysis was found to be more accurate but also more labour intensive. For the emissivity values that were calculated using CT scanning/image analysis surface areas, most data points fell within the range of $0.2 - 0.45$ with no clear trends with build angle. The samples that had emissivity values notably higher than this were only 0° samples which also reached the lowest maximum temperatures.

Although several reports in the literature found relationships between emissivity and surface texture parameters, no such relationships were found in this work for any of the measured areal surface texture parameters or their products. It should be noted that areal texture parameters were used in this work as they were thought to be more suited to describing SLM surfaces. No literature source was found that related areal surface texture parameters to emissivity. Focus variation microscopy was used to measure these areal parameters and because it only captured information from directly above, it may have been unable to properly capture recesses and re-entrant features on the surfaces. Such features could have resulted in higher amounts of internal reflections and thus higher emissivity. Not being able to measure such features which would be reflected in the texture parameters may have caused the lack of trends.

Very strong trends however were found between the surface areas measured using CT scanning/image analysis and the emissivity at any given temperature or emissive power, while no trend was found for the emissivity measured using callipers. For all samples, as the surface area increased the emissivity decreased. This may be because the

surfaces generated did not produce the wedge-like cavities necessary to increase the internal reflections and thus emissivity. Thus, for a given input power or temperature, increasing the surface area only decreased the amount of radiation emitter per unit area and time, decreasing the emissivity. This may also explain the lack of trend between the areal texture parameters and emissivity. The parameters may not have captured the wedge-like features that correlate with emissivity because there were none to be captured.

Statistically significant multiple linear regression models were successfully created linking the input parameters to the emissivity at 500 K, 700 K and the surface area measured by CT scanning/image analysis. Most notably the top input parameters that were significant for the surface area (build angle, layer thickness, square of hatch spacing and laser power) were also the top significant terms for emissivity. This indicated that surface area did affect the emissivity. It was also noteworthy that the square of hatch spacing was significant to the surface area, as this term was also the most significant in the models for Sa and Sq. However, when plotting the CT/image analysis determined surface area against the texture parameters no strong correlations were found, the strongest being Sdq which had an R^2 of only 0.412. These results may indicate that the average absolute height of the surfaces had some impact on surface area, but not significantly.

9.2.3. Effect of process parameter variation on resistivity

The resistivity of the 17 samples was measured using the four-probe method. Like with emissivity, the goal of this work was to investigate how the SLM process parameters affected the structure of the samples, specifically the primary cell spacing and relative densities of the parts, and how these in turn affected the resistivity. Few reports from the literature were found investigating the relationship between process parameters and resistivity of SLM parts. Those that did were not for 316L stainless steel and were limited in terms of the process parameters varied and were only at room temperature.

Overall, the resistivity of the SLM samples were higher than reports from literature for cast resistivity at measured temperatures from roughly 500 K - 1000 K. Given the

similar material composition, this was likely due to microstructural differences between cast and SLM processing. The 0° SLM samples generally had lower resistivity values than the 90° and 45° samples. This was supported by the statistical model linking resistivity and process parameters which indicated that build angle was the most significant factor affecting resistivity.

The influence of relative density on resistivity varied depending on the build angle. Only samples with relative densities greater than 98% were observed for the 45° and 90° samples. The density of these samples showed no correlation with energy density, and the density had little effect on resistivity. However, the 0° samples generally showed increasing relative density with increasing energy density and as the density of the 0° samples increased, the resistivity decreased. This trend was true both above and below 98% density. This was likely due to porosity decreasing the periodicity of the crystal lattice and creating a longer, tortuous conduction path for the electrons. The square of laser power was the most influential factor on the density of the 0° samples and was the second most significant factor in the resistivity model, indicating that relative density likely influenced the resistivity. Despite a wide range of values, the primary cell spacing did not correlate strongly with energy density or resistivity regardless of build angle or temperature. The multiple linear regression model found that scanning speed was the most significant factor, which was not amongst the most significant terms for resistivity. This likely corroborates the conclusion that primary dendrite spacing did not contribute strongly to resistivity.

9.2.4. Multiphysics modelling of the experimental setup

Simulations of the experimental setup were created in the finite element analysis software COMSOL Multiphysics. This was done to see whether the measured values for emissivity and resistivity could produce more accurate temperature simulations than models that used materials property data for cast metals taken from literature. Models were created using different combinations of sample geometry (calliper determined, CT scanning determined, nominal CAD) and emissivity and resistivity values (calliper determined, CT scanning determined, literature values for cast 316L) for comparison.

The models that used the nominal geometry all produced notably higher temperature values compared to the experimental values, even when using the CT scanning determined emissivity/resistivity values. They achieved maximum temperature differences between 28 % - 91 %. The nominal geometry was thinner than the actual geometry, causing more heat to be generated within the sample and raising the temperature.

The model that used the CT scanning/image analysis determined geometry and equivalent emissivity/resistivity values produced very accurate results, achieving a maximum 4% difference compared to the experimental values. Surprisingly, the model that used the calliper determined geometry and equivalent emissivity/resistivity values produced nearly identical results, despite having impossibly high values for emissivity and an inaccurate geometry. This was because emissivity and emissive surface area are not independent in that the emissive surface area (A_1) is used to calculate the emissivity (ε) and the two are inversely correlated. The product of emissivity and emissive surface area is constant for a specific emissive power $(\varepsilon A_1 = k)$. Any combination of emissive surface area and corresponding emissivity at a specific emissive power will result in the same temperature. This shows that future work could use callipers to determine part geometries, which are much easier and quicker to use compared to CT scanning and image analysis, and still obtain accurate estimates for the temperatures.

Temperature results were compared for models made using the CT-determined geometry with emissivity values taken from literature for cast metals against the measured emissivity values. For sample 13 they both showed good agreement with the experimental values at currents above 40 A, with sample 13 having a maximum difference of 4% and the literature values 2%. This was because the literature emissivity values coincidentally were similar to these SLM values. When compared against sample 3 which had much lower emissivity values for the same temperatures, the model results were very different. The model that used the measured emissivity values had a maximum difference of 8% while the literature values had a much larger difference of 36%, showing that the measured values produced better temperature models.

9.3. Future work

9.3.1. Effect of process parameter variation on surface topography

Several questions have arisen through this work regarding how process parameters affect the surface texture values that were outside the scope of this thesis and would need to be addressed through further work. A particular example of this was the effect that the positions of the samples on the build plate had on the surface texture parameters. This would be particularly useful for emissivity studies as if this unknown variation was eliminated specific roughness values could be related to emissivity rather than average values. This could be investigated by building samples using identical parameters and geometries to focus on the effects of build position relative to the laser and gas flow direction. Although other work in literature has addressed positional effects, they should still be studied on the machine that was used to build the samples in this study, to understand the extent of the issue and if it can be considered when designing future experiments to eliminate positional effects. Also focusing on thin-walled specimens such as those built for this work could be novel.

For this work the 0° samples were built directly onto the build plate and were removed using EDM wire cutting. This meant that the downskin surfaces of the 0° samples were not affected by the SLM process parameters, limiting the scope of this work. Future work could produce 0° samples raised from the build plate with support structures, so that the downskin surfaces can be studied and related to the emissivity. This would also allow for more comprehensive multiple linear regression models to be built.

Samples should be produced with more values of hatch spacing within the range tested in this work to better understand the shape of the response it had on Sa and Sq. Particular focus should be given to variation around hatch spacing values of 0.075 mm to understand the physical reasons behind the response shape and why this value in particular produced anomalous results. Similarly build angle, or an interaction with it, was significant in all the multiple linear regression models. Understanding the exact

contribution of build angle to the surface texture parameters would require further investigation from future work which could be achieved by looking at build angle in smaller increments. Strong relationships between energy density and build angle were found for the 0° and 90° samples. As there were only three 45° samples, no strong conclusions could be drawn for them. To build a better understanding, more 45° samples over a wider energy density range would need to be investigated.

9.3.2. Effect of process parameter variation on emissivity

In future, the emissivity of samples at lower input currents could be measured by ensuring sufficient time so that they reach steady state conditions. Generally, this should encompass input currents from 8 A to 40 A and could be accomplished by allowing for longer step times of up to 600 s for the materials in the work of this thesis.

The calorimetric method resulted in average emissivity values for each of the samples which made it harder to relate the emissivity to specific texture parameter values, which for some samples (such as the 45° samples) varied significantly by side. The emissive contributions of two sides with different surface features would need to be deconvoluted to relate emissivity to specific surface texture parameter value. This could be done by measuring a reference sample that has the same surface roughness on each side (such as if it were polished to a known roughness), so that the emissivity contribution of each side is equal. Producing samples with one side that has this known emissivity contribution may then allow for calculation of the emissivity contribution of the other side, and thus relation to specific texture parameter values.

Focus variation microscopy may not have been able to accurately capture re-entrant or recessed features. This may have affected the surface texture parameter values and their relationship with emissivity. Alternative methods for measuring surface texture should be explored. X-ray CT scanning is a potentially good option to capture recessed features, both from experience and from the literature. Profile roughness measurements could also be taken to compare more directly with literature values and to see if they show similar trends to areal parameters both generally and with emissivity.

Overall this work has shown that changing process parameters can lead to different surface areas (and thus different emissivity values). In future this can be used to optimise heat generation within and thus the performance of the resistojet, tailoring the emissivity values of specific parts of the resistojet interior for example to maximise heat generation within the centre of the thruster and minimise heat loss toward the exterior.

9.3.3. Effect of process parameter variation on resistivity

P. Pichler *et al.* showed that thermal expansion can have a large effect on resistivity values if not corrected for at elevated temperatures. As the purpose of this work was to produce as accurate resistivity values as possible especially at higher temperatures, future measurement of thermal expansion should refine the accuracy of resistivity measurements.

When carrying out relative density measurements, several issues arose with the measurement methods that could be improved upon in future experiments. A particular concern with the Archimedes method was the shape of the samples being difficult to handle. In future either a different setup including a larger fluid container should be used to properly suspend the sample without touching the container and reduce the chances of error on the fluid mass measurements, or samples should be manufactured with geometries easier to measure, such as cuboids. It was difficult to know the extent of the error for both measurement methods as there was no reference sample to compare against. In future this could be eliminated by having a sample of known density to determine the accuracy of the measurement techniques. The process parameters used in this work produced 45° and 90° samples with relative densities only greater than 98%. While this represented the possible process parameter range that might be used to build actual parts such as the resistojet, it limited the results of the study. In future it would be interesting to see if the trends seen with the 0° samples extends to other build angles with relative densities less than 98%.

The extent of the error on the image analysis technique to measure primary cell spacing needs to be better determined by comparing against a reference or with more repeat measurements. Due to difficulties clearly resolving the grains, unequal numbers

of measurements of primary cell spacings were taken for the different samples. Images were taken at random locations to try an ensure than an average cell spacing was obtained. However reports in the literature such as by I. Yadroitsev *et al.* found that cell size can vary depending on where in the sample they are measured, with areas closer to the build plate having finer cells (0.6 µm at scanning speed of 0.08 mm/s) due to a higher thermal gradient, while closer to the top of the melt pool the cell spacing was larger (roughly 1 µm at 0.08 mm/s scanning speed). It might be worth in future ensuring that measurements are carried out at specific distances along the sample height to capture as much size variation as possible. The orientations of the cellular dendrites were found to vary within samples; however it was unknown if there was a preferred growth orientation and if this varied with the process parameters. D. Wang *et al.* reported that cells partially grew along preferred crystallographic orientations which could in future be measured with Electron Back Scattered Diffraction (EBSD). As C. Silbernagel *et al.* found a strong correlation between cellular dendrite orientation and resistivity for SLM AlSi10Mg, it is worth determining if there is a preferred growth orientation, and if this affects the resistivity of the 316L samples.

Finally, only relative density was found to correlate with the resistivity, but there are other microstructural features that may impact resistivity. K. Saeidi *et al.* noted that the microstructure of SLM 316L contained silicon rich nano-inclusions. As C. Silbernagel *et al.* found that silicon enriched sub-grain boundaries of SLM AlSi10Mg increased the resistivity. Future work could investigate the distribution of silicon nano-inclusions and the potential influence on resistivity. Y. Shi *et al.* found that above 99.5% density, the solute concentration was the major factor that determined resistivity. Future studies using Energy Dispersive X-Ray (EDX) spectroscopy could assess whether the distribution of potential phases or solutes varies within the microstructure, if this distribution varies with process parameters, and how this might affect the resistivity.

9.3.4. Multiphysics modelling of the experimental setup

Due to not allowing the samples at lower input current to reach steady state, the experimental temperature values are unreliable for certain samples up to 40 A. These

tests should be repeated to obtain emissivity values at lower input currents, to then compare against the simulated values from the models.

As the peaks and valleys of the actual SLM sample geometries could not be easily translated into the simple 3D CAD models, artificial values of width and thickness were selected to match the actual samples cross-sectional areas and surface areas. While this was easy to accomplish for the flat samples in this work, this could be more difficult for more complicated geometries such as the resistojet. Thus, future work should attempt to replicate the peaks and valleys of the actual samples in CAD models, possibly by directly importing the 3D geometries from CT scans of the parts.

As the original inspiration for this thesis was the temperature difference between experiments and simulations of the resistojet, it would be interesting to repeat the parametric study of different emissivity, resistivity, and geometries on models of the resistojet itself. This would allow for further testing of the hypothesis that calliper emissivity and resistivity measurements, although physically inaccurate, can still yield accurate computational predictions for calliper measured geometries. Simulating more complex geometries such as the resistojet could also allow for testing spatially varying properties to account for different build directions in different locations of the geometry.

10. References

[1] M. Robinson, A. Grubi, G. Rempelos, F. Romei, C. Ogunlesi, and S. Ahmed, "Endurance testing of the additively manufactured STAR resistojet," vol. 180, 2019, doi: 10.1016/j.matdes.2019.107907.

[2] P. J. Sherwood, "Construction of a High Performance Resistojet for Satellite Propulsion." 1978, [Online]. Available: http://www.dtic.mil/docs/citations/ADA064236.

[3] F. Romei, A. N. Grubišić, and D. Gibbon, "Manufacturing of a high-temperature resistojet heat exchanger by selective laser melting," *Acta Astronaut.*, vol. 138, no. March, pp. 356–368, 2017, doi: 10.1016/j.actaastro.2017.05.020.

[4] E. Herderick, "Additive manufacturing of metals: A review," *Mater. Sci. Technol. Conf. Exhib. 2011, MS T'11*, vol. 2, no. 176252, pp. 1413–1425, 2011, [Online]. Available: http://www.scopus.com/inward/record.url?eid=2-s2.0-84856301323&partnerID=40&md5=e02018d10b2ca37a7e2ae1773e4fcaec.

[5] Y. Kok *et al.*, "Anisotropy and heterogeneity of microstructure and mechanical properties in metal additive manufacturing: A critical review," *Mater. Des.*, vol. 139, no. November 2017, pp. 565–586, 2018, doi: 10.1016/j.matdes.2017.11.021.

[6] K. Vartanian and T. McDonald, "Accelerating Industrial Adoption of Metal Additive Manufacturing Technology," *Jom*, vol. 68, no. 3, pp. 806–810, 2016, doi: 10.1007/s11837-015-1794-9.

[7] H. Fayazfar *et al.*, "A critical review of powder-based additive manufacturing of ferrous alloys: Process parameters, microstructure and mechanical properties," *Mater. Des.*, vol. 144, pp. 98–128, 2018, doi: 10.1016/j.matdes.2018.02.018.

[8] W. E. King *et al.*, "Laser powder bed fusion additive manufacturing of metals; physics, computational, and materials challenges APPLIED PHYSICS REVIEWS Laser powder bed fusion additive manufacturing of metals; physics, computational, and materials challenges," *Cit. Appl. Phys. Rev*, vol. 2, no. December 2015, p. 41304, 2015, [Online]. Available: http://dx.doi.org/10.1063/1.4937809http://aip.scitation.org/toc/are/2/4.

[9] C. Y. Yap *et al.*, "Review of selective laser melting: Materials and applications," *Appl. Phys. Rev.*, vol. 2, no. 4, 2015, doi: 10.1063/1.4935926.

[10] E. O. Olakanmi, R. F. Cochrane, and K. W. Dalgarno, "A review on selective laser sintering/melting (SLS/SLM) of aluminium alloy powders," *Prog. Mater. Sci.*, vol. 74, pp. 401–477, 2015, doi: 10.1016/j.pmatsci.2015.03.002 T4 - Processing, microstructure, and properties M4 - Citavi.

[11] D. D. Gu, W. Meiners, K. Wissenbach, and R. Poprawe, "Laser additive manufacturing of metallic components: Materials, processes and mechanisms," *Int. Mater. Rev.*, vol. 57, no. 3, pp. 133–164, 2012, doi: 10.1179/1743280411Y.0000000014.

[12] A. Yadollahi, N. Shamsaei, S. M. Thompson, and D. W. Seely, "Effects of process time interval and heat treatment on the mechanical and microstructural properties of direct laser deposited 316L stainless steel," *Mater. Sci. Eng. A*, vol. 644, pp. 171–183, 2015, doi: 10.1016/j.msea.2015.07.056.

[13] S. Pal, D. Igor, and T. Brajlih, "Physical Behaviors of Materials in Selective Laser Melting

Process," no. November, 2018, doi: 10.2507/daaam.scibook.2018.21.

[14] T. N. Le and Y. L. Lo, "Effects of sulfur concentration and Marangoni convection on melt-pool formation in transition mode of selective laser melting process," *Mater. Des.*, vol. 179, p. 107866, 2019, doi: 10.1016/j.matdes.2019.107866.

[15] "Surface Tension and Water | U.S. Geological Survey." https://www.usgs.gov/special-topics/water-science-school/science/surface-tension-and-water (accessed Apr. 13, 2022).

[16] M. Gugliotti *et al.*, "JCE DigiDemos : Tested Demonstrations Surface Tension Gradients Induced by Temperature : The Thermal Marangoni Effect submitted by :," *J. Chem. Educ.*, vol. 81, no. 6, pp. 824–826, 2004.

[17] Z. Chen *et al.*, "Thermal dynamic behavior during selective laser melting of K418 superalloy: numerical simulation and experimental verification," vol. 124, p. 313, 2018, doi: 10.1007/s00339-018-1737-8.

[18] N. Shamsaei, A. Yadollahi, L. Bian, and S. M. Thompson, "An overview of Direct Laser Deposition for additive manufacturing; Part II: Mechanical behavior, process parameter optimization and control," *Addit. Manuf.*, vol. 8, pp. 12–35, 2015, doi: 10.1016/j.addma.2015.07.002.

[19] B. Zheng, Y. Zhou, J. E. Smugeresky, J. M. Schoenung, and E. J. Lavernia, "Thermal behavior and microstructure evolution during laser deposition with laser-engineered net shaping: Part II. Experimental investigation and discussion," *Metall. Mater. Trans. A Phys. Metall. Mater. Sci.*, vol. 39, no. 9, pp. 2237–2245, 2008, doi: 10.1007/s11661-008-9566-6.

[20] I. Yadroitsev, P. Bertrand, and I. Smurov, "Parametric analysis of the selective laser melting process," *Appl. Surf. Sci.*, vol. 253, no. 19, pp. 8064–8069, 2007, doi: 10.1016/j.apsusc.2007.02.088.

[21] B. S. Hengfeng Gu, Haijun Gong, Deepankar Pal, Khalid Rafi, Thomas Starr, "Influences of energy density on porosity and microstructure of SLM 17-4PH stainless steel," pp. 474–489.

[22] Y. Liu, J. Zhang, Z. Pang, and W. Wu, "Investigation into the influence of laser energy input on selective laser melted thin-walled parts by response surface method," *Opt. Lasers Eng.*, vol. 103, no. August 2017, pp. 34–45, 2018, doi: 10.1016/j.optlaseng.2017.11.011.

[23] H. Gong, K. Rafi, H. Gu, T. Starr, and B. Stucker, "Analysis of defect generation in Ti-6Al-4V parts made using powder bed fusion additive manufacturing processes," *Addit. Manuf.*, vol. 1, pp. 87–98, 2014, doi: 10.1016/j.addma.2014.08.002.

[24] J. J. S. Dilip, G. D. J. Ram, T. L. Starr, and B. Stucker, "Selective laser melting of HY100 steel: Process parameters, microstructure and mechanical properties," *Addit. Manuf.*, vol. 13, pp. 49–60, 2017, doi: 10.1016/j.addma.2016.11.003.

[25] E. Liverani, S. Toschi, L. Ceschini, and A. Fortunato, "Effect of selective laser melting (SLM) process parameters on microstructure and mechanical properties of 316L austenitic stainless steel," *J. Mater. Process. Technol.*, vol. 249, no. November 2016, pp. 255–263, 2017, doi: 10.1016/j.jmatprotec.2017.05.042.

[26] K. G. Prashanth, S. Scudino, T. Maity, J. Das, and J. Eckert, "Is the energy density a reliable parameter for materials synthesis by selective laser melting?," *Mater. Res. Lett.*, vol. 5, no. 6, pp. 386–390, 2017, doi: 10.1080/21663831.2017.1299808.

[27] A. Yadollahi, N. Shamsaei, S. M. Thompson, A. Elwany, and L. Bian, "Effects of building orientation and heat treatment on fatigue behavior of selective laser melted 17-4 PH stainless steel," *Int. J. Fatigue*, vol. 94, pp. 218–235, 2017, doi: 10.1016/j.ijfatigue.2016.03.014.

[28] P. Hartunian and M. Eshraghi, "Effect of Build Orientation on the Microstructure and

Mechanical Properties of Selective Laser-Melted Ti-6Al-4V Alloy," *J. Manuf. Mater. Process.*, vol. 2, no. 4, p. 69, 2018, doi: 10.3390/jmmp2040069.

[29] F. Calignano, "Design optimization of supports for overhanging structures in aluminum and titanium alloys by selective laser melting," *Mater. Des.*, vol. 64, pp. 203–213, 2014, doi: 10.1016/j.matdes.2014.07.043.

[30] G. Strano, L. Hao, R. M. Everson, and K. E. Evans, "Surface roughness analysis, modelling and prediction in selective laser melting," *J. Mater. Process. Technol.*, vol. 213, no. 4, pp. 589–597, 2013, doi: 10.1016/j.jmatprotec.2012.11.011.

[31] L. N. Carter, C. Martin, P. J. Withers, and M. M. Attallah, "The influence of the laser scan strategy on grain structure and cracking behaviour in SLM powder-bed fabricated nickel superalloy," *J. Alloys Compd.*, vol. 615, pp. 338–347, 2014, doi: 10.1016/j.jallcom.2014.06.172.

[32] Y. Lu *et al.*, "Study on the microstructure, mechanical property and residual stress of SLM Inconel-718 alloy manufactured by differing island scanning strategy," *Opt. Laser Technol.*, vol. 75, pp. 197–206, Jul. 2015, doi: 10.1016/j.optlastec.2015.07.009.

[33] L. Thijs, K. Kempen, J. P. Kruth, and J. Van Humbeeck, "Fine-structured aluminium products with controllable texture by selective laser melting of pre-alloyed AlSi10Mg powder," *Acta Mater.*, vol. 61, no. 5, pp. 1809–1819, Mar. 2013, doi: 10.1016/j.actamat.2012.11.052.

[34] E. H. Valente, C. Gundlach, T. L. Christiansen, and M. A. J. Somers, "Effect of scanning strategy during selective laser melting on surface topography, porosity, and microstructure of additively manufactured Ti-6Al-4V," *Appl. Sci.*, vol. 9, no. 24, 2019, doi: 10.3390/app9245554.

[35] D. Pitassi *et al.*, "Finite Element Thermal Analysis of Metal Parts Additively Manufactured via Selective Laser Melting," in *Finite Element Method - Simulation, Numerical Analysis and Solution Techniques*, InTech, 2018.

[36] R. Li, J. Liu, Y. Shi, L. Wang, and W. Jiang, "Balling behavior of stainless steel and nickel powder during selective laser melting process," *Int. J. Adv. Manuf. Technol.*, vol. 59, no. 9–12, pp. 1025–1035, 2012, doi: 10.1007/s00170-011-3566-1.

[37] M. Tang, P. C. Pistorius, and J. L. Beuth, "Prediction of lack-of-fusion porosity for powder bed fusion," *Addit. Manuf.*, vol. 14, pp. 39–48, Mar. 2017, doi: 10.1016/j.addma.2016.12.001.

[38] D. Wang *et al.*, "Mechanisms and characteristics of spatter generation in SLM processing and its effect on the properties," *Mater. Des.*, vol. 117, pp. 121–130, Mar. 2017, doi: 10.1016/j.matdes.2016.12.060.

[39] P. Krakhmalev and I. Yadroitsev, "Microstructure and properties of intermetallic composite coatings fabricated by selective laser melting of Ti–SiC powder mixtures," *Intermetallics*, vol. 46, pp. 147–155, 2014.

[40] K. Mumtaz and N. Hopkinson, "Top surface and side roughness of Inconel 625 parts processed using selective laser melting," doi: 10.1108/13552540910943397.

[41] S. Lou, X. Jiang, W. Sun, W. Zeng, L. Pagani, and P. J. Scott, "Characterisation methods for powder bed fusion processed surface topography," *Precis. Eng.*, vol. 57, no. August 2018, pp. 1–15, 2019, doi: 10.1016/j.precisioneng.2018.09.007.

[42] R. Leach, *Characterisation of areal surface texture*, vol. 9783642364. 2013.

[43] B. Standard, "Geometrical product specification (GPS) - Surface texture : Profile method - Terms , definitions and surface texture parameters BS N 4287:1998," 2009.

[44] "Cut-offs and the Measurement of Surface Roughness :: Spectrum Metrology." https://www.spectrum-metrology.co.uk/surface-roughness/theory.php (accessed Jun. 17,

2020).

[45] A. Townsend, N. Senin, L. Blunt, R. K. Leach, and J. S. Taylor, "Surface texture metrology for metal additive manufacturing: a review," *Precis. Eng.*, vol. 46, pp. 34–47, 2016, doi: 10.1016/j.precisioneng.2016.06.001.

[46] P. G. Benardos and G. C. Vosniakos, "Predicting surface roughness in machining: A review," *Int. J. Mach. Tools Manuf.*, vol. 43, no. 8, pp. 833–844, Jun. 2003, doi: 10.1016/S0890-6955(03)00059-2.

[47] A. Triantaphyllou *et al.*, "Surface texture measurement for additive manufacturing," *Surf. Topogr. Metrol. Prop.*, vol. 3, no. 2, 2015, doi: 10.1088/2051-672X/3/2/024002.

[48] L. Newton *et al.*, "Areal topography measurement of metal additive surfaces using focus variation microscopy," *Addit. Manuf.*, vol. 25, no. October 2018, pp. 365–389, 2019, doi: 10.1016/j.addma.2018.11.013.

[49] ISO 25178-2, "BSI Standards Publication Geometrical product specifications (GPS) — Surface texture : Areal Part 2 : Terms , definitions and surface," 2012.

[50] ISO 25178-3, "Geometrical product specifications (GPS) — Surface texture : Areal Part 3 : Specification operators," 2012.

[51] I. 25178-1, "BSI Standards Publication Geometrical product specifications (GPS) — Surface texture : Areal Part 1 : Indication of surface texture," 2016.

[52] J. P. Holman, *Heat Transfer*, 10th ed. Boston: McGraw Hill, 2010.

[53] P. L. Kirillov and H. Ninokata, "Heat transfer in nuclear thermal hydraulics," *Therm. Water Cool. Nucl. React.*, pp. 357–492, Jan. 2017, doi: 10.1016/B978-0-08-100662-7.00007-5.

[54] Rajendra Karwa, *Heat and Mass Transfer Second Edition*. 2020.

[55] M. Kaviany, "Essentials of Heat Transfer: Principles, Materials, and Applications," *Essentials Heat Transf.*, 2011, doi: 10.1017/CBO9780511998195.

[56] "Thermal Radiation Heat Transfer, Fourth Edition - Robert Siegel - Google Books." https://books.google.co.uk/books?id=O389yQ0-fecC&pg=PA41&redir_esc=y#v=onepage&q&f=false (accessed Sep. 15, 2020).

[57] F. P. Incropera, D. P. Dewitt, T. L. Bergman, and A. S. Lavine, *Incropera's Principles of Heat and Mass transfer*. Hoboken: Wiley, 2017.

[58] Y. Touloukian, "Volume 7 : Thermal radiative properties - Metallic elements and alloys," *Thermaophysical Prop. Matter, Vol. 7*, 1972.

[59] C. Da Wen and I. Mudawar, "Modeling the effects of surface roughness on the emissivity of aluminum alloys," *Int. J. Heat Mass Transf.*, vol. 49, no. 23–24, pp. 4279–4289, 2006, doi: 10.1016/j.ijheatmasstransfer.2006.04.037.

[60] S. Taylor, J. B. Wright, E. C. Forrest, B. Jared, J. Koepke, and J. Beaman, "Investigating relationship between surface topography and emissivity of metallic additively manufactured parts," *Int. Commun. Heat Mass Transf.*, vol. 115, no. May, p. 104614, 2020, doi: 10.1016/j.icheatmasstransfer.2020.104614.

[61] W. Sabuga and R. Todtenhaupt, "Effect of roughness on the emissivity of the precious metals silver, gold, palladium, platinum, rhodium, and iridium," *High Temp. - High Press.*, vol. 33, no. 3, pp. 261–269, 2001, doi: 10.1068/htwu371.

[62] H. J. Jo, J. L. King, K. Blomstrand, and K. Sridharan, "Spectral emissivity of oxidized and roughened metal surfaces," *Int. J. Heat Mass Transf.*, vol. 115, pp. 1065–1071, 2017, doi: 10.1016/j.ijheatmasstransfer.2017.08.103.

[63] J. M. Jones, P. E. Mason, and A. Williams, "A compilation of data on the radiant emissivity of some materials at high temperatures," *J. Energy Inst.*, vol. 92, no. 3, pp. 523–534, 2019, doi: 10.1016/j.joei.2018.04.006.

[64] G. Dyos, T. Farrell, and R. Handbook, *Handbook of electrical resistivity*, vol. i, no. ohm m. .

[65] W. D. Callister and D. G. Rethwisch, *Materials Science and Engineering Eighth Edition*. John Wiley & Sons, Ltd, 2011.

[66] K. Saeidi, X. Gao, Y. Zhong, and Z. J. Shen, "Materials Science & Engineering A Hardened austenite steel with columnar sub-grain structure formed by laser melting," *Mater. Sci. Eng. A*, vol. 625, pp. 221–229, 2015, doi: 10.1016/j.msea.2014.12.018.

[67] Y. Zhong, L. Liu, S. Wikman, D. Cui, and Z. Shen, "Intragranular cellular segregation network structure strengthening 316L stainless steel prepared by selective laser melting," *J. Nucl. Mater.*, vol. 470, pp. 170–178, Mar. 2016, doi: 10.1016/j.jnucmat.2015.12.034.

[68] "What Is Stainless Steel?" https://www.bssa.org.uk/faq.php?id=1 (accessed May 18, 2020).

[69] "How many types of stainless steel are there?" https://www.bssa.org.uk/faq.php?id=10 (accessed May 19, 2020).

[70] "Type 316/316L Stainless Steels Explained." https://www.thoughtco.com/type-316-and-316l-stainless-steel-2340262 (accessed May 19, 2020).

[71] R. B. Song, J. Y. Xiang, and D. P. Hou, "Characteristics of mechanical properties and microstructure for 316L austenitic stainless steel," *J. Iron Steel Res. Int.*, vol. 18, no. 11, pp. 53–59, 2011, doi: 10.1016/S1006-706X(11)60117-9.

[72] S. Hao, P. Wu, J. Zou, T. Grosdidier, and C. Dong, "Microstructure evolution occurring in the modified surface of 316L stainless steel under high current pulsed electron beam treatment," vol. 253, pp. 5349–5354, 2007, doi: 10.1016/j.apsusc.2006.12.011.

[73] E. Tascioglu, Y. Karabulut, and Y. Kaynak, "Correction to: Influence of heat treatment temperature on the microstructural, mechanical, and wear behavior of 316L stainless steel fabricated by laser powder bed additive manufacturing (The International Journal of Advanced Manufacturing Technology, (20," *Int. J. Adv. Manuf. Technol.*, vol. 107, no. 5–6, p. 1957, 2020, doi: 10.1007/s00170-020-05115-1.

[74] D. Wang, C. Song, Y. Yang, and Y. Bai, "Investigation of crystal growth mechanism during selective laser melting and mechanical property characterization of 316L stainless steel parts," *Mater. Des.*, vol. 100, pp. 291–299, 2016, doi: 10.1016/j.matdes.2016.03.111.

[75] I. Yadroitsev, P. Krakhmalev, I. Yadroitsava, S. Johansson, and I. Smurov, "Energy input effect on morphology and microstructure of selective laser melting single track from metallic powder," *J. Mater. Process. Technol.*, vol. 213, no. 4, pp. 606–613, Apr. 2013, doi: 10.1016/j.jmatprotec.2012.11.014.

[76] H. L. Wei, J. Mazumder, and T. DebRoy, "Evolution of solidification texture during additive manufacturing," *Sci. Rep.*, vol. 5, no. 1, pp. 1–7, Nov. 2015, doi: 10.1038/srep16446.

[77] X. Su, Y. Yang, D. Xiao, and Z. Luo, "An investigation into direct fabrication of fine-structured components by selective laser melting," pp. 1231–1238, 2013, doi: 10.1007/s00170-012-4081-8.

[78] S. Greco, K. Gutzeit, H. Hotz, B. Kirsch, and J. C. Aurich, "Selective laser melting (SLM) of AISI 316L-impact of laser power, layer thickness, and hatch spacing on roughness, density, and microhardness at constant input energy density," doi: 10.1007/s00170-020-05510-8.

[79] Y. Deng, Z. Mao, N. Yang, X. Niu, and X. Lu, "Collaborative optimization of density and surface roughness of 316L stainless steel in selective laser melting," *Materials (Basel).*, vol. 13, no. 7, 2020, doi: 10.3390/ma13071601.

[80] J. Y. Lee, A. P. Nagalingam, and S. H. Yeo, "A review on the state-of-the-art of surface

finishing processes and related ISO/ASTM standards for metal additive manufactured components," *Virtual Phys. Prototyp.*, 2020, doi: 10.1080/17452759.2020.1830346.

[81] R. K. Leach, D. Bourell, S. Carmignato, A. Donmez, N. Senin, and W. Dewulf, "Geometrical metrology for metal additive manufacturing," *CIRP Ann.*, vol. 68, no. 2, pp. 677–700, 2019, doi: 10.1016/j.cirp.2019.05.004.

[82] "Filtration Techniques - Surface Metrology Guide - Digital Surf." https://guide.digitalsurf.com/en/guide-filtration-techniques.html (accessed Feb. 02, 2021).

[83] ISO, "BN EN ISO 4288:1998. Geometrical Product Specifications (GPS)- Surface texture: Profile method- Rules and procedures for the assessment of surface texture," *Geom. Prod. Specif.*, no. 1, pp. 1–8, 1998, [Online]. Available: https://bsol-bsigroup-com.sheffield.idm.oclc.org/Bibliographic/BibliographicInfoData/000000000001345614.

[84] F. Cabanettes *et al.*, "Topography of as built surfaces generated in metal additive manufacturing: A multi scale analysis from form to roughness," *Precis. Eng.*, vol. 52, no. October 2017, pp. 249–265, 2018, doi: 10.1016/j.precisioneng.2018.01.002.

[85] M. A. Beard, O. R. Ghita, and K. E. Evans, "Using Raman spectroscopy to monitor surface finish and roughness of components manufactured by selective laser sintering," *J. Raman Spectrosc.*, vol. 42, no. 4, pp. 744–748, Apr. 2011, doi: 10.1002/jrs.2771.

[86] Y. Tian, D. Tomus, A. Huang, and X. Wu, "Experimental and statistical analysis on process parameters and surface roughness relationship for selective laser melting of Hastelloy X," *Rapid Prototyp. J.*, vol. ahead-of-p, no. ahead-of-print, 2019, doi: 10.1108/RPJ-01-2019-0013.

[87] P. B. Bacchewar, S. K. Singhal, and P. M. Pandey, "Statistical modelling and optimization of surface roughness in the selective laser sintering process," *Proc. Inst. Mech. Eng. Part B J. Eng. Manuf.*, vol. 221, no. 1, pp. 35–52, 2007, doi: 10.1243/09544054JEM670.

[88] I. C. M. Król, L.A. Dobrzański, Ł. Reimann, "Surface quality in selective laser melting of metal powders." https://www.researchgate.net/publication/280720929_Surface_quality_in_selective_laser_melting_of_metal_powders (accessed Feb. 01, 2021).

[89] E. Yasa and J. Kruth, "Application of Laser Re-Melting on Selective Laser Melting Parts," *Adv. Prod. Eng. Manag.*, vol. 6, no. 4, pp. 259–270, 2011.

[90] F. Calignano, D. Manfredi, E. P. Ambrosio, L. Iuliano, and P. Fino, "Influence of process parameters on surface roughness of aluminum parts produced by DMLS," *Int. J. Adv. Manuf. Technol.*, vol. 67, no. 9–12, pp. 2743–2751, Aug. 2013, doi: 10.1007/s00170-012-4688-9.

[91] G. Strano, L. Hao, R. M. Everson, and K. E. Evans, "Surface roughness analysis, modelling and prediction in selective laser melting," *J. Mater. Process. Technol.*, vol. 213, no. 4, pp. 589–597, 2013, doi: 10.1016/j.jmatprotec.2012.11.011.

[92] D. Ahn, H. Kim, and S. Lee, "Surface roughness prediction using measured data and interpolation in layered manufacturing," vol. 9, pp. 664–671, 2008, doi: 10.1016/j.jmatprotec.2008.02.050.

[93] R. I. Campbell, M. Martorelli, and H. S. Lee, "Surface roughness visualisation for rapid prototyping models," vol. 34, pp. 717–725, 2002.

[94] R. Shrestha, J. Simsiriwong, and N. Shamsaei, "Fatigue behavior of additive manufactured 316L stainless steel parts: Effects of layer orientation and surface roughness," *Addit. Manuf.*, vol. 28, no. April, pp. 23–38, 2019, doi: 10.1016/j.addma.2019.04.011.

[95] Y. Kaynak and O. Kitay, "The effect of post-processing operations on surface characteristics of 316L stainless steel produced by selective laser melting," *Addit. Manuf.*, vol. 26, no. December 2018, pp. 84–93, 2019, doi: 10.1016/j.addma.2018.12.021.

[96] "Non-contact Surface Roughness/Profile Measuring Instruments | Instruments used for roughness measurements | Solving the questions about profile and surface roughness measurements! Introduction to 'Roughness' | KEYENCE International Belgium." https://www.keyence.eu/ss/products/microscope/roughness/equipment/line_02.jsp (accessed Feb. 02, 2021).

[97] T. Grimm, G. Wiora, and G. Witt, "Characterization of typical surface effects in additive manufacturing with confocal microscopy," *Surf. Topogr. Metrol. Prop.*, vol. 3, no. 1, p. 014001, Jan. 2015, doi: 10.1088/2051-672X/3/1/014001.

[98] C. Gomez, R. Su, A. Thompson, J. DiSciacca, S. Lawes, and R. Leach, "Optimization of surface measurement for metal additive manufacturing using coherence scanning interferometry," *Opt. Eng.*, vol. 56, no. 11, p. 111714, Jul. 2017, doi: 10.1117/1.oe.56.11.111714.

[99] A. Townsend, L. Pagani, P. Scott, and L. Blunt, "Areal surface texture data extraction from X-ray computed tomography reconstructions of metal additively manufactured parts," *Precis. Eng.*, vol. 48, no. February 2017, pp. 254–264, 2017, doi: 10.1016/j.precisioneng.2016.12.008.

[100] N. Senin, A. Thompson, and R. K. Leach, "Characterisation of the topography of metal additive surface features with different measurement technologies," *Meas. Sci. Technol.*, vol. 28, no. 9, p. 95003, Aug. 2017, doi: 10.1088/1361-6501/aa7ce2.

[101] R. Danzl, F. Helmli, and S. Scherer, "Focus Variation – a Robust Technology for High Resolution Optical 3D Surface Metrology," *Strojniški Vestn. – J. Mech. Eng.*, vol. 2011, no. 03, pp. 245–256, Mar. 2011, doi: 10.5545/sv-jme.2010.175.

[102] "Focus Variation| Form & roughness with one system | Alicona." https://www.alicona.com/en/our-technology/focus-variation/ (accessed Feb. 03, 2021).

[103] J. C. Fox, S. P. Moylan, and B. M. Lane, "Preliminary study toward surface texture as a process signature in laser powder bed fusion additive manufacturing," *Proc. - ASPE/euspen 2016 Summer Top. Meet. Dimens. Accuracy Surf. Finish Addit. Manuf.*, pp. 168–173, 2016.

[104] K. Vetterli, Marc; Schmid, Manfred; Wegener, "Comprehensive investigation of surface characterization for laser sintered parts," *Brisk Bin. Robust Invariant Scalable Keypoints*, vol. 2, no. 6, pp. 0–8, 2014, [Online]. Available: https://doi.org/10.3929/ethz-a-010025751.

[105] M. Wüthrich, C. G. Cifuentes, S. Trimpe, and S. Schaal, "Robust Gaussian Filtering," no. 2, pp. 1–9, 2015, [Online]. Available: http://arxiv.org/abs/1509.04072.

[106] R. Leach and H. Haitjema, "Bandwidth characteristics and comparisons of surface texture measuring instruments," *Meas. Sci. Technol.*, vol. 21, no. 3, 2010, doi: 10.1088/0957-0233/21/3/032001.

[107] D. Wang, Y. Liu, Y. Yang, and D. Xiao, "Theoretical and experimental study on surface roughness of 316L stainless steel metal parts obtained through selective laser melting," *Rapid Prototyp. J.*, vol. 22, no. 4, pp. 706–716, 2016, doi: 10.1108/RPJ-06-2015-0078.

[108] S. Kleszczynskia, A. Ladewigb, K. Friedbergerb, J. zur Jacobsmühlenc, D. Merhofc, and G. Witta, "Position Dependency of Surface Roughness in Parts From Laser Beam," *Proc. 26th Int. Solid Free Form Fabr. Symp.*, pp. 360–370, 2015.

[109] T. Kralik, P. Hanzelka, V. Musilova, and A. Srnka, "Factors influencing thermal radiative properties of metals," vol. 1, 2004.

[110] F. Ghmari, T. Ghbara, M. Laroche, R. Carminati, and J. J. Greffet, "Influence of microroughness on emissivity," *J. Appl. Phys.*, vol. 96, no. 5, pp. 2656–2664, 2004, doi: 10.1063/1.1776634.

[111] C. Zhu, M. J. Hobbs, and J. R. Willmott, "An accurate instrument for emissivity measurements by direct and indirect methods," *Meas. Sci. Technol.*, vol. 31, no. 4, 2020, doi: 10.1088/1361-6501/ab5e9b.

[112] G. A. Greene, C. C. Finfrock, and T. F. Irvine, "Total hemispherical emissivity of oxidized Inconel 718 in the temperature range 300-1000°C," *Exp. Therm. Fluid Sci.*, vol. 22, no. 3–4, pp. 145–153, 2000, doi: 10.1016/S0894-1777(00)00021-2.

[113] K. L. Walton, R. K. Maynard, T. K. Ghosh, R. V. Tompson, D. S. Viswanath, and S. K. Loyalka, "Total Hemispherical Emissivity of Potential Structural Materials for Very High Temperature Reactor Systems: Alloy 617," *Nucl. Technol.*, vol. 5450, 2018, doi: 10.1080/00295450.2018.1521177.

[114] C. E. Mendenhall, "AN INTERNATIONAL REVIEW OF SPECTROSCOPY AND ASTRONOMICAL PHYSICS VOLUME XXXIII MARCH I 9 I I NUMBER 2 ON THE EMISSIVE POWER OF WEDGE-SHAPED CAVITIES AND THEIR USE IN TEMPERATURE MEASUREMENTS."

[115] C. G. Ren, Y. L. Lo, H. C. Tran, and M. H. Lee, "Emissivity calibration method for pyrometer measurement of melting pool temperature in selective laser melting of stainless steel 316L," *Int. J. Adv. Manuf. Technol.*, vol. 105, no. 1–4, pp. 637–649, 2019, doi: 10.1007/s00170-019-04193-0.

[116] B. Cheng, J. Lydon, K. Cooper, V. Cole, P. Northrop, and K. Chou, "Infrared thermal imaging for melt pool analysis in SLM: a feasibility investigation," *Virtual Phys. Prototyp.*, vol. 13, no. 1, pp. 8–13, 2018, doi: 10.1080/17452759.2017.1392685.

[117] N. Boone, C. Zhu, C. Smith, I. Todd, and J. R. Willmott, "Thermal near infrared monitoring system for electron beam melting with emissivity tracking," *Addit. Manuf.*, vol. 22, no. March, pp. 601–605, 2018, doi: 10.1016/j.addma.2018.06.004.

[118] G. Mohr, S. Nowakowski, S. J. Altenburg, C. Maierhofer, and K. Hilgenberg, "Experimental Determination of the Emissivity of Powder Layers and Bulk Material in Laser Powder Bed Fusion Using Infrared Thermography and Thermocouples."

[119] F. Valiorgue, A. Brosse, P. Naisson, J. Rech, H. Hamdi, and J. M. Bergheau, "Emissivity calibration for temperatures measurement using thermography in the context of machining," *Appl. Therm. Eng.*, vol. 58, no. 1–2, pp. 321–326, 2013, doi: 10.1016/j.applthermaleng.2013.03.051.

[120] S. K. Loyalka *et al.*, "Total Hemispherical Emissivity of SS 316L with Simulated Very High Temperature Reactor Surface Conditions," *Nucl. Technol.*, vol. 198, no. 3, pp. 293–305, 2017, doi: 10.1080/00295450.2017.1311120.

[121] S. Frachet, M. Boutrais, and P. Pradel, "Measurements of Emissivity: THEMIS Facility," 1986.

[122] T. Fu, P. Tan, and M. Zhong, "Experimental research on the influence of surface conditions on the total hemispherical emissivity of iron-based alloys," *Exp. Therm. Fluid Sci.*, vol. 40, pp. 159–167, 2012, doi: 10.1016/j.expthermflusci.2012.03.001.

[123] A. El Bakali, R. Gilblas, T. Pottier, and Y. Le Maoult, "A fast and versatile method for spectral emissivity measurement at high temperatures," *Rev. Sci. Instrum.*, vol. 90, no. 11, pp. 1–19, 2019, doi: 10.1063/1.5116425.

[124] L. P. Wang, S. Basu, and Z. M. Zhang, "Direct and indirect methods for calculating thermal emission from layered structures with nonuniform temperatures," *J. Heat Transfer*, vol. 133, no. 7, pp. 1–7, 2011, doi: 10.1115/1.4003543.

[125] J. P. Monchau, J. Hameury, P. Ausset, B. Hay, L. Ibos, and Y. Candau, "Comparative study of radiometric and calorimetric methods for total hemispherical emissivity measurements," *Heat Mass Transf. und Stoffuebertragung*, vol. 54, no. 5, pp. 1415–1425, 2018, doi: 10.1007/s00231-017-2238-6.

[126] B. P. Keller, S. E. Nelson, K. L. Walton, T. K. Ghosh, R. V Tompson, and S. K. Loyalka, "Total hemispherical emissivity of Inconel 718," *Nucl. Eng. Des.*, vol. 287, pp. 11–18, 2015, doi: 10.1016/j.nucengdes.2015.02.018.

[127] R. K. Maynard, T. K. Ghosh, R. V. Tompson, D. S. Viswanath, and S. K. Loyalka, "Total hemispherical emissivity of potential structural materials for very high temperature reactor systems: Hastelloy X," *Nucl. Technol.*, vol. 172, no. 1, pp. 88–100, 2010, doi: 10.13182/NT10-6.

[128] C. Silbernagel, L. Gargalis, I. Ashcroft, R. Hague, M. Galea, and P. Dickens, "Electrical resistivity of pure copper processed by medium-powered laser powder bed fusion additive manufacturing for use in electromagnetic applications," *Addit. Manuf.*, vol. 29, no. August, p. 100831, 2019, doi: 10.1016/j.addma.2019.100831.

[129] S. J. Raab, R. Guschlbauer, M. A. Lodes, and C. Körner, "Thermal and Electrical Conductivity of 99.9% Pure Copper Processed via Selective Electron Beam Melting," *Adv. Eng. Mater.*, vol. 18, no. 9, pp. 1661–1666, 2016, doi: 10.1002/adem.201600078.

[130] P. Frigola *et al.*, "Fabricating Copper Components," *Adv. Mater. Process.*, p. 20, 2014.

[131] C. Silbernagel, I. Ashcroft, P. Dickens, and M. Galea, "Electrical resistivity of additively manufactured AlSi10Mg for use in electric motors," *Addit. Manuf.*, vol. 21, no. March, pp. 395–403, 2018, doi: 10.1016/j.addma.2018.03.027.

[132] T. El-Wardany, Y. She, V. Jagdale, J. K. Garofano, J. Liou, and W. Schmidt, "Challenges in 3D Printing of High Conductivity Copper." Aug. 29, 2017, doi: 10.1115/IPACK2017-74306.

[133] A. P. Ventura *et al.*, "The Effect of Aging on the Microstructure of Selective Laser Melted Cu-Ni-Si," *Metall. Mater. Trans. A*, vol. 48, doi: 10.1007/s11661-017-4363-8.

[134] S. Uchida *et al.*, "Microstructures and electrical and mechanical properties of Cu-Cr alloys fabricated by selective laser melting," *Mater. Des.*, vol. 175, p. 107815, 2019, doi: 10.1016/j.matdes.2019.107815.

[135] S. Hou, S. Qi, D. A. Hutt, J. R. Tyrer, M. Mu, and Z. Zhou, "Three dimensional printed electronic devices realised by selective laser melting of copper/high-density-polyethylene powder mixtures," *J. Mater. Process. Technol.*, vol. 254, no. November 2017, pp. 310–324, 2018, doi: 10.1016/j.jmatprotec.2017.11.020.

[136] H. Tiismus, A. Kallaste, T. Vaimann, A. Rassolkin, and A. Belahcen, "Electrical resistivity of additively manufactured silicon steel for electrical machine fabrication," *2019 Electr. Power Qual. Supply Reliab. Conf. 2019 Symp. Electr. Eng. Mechatronics, PQ SEEM 2019*, 2019, doi: 10.1109/PQ.2019.8818252.

[137] Y. Shi, P. Rometsch, K. Yang, F. Palm, and X. Wu, "Characterisation of a novel Sc and Zr modified Al–Mg alloy fabricated by selective laser melting," *Mater. Lett.*, vol. 196, pp. 347–350, 2017, doi: 10.1016/j.matlet.2017.03.089.

[138] K. A. Ibrahim, B. Wu, and N. P. Brandon, "Electrical conductivity and porosity in stainless steel 316L scaffolds for electrochemical devices fabricated using selective laser sintering," *Mater. Des.*, vol. 106, pp. 51–59, 2016, doi: 10.1016/j.matdes.2016.05.096.

[139] P. Pichler, B. J. Simonds, J. W. Sowards, and G. Pottlacher, "Measurements of thermophysical properties of solid and liquid NIST SRM 316L stainless steel," *J. Mater. Sci.*, vol. 55, no. 9, pp. 4081–4093, 2020, doi: 10.1007/s10853-019-04261-6.

[140] "United Performance Metals data sheet - Stainless 316, 316L, 317, 317L."

[141] "Stainless Steel - Grade 316L (UNS S31603)." https://www.azom.com/article.aspx?ArticleID=2382 (accessed Sep. 02, 2021).
[142] "Stainless Steel 316L - 1.4404 Data Sheet - thyssenkrupp Materials (UK)." https://www.thyssenkrupp-materials.co.uk/stainless-steel-316l-14404.html (accessed Sep. 02, 2021).
[143] "Stainless Steel - Austenitic - 1.4404 (316L) Bar and Section." https://www.aalco.co.uk/datasheets/Stainless-Steel-14404-316L-Bar-and-Section_39.ashx (accessed Sep. 02, 2021).
[144] "ASM Material Data Sheet." http://asm.matweb.com/search/SpecificMaterial.asp?bassnum=MQ316Q (accessed Sep. 02, 2021).
[145] T. L. Wire, E. Conductors, and I. Tem-, "Standard Test Method for Resistivity of Electrical Conductor Materials 1," vol. 02, no. Reapproved 2008, pp. 1–5, 2013, doi: 10.1520/B0193-02R08.2.
[146] T. Force, "Standard Test Method for Total Hemispherical Emittance of Surfaces up to 1400 ° C 1," *ASTM International*, vol. i, no. C. pp. 1–10, 2011, doi: 10.1520/C0835-06.2.
[147] W. Conshohocken, "ASTM International, E112: Standard Test Methods for Determining Average Grain Size," *West Conshocken*, vol. 96, no. 2004, pp. 1–26, 1996, doi: 10.1520/E0112-10.Copyright.
[148] "Standard Test Methods for Density of Compacted or Sintered Powder Metallurgy (PM) Products Using Archimedes' Principle 1," Accessed: Aug. 30, 2021. [Online]. Available: www.astm.org,.
[149] Concept Laser GmbH, "1.4404 Materialdatenblatt," 2014.
[150] "Design of experiments | Introduction to Statistics | JMP." https://www.jmp.com/en_ph/statistics-knowledge-portal/what-is-design-of-experiments.html (accessed Sep. 01, 2021).
[151] "Screening Designs." https://www.jmp.com/support/help/en/16.1/index.shtml#page/jmp/screening-designs.shtml%23 (accessed Sep. 01, 2021).
[152] T. Fu, P. Tan, and C. Pang, "A steady-state measurement system for total hemispherical emissivity," *Meas. Sci. Technol.*, vol. 23, no. 2, 2012, doi: 10.1088/0957-0233/23/2/025006.
[153] L. C. Wei, L. E. Ehrlich, M. J. Powell-Palm, C. Montgomery, J. Beuth, and J. A. Malen, "Thermal conductivity of metal powders for powder bed additive manufacturing," *Addit. Manuf.*, vol. 21, pp. 201–208, May 2018, doi: 10.1016/J.ADDMA.2018.02.002.
[154] R. Holm, "The contact resistance. General theory.," in *Electric Contacts*, Berlin: Springer, 1967, pp. 9–11.
[155] "(PDF) Electrical Conductivity and Resistivity | Michael B Heaney - Academia.edu." https://www.academia.edu/29112469/Electrical_Conductivity_and_Resistivity (accessed Aug. 27, 2021).
[156] Y. SINGH, "Electrical Resistivity Measurements: a Review," *Int. J. Mod. Phys. Conf. Ser.*, vol. 22, pp. 745–756, 2013, doi: 10.1142/s2010194513010970.
[157] D. Sheet, "Keysight Technologies 34401A Digital Multimeter," 2016.
[158] V. Models, "A Next-Generation Rack-Mounted Power Supply 1U Multi Range Programmable DC Power Supply," vol. 99, pp. 1–15, 2014.
[159] T. Direct, "Thermocouple characteristics datasheet." .
[160] J. J. Lifton and T. Liu, "Evaluation of the standard measurement uncertainty due to the ISO50 surface determination method for dimensional computed tomography," *Precis. Eng.*, vol. 61, no. August 2019, pp. 82–92, 2020, doi: 10.1016/j.precisioneng.2019.10.004.

[161] Mitutoyo Corporation, "Digital Caliper CD-AX/APX Series," 2015, [Online]. Available: https://www.mitutoyo.co.jp/eng/support/service/catalog/08/E12021.pdf.

[162] J. P. Holman, *Experimental Methods for Engineers 8th edition*. 2012.

[163] "General basic questions - µ-VIS." http://muvis.soton.ac.uk/wiki/index.php/General_basic_questions#What_are_big-endian_and_little-endian.3F (accessed Aug. 28, 2021).

[164] "Otsu Thresholding - The Lab Book Pages." http://www.labbookpages.co.uk/software/imgProc/otsuThreshold.html (accessed Aug. 28, 2021).

[165] "ImageJ User Guide - IJ 1.46r | Analyze Menu." https://imagej.nih.gov/ij/docs/guide/146-30.html#toc-Subsection-30.2 (accessed Aug. 28, 2021).

[166] M. Ma, Z. Wang, M. Gao, and X. Zeng, "Layer thickness dependence of performance in high-power selective laser melting of 1Cr18Ni9Ti stainless steel," *J. Mater. Process. Technol.*, vol. 215, no. 1, pp. 142–150, Jan. 2015, doi: 10.1016/J.JMATPROTEC.2014.07.034.

[167] A. B. Spierings, M. Schneider, and R. Eggenberger, "Comparison of density measurement techniques for additive manufactured metallic parts," doi: 10.1108/13552541111156504.

[168] J. Kozhuthala *et al.*, "Build position-based dimensional deviations of laser powder-bed fusion of stainless steel 316L," *Precis. Eng.*, vol. 67, no. April 2020, pp. 58–68, 2021, doi: 10.1016/j.precisioneng.2020.09.024.

[169] Z. Zhu, S. Lou, and C. Majewski, "Characterisation and correlation of areal surface texture with processing parameters and porosity of High Speed Sintered parts," *Addit. Manuf.*, vol. 36, no. January, p. 101402, 2020, doi: 10.1016/j.addma.2020.101402.

[170] "Sdq (Root Mean Square Gradient) | Area Roughness Parameters | Introduction To Roughness | KEYENCE America." https://www.keyence.com/ss/products/microscope/roughness/surface/sdq-root-mean-square-gradient.jsp (accessed Nov. 01, 2021).

[171] Z. Dong, Y. Liu, W. Wen, J. Ge, and J. Liang, "Effect of hatch spacing on melt pool and as-built quality during selective laser melting of stainless steel: Modeling and experimental approaches," *Materials (Basel).*, vol. 12, no. 1, 2018, doi: 10.3390/ma12010050.

[172] Y. Tian, D. Tomus, P. Rometsch, and X. Wu, "Influences of processing parameters on surface roughness of Hastelloy X produced by selective laser melting," *Addit. Manuf.*, vol. 13, pp. 103–112, 2017, doi: 10.1016/j.addma.2016.10.010.

[173] P. Wüst, A. Edelmann, and R. Hellmann, "Areal surface roughness optimization of maraging steel parts produced by hybrid additive manufacturing," *Materials (Basel).*, vol. 13, no. 2, 2020, doi: 10.3390/ma13020418.

[174] W. Conshohocken, "Standard Test Method for Total Hemispherical Emittance of Surfaces up to 1400 ° C 1," *ASTM International*, vol. i, no. C. pp. 1–10, 2011, doi: 10.1520/C0835-06.2.

[175] W. Liu *et al.*, "FVM and XCT Measurement of Surface Texture of Additively Manufactured Parts," no. September, pp. 2–4, 2021.

[176] W. P. W. Lam, C. Kerr, A. J. Chaudhary, and S. M. Grimes, "The use of Physical Grinding with SiC Abrasive Papers as Preparation Techniques for Increasing the Surface Area of a Substrate Material," *Struct. Struers e-Journal Mater.*, no. 1, 2004.

[177] P. Pichler, B. J. Simonds, J. W. Sowards, and G. Pottlacher, "Measurements of thermophysical properties of solid and liquid NIST SRM 316L stainless steel Metals & corrosion," *J. Mater. Sci.*, vol. 55, pp. 4081–4093, 2020, doi: 10.1007/s10853-019-04261-6.

[178] M. Yakout, M. A. Elbestawi, and S. C. Veldhuis, "A study of thermal expansion coefficients and microstructure during selective laser melting of Invar 36 and stainless steel 316L," *Addit. Manuf.*, vol. 24, pp. 405–418, Dec. 2018, doi: 10.1016/J.ADDMA.2018.09.035.

[179] A. M. Khorasani, I. Gibson, U. S. Awan, and A. Ghaderi, "The effect of SLM process parameters on density, hardness, tensile strength and surface quality of Ti-6Al-4V," *Addit. Manuf.*, vol. 25, no. August 2018, pp. 176–186, 2019, doi: 10.1016/j.addma.2018.09.002.

[180] ISO, "Steels — Micrographic determination of the apparent grain size." .

[181] M. S. Kim, "Effects of processing parameters of selective laser melting process on thermal conductivity of alsi10mg alloy," *Materials (Basel).*, vol. 14, no. 9, 2021, doi: 10.3390/ma14092410.

[182] F. Romei and A. N. Grubišić, "Validation of an additively manufactured resistojet through experimental and computational analysis," *Acta Astronaut.*, vol. 167, pp. 14–22, Feb. 2020, doi: 10.1016/j.actaastro.2019.10.046.

[183] Calex electronics, "Emissivity Table - Calex Electronics limited," vol. 44, no. 0, [Online]. Available: https://www.calex.co.uk/site/wp-content/uploads/2015/07/emissivity-tables.pdf.

[184] F. Romei, "High-Temperature Resistojets for All-Electric Spacecraft," University of Southampton, 2019.

[185] F. Romei, "High Temperature Resistojets for All-Electric Spacecraft Purpose of the PhD research," 2016.

[186] "COMSOL Documentation." https://doc.comsol.com/6.0/docserver/#!/com.comsol.help.heat/heat_ug_theory.07.02.html (accessed Jan. 10, 2022).

[187] E. Isetti, C., Nannei and C. Pisoni, "Oxidation and roughness effects on the total normal emittance of stainless steel," *High Temp. Press.*, vol. 11, no. 4, pp. 393–397, 1979.

[188] M. Rouby and P. Blanchard, "Physical and Mechanical Properties of Stainless Steels," *Stainl. Steels, les Ed. Phys.*, pp. 111–158, 1993.

[189] A.F. Clark, G.E. Childs, and G.H. Wallace, "Electrical resistivity of some engineering alloys at low temperatures," *Cryogenics (Guildf).*, vol. 10, no. 4, pp. 295–305, 1970, doi: 10.1016/0011-2275(70)90056-1.